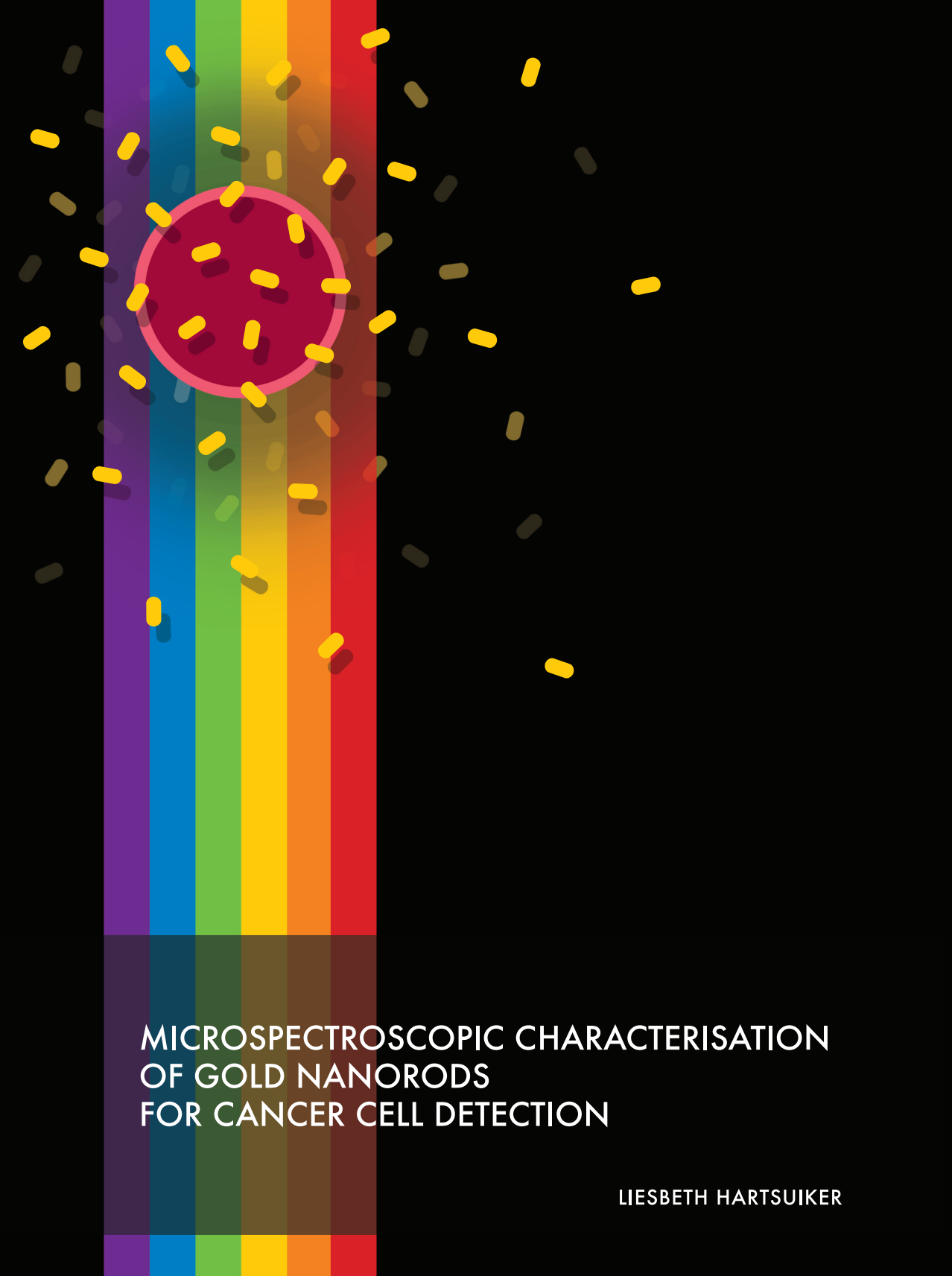

MICROSPECTROSCOPIC CHARACTERISATION OF GOLD NANORODS FOR CANCER CELL DETECTION

LIESBETH HARTSUIKER

Microspectroscopic characterisation of gold nanorods for cancer cell detection

Liesbeth Hartsuiker

Members of the dissertation committee:

Prof. dr.	L.W.M.M. Terstappen (MD)	University of Twente (promotor)
Prof. dr.	T.G. van Leeuwen	University of Amsterdam (promotor)
Dr.	C. Otto	University of Twente (assistent promotor)
Prof. dr.	J.L. Herek	University of Twente
Prof. dr.	J. Greve	University of Twente
Prof. dr.	H.J.C.M. Sterenborg	Erasmus Medical Center
Dr.	S. Manohar	University of Twente
Dr.	A.A. Poot	University of Twente
Prof. dr.	G. van der Steenhoven	University of Twente (chairman and secretary)

This work was funded by SenterNovem IOP Photonic Devices project PRESMITT:
Plasmon resonant nanoparticles for molecular imaging and therapy of tumours: in vitro to preclinical studies (IPD067771).

MIRA Institute for Biomedical Technology and Technical Medicine
University of Twente, P.O.Box 217, NL–7500 AE Enschede

Typeset with LaTeX.
This thesis was printed by Gildeprint, The Netherlands.

ISBN 978-90-365-3240-2

DOI 10.3990/1.9789036532402

Microspectroscopic characterisation of gold nanorods for cancer cell detection

Proefschrift

ter verkrijging van
de graad van doctor aan de Universiteit Twente,
op gezag van de rector magnificus,
prof. dr. H. Brinksma,
volgens besluit van het College voor Promoties
in het openbaar te verdedigen
op donderdag 10 november 2011 om 16.45 uur

door

Liesbeth Hartsuiker

geboren op 19 augustus 1982
te Eindhoven

Dit proefschrift is goedgekeurd door:

Prof. dr.	L.W.M.M. Terstappen	(promotor)
Prof. dr.	T.G. van Leeuwen	(promotor)
Dr.	C. Otto	(assistent promotor)

Contents

CHAPTER 1

Introduction

The application of gold colloids in medicine has a long history. Already in the Middle Ages gold solution (gold water) was considered a curative for various ailments such as pulmonary tuberculosis.[1] Gold drugs appeared more effective in treatment of rheumatoid arthritis, which was developed in the 1930s.[1]

Currently, the use of nanoparticles in biomedical applications is emerging rapidly. Recent developments have led to numerous studies of gold nanoparticles, down to the level of single molecule detection in living cells[2–4]. The application of gold nanoparticles in diagnostics and treatment of early stage carcinomas is the subject of many present small animal studies.

This chapter has been published in Clinical and Biomedical Spectroscopy and Imaging II, Proceedings of SPIE/OSA Biomedical Optics, SPIE, Vol 8087, ISBN: 978-0-8194-8684-4, pp. 80871O.

1.1 Optical properties of gold nanoparticles

Besides their inertness, gold nanoparticles offer unique optical advantages by virtue of surface plasmons.[5,6] Surface plasmons are electron density fluctuations at the boundary of two materials (Figure 1.1A), which oscillate in response to an applied field (Figure 1.1B). If the frequency of the light matches the resonance condition for the nanoparticle, localized surface plasmon resonance (LSPR) occurs (Figure 1.1C). The resonance condition for nanoparticles depends on the material's dielectric function, size or shape of the particles and properties of the embedding medium.[7] Gold nanoparticles exhibit intense and narrow optical absorption bands and, due to LSPR, enhanced absorption cross-sections.[5] In addition, surface plasmons are very sensitive to boundary changes, e.g. adsorption of molecules onto these nanoparticles.

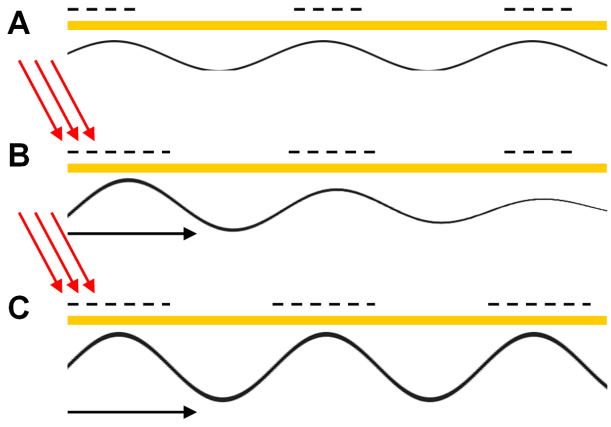

Figure 1.1 : A) Surface plasmon: fluctuating electron density at the boundary of two materials; B) Surface plasmon oscillating in response to incoming (photon) field; C) In case the incoming field matches the surface plasmon frequency, surface plasmon resonance occurs.

Since the surface plasmon bands (SPB) are dependent on the shape, size and clustering of the nanoparticles, by tuning these parameters, the SPB can be customized. Gold nanospheres and shells exhibit a single SPB that can be controlled by altering the size and the ratio of core radius: total radius.[8–13] Rodshaped noble metal nanoparticles have two SPB, which are aspect ratio dependent.[5,8,9,14,14–24] Gold nanoparticle aggregates exhibit even larger enhanced SPR effects, due to a phenomenon called hot spot formation.[2,8,25–27] This morphology dependency enables the SPB of gold nanoparticles to be tuned into the tissue transparent optical window in the near infrared (NIR, i.e., 700-1100 nm, Figure 2.1). These unique

photophysical properties make gold nanoparticles particularly interesting for application in biomedical imaging.

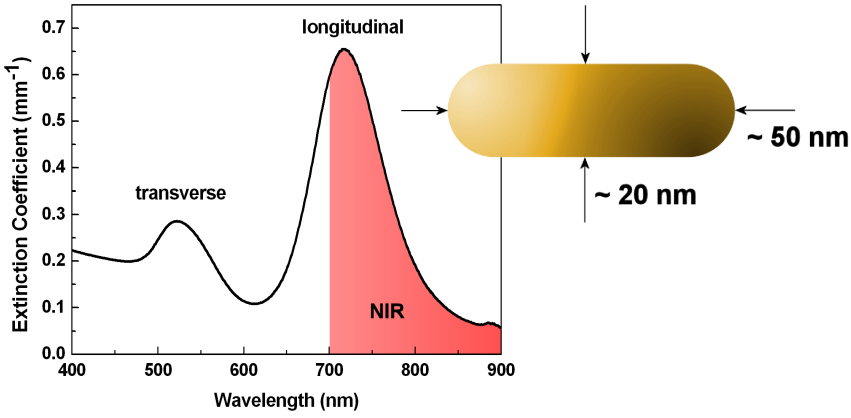

FIGURE 1.2 : By tuning the aspect ratio of gold nanorods, the longitudinal plasmon peak can be shifted into the (near) infrared.

1.2 SYNTHESIS OF GOLD NANOPARTICLES

The ability to tune SPB has led to the synthesis and investigation of a variety of noble metal nanoparticles. Although nanoparticles are also synthesized from palladium,[5,28–30] platinum[31] and bimetallic combinations,[21,32,32,33] gold and silver are the most popular materials for nanoparticle applications[2,14–18,21,32,34–63] because of their stronger surface plasmon band absorbance[33,64] in combination with ease of formation, handling and functionalization.[63]

Although the absorption cross-section of silver nanoparticles is larger than that of gold,[2] gold nanoparticles are in general preferred for molecular sensing and imaging purposes, by virtue of their low toxicity[37,40] and long term history in biomedical applications.[1]

The morphology of gold nanoparticles is mainly directed by their synthesis, which is based on chemical methods.[63] Spherical gold particles can be prepared in roughly two ways. The citrate reduction method results in approximately 20 nm spheres with a citrate capping.[34,35,37,41,47,48,65] The Brust-Schiffrin biphasic synthesis produces spheres variable in diameter from 1.5 to 5.2 nm with an alkanethiol capping.[34,45,58,66]

Such small gold nanospheres are used as seed particles in the preparation of gold nanorods, which are generally prepared by wet chemical synthesis or so-called seeding growth method, which involves cetyl trimethylammoniumbromide (CTAB) micellar templates, resulting in nanorods capped with

a CTAB bilayer (Figure 1.3).[14–18,37,38,40,44,45,50,53,54,67] Gold nanorod sizes can be tuned by altering the ratios of chemicals involved.[14,16–18,20,22,23,67–69]

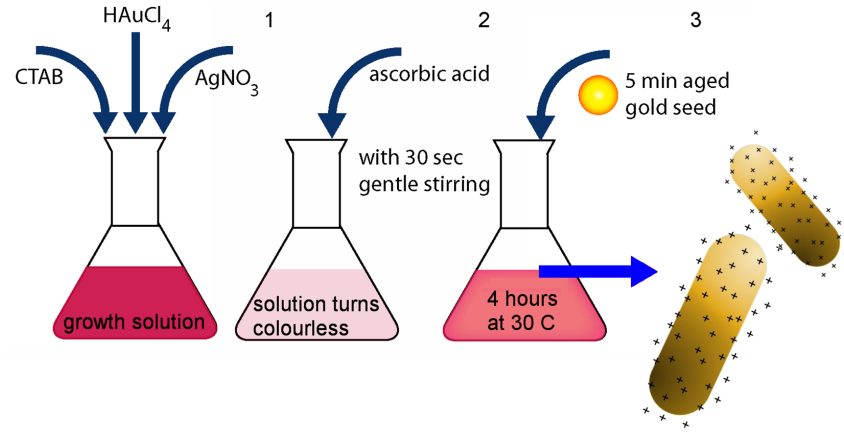

FIGURE 1.3 : Wet chemical synthesis results in GNR covered with positively charged CTAB surfactant

1.3 SURFACE CHEMISTRY

The synthesis of gold nanoparticles directs the particles' surface chemistry, as described in the previous section. The surface chemistry is of great importance, because it determines crucial particle properties such as colloidal stability, cytotoxicity and ease of functionalization.

In general, gold nanoparticles are unstable due to their high surface tension.[70] Stability under physiological conditions is an additional requirement for medical applications. Therefore, depending on the application, a suitable surface modification for stabilization against aggregation has to be applied.

As-prepared (straight from synthesis) gold nanospheres and nanoshells can be readily used in biomedical applications.[47,49] However, gold nanorods are often subjected to surface modifications, because the CTAB bilayer involved in their synthesis (Figure 1.3) is highly cytotoxic[37,50] Although bound CTAB does not appear to be cytotoxic,[37] the general tendency is to remove CTAB from the rod surface by exchange with more biocompatible capping agents.

Biomolecules such as proteins and antibodies are coupled to nanoparticles to increase biorecognition.[14,16–18,32,34–36,42,43,45,48,51–53,55–57,62,65,71–73] For example, nonspecific adsorption of serum proteins mediates the uptake of the nanoparticles *in vivo*.[35,40] Biomolecules have the advantage of inducing very specific cell interactions but their versatility is often limited.

Also synthetic materials, such as polymers can be used for functionalisation. These materials offer the advantages of large-scale reproducibility and controllable chemical structures. Gold nanoparticles have the advantage of easy surface modification by reaction and self assembly of thiolated (-SH) molecules on the gold surface.[63,74] In addition, cyano (-CN) and amino ($-NH_2$) groups have high affinity for gold.[75] Polyelectrolytes (PE) are used to manipulate the surface charge and functional groups on the nanoparticle surface to tune the charge dependent particle-cell interaction.[34,40,41,53,58,76] Bifunctional polymers often are employed as a linker between the gold nanoparticle and targeting antibodies.[32,48,61]

Thiolated polyethylene glycol (PEG-SH) is widely used on the surface of gold nanoparticles[34,36,38,42–44,46,48,65,74,77–79] as well as alkanethiolates[34,45,58] and alkaneamines.[36] PEG is particularly popular due to its *in vivo* stealth character: it discourages protein adsorption (protein corona) to the particle surface (preventing uptake by the reticuloendothelial system, RES) and therewith increases the biocirculation time.[43,44,46] For enhanced sensing or imaging properties, dyes or markers can be incorporated in the surface chemistry.[39,48,60,71,74,76]

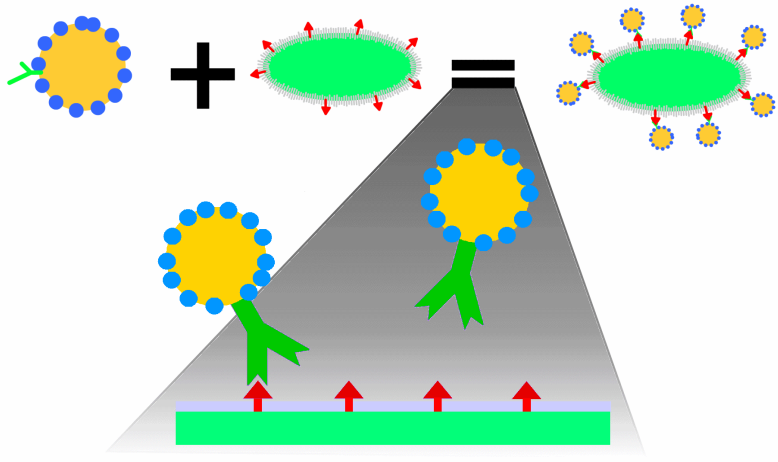

FIGURE 1.4 : Active targeting of cancer cells with antibody-functionalized gold nanoparticles. The GNP bind to specific cell receptors, which are (over)expressed in cancer cells.

1.4 Gold nanoparticles as contrast agent

Tumour imaging suffers from low contrast with respect to the surrounding tissue. By administering gold nanoparticles with NIR-SPB to the tumour site, high contrast non-invasive cancer imaging can be achieved. For tumour imaging, the gold nanoparticles ought to be directed to the target tumour cells, which can be achieved by passive and active targeting.

Passive targeting comprises the accumulation of metal nanoparticles in target tissues due to non-specific effects related to its physicochemical characteristics (e.g. size, surface charge, hydrophobicity). Tumours generally exhibit the enhanced permeability and retention (EPR) effect: a leaky vasculature, which in combination with a lack of effective lymphatic drainage leads to abnormal molecular transport dynamics, allowing nonspecific accumulation by means of extravasation.[80]

Active targeting aims at specific cell receptors overexpressed in target tissues (e.g. epidermal growth factor receptor EGFR on several types of cancer cells) being recognized by antibody ligands displayed on the metal nanoparticle (Figure 1.4). By conjugating gold nanoparticles to certain peptides, cell nuclei can also be effectively targeted[45,51,52] which offers opportunities for applications in the field of gene therapy.[54]

Once the gold nanoparticles are situated at the target site, they can be detected by several techniques ranging from conventional light-based microscopy (including fluorescence microscopy) to non-invasive photoacoustics or Raman spectroscopy. The use of gold nanoparticles eliminates the need for cell staining, due to their enhanced and selective scattering properties and the optional incorporation of dyes or markers in their surface chemistry. However, due to the lack of contrast in bright field imaging of cells, generally alternative contrast improving light based microscopy techniques are applied.

1.5 Microscopic detection - *in vitro*

In general, light microscopy based techniques are used to demonstrate principles of cell membrane targeting and endocytosis of gold nanoparticles. Staining with fluorescently labelled secondary antibodies is often applied to verify the nanoparticle targeting of cells (Figure 1.5A),[55] but scanning electron microscopy (SEM) is gaining in popularity as well because of its high resolution (Figure 1.5B).[55,56]

Whereas light microscopy and SEM are sufficient to determine whether gold nanoparticles are on or in the cells, higher resolution transmission electron microscopy (TEM) is required to resolve where exactly gold nanoparticles end up in cells and tissues (Figure 1.5C, D).[81]

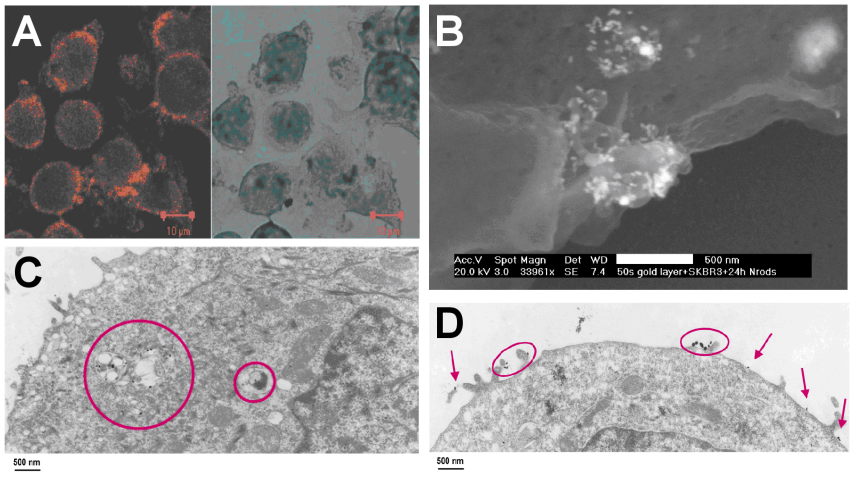

FIGURE 1.5 : A) Confocal reflectance images (left) and bright field images (right) of (a) SKBR3 cells incubated with silver-stained HER81-gold sphere conjugates; B) Conventional below lens SEM image of an SKBR3 cell incubated overnight with HER81-gold nanorod conjugates showing intracellular GNR clusters ; C) TEM image of an SKBR3 cell incubated with HER81-gold nanorod conjugates overnight showing the nanoparticles present within intracellular vesicles and D) TEM image of an SKBR3 cell briefly incubated with HER81-gold nanorod conjugates showing the nanoparticles bound to the cell membrane.[81]

1.6 SPECTROSCOPIC DETECTION - *in vivo*

In addition to *in vitro* studies, TEM is used as analysis tool in for example *in vivo* biodistribution studies to track where gold nanoparticles travel in animal models, usually mice.[41,48,57] Like TEM, generally applied spectroscopy techniques such as instrumental neutron activation analysis (INAA),[34,41] inductively coupled plasma mass spectrometry (ICP)[43,44] and graphite furnace atomic absorption spectrometry (GFAAS)[59] require *ex vivo* tissue samples, for which the test animals need to be sacrificed. Recently, these analysis techniques are applied to verify the outcomes of non-invasive *in vivo* sensing techniques that are currently being developed, such as photoacoustic and Raman imaging,[15,38,82] which may be particularly interesting for sensing gold nanoparticles.

In photoacoustics, the emission of sound originating from local heating after irradiation with light is detected. Using photoacoustic tomography, the distribution of optical absorbance in tissue can be mapped, enabling for example whole breast imaging.[83] Due to the strong optical response of gold nanoparticles, they can well serve as contrast agents in photoacoustic imaging (Figure 1.6), which, in case they are tumour targeted, allows photoacoustic tumour imaging.

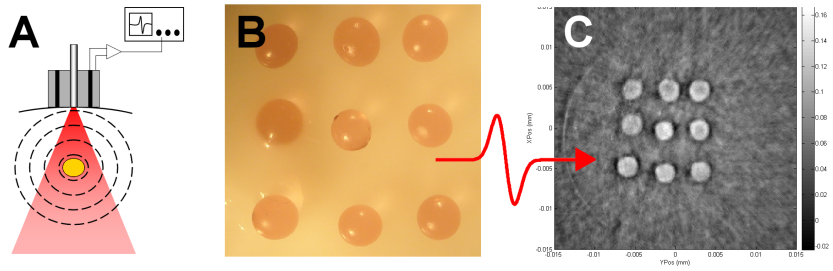

FIGURE 1.6 : A) Photoacoustic principle of detecting the sound generated by a pressure wave from a gold nanoparticle after absorption of a laser pulse; B) Gel beads encapsulating 25nm gold spheres, embedded in tissue mimicking medium; C) Photoacoustic image from the gel beads in B (top illumination).

Raman spectroscopy is based on the detection of energy differences in inelastic photon scattering which are specific for a given chemical bond, allowing identification of molecules: the vibrational information forms a spectral fingerprint of the molecule (Figure 1.7).

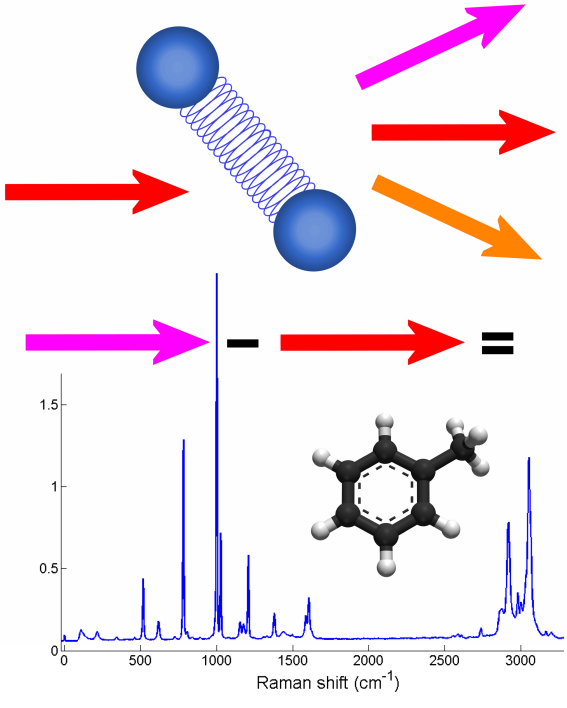

FIGURE 1.7 : Molecules can be identified with Raman scattering due to atomic bond specific interactions with monochromatic light. Interaction with a photon alters the state of the atomic vibration, causing the scattered light to be of a different frequency than the incident light. This shift in frequency is characteristic for each atomic bond vibration, enabling the identification of molecules, in this example toluene.

The typically very weak spontaneous Raman scattering is greatly enhanced in the proximity of gold surfaces, due to the presence of local surface plasmons[5]: so-called Surface enhanced Raman scattering (SERS). In surface enhanced resonance Raman spectroscopy (SERRS), the excitation wavelength is equal or close to the optimum of the plasmon band and a localized surface plasmon resonance (LSPR) occurs, increasing the Raman scattering cross section even more. SERS based gold nanoparticles enable targeted studies in living biological systems[32,39,42,62] (Figure 1.8), allowing molecular analysis of cancerous environments, even down to single molecule detection as was claimed recently.[2–4]

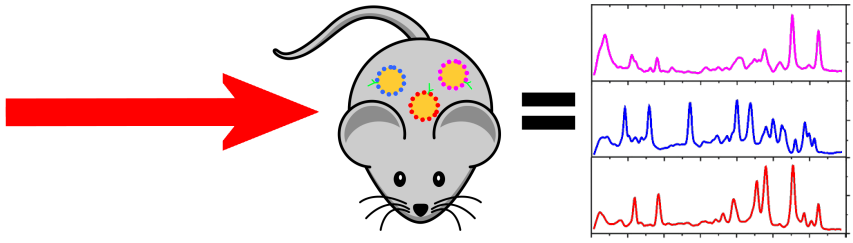

FIGURE 1.8 : Schematic representation of *in vivo* Raman probing of SERS-based gold nanoparticles. Upon laser irradiation (red arrow), the Raman-active coating of the gold nanoparticles produces a unique spectral fingerprint. This allows detection of multiple tags simultaneously within the same animal.

1.7 GOLD NANOPARTICLES FOR TUMOUR TREATMENT

Gold nanoparticle applications involve not only the detection of (early stage) tumours; ideally, they can also be used in non-invasive cancer treatment once they are at the target tissue site.

Gold nanoparticles intensely absorb light in their plasmon resonance band(s), causing an increase of the local temperature. Since the plasmon bands of gold nanoparticles can be tuned into the near-infrared (NIR) tissue transparent window by altering the particles shape or dimensions (Figure 1.2), this offers a great opportunity for minimally invasive *in vivo* thermal ablation treatments (photothermolysis): conforming a lethal dose of heat to the gold targeted tissue volume with little damage to intervening and surrounding normal tissue (Figure 1.9A). Alternatively, cancer cell membrane rupture can be induced by generating microbubbles by cavitation dynamics around clusters of membrane-targeted gold nanoparticles.[84–86] Both techniques make use of pulsed laser light.

In addition to photothermal therapies, the optical absorbance properties of gold nanoparticles can also be exploited in drug delivery mechanisms. Recently explored mechanisms comprise actively targeted gold nanoparti-

cles, which release an anticancer therapeutic by localized heating (Figure 1.9B)[46,54,87] or by environmentally triggered chemical exchange reactions.[60]

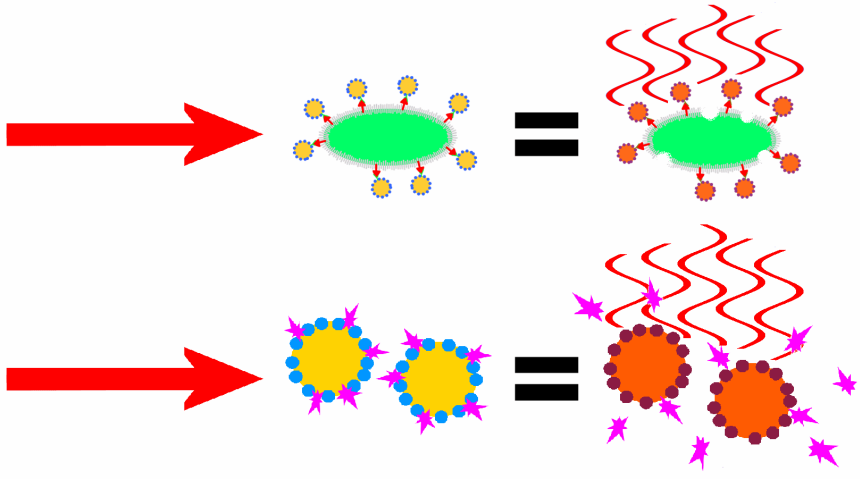

FIGURE 1.9 : Gold nanoparticles as agents for tumour treatment by localized heating effects: A) cell damage (photothermolysis) and B) controlled drug delivery

1.8 OUTLINE OF THE THESIS

Due to their biocompatibility in combination with their enhanced absorption cross-sections tuneable into the near-infrared, gold nanoparticles are promising agents for both detection and treatment of tumours. Gold nanospheres are widely available, by virtue of their well-known synthesis procedures and are therefore mostly used in cell applications. However, for non-invasive detection and treatment shells and rods are the more popular species, because their tunable plasmon bands enable application within the near-infrared optical window.

There is a remarkable variance in the cytotoxicity and uptake of gold nanoparticles with respect to functionalization, surfactant coating, size, and shape. The effects of gold nanoparticles are dependent on the type of cells used as well, due to the complexity of biological processing, which involves physicochemistry, aggregation, and interactions with biomolecules (e.g. serum proteins).

Before therapeutic applications of gold nanoparticles can be approved, proper characterization of gold nanoparticles and their interactions with and effects on cancer cells need to be addressed. The aim of this thesis is to characterize gold nanorods (GNR) and their interactions with breast cancer cells in a non-invasive manner. The optical response of gold nanoparticles is

used as a sensitive reporter of these interactions. GNR exhibit characteristic absorption and emission spectra due to surface plasmon effects. For the detection of fluorescence and Raman spectra, Raman microspectroscopy is the main tool used during these studies. Chapter 2 discusses our confocal micro-Raman setup and the data correction and analysis routines which we apply throughout the remainder of the thesis.

At first, unperturbed breast cancer cells are subjected to Raman mapping. Chapter 3 describes the chemical composition of single live cells from the breast carcinoma cell lines MDA-MB-231, MDA-MB-435s and SK-BR-3, as revealed by Raman microspectroscopy. These three ductal breast carcinoma cell lines have a different expression of the Her2/neu receptor, which is overexpressed in 25 to 30 percent of human primary breast carcinomas and is a common prognostic and predictive factor in tumour subtype screening.

Secondly, we discuss the optical responses of in house synthesized GNR, in chapter 4 of this thesis. We show that the GNR exhibit fluorescence emission which dominates its optical emission spectra. We show, using Raman mapping, that the optical response of GNR in SK-BR-3 breast cancer cells differs from the response of GNR in dispersion and that the spectral distribution is spatially non-uniform. The fluorescence emission maxima, as well as the band shapes, change for nanorods at different locations in the cells. The fluorescence emission coincides mostly with the Raman fingerprint region from 500 cm^{-1} to 1800 cm^{-1}, when excited with light with a wavelength of 647.1 nm. The Raman response in the high wavenumber region from 2700 cm^{-1} to 3600 cm^{-1} is little or not affected by fluorescence from the gold nanorods and reveals a coincidence of increased lipid signals with locations of the nanorods in the cells. This observation suggests that gold nanorods are locally accumulating in lipid vesicles within the cells.

In order to gain deeper understanding of the fluorescence emission of GNR, chapter 5 discusses the mechanisms of photoluminescence of gold nanostructures on the basis of a literature overview. This discussion includes emission in both the visible and the infrared (IR). Both single photon induced luminescence and non-linear effects are covered, as well as emission enhancement mechanisms involving surface plasmons. By comparing the optical responses of GNR in our systems to the profiles reported in literature, we position our results within the current field.

In chapter 6, the interaction of gold nanoparticles with breast cancer cells is visualized, exploiting a conventional below lens scanning electron microscopy (SEM) system. We show that high resolution images of GNP on and in SK-BR-3 tumour cells can be obtained using conventional SEM. For this purpose, we developed a novel procedure to prepare samples without the use of metals to cover or chemically treat the cells.

In order to increase their contrast as molecular probes for *in vivo* tissue imaging, gold nanoparticles are often additionally labelled. In chapter 7, the properties of the adsorption of common near-infrared dye indocyanine

green (ICG) to gold nanoparticles are investigated. ICG is approved by the food and drug administration (FDA) for *in vivo* applications and is currently used extensively as a marker in clinical imaging applications, where it has obtained a major role in applications concerning the detection of tumorous metastasis. The amphiphilic nature of ICG leads to an environment dependent organization of the dye and is accompanied by changes in optical properties, which are measured with absorbance and fluorescence spectroscopy. Based on the optical responses of ICG in different systems, corresponding to different stages in the GNR synthesis, we proposed a model for ICG adsorption on GNPs in relation to the dye monomer-dimer equilibrium in the bulk solution. The concentrations of chemicals crucial to GNR synthesis significantly affect the ICG monomer-dimer equilibrium, stressing the importance of careful control of experimental conditions for effective dye labelling of gold nanostructures.

To gain better insight in the interaction of GNR with breast cancer cells on a biochemical level, literally, a deeper look will have to be taken into the cells. In chapter 8, the trajectory towards 3D Raman imaging is outlined. The resolution of the Raman imaging setup in the z-direction is discussed as well as the adjustment of the setup to enable depth imaging accordingly. Initial depth measurements were carried out and z-stack images of unperturbed SK-BR-3 breast cancer cells are presented. In addition, recommendations for future work in this field are provided.

CHAPTER 2

Confocal Raman mapping of breast carcinoma cells

Newly developed strategies for the detection and treatment of early stage carcinomas often make use of gold nanoparticles for contrast enhancement. Gold nanoparticles of many different shapes and sizes have been administered to cancer cells and detected with different techniques, as was discussed in Chapter 1. However, in order to be able to evaluate the potential influence of nanoparticles on the appearance, morphology and chemical response of the target cells, we first need to determine the "natural" or unperturbed response of those cells. In this thesis, Raman microspectroscopic imaging is the main tool in assessing the interaction between gold nanorods and breast cancer cells on a biochemical level.

We established initial Raman fingerprints of plain SK-BR-3 cells, which are often used as a model in breast cancer research. We were able to obtain detailed Raman mapping of live cells with low laser doses. In addition, we determined the effect of standard paraformaldehyde fixation on the Raman signature of the cells.

Part of this chapter has been published in the Programme and abstract book of the Annual Symposium of the IEEE-EMBS Benelux Chapter, 2009, ISBN: 978-90-365-2933-4, pp. 32-35

2.1 Raman microspectroscopy

Raman microspectroscopy is an optical spectroscopy technique based on the detection of energy differences in inelastic photon scattering. Although most of the photons are absorbed or transmitted when monochromatic light interacts with matter, a small fraction is scattered. The bulk of these scattered photons are elastically scattered (Rayleigh scattering), implying that the scattered photons have the same energy (frequency) and wavelength as the incident photons (Figure 2.1a, $h\nu_0$). However, a small fraction of the scattered photons (approximately 1 in 10 million) are emitted with a frequency different from the frequency of the incident photons. This process is called inelastic scattering or Raman scattering named after its discoverer C.V. Raman.[88] Two kinds of Raman scattering can be distinguished. In Stokes Raman scattering, a photon is emitted that possesses less energy than the incident photon ($h\nu_0$-$h\nu_s$) and as a result is shifted to the red part of the spectrum (Figure 2.1b). In anti-Stokes Raman scattering, emission of a photon occurs that has gained energy with respect to the incident photon ($h\nu_0$+$h\nu_s$) and which therefore is blue-shifted (Figure 2.1c).

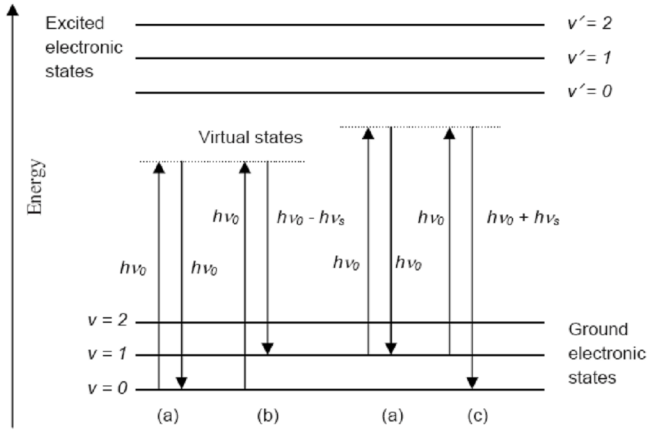

Figure 2.1 : Photon interaction with a chemical bond in terms of molecular energy diagrams: a) elastic, Rayleigh scattering; b) Stokes Raman scattering and c) anti-Stokes Raman scattering.

The intensity of Raman scattering depends on the initial population of the energy level of the molecule, the intensity of the incident radiation and the amount of change in polarizability of the molecule (see Appendix to this Chapter) and is represented as a function of the wavenumber shift $\Delta(\mathrm{cm}^{-1})$:

$$\Delta = \left(\frac{1}{\lambda_0} - \frac{1}{\lambda_s}\right) 10^7 \tag{2.1}$$

Where λ_0(nm) is the excitation wavelength and λ_s(nm) is the scattering wavelength of the photons. The frequency shifts in Raman scattering are specific for a given chemical bond vibration, which allows identification of molecules: the vibrational information forms a spectral fingerprint of the molecule. When applied to biological samples, such as cells, Raman microspectroscopy can be used to determine the spatial molecular composition from small sample volumes.

2.2 Confocal microspectroscopy

2.2.1 confocal raman setup

Raman spectra were acquired on an in-house developed instrument, which has been described before.[89] Briefly, as shown in Figure 2.2, the 647 nm excitation light from a Kr^+ laser (Innova 90-K; Coherent Inc., Santa Clara, CA) is focused through a 63×/1.0 NA water-dipping objective (Zeiss W Plan Apochromat; Carl Zeiss MicroImaging GmbH, Göttingen, Germany) onto the sample. The same objective collects the scattered light, which passes through a dichroic beamsplitter (DCLP660; Chroma Technology, Rockingham, VT) and a RazorEdge 647 filter (Semrock Inc., Rochester, NY).

The use of a pinhole allows the suppression of image degrading out-of-focus information (Figure 2.2B), the control of depth of field and thereby enables collection of serial optical sections of specimens thicker than the focal plane (3D imaging). In turn, this increases the effective resolution and improves the signal-to-noise ratio. The achievable thickness of the focal plane is largely determined by the wavelength of the used light divided by the numerical aperture of the objective lens.

We used a 15 μm pinhole at the entrance of a custom made spectrograph, dispersing in the range of 646-849 nm, and detected the Raman signal by a 1600×200 pixels back-illuminated CCD camera (Newton DU-970N-BV; Andor Technology, Belfast, Northern Ireland). This spectrograph/CCD combination allowed us to record Raman shifts from -50 to 3600 cm^{-1}. This large spectral region enabled us to simultaneously record vibrations in the cellular fingerprint region, in the intermediate region (or Raman silent region) and in the high frequency region with an average spectral resolution of 2.3 cm^{-1}/pixel.

Raman spectral mapping experiments were performed by scanning the laser beam over a cell of interest in a raster pattern and accumulating a full Raman spectrum at each pixel. Raman maps of 32×32 or 64×64 spectra in

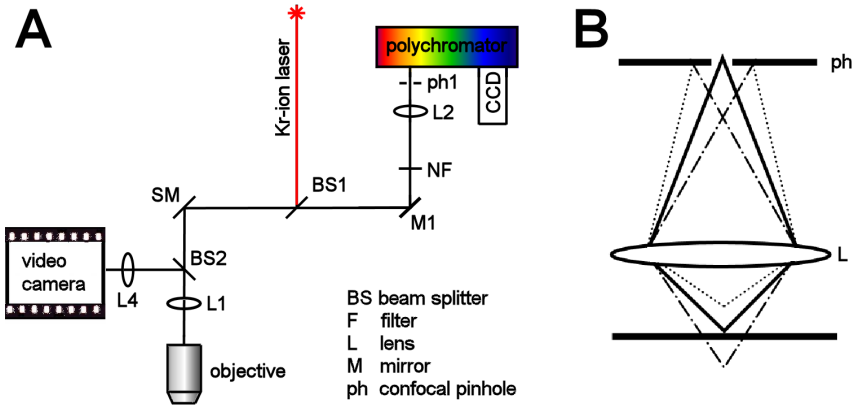

FIGURE 2.2 : A) Schematic representations of the confocal Raman setup with lenses L1, L2 and L4 with focal lengths of 100, 30 and 75 mm respectively, a confocal pinhole of 15 ţm in front of a polychromator dispersing in the range of 646-849 nm; B) Schematic illustration of the confocality principle: only light coming from the focal plane is focussed at the position of the confocal pinhole, out-of-focus light is rejected.

a scanning area of 20×20 μm were acquired with an acquisition time of 0.5 s per pixel. Laser powers were varied from 50 mW to 25 mW and 10 mW under the objective.

2.2.2 CONFOCAL RESOLUTION

In a diffraction limited lens, the lateral laser spot size under the objective ω_0, thus the lateral resolution, can be determined using Equation 2.2,[90,91] provided that the Gaussian beam profile is truncated at $1/e^2$ intensity level:

$$\omega_0 = \frac{1.83\lambda_0}{4NA} \tag{2.2}$$

Where λ_0(nm) is the laser wavelength in vacuum and NA the numerical aperture of the objective. The lateral resolution is only limited by the diffraction, since the back-projection of the confocal pinhole in the focal plane is larger than the diffraction-limited illumination spot. However, due to spherical aberrations, the lateral spot size is estimated to be 20% larger than the value calculated using Equation 2.2, resulting in a ω_0 of approximately 350 nm for the 647.1 nm excitation wavelength.

The focal depth of the Gaussian laser beam depends on the lateral beam waist, according to Equation 2.3[92,93]:

$$\omega_z = \omega_0 \sqrt{1 + \frac{Z_R^2 \lambda^2}{\pi^2 \omega_0^4}} = \omega_0 \sqrt{2} \tag{2.3}$$

Where Z_R is the Rayleigh range:

$$Z_R = \frac{\pi \omega_0^2}{\lambda} \tag{2.4}$$

In our setup, we use a circular pinhole to reject out of focus light and to set the desired confocal resolution. Therefore, the axial resolution passed through the field stop would be limited directlyt o the chosen pinhole size[93,94]:

$$\omega_{ph} = A\omega_Z \tag{2.5}$$

Where A represents the total magnification of the imaging system. The axial resolution of the system is defined as the full width half maximum (FWHM) of the beam passing through the confocal pinhole[93,94]:

$$I_{ph} = P_0 \left(1 - exp\left(\frac{-2R_{ph}^2}{\omega_{ph}^2}\right)\right) \tag{2.6}$$

In which P_0 is the total beam power, R_{ph} the pinhole radius and ω_{ph} proportional to ω_0. With a pinhole diameter of 15μm, the axial resolution of the Raman microspectroscope was calculated to be approximately 1.5 μm.
Note that the measurement volume is not dependent on the pinhole, but on the illumination as well as the detection geometry (Equation 2.3). The probe volumes of our setup, when a 63×/1.0 NA water-dipping objective is used is estimated at 0.3 fL.

2.3 Data correction

Each Raman image results in a 3D hyper-spectral data cube (spatial × spatial × spectral), which is converted to a 2D data matrix (spatial × spectral) for subsequent corrections. Data pre-procession consisted of 1)

removal of cosmic ray events, 2) subtraction of the CCD camera offset, 3) calibration of the wavenumber axis and 4) correction of frequency dependent setup transmission. All data manipulations were performed in routines written in MATLAB 7.6 (The Math-Works Inc., Natick, MA).

2.3.1 COSMIC RAYS

The detection of cosmic rays (CR) leads to high intensity spikes in the acquired signal, with an average width of 1-4 pixels and an intensity much higher than the detected Raman signal. CR are removed from the signal using an estimation of the first derivative of the signal and setting a threshold accordingly.

2.3.2 CCD OFFSET

The CCD gives a default spectral readout in absence of photons. This CCD offset is a systemic contribution resulting from the analogue-to-digital converter (ADC) in a CCD camera system. An ADC can not process negative numbers and thus works on a set of positive numbers. To avoid the negative-number problem, the bias voltage is set to a certain level, implying that even when no photons hit the CCD and the exposure time is set to zero, the output value is non-zero. This bias or offset is present in every collected Raman spectrum. Before each measurement, a set of spectra was acquired with no light (laser light blocked) and with acquisition settings (acquisition time, gain) equal to the sample acquisition settings. The mean value of these bias spectra was considered as an offset and subtracted from each Raman spectrum obtained.

2.3.3 WAVENUMBER CALIBRATION

During calibration of the wavenumber axis, pixels are converted to wavenumbers, using the laser band at 0 cm^{-1} and the well-known toluene bands at 521, 785, 1004, 1210, 1604, 2738, 2866, 2921, 2981, and 3054 cm^{-1}.

2.3.4 SETUP RESPONSE

Every optical component in the confocal Raman setup has its specific transmission characteristics, the sum of which makes up the total Raman setup transmission. Especially the transmissions of the objective, dichroic beamsplitter, monochromator gratings and the CCD camera are dependent on the optical frequency. Moreover, as the CCD chip consists of several semi-reflecting surfaces, reflection of reflected light occurs. This effect, also known as etaloning, causes an interference pattern generated by CCD, which is illustrated in Figure 2.3.

For the correction of frequency dependent optical detection efficiency, two calibration spectra were acquired. Besides a mean bias spectrum (CCD

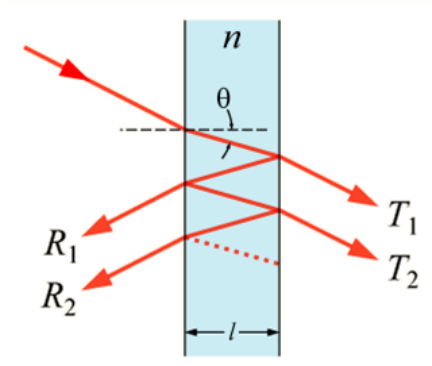

FIGURE 2.3 : Schematic illustration of the etaloning effect: light enters the CCD and undergoes multiple internal reflections. R_i marks reflected light, while T_i marks the transmitted light, θ the angle the light travels through the etalon n (the CCD) and l its thickness.

offset), a flat field frame is recorded, also with acquisition settings (acquisition time, gain) equal to the sample acquisition settings. The flat field frame measures the response of each CCD pixel to illumination of the known emission profile of a tungsten halogen light source (AvaLight-HAL; Avantes BV, Eerbeek, The Netherlands). The measured spectrum of the lamp was corrected for CCD offset and the correction spectrum (flat-field spectrum) was obtained by division of the measured spectrum of the lamp by its theoretical emission (Figure 2.4), as determined by:

$$P = \frac{2\pi c^2 h}{\lambda^5 exp^{\frac{hc}{\lambda kT}} - 1} \tag{2.7}$$

Which is the spectrum of the radiating black body, or Planck's curve. The correction spectrum was then normalized to unity before the measured Raman spectra were divided by it to correct them for the setup's frequency dependent throughput.

2.3.5 SINGULAR VALUE DECOMPOSITION

Despite the sensitivity of the setup, the signal-to-noise ratio (SNR) in non-resonant Raman imaging is low due to the small Raman cross-sections of the biological components in cells. In order to suppress random noise, we applied singular value decomposition (SVD).[95,96]

The main idea of SVD-based filtering is to consider the noisy signal as a vector in n-dimensional vector space, which is determined by a number of measured variables. This vector space is separated in orthogonal components, the singular vectors, which can then be verified and rejected if they belong to the noisy basis vectors. After singular value rejection, a new data matrix is constructed, containing less noise.

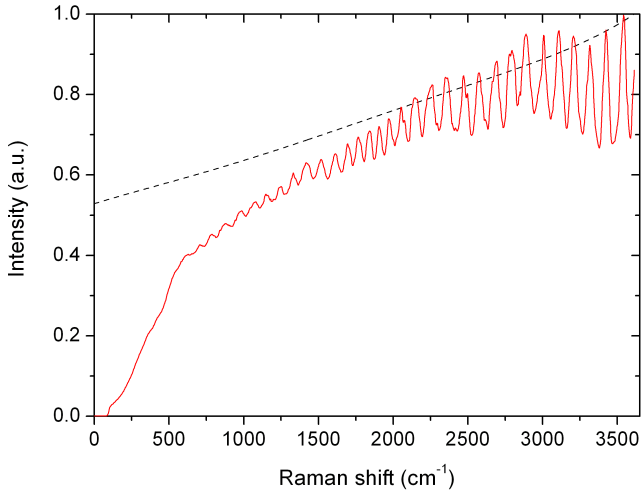

FIGURE 2.4 : Normalized theoretical (dashed line) and experimental (line) emissions of the tungsten halogen light source used to construct the normalized flat-field spectrum for correction of the Raman spectra for frequency dependent setup response.

The challenge in the use of SVD filtering is to rationally decide on the number of statistically significant singular values. Initially, rejection of noisy singular vectors was based on the magnitude of the singular vectors as well as the autocorrelation for each basis vector, which indicates the noise level within the vectors.[97] However, for complex Raman spectra, as is the case for biological systems and especially in combination with gold nanoparticles (Chapter 4), autocorrelation of the basis vectors is not straightforward. Moreover, as the occurrence of gold nanoparticle-related Raman spectra is limited, the magnitude of their singular vectors is small. Therefore, application of the above mentioned selection procedure can result in premature discard of important information. To prevent this, for all data sets mentioned, the first 20 singular vectors were kept, while the rest were rejected. The first 20 singular vectors include all important spectral information, as was verified by the mentioned selection criteria.[97] The additional noise, which is inevitably included by the arbitrary choice of important singular vectors, is, to a large extent, removed during further data processing after multivariate analysis.

2.4 Data analysis

The SVD treated data was analyzed by both univariate and multivariate data analysis procedures.

2.4.1 UNIVARIATE ANALYSIS

Univariate Raman images were constructed by plotting the integrated intensity of the vibrational areas of interest as a function of position.[95] Figure 2.5A shows a Raman intensity map of an SK-BR-3 cell, integrated over the entire fingerprint region (Figure 2.5B, 500-1800 cm^{-1}) revealing that Raman scattering is most intense in the cell's cytoplasm. Distributions of cellular components such as DNA, proteins and lipids can also be obtained, by selecting representative Raman bands for signal integration (Figure 2.5CD).

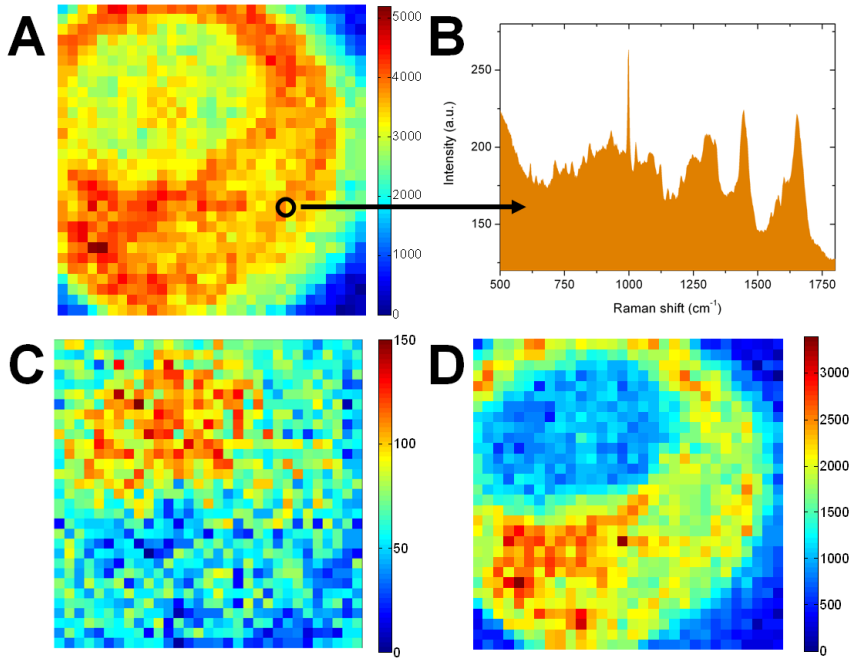

FIGURE 2.5 : A) The univariate image of the fingerprint region (500-1800 cm^{-1}) of an SK-BR-3 cell. Each pixel represents the integrated Raman signal over the entire fingerprint region, illustrated in B). In case we integrated over a specific Raman band, distributions of cellular components can be mapped. C) DNA distribution (780 cm^{-1}, Δ=25 cm^{-1}) and D) lipid distribution (2850 cm^{-1}, Δ=30 cm^{-1}) .

2.4.2 MULTIVARIATE ANALYSIS

In multivariate analysis, both principal component analysis (PCA) and hierarchical cluster analysis (HCA) were performed on the hyperspectral data sets.

PCA identifies existing dependencies between registered wavenumbers in the measured Raman spectra and represents the data in a new orthogonal space of reduced dimensionality. If there is a correlation between the observed m variables, m can be represented as a linear combination of n linearly independent variables, the principal components ($n < m$). The higher the correlation, the smaller the number of principal components describing the original variables.
The results of a PCA are typically discussed in terms of component scores and loadings. Component scores are the transformed variable values corresponding to a particular case in the data; loadings represent the variance each original variable would have if the data were projected onto a given PCA axis.[98]

HCA is an unsupervised multivariate analysis technique that clusters spectra of high similarity together, i.e. creates a partitioning of the cellular space into several clusters based on the measured Raman spectra of the cell.[95,96] Hierarchical clustering creates a hierarchy of clusters which may be represented in a dendrogram (Figure 2.6). We used the scores obtained from PCA as input variables, squared Euclidean distances as distance measure and Ward's algorithm to partition Raman spectra into clusters.[99]

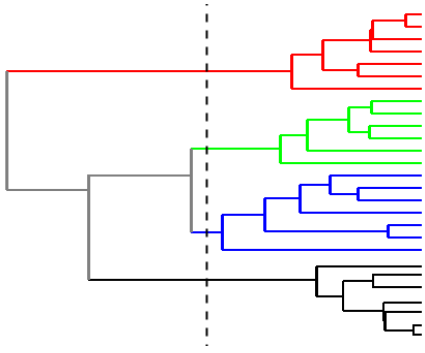

FIGURE 2.6 : Dendrogram of the hierarchical binary cluster tree. The height of each branch represents the distance between the two connected objects (Ward's distance). In this case, the number of clusters was specified as 4 (dashed cut-off line).

With HCA we can visualize the regions in cells with high Raman spectral similarity (Figure 2.8B). Average Raman spectra calculated from each cluster can reliably be assigned to particular cellular structures, based on characteristic Raman bands (Figure 2.7). To further reduce common noise, the average Raman cluster spectrum assigned to the surrounding medium was subtracted from the cell's cluster average spectra (Figure 2.8C).

2.5 Cell sample preparation

For the experiments described here and in the remainder of this thesis, in principle SK-BR-3 cells were used, which are often used as a model in breast cancer research.[100]

SK-BR-3 cells were cultured in RPMI 1640 medium (Invitrogen) supplemented with glutamine, 10% FBS (Fetal Bovine Serum) with antibiotics. Cells were maintained in an incubator at 37 °C and 5% CO_2. The cells were detached from the tissue culture substrates using trypsin. The cells were then replated on individual subtrates with a seeding density of 60,000 cells/cm^2 and allowed to grow to 80% confluence for 2 days. Initially, glass microscopy cover slips (10 mm diameter, 170 μm thickness) were used as cell substrate, because of their ease of use. Due to the confocality of our Raman microspectrometer, the fluorescence background of the glass on the Raman signal was negligible, provided the focal plane was set above the substrate. In order to suppress any background signals, for high quality Raman spectra of cells, CaF_2 slides (20 mm diameter, 2 mm thickness) were used as substrates.

We have performed measurements in different cell media. Initially, just before the measurements took place, the substrates with attached live SK-BR-3 cells were removed from the cell medium and immersed in a 1X phosphate buffered saline (PBS) solution. However, the viability of cells in PBS is limited. Therefore, a day before measurement, the proliferation medium was exchanged for RPMI without the pH indicator phenol red, to preclude fluorescence emission of phenol red during Raman probing. This RPMI medium was also supplemented with 10% Fetal Calf Serum (FCS) and 1% Penicillin Streptomycin (PS). Prior to the transfer of cells from the incubator to the Raman microscope, HEPES buffer was added to the cell medium, which maintains the physiological pH of the medium while the cells are outside the incubator.

A part of the cells was fixed using a 4% paraformaldehyde (PFA) solution in 1X PBS during 20 minutes at room temperature (Tr = 22 °C). Fixed cells were rinsed with 1X PBS at least three times before measuring.

2.6 Results and discussion

Figure 2.7 shows high resolution, background corrected average cluster spectra in the fingerprint region (550-1800 cm^{-1}) of an SK-BR-3 cell. The Raman bands are identified and assigned based on literature values.[94,95,101–103] The vertical bars highlight typical prominent differences in the average cluster spectra and their assignments. Based on the assignments, one can distinguish clusters related to different cellular components (e.g. DNA, lipids).

Probing SK-BR-3 with 50 mW of laser power resulted in a high signal-to-noise ratio (SNR) in the Raman spectra, as is illustrated in Figure 2.7. When a 64×64 spectral image is acquired, a more detailed map of the distribution of the cell contents can be obtained. However, the acquisition of a 64×64 map with an accumulation time of 0.5 s per spectrum takes over 30 minutes, which leads to difficulties when imaging live cells. As cells

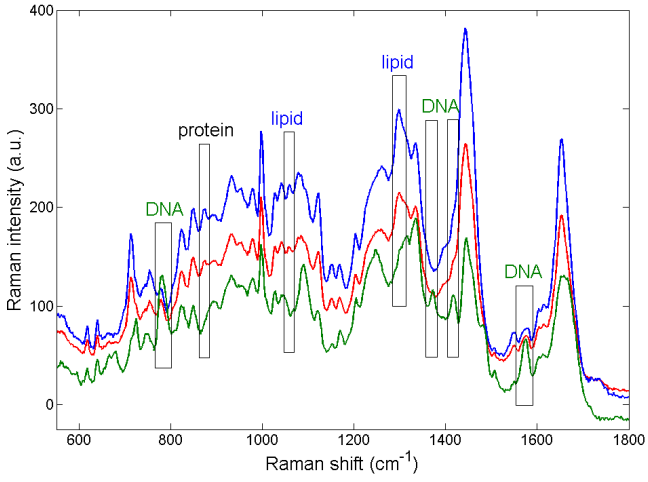

FIGURE 2.7 : Fingerprint region of the average cluster spectra (background corrected) from 4 hierarchical cluster analysis of a 64×64 Raman map of an SK-BR-3 cell acquired with 50 mW and 0.5 s per pixel.

live, they move and pass through different stages in the cell cycle, changing shape and most of all, the distribution of cell contents.

Figure 2.8A shows a whitelight image of an SK-BR-3 cell, Figure 2.8B-D show the corresponding 32×32 Raman mapping of an SK-BR-3 cell obtained with 10mW laser power and 0.5 s per pixel: hierarchical cluster image (4 levels), and corresponding background corrected average cluster spectra. Figure 2.8 demonstrates that cellular information can be well-resolved with laser powers as low as 10 mW, which amounts to a light dose of 5 mJ per pixel. A similar laser dose per pixel is acquired when probing with 50 mW for 0.1 s per pixel, which reduces the imaging time considerably.

The cytoplasm cluster average spectra of SK-BR-3 show pronounced presence of lipid bands, as marked with a triangle in Figure 2.8C (e.g., C-C stretch at 1077 cm^{-1} CH_2 twist at 1299 cm^{-1} in spectrum (a)), and in Figure 2.10A (CH_2 symmetric and antisymmetric stretch, 2850 cm^{-1} and 2885 cm^{-1}, respectively). The high lipid content of SK-BR-3 cells was also evident in the univariate images (Figure 2.5D, 2850 cm^{-1}) and is inherent to the nature of the cells and the tissue SK-BR-3 adenocarcinoma's manifest in: breast tissue consists of glandular and fatty tissue.

The nuclei of the SK-BR-3 cells are large and in the vast majority of the data sets, DNA was detected outside the cell nucleus (Figure 2.5D and Figure 2.8B), suggesting high mitochondrial activity.[104,105] In addition, the univariate image (Figure 2.5D) shows that the intensity of the DNA band at 780 cm^{-1} is low, compared to the 780 cm^{-1} bands observed in

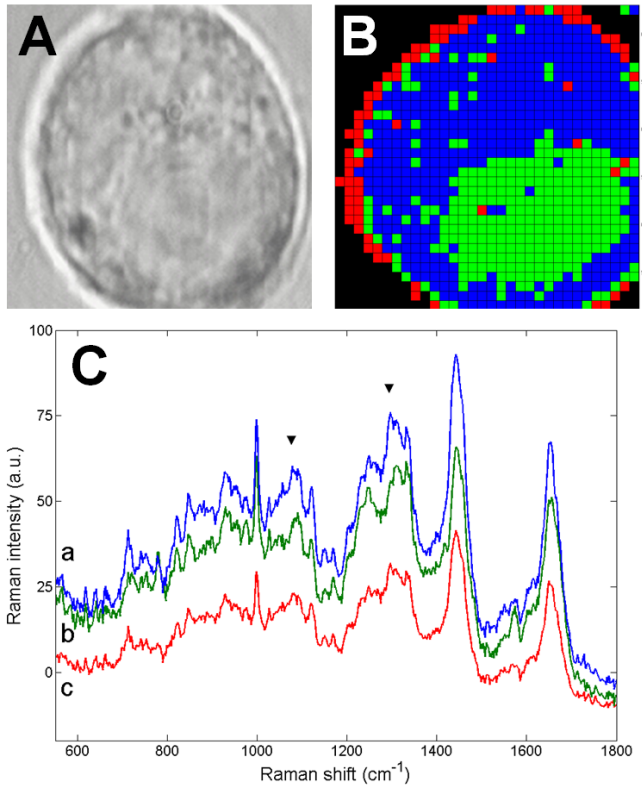

FIGURE 2.8 : Raman mapping of spherical SK-BR-3 cell (A) whitelight image; (B) cluster image resulting from a 4-level hierarchical cluster analysis applied to the 32×32 data matrix of the SK-BR-3 cell shown in (A); (C) Corresponding cluster averages corrected for the black background cluster: blue (a) represents the cell cytoplasm, green (b) the nucleus and red (c) the cell membrane. Triangles mark the Raman bands characteristic for lipids at 1077 cm^{-1} and 1299 cm^{-1} in the cytoplasm cluster (a, blue). Raman data was obtained with 10 mW laser power and 0.5 s per pixel.

previous studies.[89,94–96,106] This relatively low Raman signal of DNA is consistent for SK-BR-3 cells[107] and indicates that the DNA is present in a non-condensed state, which is not uncommon, since, in general, cancerous cells are genetically very active cells.[108]

In case the cells are fixed in 4% paraformaldehyde (PFA, for 15 minutes at room temperature) as was done in previous studies,[14] changes in Raman peak intensities as well as the appearance of additional Raman bands were observed in the cytoplasm cluster (Figure 2.9).

PFA fixed SK-BR-3 cells show new Raman bands at 607, 1730 and 1739 cm^{-1} (Figure 2.9, marked with diamonds), as well as the increased

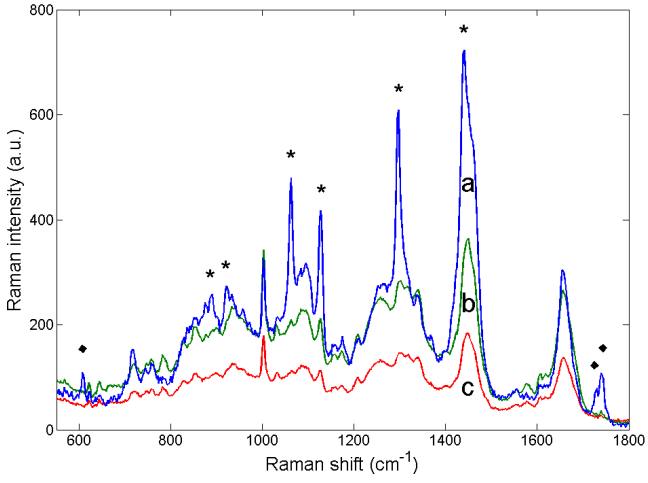

FIGURE 2.9 : Background corrected cluster averages for cytoplasm (a: blue), DNA (b: green), and cell membrane (c: red) of an SK-BR-3 cell fixed with 4% PFA, Raman probed with 25 mW for 0.5 s per spectrum.

intensity of the Raman bands at 890, 922, 1062, 1127, 1296 and 1441 cm^{-1}. The increased Raman bands can all be assigned to saturated fatty acid chains.[109] Moreover, the combination of these increased bands with the newly appeared bands at 607, 1730 and 1739 cm^{-1} is characteristic for triacylglyceride,[109] an ester formed from glycerol and fatty acids. Although ester groups are present in lipids in SK-BR-3 cells, the Raman intensities of the 1730, 1740 and 1750 cm^{-1} bands in live cells are hardly recognizable (Figures 2.7 and 2.8C). It is unclear to us what mechanism may lead to the increase in Raman signal of lipid esters in SK-BR-3 cells upon 4% PFA fixation. Possibly, formation of lipids is induced in SK-BR-3 as a stress response to fixation with PFA.

Figure 2.10A shows the high frequency Raman signal of background corrected cluster averages for cytoplasm, DNA and cell membrane of a living SK-BR-3 cell (in decreasing overall Raman intensity, respectively). Figure 2.10B shows the corresponding cluster averages for an SK-BR-3 cell fixed with 4% PFA. The Raman intensities of peaks characteristic of lipids at 2730, 2850 cm^{-1} and 2885 cm^{-1} are clearly increased (marked with an asterisk in Figure 2.10B. Besides the overall intensity increase in the blue cluster, the relative band intensities in this cluster changed. Moreover, PFA fixation affects the cells by shrinkage and causes uneven appearance of the cell membrane, in correspondence with Chan *et al.*[110]

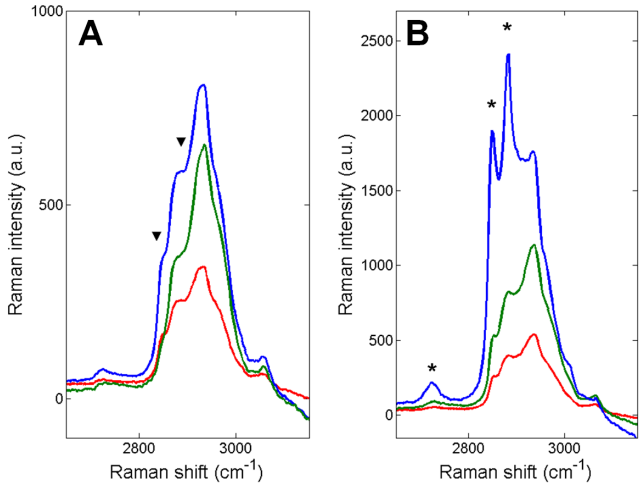

FIGURE 2.10 : High frequency Raman cluster averages (A) live SK-BR-3 cell and (B) 4% PFA fixed SK-BR-3 cell. Both cells were Raman mapped with 25mW and 0.5 acquisition time.

2.7 CONCLUSIONS

We presented our high resolution confocal Raman microspectroscope, based on the 647.1 nm excitation line of a krypton-ion laser. The custom made detection system covers a bandwidth of 646 nm to 849 nm, which corresponds to a Raman spectrum from -20cm^{-1} to 3670 cm^{-1}, covering the fingerprint region of cells as well as the high wavenumbers.

We determined initial Raman fingerprints of plain SK-BR-3 cells, which are often used as a model in breast cancer research. We are able to obtain detailed Raman mapping of live cells with laser doses as low as 5 mJ per pixel. In addition, we determined the effect of standard paraformaldehyde fixation on the Raman signature of the cells. SK-BR-3 cells exhibit high lipid contents, which is regarded inherent to the nature of the cells and the tissue of origin. SK-BR-3 cell nuclei are large and DNA was detected outside of the cell nuclei as well, reflecting the cells' high degree of mitochondrial activity.

Fixation of SK-BR-3 cells with a standard 4% paraformaldehyde (PFA) fixative results in increased Raman signatures of lipid esters in the cells. Therefore, for Raman microspectroscopy, cells are preferably probed unfixed. Our Raman microspectroscope appeared very suitable for live cell imaging, as the low laser doses applied provide room for even shorter image acquisition times.

CHAPTER 3

Raman characterisation of breast cancer tumour cells

Evaluation of possible effects of gold nanoparticles on cancer cells requires knowledge of the unperturbed cells. Here, we use Raman microspectroscopic imaging to reveal the chemical composition of single live cells from breast carcinoma cell lines MDA-MB-231, MDA-MB-435s and SK-BR-3, which express Her2/neu receptor in different extent. The Her2/neu proto-oncogene is amplified in 25 to 30 percent of human primary breast carcinomas and is often utilized as target for therapy. The roles of Her2/neu have been reported before in literature, showing different relations to intracellular lipid composition.

Average Raman spectra of the different cell populations show prominent lipid presence in all cell lines. With high significance, Raman difference spectra reveal increased lipid contents, as well as a lower degree of fatty acid saturation in the MDA-MB cell lines with respect to the SK-BR-3 cells. These results are confirmed by hierarchical cluster analysis of single cells. High internal consistency of the chemical compositions in the cell lines is shown by hierarchical cluster analysis on a single matrix composed of the data of different cells from a single cell line.

Although Her2/neu expression is highest for SK-BR-3 cells, their lipid contents are lower than that of the MDA-MB cell lines, which express less to no Her2/neu receptors. Rather than metabolic rate or senescence, the degree of metastaticity of the cells appears to be related to the polyunsaturated fatty acid contents of the cells.

This chapter has been published in Analyst, 2010 DOI: 10.1039/c0an00524j

3.1 Introduction

Breast cancer, with an occurrence of 23% of all cancers, is by far the most frequent cancer among women, with an estimated 1.38 million new cancer cases diagnosed in 2008. It is now the most common type of cancer in both developed and developing regions with annually around 690,000 new cases estimated in each region.[111] Although in the last decades, major advancements have been made in our understanding and treatment of breast cancer that have resulted in a decline in breast cancer mortality, breast cancer is still the most frequent cause of cancer death in women worldwide.[111]

The cause of breast cancer is believed to lie in accumulations of mutations in essential genes, such as inhibition of tumour suppressor genes or the amplification of tumour-inducing genes, called proto-oncogenes. The expression of the Her2/neu proto-oncogene is amplified in 25 to 30 percent of human primary breast carcinomas.[112,113] It encodes a protein that has extracellular, transmembrane and intracellular domains consistent with the structure of a growth factor receptor.

Amplification of Her2/neu is directly correlated to the overexpression of its receptor.[113] Her2/neu receptor overexpression is considered a predictor of poor prognosis and short overall survival.[112–114] The presence of the Her2/neu receptor correlates with a high metastatic activity.[112] Therefore, biomarkers such as Her2/neu are currently included as prognostic and predictive factors in tumour subtype screening to determine appropriate therapies.[114,115] In addition, Her2/neu receptors are utilized as target for therapy incorporating agents that inhibit uncontrollable tumour growth.[116]

In breast cancer cell lines that overexpress the Her2/neu receptor, increased lipogenesis has been reported. This condition of the cell has been suggested to be in favour of proliferation, by activating regulatory circuits that stimulate and fuel the lipogenic enzyme FASN.[117,118] Alternatively, it has been suggested that upregulation of the expression of the Her2/neu receptor provokes premature senescence, which limits the cell's ability to divide.[119,120] It has been proposed that the presence and ratio of cis- and trans-unsaturated membrane lipids could be used as a molecular marker for senescence and tumourigenesis.[119]

Raman microspectroscopy is a label-free method to determine the conformation of unsaturated bonds in lipid mixtures, cells and tissues. Raman microspectroscopic techniques have become increasingly attractive for biological sample analysis and imaging, because of the ability to visualize samples down to a 500 nm resolution without the use of additional labels or sample perturbations. Raman microspectroscopic imaging can distinguish between local cellular compositions of different breast cancer cell lines,[121] providing a wealth of chemical information pertaining to cell composition, structural organisation and cell functionality.[89]

Here, we use Raman microspectroscopic imaging to compare the breast

carcinoma cell lines MDA-MB-231, MDA-MB-435s and SK-BR-3, which are commonly used as breast cancer models and express Her2/neu receptor to different extents. MDA-MB-231 are Her2/neu negative, while MDA-MB-435s exhibit intermediate Her2/neu expression and SK-BR-3 is known for its Her2/neu receptor overexpression.

All cell lines used are adherent human cell lines of tumourigenic nature, the SK-BR-3 cells being of low metastaticity, while the MDA-MB cell lines are highly metastatic.[122] SBKR3 and MDA-MB-231 are of epithelial morphology. The origin of the parental cell line MDA-MB-435s is currently under debate, because the cell line also expresses melanoma-specific genes.[123,124]

Confocal Raman microspectroscopic imaging was used to investigate the chemical composition of the different breast cancer cell lines. Different analysis routines showed the prominent role of lipids in the cell lines, as well as a lower degree of fatty acid saturation in the MDA-MB cell lines with respect to the SK-BR-3 cells.

3.2 Materials and methods

3.2.1 cell culture

Day 0:
Cells were cultured on CaF_2 slides (20mm diameter) and were left to attach overnight.

SK-BR-3 cells were cultured in DMEM supplemented with L-glutamine (1%), Fetal Bovine Serum (FBS, 10%) and Penicillin Streptomycin (PS, 1%). MDA-MB-231 and MDA-MB-435s were cultured in RMPI-1640 supplemented with L-glutamine (1%), 10% FBS and 1% PS).

The seeding densities of the cells depended on their proliferation rates. SK-BR-3 have a low proliferation rate and were therefore seeded at a density of 2.0×10^4 cells/cm^2. MDA-MB-231 and MDA-MB-435s have higher proliferation rates and were therefore seeded at at 2.0×10^3 cells/cm^2 and $3.0\times*10^3$ cells/cm^2 , respectively. These cell seeding densities resulted in a cell confluence of approximately 60% on day 2.

Day 1:
For all cell lines, the proliferation medium was exchanged for RPMI without the pH-indicator phenol red, to preclude fluorescence emission of phenol red during Raman probing. The RPMI medium was supplemented with 10% FCS and 1% PS.

Day 2:
HEPES buffer was added to the cell medium prior to the transfer of cells from the incubator to the Raman microscope. HEPES maintains the physiological pH of the medium while the cells are outside the incubator.

The MDA-MB-231 and MDA-MB-435s cells spread onto the CaF_2 substrate on day 2, while the SK-BR-3 cell population contained many

round cells. Round SK-BR-3 cells were initially included in the Raman measurements as a distinguishable cell state. The round SK-BR-3 cells were tested for adherence by gently stirring and were observed to be adhered.

3.2.2 RAMAN SPECTROSCOPY AND IMAGING

Raman measurements were carried out on a confocal Raman microspectrometer, similar to the setup previously described by Van Manen *et al.*[89] The 647.1 nm excitation light from a Krypton ion laser light source (Innova 90-K; Coherent Inc., Santa Clara, CA) was focused through a 63×/1.0 NA water-dipping objective (Zeiss W-Plan Apochromat; Carl Zeiss MicroImaging GmbH, Göttingen, Germany) onto single living cancer cells.

The Raman image plane was selected to be at the same height above the CaF_2 substrate in all strongly adhered cells. The height was adjusted based on the intensity of the 322 cm^{-1} Raman signal of CaF_2 of the substrate. The image plane of the round SK-BR-3 cells was set to the height at which a maximum Raman signal intensity was acquired.

Hyperspectral Raman imaging was performed by stepping the laser beam over the sample in a 32×32 raster pattern and spectral acquisition at each position with a laser power of 50 mW under the objective and dwell time of 0.1 s/pixel, with a step size of 0.55 μm. Univariate and multivariate analyses were performed over the hyper spectral Raman data as described earlier.[95,96]

3.2.3 DATA ANALYSIS

Noise in the resulting 3D (spatial × spatial × spectral dimension) data matrix was reduced by singular value decomposition.[95,125] Hierarchical cluster analysis (HCA) was performed on Raman imaging data matrices to visualize regions in cells with high Raman spectral similarities. In the cluster analysis routine, principal component analysis scores were taken as input variables, squared Euclidean distances were used as distance measure, and Ward's algorithm was used to partition Raman spectra into clusters. All data manipulations were performed in routines written in MATLAB 7.6 (MathWorks, Natick, MA).

An average Raman fingerprint of a cell type was obtained by subtracting the spectrum of the cluster corresponding to the background, corresponding to the cell medium, from the spectrum of the cluster of the cell after a two level cluster analysis. The difference spectra were subsequently normalized with respect to the total Raman intensity between 150 cm^{-1} and 3600 cm^{-1}. Raman difference spectra were obtained by subtraction of the normalized average Raman spectra and are displayed as a percentage of the normalized spectra, following Equation 3.1:

$$S_{dif} = \frac{\bar{S}(A) - \bar{S}(B)}{\frac{1}{2}\left(\bar{S}(A) + \bar{S}(B)\right)} \tag{3.1}$$

Cell-to-cell variability within each cell type was determined by calculating the standard deviation for each recorded wavenumber. Variability between the cell types was defined using Student's $t-$test statistics (95% confidence interval), assuming equal variability within the cell types. The Student's t-test was performed for each spectral data point and the "spectrum of $p-$value" was plotted in a semi-logarithmic plot. This representation immediately reveals for which spectral position the individual datasets are significantly different. We have taken p <0.001 as a lower level for a significant difference. In order to test the correspondence between cells of one group, hyperspectral data matrices of different cells from a group were assembled into a single matrix and hierarchical cluster analysis was performed.

3.3 Results and discussion

The difference in Her2/neu receptor expression of the MDA-MB-231, MDA-MB-435s and SK-BR-3 cell lines was verified by measuring the amount of bound fluorescent PE (phycoerythrin) labeled Her81 antibody with fluorescence assisted cell sorting (FACS). As expected, MDA-MB-231 showed a negative response, MDA-MB-435s a medium response and SK-BR-3 showed a strong positive response for Her2/neu receptor expression (data not shown).

The MDA-MB-231 and MDA-MB-435s cells showed spread morphologies, while the SK-BR-3 cell population contained many round cells. This morphology of the SK-BR-3 cells is caused by a relatively low cell confluence.[126] Measurements on both round and adhered SK-BR-3 cells were therefore included in the Raman measurements as a distinguishable cell type.

In Figure 3.1, the average Raman spectra (solid lines) are shown of all four cell types. The spectral variations within a group of cells are plotted, as well as ± 1 time the standard deviation (shaded lines). Although the spatial variation in Raman spectra of individual cells is high,[95] the variation between Raman spectra of individual cells within a single cell type is low, as can be observed for both the fingerprint region (Figure 3.1A) and the high frequency region (Figure 3.1B). The variation between spectra of cells from the same group is probably due to fluctuations of the cell content in the probe volume of the confocal microscope, due to internal cellular dynamics.

To reveal the differences between spread SK-BR-3 cells and round SK-BR-3 cells, a Raman difference spectrum was calculated from the normalized average Raman spectra, which is shown in Figure 3.2 as a percentage of the

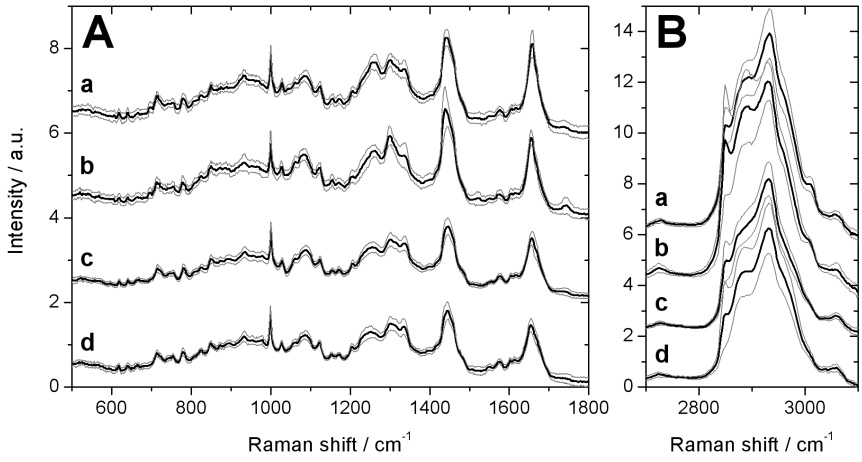

FIGURE 3.1 : Average Raman spectra of individual breast cancer cells a) MDA-MB-231, b) MDA-MB-435s, c) round SK-BR-3 and d) spread SK-BR-3 in A) the fingerprint range (500-1800 cm^{-1}) and in B) the high frequency Raman range (2700-3100 cm^{-1}). Each spectrum is obtained by averaging the spectra of several individual spectra (10-15 cells per cell line). Solid lines represent the average spectra and the shaded lines delineate one standard deviation. Spectra are offset for clarity.

normalized spectra. Figure 3.2A shows that the average spectral difference between spread SK-BR-3 cells and round SK-BR-3 cells in the fingerprint region lies within 5%. Slightly increased phospholipid content in round SK-BR-3 is indicated by positive Raman differences at 525, 774, 820 and 1120 cm^{-1},[109,127,128] which were defined to be significant (p <0.001) for all individual SK-BR-3 cells in both the round and spread populations (Figure 3.2C). Differences in (phospho)lipid contents were reflected by the less significant (p <0.05) positive difference bands at 1026, 1070, 1228 and 1330 cm^{-1} [129–131] as well as in the high wavenumbers at 2878, 2965 and 2974 cm^{-1} (Figure 3.2B,D).[109,132]

Remarkable is the prominent presence of a large positive band at 1040 cm^{-1} (p <0.001), which is specific for proline in ductal carcinomas.[133] However, no accompanying proline bands at 856 and 920 cm^{-1} show in the difference spectrum, casting uncertainty on the origin of the 1040 cm^{-1} band.

In case of low confluence of the SK-BR-3 cells culture, intercellular interactions are weak, which reduces cell spreading. In addition, different phases of the cells proliferation cycle are closely related to different cell morphologies.[126] For example, for cell division, cells need to loosen the actin skeleton to provide space for the DNA to condensate. The increased phospholipid expression in round SK-BR-3 cells may be due to their intensified cell membrane synthesis in the cell division process.[134] However,

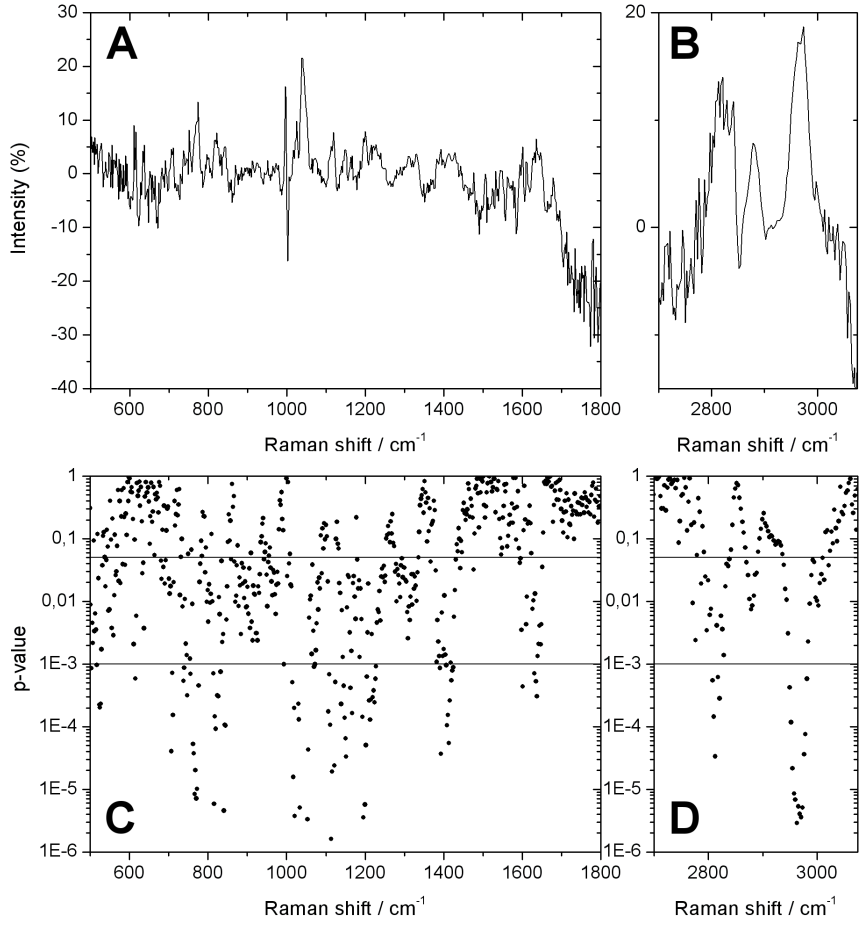

FIGURE 3.2 : Raman difference spectrum round SK-BR-3 vs. spread SK-BR-3 as a percentage of the normalized averaged Raman spectra in A) the fingerprint range (500-1800 cm^{-1}) and in B) the high frequency Raman range (2700-3100 cm^{-1}) and Student's t-test p-values show significant Raman differences for the round SK-BR-3 vs. spread SK-BR-3 for $p < 0.05$ and $p < 0.001$ in C) the fingerprint range (500-1800 cm^{-1}) and in D) the high frequency Raman range (2700-3100 cm^{-1}).

apoptotic cells have disrupted actin skeletons as well and round up before detaching. Since spread cells are not apoptotic, and can be measured in a focal plane which is set in a manner equal to that of the spread MDA-MB cells, we will be focussing on the spread SK-BR-3 cells for the remainder of this study.

Figure 3.3 shows the Raman difference spectra of the MDA-MB cell lines with respect to spread SK-BR-3 cells, revealing a pronounced increase

in lipid expression in the MDA-MB cell lines. In contrast to the SK-BR-3 difference spectra (Figure 3.2), the intensity of the difference spectra varies more, fluctuating between -20 and 20% of the normalized cell spectra, with extremes up to 65% in the high wavenumbers (Figure 3.3B).

Difference spectra a) and b) show increased unsaturated fatty acid content of the MDA-MB cell lines with respect to spread SK-BR-3 by the strong positive differences at 1265, 1298, 1440 and 1656-1660 cm^{-1}.[109,127,130,133] High lipid content is also illustrated by strong positive differences in the high wavenumbers (2850, 3015 cm^{-1} [132,135]). All indicated peaks have significantly different (p <0.001) mean intensities as determined by $t-$test analysis and are marked with an asterisk in Figure 3.3.

The position of the 1660 cm^{-1} band suggests the presence of cis-isomers of membrane lipids (1650-1665 cm^{-1}), rather than trans-form for which this Raman band is usually shifted to 1670-1680 cm^{-1}.[89]

Upregulation of cis-isomers in combination with absence of glycoprotein bands at 1313 and 1339 cm^{-1} , has been reported as a marker for tumour cell senescence.[119] However, these glycoprotein bands are prominently present in all cell lines (Figure 3.1) and do not appear in the difference spectra (Figure 3.3A), confirming the tumourigenic nature of all cell lines used.[122] Moreover, the presence of unsutaturated fatty acids in cis-conformation has been observed before in HeLa cells.[95]

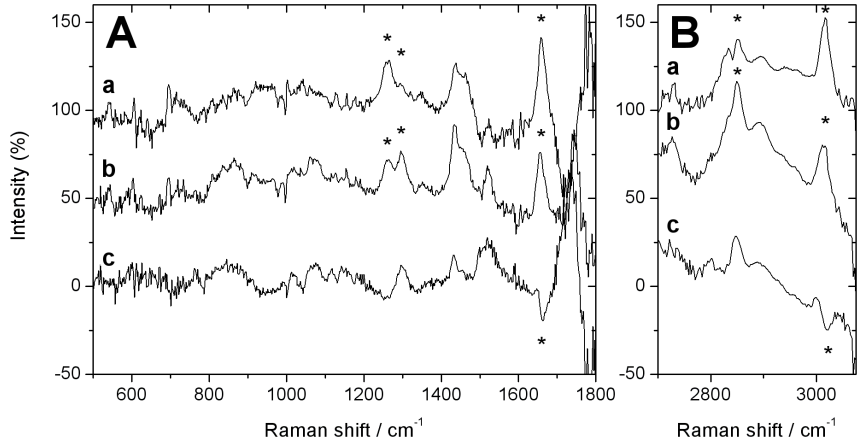

FIGURE 3.3 : Raman difference spectra comparing (a) MDA-MB-231 with spread SK-BR-3, (b) MDA-MB-435s with SK-BR-3 and (c) MDA-MB-435s with MDA-MB-231, as a percentage of the normalized averaged Raman spectra in A) the fingerprint range (500-1800 cm^{-1}) and B) the high frequency Raman range (2700-3100 cm^{-1}). Spectrum (a) is offset for clarity with 100%, spectrum (b) with 50%. Statistically significant values (p <0.001) are marked with an asterisk

Between the MDA-MB-231 and MDA-MB-435s cells the fatty acid composition differs as well. The ratio of intensities of the 1265 cm^{-1} (=CH in-plane deformation) and 1298 cm^{-1} (in-phase CH_2 twisting motion) difference bands in traces a) and b) shows a lower degree of saturation in MDA-MB-231 fatty acids.[95]

However, these spectral differences between MDA-MD-435s and MDA-MB-231 occur on average within 10% (Figure 3.3, trace C). Moreover, Student's $t-$test analysis revealed that only few differences are significant. For MDA-MB-435s with respect to MDA-MB-231, protein expression is lower, at 1660 and 3022 cm^{-1} ($p < 0.001$, marked with asterisk in Figure 3.3, trace C), and lipid contents is higher, illustrated by positive differences at 1062, 1075, 1298, 1434, 1744 and 2845 cm^{-1} ($p < 0.05$).

No differences in melanin characteristic bands at 1380 and 1580 cm^{-1} are observed between the MDA-MB-435s and MDA-MB-231 cell lines.[136] However, a possible melanocytic nature of MDA-MB-435s cells can be expressed in different ways.[123,124]

Representative whitelight micrographs of the nucleus and the perinuclear region are shown for the different cell types (Figure 3.4). Their corresponding hierarchical cluster images (seven levels) are represented as well. The whitelight images are intended to illustrate the morphology of the cells prior to Raman measurements. The colours assigned to the clusters are similar for all cells shown, showing different Raman signal from different locations within the cells. Yellow marks the medium surrounding the cells, red marks the cell membrane, black the cytoplasm and magenta the nucleus. The nuclei of the breast carcinoma cell lines under investigation appear large in contrast to the nuclei of, for example, peripheral blood lymphocytes.[94,95] However, a large nucleocytoplasmic ratio is not uncommon for either SK-BR-3[137] or MDA-MB cell lines.[138] Moreover, the size of the nucleus is related to the proliferative activity of breast cancer cells, which may in turn reflect the aggressiveness of the neoplastic process.[108]

The green and cyan clusters mark the lipid rich regions in the cell. The cyan cluster represents the lipid droplets, which can also be seen in the whitelight micrographs as either dark or bright circles, their degree of scattering depending on the precise location of the droplet. Blue is assigned to a different lipid cluster in the SK-BR-3 Raman data, while in the MDA-MB data blue indicates a subcluster in the cell medium, caused by differences in extracellular material. The lipid rich clusters (cyan in Figure 3.4) were distinguished at the same level during the cluster analysis for the different cell types.

Figure 3.5 shows the cyan cluster averages of the cluster images from Figure 3.4. The lower signal-to-noise ratio (SNR) of the MDA-MB-231 lipid cluster is due to the smaller number of individual spectra in the cyan cluster. Nevertheless, a difference in lipid composition of the lipid droplets is shown. Bands at 1265, 1298, 1440 and 1660 cm^{-1}, characteristic for unsaturated fatty acids, are more intense in the MDA-MB cluster averages

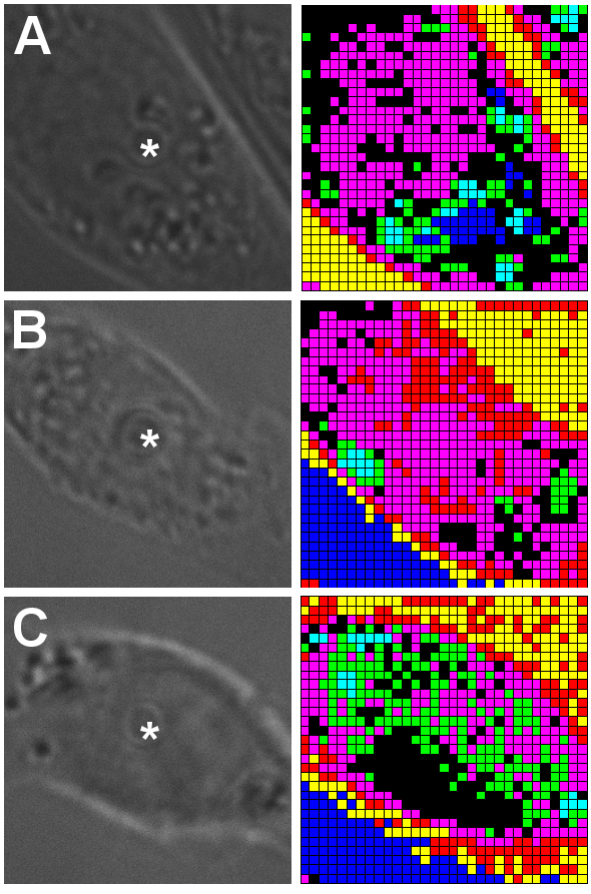

FIGURE 3.4 : Bright-field images and corresponding Raman cluster images of A) a spread SK-BR-3 cell, B) an MDA-MB-231 cell and C) an MDA-MB-435s cell, acquired by scanning the confocal laser bundle in a 32×32 raster pattern, pixel size approximately 550 nm, with 50 mW power under the objective and a pixel dwell time of 0.1 s. Analysis with 7 levels of clustering illustrates the spatial variation of Raman signal within single cells by distinguishing subcellular structures. The circular artifacts due to damage on an optical component in the path of the whitelight micrographs are marked with an asterisk.

(band positions marked with an asterisk in Figure 3.5A). A difference in degree of lipid saturation between the MDA-MB-231 and MDA-MB-435s is reflected by the 1265-1298 cm^{-1} ratio. The high wavenumbers reflect the differences in lipid-protein distributions for the different cells (Figure 3.5B).

High phosphoester content in the MDA-MB-435s lipid cluster is indicated by an increased 1298 cm^{-1} contribution in combination with the presence of the bands at 1080 cm^{-1} and 1744 cm^{-1}(Figure 3.5A). In addition, phosphocholine is prominently present at 715 cm^{-1}. Elevated phosphocholine levels and total choline containing phospholipid metabolite levels are related to the aggressive nature of the MDA-MB-435s cell line. [122]

Single cell HCA thus also shows the differences in degree of lipid contents, saturation and composition as seen in the Raman difference spectra averaged over cell populations. The high consistency of the chemical compositions within different cells of the same cell line is illustrated in Figure 3.6. Here,

four Raman data sets of different MDA-MB-231 cells are merged into a single matrix and subjected to a single hierarchical cluster analysis (HCA, seven levels) over the full Raman region (150-3600 cm^{-1}).

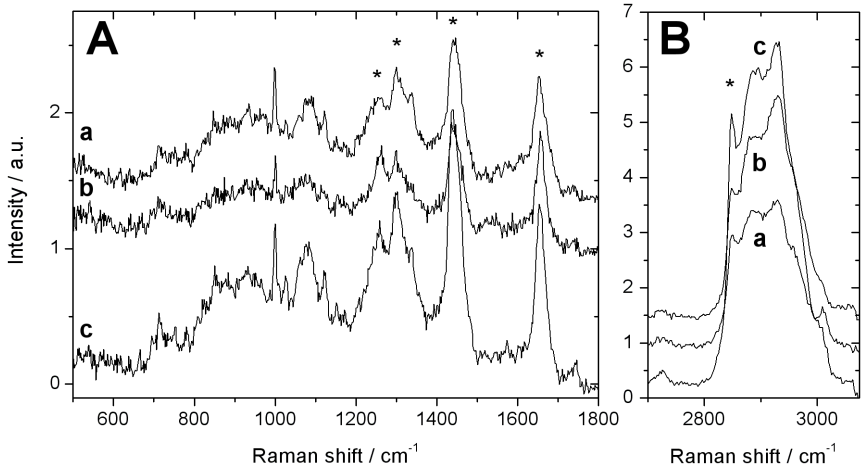

FIGURE 3.5 : Raman difference spectra of cyan cluster average of a) SK-BR-3 b) MDA-MB-231 and c) MDA-MB-435s cells after subtraction of the cell medium cluster average (yellow for the SK-BR-3 cells, blue for the MDA-MB cells) show differences in lipid composition of lipid droplets in A) the fingerprint range (500-1800 cm^{-1}) and B) the high frequency Raman range (2700-3100 cm^{-1}). Spectra are offset for clarity. Band positions characteristic for unsaturated fatty acids are marked with an asterisk.

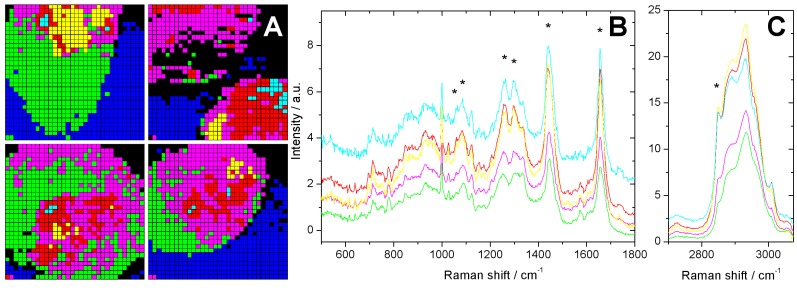

FIGURE 3.6 : A) Raman cluster image of four different MDA-MB-231 cells subjected to a single hierarchical cluster analysis (HCA) over the full Raman region (150-3600 cm^{-1}) reflects identical overall intracellular chemical composition in both B) the fingerprint region (500-1800 cm^{-1}) and C) the high wavenumbers (2700-3100 cm^{-1}). All cells were imaged with 50mW under the objective and 0.1s dwell time per pixel. The pixel size is approximately 550 nm. Lipid characteristic band positions are marked with an asterisk.

The Raman cluster image is shown in Figure 3.6A, displaying the surrounding medium divided into two clusters (black and blue), due to differences in extracellular material. Figure 3.6B shows the corresponding cluster averages, corrected for the blue background spectrum. The magenta cluster marks the cell cytoplasm, green the nucleus. Red, yellow and cyan show pronounced lipid contributions of Raman bands at 1060, 1082, 1265, 1298, 1440 and 1660 cm^{-1}, illustrating again the low degree of fatty acid saturation. The lipid contribution in these spectra is additionally marked by a sharper 2850 cm^{-1} band. All mentioned lipid bands are marked with an asterisk in Figure 3.6BC. The lipid rich clusters are mutually mainly clustered on signal intensity, which is also reflected in the high wavenumbers (Figure 3.6C).

3.4 Conclusions

Using confocal Raman microspectroscopic imaging, we observed low variability in the chemical composition within single cell types of live populations of SK-BR-3, MDA-MB-231 and MDA-MB-435s cells. Even though they are very small, spectral differences could be distinguished between the distinct round and spread morphologies within the SK-BR-3 cell line. Spectral differences between the different cell lines appeared to be typically larger. With respect to the SK-BR-3 cells, both MDA-MB cell lines showed a significant ($p < 0.001$) increased content of unsaturated fatty acids, present in cis- rather than trans-conformation. MDA-MB-435s showed increased lipid unsaturation with respect to the MDA-MB-231, as well as increased expression of phospholipids, which reflects the aggressive nature of the MDA-MB-435s cell line.[122]

Although the SK-BR-3 cells show Her2/neu overexpression, their lipid contents were found to be lower than those of the MDA-MB cell lines, which express less to no Her2/neu. However, taking into account the degree of metastaticity of the cells,[122] our observation is in good agreement with Hedegaard *et al.*, who recently identified the polyunsaturated fatty acid contents as the one component differentiating between metastatic and nonmetastatic cell lines.[139]

All indicated spectral differences could be observed in both the HCA of single cells as well as of groups of four different cells within a cell line and in the average difference spectra of a larger cell population, demonstrating consistency in chemical composition within the cell lines as well as the robustness of the acquired Raman data.

CHAPTER 4

In vitro RAMAN CHARACTERISATION OF GOLD NANORODS

The optical properties of PEGylated gold nanorods (PEG-GNR) in interaction with cells have been investigated with Raman and fluorescence microspectroscopic imaging. The emission spectra were compared with those from suspensions of GNR, which can be characterized by a broad emission bandwidth of approximately 60 nm with a band maximum around 675 nm. These properties are in good agreement with observations from various other gold substrates and (nano)particles.

The emission spectra from cells incubated with PEG-GNR were dominated by Raman scattering from locations where no GNR were present. Intense fluorescence spectra, in peak-amplitude comparable with the Raman scattering from cells, were observed from locations with GNR. The frequency range of the fluorescence emission spectra coincided mainly with the Raman fingerprint region from 500 cm^{-1} to 1800 cm^{-1}, excited by the laser emission line at 647.1 nm. No surface enhanced Raman spectra were observed. It was furthermore observed from cluster analysis of the Raman and fluorescence hyperspectral datasets that the GNR-related integrated fluorescence emission band from an individual cell could be sub-divided in multiple bands with slightly varying band maxima.

Raman difference spectra of cells with GNR minus control cells showed that the amplitude of lipid signal in PEG-GNR-incubated cells was increased. An excellent correlation occurred between the increased lipid signals and locations of the nanorods. This positive correlation between Raman signals from lipids and fluorescence signals from gold nanorods supports that gold nanorods are locally accumulating in lipid vesicles within the cells.

This chapter has been submitted for publication to Applied Spectroscopy

4.1 Introduction

Gold nanoparticles are rapidly emerging for use in biomedical applications due to their biocompatibility and their favourable optical properties, such as an enhanced absorption cross-section at optical frequencies.[5] The latter is a result of a surface plasmon resonance, which depends on the size and geometry of the nanoparticles.[5,6,12,140]

Rod-shaped gold nanoparticles are attractive as a contrast agent as they are easy to synthesize and provide a high yield of uniform-sized particles, the size of which, and hence the peak wavelength of the plasmon absorption band, can be controlled during synthesis.[14,22,69] The geometry of gold nanorods (GNR) gives rise to two surface plasmon bands, one along the long axis of the nanorod and one along the short axis. The plasmon along the short axis gives rise to a high-energy resonance band at approximately 520 nm, similar to that observed from spherical gold nanoparticles. The plasmon along the long axis produces a low-energy longitudinal plasmon (LP) band. The band maximum of the absorption is very sensitive to the aspect ratio (AR) of the rod. By altering the AR of the rod, the LP resonance can be tuned to far-red (FR) or near-infrared (NIR) spectral regions.[141] In the NIR spectral region, tissue is relatively transparent and light scattering is strongly reduced with respect to the visible and ultra-violet spectral regions and, as a consequence, a relatively high penetration depth of light in tissues is achieved.

Conventional biomedical imaging techniques suffer from low contrast with respect to the surrounding tissue. However, by administering gold nanorods with NIR-surface plasmon bands (SPB) to the tumour site, high contrast non-invasive cancer imaging can be achieved with techniques such as photoacoustic imaging,[38,142] optical coherence tomography,[12] and optical[143] and Raman imaging.[48] Moreover, light absorption by the particles can cause local heating, which can be sufficient to kill cells locally.[73] Therefore, the optical properties of GNR make them promising agents for diagnostic purposes and treatment of early stage carcinomas.

The most generally used method for synthesizing GNR is the silver-assisted seed-mediated protocol[22] or one of its many variants.[14,69] Cetyl trimethylammonium bromide (CTAB) is crucial as a shape-directing component in this method,[14,69,144] and gold nanorod particles have therefore been subjected to surface modification with methoxy-(polyethylene glycol)-thiol (mPEG-SH) before administration to cells in biomedical applications. Such PEGylated GNR (PEG-GNR) have been shown to be non-toxic for various cell lines.[81]

Hyperspectral Raman microspectroscopy was used to investigate the interaction of PEG-GNR with cells in more detail, Raman spectroscopy enables correlations between the optical response of the different cellular organelles and molecular components[107,145] and the nanorods in the cells. In addition, both the field at the laser excitation wavelength and the Raman

field in resonance with the local surface plasmons of gold nanoparticles may enhance the relatively weak Raman scattering, which could result in surface enhanced Raman scattering (SERS).[2,146] Kneipp *et al.* observed a SERS effect of gold nanoparticles which had accumulated inside endosomal compartments of living epithelial and phagocytic cells 20 under Raman excitation conditions. It will be shown here that favourable use can be made of the intrinsic fluorescence emission properties of gold nanorods.[147–149] The quantum yield of the gold fluorescence emission is extremely small, but is enhanced by the field associated with the surface plasmon resonance in GNR. The GNR fluorescence emission can be efficiently excited with 647.1 nm and the emission falls well within the detection limits of the Raman emission range, between 647.1 nm and 850 nm. This situation enables simultaneous detection of Raman and fluorescence spectra of both breast cancer cells and GNR.

4.2 Materials and methods

4.2.1 gold nanorod synthesis and characterisation

Gold nanorods were synthesized as previously described,[14,81] using the seed-mediated method[22,150] that requires the addition of gold seed to a growth solution with shape directing surfactant CTAB. Tetrachloroauric acid $HAuCl_4.3H_2O$ was purchased from Acros Organics (Belgium); hexadecyltrimethylammonium bromide (CTAB >99%), sodium borohydride ($NaBH_4$ 99%), ascorbic acid (99%) and methoxy PEG-thiol (mPEG-SH; 5000 MW) from Fluka (The Netherlands). Silver nitrate ($AgNO_3$ 99.8%) was purchased from Merck (Germany).

Freshly synthesized GNR dispersions were concentrated by centrifuging twice at 7500 rcf for 20 minutes which also enabled removal of the excess unbound CTAB. After the first centrifugation cycle, the NR pellet was dispersed in MilliQ water. After the second cycle, the NR pellet was dispersed in 0.5 ml of 5 mM mPEG-SH with vigorous vortexing for 20 seconds. To this dispersion, 0.5 ml of PBS (Phosphate Buffered Saline) was added followed by continuous rotation for 24 hours at room temperature. The resultant was subjected to two centrifugation steps (7500 rcf, 20 minutes) to remove excess mPEG-SH from the dispersion and the pellet was dispersed in SK-BR-3 culture medium.

At all stages of the PEG-GNR synthesis transmission spectra were acquired, using a Shimadzu PC3101 UV-Vis-NIR spectrophotometer. Retention of the plasmon peaks in the spectra is taken as evidence of colloidal stability during the processing steps.

In addition, the spectra are used for estimating number densities as Equation 4.1:

$$N = \frac{\mu_{ext}}{Q_{ext}\pi r^2} \tag{4.1}$$

Here, μ_{ext} is the extinction coefficient of the samples calculated from transmission data, using the Beer-Lambert law. Q_{ext} is the extinction efficiency of a particle calculated using the Discrete Dipole Approximation method, DDSCAT,[151,152] and r is the radius of an equivalent sphere obtained from actual size determination from SEM images (data not shown, see Rayavarapu *et al.*[81]). The PEG-GNR aspect ratio of 2.4 ± 0.2 was derived from analysis of at least 250 particles in each case from SEM images, as was shown by Rayavarapu *et al.*[81]

4.2.2 CELL CULTURE

SK-BR-3 mammary adenocarcinoma cells were maintained using RPMI 1640 medium supplemented with 1% glutamine, 10% FBS (Fetal Bovine Serum) and 1% antibiotics (Penicillin Streptomycin, PS). The cells were passaged every 3 days.

SK-BR-3 cells were seeded on calciumfluoride (CaF_2) slides (20 mm diameter, 2 mm thickness), to obtain approximately 16.000 cells/cm^2. The cells were equilibrated over night at 37 °C in a humidified 5% CO_2 atmosphere. PEG-GNR dispersed in SK-BR-3 culture medium were added to the cells resulting in a gold nanorod to cell ratio of approximately 1.6×10^6 : 1, and incubated overnight. The PEG-GNR LC50 was previously determined to be more than 2.4×10^6 nanorods per cell.[81] SK-BR-3 cultured in medium without PEG-GNR were used as a control.

The culture media were removed and the cells were washed three times with PBS after which fresh culture medium was supplied before Raman measurements of living cells commenced.

4.2.3 CONFOCAL RAMAN MICROSPECTROSCOPY AND IMAGING

Raman measurements were carried out on a confocal Raman microspectrometer similar to the setup previously described by Van Manen *et al.*[89] The 647 nm excitation light from a krypton ion laser light source (Innova 90-K; Coherent Inc., Santa Clara, CA) was focused through a 40×/0.75 NA objective (Olympus UPFLN; Olympus, Hamburg, Germany) to measure the optical emission spectra of GNR dispersions sealed under a glass coverslip.

Raman imaging of single, living SK-BR-3 cells, which were grown on a CaF_2 substrate, was performed using a 63×/1.0 NA water-dipping objective (W-Plan Apochromat; Carl Zeiss, Jena, Germany). Only SK-BR-3 cells with a spherical appearance were selected for Raman imaging. This was the preponderant cellular geometry at low seeding density. The Raman image plane was selected to be at the same height above the CaF_2 substrate in all cells. The height was adjusted based on the intensity of the 322 cm^{-1} Raman signal of CaF_2 of the substrate.

Hyperspectral Raman imaging was performed by stepping the laser beam over the sample in a raster pattern and spectral acquisition at each position with a laser power of 10 mW under the objective and a dwell time of 0.5 s/pixel. The step size was 0.5 μm, which was small enough to resolve basic cell structures such as the nucleus and the cytoplasm or to detect the cell membrane.

4.2.4 DATA ANALYSIS

Raman data was corrected for setup response. The emission spectra GNR dispersions were averaged over 1024 (32×32) measurements to obtain a smooth average response of the non-aggregated individual nanoparticles in the dispersion.

Univariate and multivariate analyses were performed on the hyperspectral Raman data of the SK-BR-3 cells, as described earlier.[95,96] Noise in the resulting 3D (spatial × spatial × spectral dimension) data matrix was reduced by singular value decomposition.[95,125] Raman images were constructed by plotting the integrated intensity of the vibrational areas of interest as a function of position. Hierarchical cluster analysis (HCA) was performed on Raman imaging data matrices to visualize regions in cells with high Raman spectral similarities. HCA is an unsupervised multivariate analysis technique that clusters spectra of high similarity together. In the cluster analysis routine, principal component analysis scores were taken as input variables, squared Euclidean distances were used as distance measure, and Ward's algorithm was used to partition Raman spectra into clusters. All data manipulations were performed in routines written in MATLAB 7.6 (MathWorks, Natick, MA).

The reproducibility of the hyperspectral Raman data sets from individual SK-BR-3 cells was assessed by merging data sets of four cells to a 64×64 hyperspectral data set. Subsequently, multivariate analysis was performed and the results established the chemical correspondences among SK-BR-3 cells. The spectra of these control cells were compared to the spectra of SK-BR-3 cells incubated with PEG-GNR.

Cumulative Raman fingerprints of cells were obtained by summing the weighed cell clusters, after subtracting the spectrum of the cluster corresponding to the background signal, which arises due to the cell medium, following Equation 4.2:

$$f = \sum_{i=1}^{j} N_i \left(C_{av,i} - C_{bk} \right) \tag{4.2}$$

Where N_i represents the number of spectra in cluster i, $C_{av,i}$ the average cluster spectrum of cell cluster i and C_{bk} the cluster average of the background.

Cumulative spectra were normalized with respect to the total Raman intensity between 150 cm^{-1} and 3600 cm^{-1}. Raman difference spectra were obtained by subtraction of the normalized cumulative Raman spectra.

4.3 Results and discussion

4.3.1 Raman fingerprint of live SK-BR-3 cells

Figure 4.1A shows a white-light image of a single, live, SK-BR-3 cell with the corresponding univariate Raman intensity image in Figure 4.1B. The univariate image is based on the total Raman scattering in the entire fingerprint region (500-1800 cm^{-1}) and reveals the large amounts of Raman scattering from the SK-BR-3 cell. Figure 1C shows the hierarchical cluster analysis (HCA) image of the cell. Average Raman spectra calculated from each cluster can reliably be assigned to particular cellular structures.

In Figure 4.1C, the green cluster is recognized as the nucleus from Raman bands of DNA, the blue cluster represents the cytoplasm, which is very rich in lipids, the red cluster is assigned to the cell membrane and the black cluster is the Raman spectrum of the cell culture medium in the extracellular space (cluster data not shown). The cell medium spectrum has been used as a subtractant in the Raman difference spectra in Figures 4.1D and 4.1E.

The sum of all cell related Raman spectra, corrected for cell medium background, is shown in Figure 4.1D for the fingerprint region and in Figure 4.1E for the high frequency region. Figures 4.1D and 4.1E show that the high scattering is predominantly due to the presence of large amounts of lipids (marked positions) in the cytoplasm of the cell (blue cluster in Figure 4.1C, cluster data not shown). The high lipid content of SK-BR-3 cells is an important feature of the cells and the adenocarcinoma tissue from which the SK-BR-3 cells are derived. In general, live populations of SK-BR-3 cells exhibit low variability in the chemical composition, as was demonstrated before.[107]

4.3.2 Characterisation of pegylated GNR

In Figure 4.2, schematic representations are shown of the gold nanorod surface before and after surface treatment. Before surface treatment, the as-prepared GNR is covered with a bilayer of CTAB, which is arranged at certain facets of the gold nanorod surface by ionic interactions[153] (Figure 4.2A). After treatment with mPEG-SH, the GNR is covered with PEG chains, which covalently bind to the gold surface (Figure 4.2B).

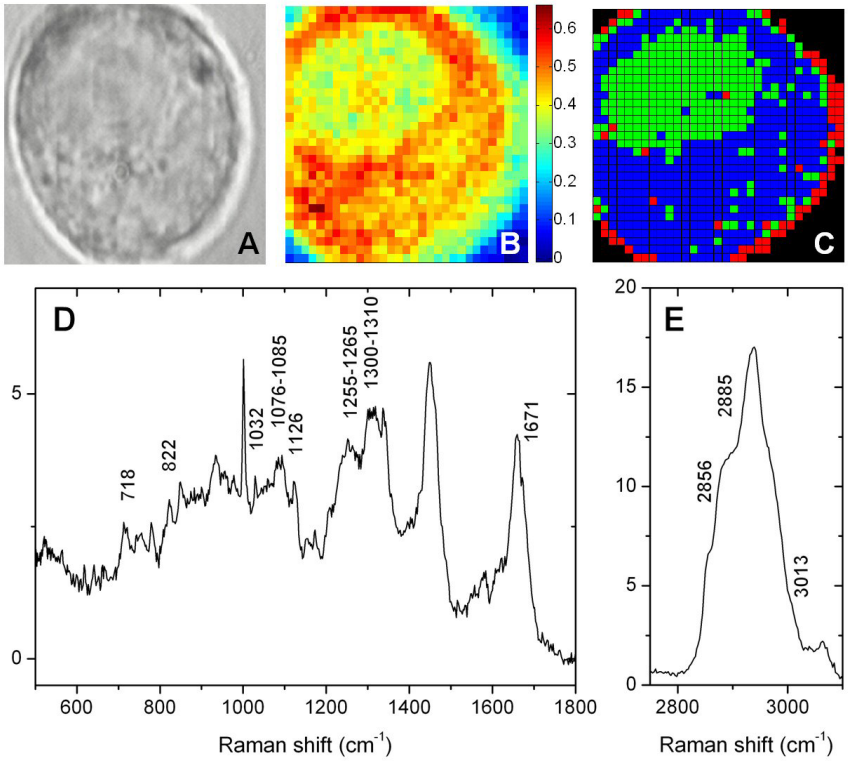

FIGURE 4.1 : Raman analysis of a 32×32 Raman map of an SK-BR-3 cell acquired with 10 mW under the objective and 0.5 s dwell time per pixel: A) brightfield image; B) univariate Raman plot of the fingerprint region (500-1800 cm^{-1}); C) cluster image of 4 Raman clusters: in green the cell nucleus, in blue the cytoplasm, in red the cell membrane and black the surrounding cell medium; D) the sum of all cell related Raman spectra in the fingerprint region (500-1800 cm^{-1}) and E) in the high wavenumbers (2700-3100 cm^{-1}). Raman band positions characteristic for lipids and phospholipids are marked.

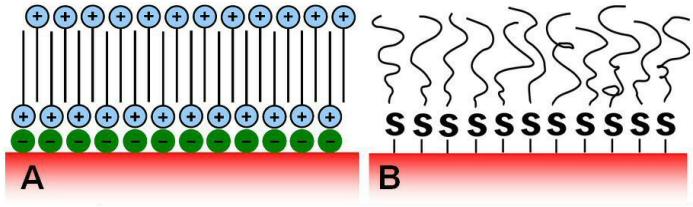

FIGURE 4.2 : Schematic representation of PEGylation of the gold nanorod surface: displacement of A) CTAB, arranged at certain facets of the gold nanorod surface by B) mPEG-SH which covalently binds to the gold surface.

In Figure 4.3A, the optical extinction profiles of the GNR show the retention of the LP peak of the as-prepared GNR (solid curve, CTAB 0x), the GNR after PEGylation (dashed curve, PEG 0x) and the PEGylated GNR after washing and dispersion in cell culture medium (dotted curve, PEG 3x). The absence of a shift in the plasmon peak indicates that no particle clustering or aggregation has taken place. The decrease in peak intensity is due to minor losses of PEG-GNR in the washing process. The 647 nm excitation laser line for Raman is indicated with a red line in Figure 4.3A, the shaded area marks the Raman detection area.

Fluorescence emission spectra of GNR with an aspect ratio of 2.5 are presented in Figure 4.3. Spectra have been acquired after several washing and surface treatment steps necessary for the surfactant replacement of CTAB for PEG. The solid trace (dashed trace) represents the as-prepared CTAB-GNR solution after the first (second) washing step. The dotted (dashed-dotted) profile shows the fluorescence emission spectrum of PEGylated GNR after a first (second) washing step. The fluorescence emission spectra also reflect that the surface treatment process does not change the properties of the suspensions of GNR.

In order to investigate the Raman and fluorescence emission properties of PEG-GNR in cells, the optical response of GNR was measured in a Raman spectrometer. Figure 4.4A shows the emission profiles of gold nanorods dispersed in MilliQ water (trace a). For comparison, the Raman response of plain MilliQ water is displayed as well (Figure 4.4, trace b). Both spectra clearly show the Raman OH-bending vibration around 1630 cm^{-1} and the OH-stretching vibration near 3350 cm^{-1}. The corresponding difference spectrum, presented in the inset on a nanometer scale (Figure 4.4A), illustrates the band shape of the broadband fluorescence response from suspended GNR. Although the aspect ratio of the GNR was 2.0 (Figure 4.4), the shape of the fluorescence emission spectrum is in good correspondence with GNR with aspect ratio 2.5 (Figure 4.3), with maxima around 660 nm and near 685 nm.

The excitation power dependence (Figure 4.4B; square markers) reveals a clear saturation behaviour. This is particularly pronounced in a direct comparison with the Raman signal of plain MilliQ water, which was simultaneously measured. The Raman scattering intensity of water shows the expected linear relationship with power. The saturation behaviour of the broadband features in the emission spectrum further originates from the relatively long lifetime of the fluorescent excited state and results in the broadband emission from GNR. The emission has been attributed to $sp \rightarrow d$ interband transitions in the electronic structure of bulk gold,[147,148,154] as first reported by Mooradian in 1969.[149] The exact position of the emission maxima are related to the GNR in a shape-dependent manner and are in good agreement with previous results from the El-Sayed group.[147,148]

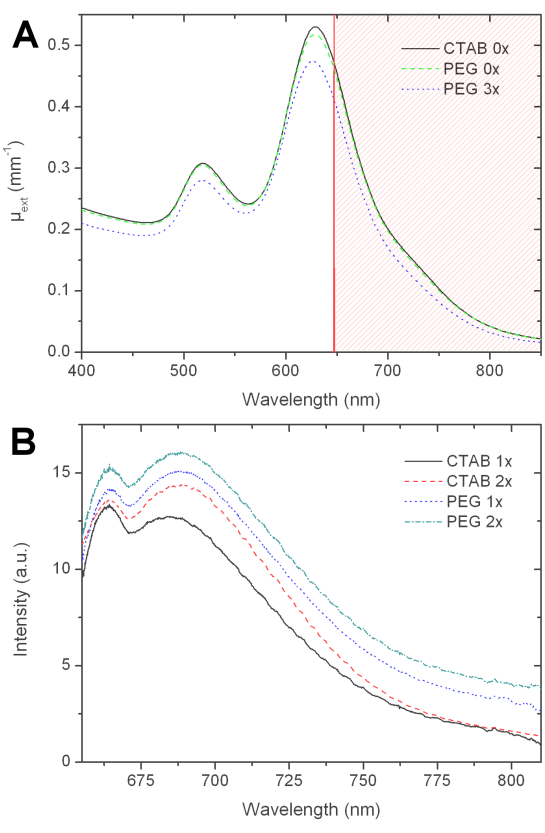

FIGURE 4.3 : A) The extinction spectra show that 24 hours of PEGylation (dashed) and dispersion in cell culture medium after washing (dotted) do not change the optical extinction properties of the gold nanorods as synthesized (line). The 3x refers to the amount of washing steps that were conducted before the sample was subjected to measurement.The vertical line indicates the 647 nm excitation laser line for Raman, the shaded area the Raman detection area; B) ensemble Raman spectra of dispersions of non-aggregated, individual GNR display fluorescence emission in the wavenumber region corresponding to 650-810 nm show that the fluorescence emission does not change upon washing and surface treatment steps, during the exchange of CTAB for PEG. All spectra are corrected for water contribution. Spectra are offset for clarity.

The GNR used for SK-BR-3 cell experiments in the remainder of this work have a longitudinal plasmon absorption maximum at 630 nm (Figure 4.3A), which provides then resonance conditions for the excitation and emission wavelength.

4.3.3 RAMAN FINGERPRINT OF LIVE GNR-INCUBATED SK-BR-3 CELLS

Living SK-BR-3 cells were incubated overnight with PEG-GNR. The Raman spectrum in the fingerprint region of SK-BR-3 cells incubated with GNR changed drastically with respect to the control cultures. The bright-field image in Figure 4.5A shows a PEG-GNR-incubated SK-BR-3 cell with a spherical appearance, similar to the SK-BR-3 cell in Figure 4.1A.

Spectral analysis of a 32×32 pixel map of the PEG-GNR-incubated cell shows that intense amplitudes in relatively few pixels dominate the total intensity from a SK-BR-3 cell in the univariate image in the fingerprint region (Figure 4.5B). These high intensity pixels are clustered together

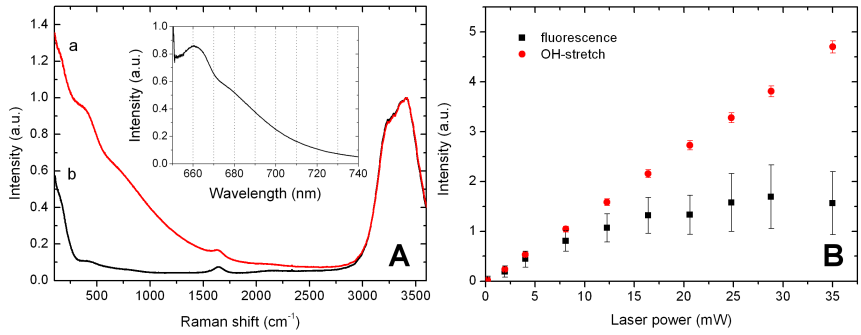

FIGURE 4.4 : A) Full Raman response of a PEG-GNR solution (a) shows a broadband background contribution, whereas a regular MilliQ water solution (b) does not. Both spectra represent an average over 1024 measurements, acquired with 10 mW during 0.5 s. Data was corrected for setup response and normalized to the OH-stretching bands of water (3000-3600 cm^{-1}). The inset shows the corresponding difference spectrum on a nanometer scale corresponding to 75-1950 cm^{-1}. B) The broadband background contribution of the PEG-GNR solution shows a nonlinear behaviour with increasing laser power (squares), while the OH-stretching region scale linearly with applied laser power (dots). Each data point represents an average of 200 measurements, the error bars depict the standard deviation.

in the green and blue pixels in the 7 cluster image (Figure 4.5C). The corresponding cluster averages (Figure 4.5D, spectra a, b and c) show the presence of fluorescence emission contributions in these clusters. It has to be noted that the blue (Figure 4.5D, a) and cyan cluster (Figure 4.5D, b) spectra are related to an individual and double pixel event, respectively. The green spectral trace (Figure 4.5D, c), however, corresponds to 31 pixels and is therefore related to a more common occurrence.

As in the GNR dispersions (Figure 4.3B and 4.4A), the fluorescence observed in PEG-GNR-incubated SK-BR-3 cells has a large influence in the low to intermediate wavenumbers (500-1800cm^{-1}), but hardly affects the high frequency Raman region (Figures 4.5D and 4.5E). Due to the very high intensity of the broadband contributions, the magenta, red and yellow cluster averages are overshadowed.

Although others have reported surface enhanced Raman scattering (SERS) from molecules at or near gold nanoparticles inside cells,[48,155–157] we do not observe intense "SERS-like" contributions. However, normal signal levels corresponding to spontaneous Raman scattering can be observed in combination with the fluorescence emission (Fig 4.5D, traces a, b and c) from the PEG-GNR.

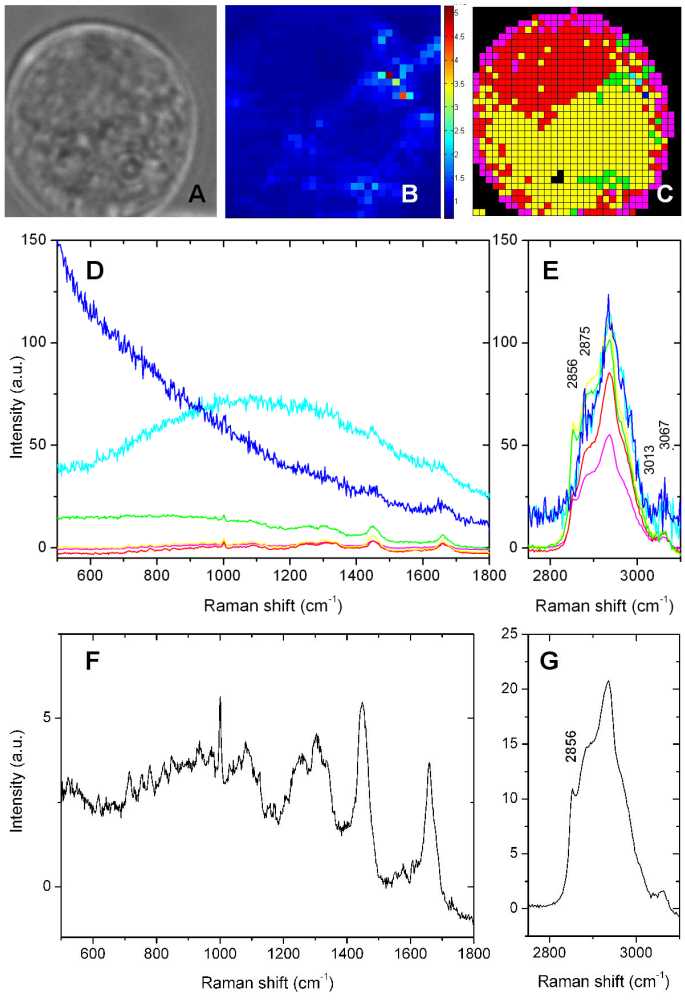

FIGURE 4.5 : Raman analysis of a 32×32 Raman map of an SK-BR-3 cell incubated with PEGylated gold nanorods, acquired with 10 mW and 0.5 s dwell time per pixel: A) brightfield image; B) univariate Raman plot of the fingerprint region (500-1800 cm^{-1}); C) cluster image of 7 Raman clusters: in red the cell nucleus, in yellow the cytoplasm, in magenta the cell membrane and black the surrounding cell medium. The green, cyan and blue pixels represent PEG-GNR fluorescence signal. D) the corresponding average cluster spectra corrected for extracellular cluster (black cluster in C) in the fingerprint region (500-1800 cm^{-1}) and E) in high wavenumber region (2700-3100 cm^{-1}) showing dominating broadband contributions (a-c); F) the weighed sum of all cell related Raman spectra shows that gold nanorod fluorescence dominates the Raman signal in the fingerprint region while in the high wavenumbers (G) the fluorescence influence is negligible. Raman bands indicating the GNR-induced shift in lipid-protein ratio are marked.

In these traces, Raman peaks at 2856, 2875, 3013 and 3067 cm^{-1} are increased with respect to the cell average Raman signature (Figure 4.1E). This suggests colocalisation of GNR with lipid vesicles, as was previously demonstrated by others.[35,143,158,159] The GNR fluorescence from within the cells differs from that of GNR in dispersion (Figures 4.3B and 4.4A). However, as the emission profiles are particle and shape dependent,[147,148] the varying spectral shape in Figure 4.5D may be a result of particle clustering within intracellular vesicles.[35,143,158,159]

Figures 4.5F and 4.5G show the sum of all the spectra from the Raman images that can be attributed to the cell. The Raman spectra are corrected for medium background in the fingerprint region and the high frequency region, respectively. A comparison of the summation of the Raman spectra of the fingerprint of a whole SK-BR-3 cell incubated with PEG-GNR (Figures 4.5F and 4.5G) to that of a control and unperturbed SK-BR-3 cell reveals that the two spectra are very similar. The spectral similarity suggests there is little effect of the PEG-GNR on SK-BR-3 cells.

The summation of the spectra in the fingerprint region of a PEG-GNR-incubated cell shows an increase in baseline in the first half of the wavenumber scale (Figure 4.5F). This is due to the fluorescence of the PEG-GNR inside the cell. However, this fluorescence contribution is not very prominent because the few pixels containing fluorescence signal are outweighed by the large number of pixels dominated by the Raman scattering of the cell. In the high wavenumber region (Figure 4.5G), a virtual absence of the luminescent emission renders an undisturbed view on the pronounced lipid band at 2856 cm^{-1}, which appears to be increased in terms of the unperturbed cell (Figure 4.1E).

Subtle changes between the incubated cells with PEG-GNR and the control cells become more apparent after spectral subtraction as shown in Figure 4.6, which shows the difference spectrum of the Raman sum spectra of a PEG-GNR-incubated SK-BR-3 cell (Figures 4.5F and 4.5G) from which an unperturbed SK-BR-3 cell (Figures 4.1D and 4.1E) was subtracted.

The most prominent differences are observed in the high wavenumber Raman difference spectrum (Figure 4.6B), which show a shift in lipid-protein ratio. The Raman band at 2856 cm^{-1}, representing lipids, is increased after PEG-GNR-incubation, while protein signatures (2950-65cm^{-1}) are decreased. An increase in lipid expression can be explained by the formation of lipid vesicles (endosomes, lysosomes) that encapsulate the PEG-GNR inside the SK-BR-3 cells.[143,158]

Accordingly, in the fingerprint region (Figure 4.6A), the shift in lipid-protein ratio in the cell is illustrated by a decrease in the Amide bands (Amide III between 1200-1375 cm^{-1}, Amide I between 1655-80 cm^{-1}) as well as an increase in lipid characteristic bands (e.g. at 1434 cm^{-1}). In addition, the fluorescence contribution of the PEG-GNR is reflected in the slope of the spectrum. The low signal-to-noise ratio (SNR) of Figure 4.6A emphasizes the subtlety of these differences. The slope in the spectrum of

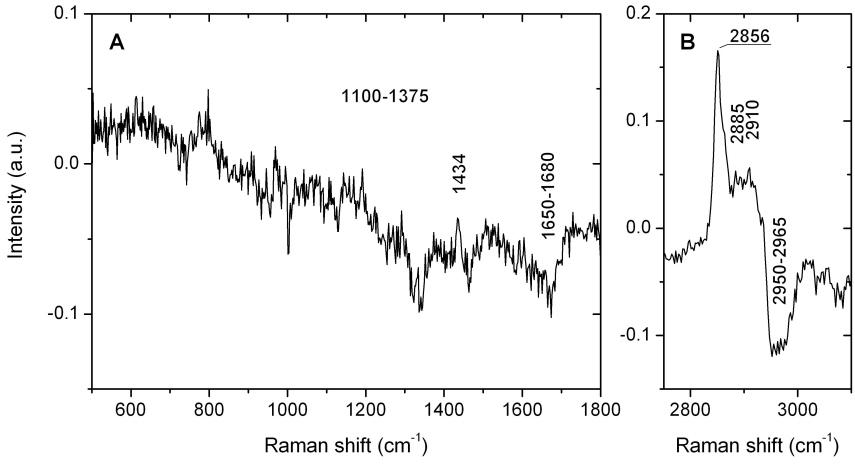

FIGURE 4.6 : Difference Raman spectra of an SK-BR-3 cell before and after 24 hour of PEG-GNR incubation shows GNR fluorescence in A) the fingerprint region (500-1800 cm^{-1}) and enhanced lipid Raman signal in B) the high wavenumbers (2700-3100 cm^{-1}).

Figure 4.6A is a result of the fluorescence contribution of the PEG-GNR.

The active uptake of untargeted PEG-GNR through receptor-mediated endocytosis by cells is unlikely, because the PEG outer layer of the GNR inhibits biorecognition.[43,44,78,160] However, PEG-GNR can enter the cells by pinocytosis of extracellular fluid. As the degree of internalization of nanoparticles is directly proportional to their concentration in the medium,[161] the cells are prone to take up some PEG-GNR, which are present in large surplus with respect to the cells (1.6×10^6 nanorods per cell), albeit at very low concentration of a few picomole.

Inside the cell, nanoparticles cluster within endosomes or lysosomes,[35,143,158,159] where molecules and particles are gathered before being secreted (exocytosis) or degraded. Since GNR fluorescence varies with the dimensions of the particles,[147,148] GNR clustering inside intracellular vesicles may account for the different shapes and intensities of the fluorescence response that are observed (Figure 4.5D). In addition, cell organelle confinement and viscosity affects the diffusion of GNR,[162] which vary with particle size. GNR diffusion rates influence the GNR distribution in different organelles[143] and the local fluorescence emission intensity accordingly.

The experiments reported were repeated on many different individual cells. The statistical relevance of the observations described above are reflected in Figure 4.7. Figure 4.7 shows Raman data matrices of four different PEG-GNR SK-BR-3 cells combined and subjected to a single HCA analysis. This approach directly illustrates the correspondence between different individual SK-BR-3 cells after PEG-GNR addition. In complete

agreement with Figures 4.4A and 4.5D, the influence of the GNR fluorescence dominates in the fingerprint region (Figures 4.7A and 4.7C) and different fluorescence patterns are displayed at different locations in the cells.

In the high wavenumbers (2700-3100 cm^{-1}, Figures 4.7B and 4.7D), a region not affected by the spectral distribution of the luminescence and dominated by lipid contributions, the correspondence in intracellular chemical composition of the cells is reflected by the 4-in-1 cluster analysis. As was demonstrated before,[107] the chemical composition of live populations of SK-BR-3 is consistently measured with Raman imaging. Figure 4.7D shows that the increase in the Raman band at 2856 cm^{-1} is a general feature for different PEG-GNR-incubated SK-BR-3 cells. This band is characteristic for lipid molecules.

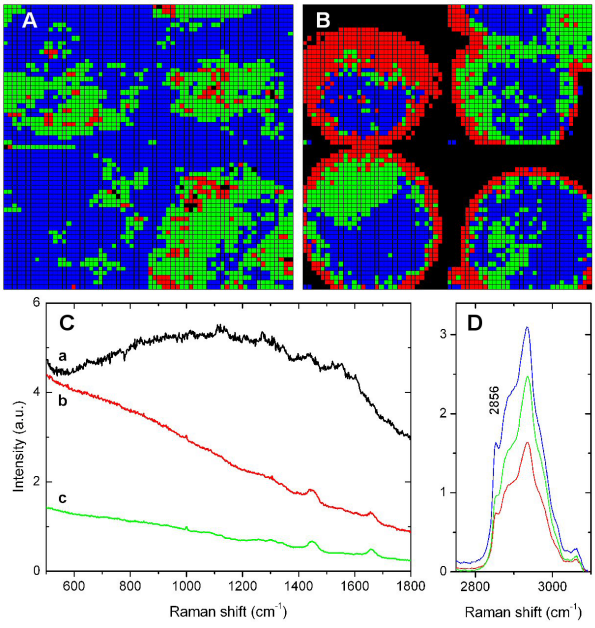

FIGURE 4.7 : Four different SK-BR-3 cells incubated with PEGylated gold nanorods were subjected to a single hierarchical cluster analysis (HCA) of 4 levels showing the presence of a dominating feature in A) the fingerprint region (500-1800 cm^{-1}), while in B) the high wavenumbers (2700-3100 cm^{-1}) still the identical overall intracellular chemical composition is reflected. All cells were imaged with 10 mW under the objective and 0.5 s dwell time per pixel. Corresponding cluster averages are depicted in C) and D) respectively.

4.4 Conclusions

We have incubated SK-BR3 breast cancer cells with PEGylated gold nanorods. These PEG-GNR were acquired by PEGylation of CTAB-coated gold nanorods. The absorption and fluorescence emission spectra after each preparatory step in the conversion from CTAB-GNR to PEG-GNR showed that the aspect ratio of the gold nanorods was maintained and no evidence of aggregation was observable from the spectra. Single-cell confocal Raman microscopy with low laser doses was used to map the chemical composition of SK-BR-3 breast carcinoma cells in the presence and in the absence of untargeted PEGylated GNR after overnight incubation. The PEG-GNR nanoparticles were recognized inside the cell with the typical fluorescence emission spectrum for gold nanostructures. The plasmon enhanced fluorescence spectrum of gold nanorods, with aspect ratio's between 2.0 and 2.5, overlaps with the fingerprint region (500-1800 cm^{-1}) in the Raman spectra of SK-BR-3 cells. It was shown, by simultaneous hierarchical cluster analysis (HCA) of independently measured cells, that the optical properties of both GNR and cells, were representative for the sample.

The Raman spectra of the cells incubated in the presence and absence of PEG-GNR also revealed subtle differences. The spectral differences were related to an increase in signals at wavenumber positions common for lipid molecules. HCA of single SK-BR-3 cells and of groups of four different SK-BR-3 cells established that different cells react in a similar way to PEG-GNR incubation.

We conclude that the typical fluorescence emission of gold nanorods provides an excellent contrast to visualize the nanoparticles inside cells. The signal can be disentangled easily from the Raman signals of the cellular material itself by multivariate methods. The correlation between fluorescence emission of gold nanorods and Raman emission from cell material leads us to conclude that GNR-incubated cells have a higher lipid content then cells without GNR.

CHAPTER 5

Photo-induced luminescence of gold nanostructures

In order to gain deeper understanding of the fluorescence emission from our gold nanorods (GNR), a critical overview of the literature on the fluorescence emission of gold nanostructures is provided. We discuss the reported emission values and the proposed mechanisms for the observed emission, starting with the mechanisms on the basis of gold luminescence in the visible and in the infrared (IR). Next, single photon induced emission is discussed, as well as emission enhancement mechanisms involving surface plasmons.

Gold fluorescence has also been observed in non-linear optical imaging studies, concerning mainly two-photon luminescence. This luminescence appears to be based on the same visible emission mechanisms as single photon fluorescence. Surface plasmon resonances can enhance the fluorescence emission of gold in both single and multiple photon excitation systems.

The geometry of gold nanoparticles determines the shape and intensity of the surface plasmon bands. Therefore, the nanoparticle geometry strongly affects surface-enhancement effects, such as surface enhanced Raman scattering or surface enhanced fluorescence.

This chapter is concluded by comparing our own results on fluorescence emission of gold nanoparticles to the literature reports, positioning our results in the context of the current field.

5.1 Visible emission

Luminescence of bulk gold was first reported by Mooradian in 1969.[149] The photoemission band displayed a maximum at approximately 560 nm. This luminescence was attributed to fluorescence emission, as the peak position did not change with different excitation wavelengths. More specifically, the author assigned the observed fluorescence to transitions of electrons from the conduction band, via the Fermi level to holes in the *d*-band, because the fluorescence band emission was centered near the interband absorption edge of gold (2.2 eV).[149] Figure 5.1 presents the photoluminescence as a three-step process consisting of the excitation of an electron from a ground state to a high-energy state, followed by relaxation of the excited electron and finally, recombination of electrons and holes. The conduction band represents an *sp*-conduction band, two sets of *d*-bands as indicated by the shaded regions. Because of the small photon momenta involved, the interband transitions were assumed to be direct.[149]

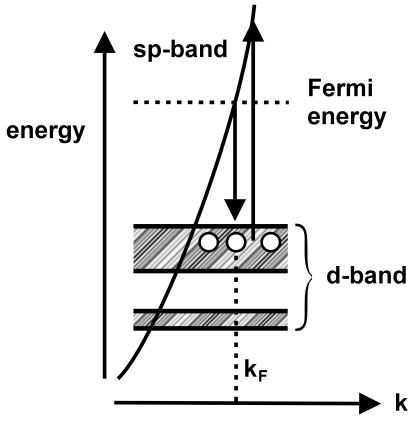

Figure 5.1 : Schematic band structure of gold, after Mooradian.[149] Direct recombination of *sp*-band electrons with holes in the *d*-bands leads to fluorescence emission. The *d*-band consists of a number of sub-bands, lying close to each other in k space. The holes in the *d*-bands have been scattered to momentum states below the Fermi momentum k_F.

In the last decade luminescence from gold structures has been investigated extensively,[147,154,163–170] and direct radiative electron-hole recombination as proposed by Mooradian is still considered the main emission mechanism.

However, the fluorescence of bulk gold was found to be rather weak with a quantum yield of 10^{-10},[149] as was confirmed by Whittle *et al.* a decade later.[171] Both experimental and theoretical results by Boyd *et al.*[172,173] showed that large enhancements in fluorescence emission of gold could be obtained, which were attributed to localized plasmon resonances. These local enhancements of the incoming and outgoing fields near the surface of the metal are caused by interaction of incident radiation with metal electrons in a plasma-type oscillation of the valence electrons.[172,173] The surface

plasmon enhancing effect becomes even more pronounced in structures with a submicron size, which exhibit strong resonant interactions with the incident radiation.[141] Around that same time, similar enhancements were observed in SERS activity.[174–177] Based on the observations of Mooradian and Boyd, Apell *et al.*[178] developed a theoretical model to explain the radiative recombination in noble metals. This model predicts that when the plasmon resonance is around the *d*-orbital transitions, the emission is enhanced as a result of changing population distributions of the electrons and holes.[173,178]

Even though there appears to be a general agreement on the origin of gold luminescence in the visible, connected to the radiative interband transitions described above, experimental values recently reported by various researchers cover a wide range of both excitation and emission wavelengths of gold structures. Table 5.1 provides an overview of the single photon induced luminescence of gold nanostructures which have recently been reported. For completeness and comparison, the luminescence values reported in the early studies by Mooradian and Boyd are also included.

Although these early studies reported solely on luminescence in the visible,[149,172,173] more recently acquired results show additional emissions in the near-infrared (NIR) to infrared (IR).[179–182]

5.2 IR emission

While visible emission is well explained by interband transitions of *d*-band electrons into the conduction band and subsequent radiative recombination,[149] emission in the IR is believed to be caused by a different photophysical mechanism.[179,182,183] IR emission was proposed to be generated by intraband transitions,[179,182,183] and involved the highest occupied molecular orbital and lowest unoccupied molecular orbital (HOMO-LUMO gap) within the *sp*-conduction band (1.3 eV, ∼950 nm), as illustrated in Figure 5.2.[182,183]

It has to be noted that for intraband recombination to occur, non-radiative recombination of the hole in the *d*-band has to take place. Therefore, the existence of intraband transitions is usually forbidden or is accompanied by non-radiative decay.[9,184]

However, the IR emission appears to be only present for surfaces with nanometer-scale roughness.[179–183] The localized surface plasmons near rough metal nanostructures are presumed to perform a mediating role in the IR emission,[184,185] because these strongly confined fields possess resonances of electrons in the metal, and the associated field gradients give rise to higher-order multipolar transitions.[179] Independently, Varnavski *et al.* also speculated upon a possible role of surface plasmons in intraband excitations.[186]

Type	Dimensions	$\lambda_e m$(nm)	$\lambda_e xc$(nm)	By
surface		520	488, 514	Mooradian 1969[149]
			300-400	
surface		516	529	Boyd 1986[173]
		420, 496	354	
		387, 413, 486, 563, 653	265	
surface	smooth	520	400	Beversluis 2003[179]
surface	rough	900	780	Beversluis 2003[179]
GNR	AR 2.0	548	480	Mohamed 2000[148]
	AR 2.6	552		
	AR 3.3	568		
	AR 4.3	579		
	AR 5.4	588		
GNR	AR 1.8	530, 600	400	Varnavski 2003,[186]
	AR 2.7	530, 610	267	Varnavski 2005[187]
GNR	AR 2.5	370, 670	300	Jian 2004[188]
GNR	AR 2.25	575, 740	480, 407-437	Eustis 2005[147]
	AR 3.25	600, 740		
GNR	AR 3.2	737	636, 465	Chen 2009[143]
shells	114+20 nm	570, 630	514	Kang 2006[189]
GNS	25 nm	530	385-415	Varnavski 2003[186]
GNS	25 nm	530	267	Varnavski 2005[187]
GNS	1-6 nm	530, 440	375	Dulkeith 2004[190]
GNS	18 nm	430	300	Jian 2004[188]
GNS	10 nm	670	525	Jian 2004[188]
clusters	5 nm	440	230	Wilcoxon 1998[191]
	<5 nm	v352, 420, 670		
clusters	Au38	1100-1600	1064	Bigioni 2000[180]
	Au145	1100-1600		
clusters	1.8 nm	770	451	Huang 2001[192]
	<1.8 nm	750		
clusters	Au28	800	500	Link 2002[182]
	Au28	1100	514	
clusters	Au38	902, 1025	400, 685	Lee 2004[181]
			650, 750	
			680, 600	
clusters	Au5	385	329	Zheng 2004[164]
	Au8	455	385	
	Au13	510	433	
	Au23	760	670	
	Au31	866	765	
clusters	Au7	432	366, 387	Bao 2007[165]
	Au8	452		
	Au8	458		
	Au9	470		
	Au13	540		
	Au17	570		
	Au23	610		
dendrimers		570	395	Varnavski 2001[193]
chains		370, 660, 735	300	Jian 2004[188]

TABLE 5.1 : Experimental values of single photon induced gold luminescence in literature. The emission wavelength ($\lambda_e m$) from different gold structures is provided, as well as the wavelengths used to excite these structures ($\lambda_e xc$). The surface type of gold refers to bulk surfaces, such as thin evaporated films. The dimensions of the gold structures are given refer to either the aspect ratio (AR) or the diameter for the gold nanorods (GNR) and nanospheres (GNS), respectively. For the nanoshells the diameter of the silica core plus the thickness of the gold shell are indicated. In case of the nanoclusters, either the number of gold atoms or the cluster diameter is indicated.

Localized surface plasmons appear to play a role in the emission of gold. It has therefore been proposed that gold fluorescence is related to the shape of gold nanoparticles, since surface plasmon bands are dependent on the particle shape.[14,21,69,194] Therefore, the geometry of nanoparticles may give rise to dependence in the emission properties.

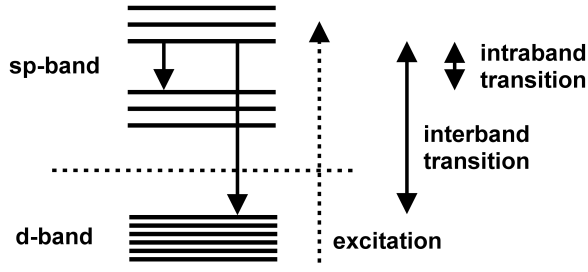

FIGURE 5.2 : Solid state model for the origin of two luminescence bands, after Link *et al.*[182]

5.3 NANOPARTICLES

Gold nanoshells generally consist of a silica nanospherical core, which is covered by a gold layer.[12] Gold nanoshells exhibit localized surface plasmon resonances that can be tuned by varying the ratio of the radius of the silica core to the radius of the overall nanoparticle.[10] Although nanoshells and their surface plasmons have been subjected to extensive research,[10,11,195–197] their photoluminescence properties have been left relatively untouched (Table 5.1). We will therefore not discuss the photophysical properties of gold nanoshells, but, instead, we will focus on solid gold nanostructures, such as spheres, clusters and rods, as the latter are mostly used in the experiments described in this thesis.

The distinction between gold nanospheres and nanoclusters in the literature is not well-defined. Different names to apparently similar objects have also been used: nanospheres are sometimes referred to as nanodots[148] and nanoclusters are also called nanocrystals,[180,198] because of their atomic crystalline arrangements. For example, Lugunov *et al.* refer to gold arrangements of roughly 200 gold atoms, which are approximately 1.9 nm in diameter, as gold nanocrystals,[198] and Schaaff *et al.* use the term nanoclusters for structures with diameters up to 4 nm.[199] On the other hand, structures with diameters ranging from 1 nm to 6 nm have been certified as gold nanospheres.[163,190] Here, all spherical gold structures with a diameter larger than 5 nm are considered gold nanospheres (GNS).[183]

5.3.1 NANORODS

For gold nanorods (GNR), experimental results with regard to the size dependency of photoluminescence emission appear to be contradictory. As seen in Table 5.1, Mohamed *et al.* and Eustis *et al.* report that GNR fluorescence emission is aspect ratio (AR) dependent,[147,148] while Varnavski *et al.* show similar emission profiles for GNR of different aspect ratios.[186,187] Moreover, comparison of the reported emission profiles from different groups is aggravating. For example, Mohamed *et al.* reported the emission peaks for GNR with aspect ratios of 2.0 and 2.6 to occur at 548 nm and 552 nm, respectively, others[147,188] demonstrated maximum emissions at 575 nm for 2.25 AR GNR and at 670 nm for 2.5 AR GNR. In addition to the main GNR emission, which is generally observed to be between approximately 550 nm and 670 nm, other emission contributions have been presented. Varnavski *et al.* report a shoulder in the emission profile at 530 nm, which coincides with an emission peak they observed for spherical particles of 25 nm diameter.[186,187] This observation illustrates an effect of both surface plasmons of gold nanorods, the longitudinal plasmon along the long axis and the transverse plasmon along the short axis, the latter coinciding with the plasmon of the nanospheres. Eustis and El-Sayed observed an emission band around 740 nm, which appeared in all their GNR samples, as well as in solutions of gold nanospheres (GNS) and was therefore considered a property of the metal.[147] The exact origin of this band is still under debate, but the general consensus is that this emission cannot be accounted for by the same mechanism as the visible emission,[147,179] as depicted in Figures 5.1 and 5.2.

5.3.2 NANOSPHERES

There are not many results published on the single-photon induced luminescence of gold nanospheres, which is probably due to their limited emission properties.[9] Several studies have shown that GNS do not emit at all.[148,183,191]

However, Jian *et al.* reported different emission peaks for GNS with a diameter of 10 nm and 18 nm.[200] The weak emission they observe from the 10 nm GNS at 670 nm occurs after excitation at the 525 nm maximum absorption.[200] The absorption peak at 525 nm is ascribed to the plasmon resonance, which is therefore thought to play an important role in the photoluminescence of GNS.[200] In related work, Jian *et al.* claimed to excite the surface plasmon coherent electronic motion as well as the *d*-electrons of 18 nm GNS with 300 nm light, resulting in a single emission peak in the blue (430 nm).[188] In this case, fluorescent emission occurs when relaxation of these electronic motions is followed by the recombination of the *sp*-electrons with holes in the *d*-band, which is in agreement with earlier studies.[148,149,173]

The role of plasmon resonances in gold photoluminescence of gold nanospheres was further explored by Varnavski *et al.*, who investigated the time-resolved emission from gold nanostructures. They showed that photoluminescence of gold nanoparticles consists of a fast and a slow emission component, on the femtosecond and picosecond time scale, respectively.[186,187] Similarly, Dulkeith *et al.* optically excited gold nanoparticles and observed a strong fast emission component, also in the order of some 10 ps, peaking at 520 nm, which was followed by a weak nanosecond long-lived component at 440 nm.[190]

The fast and slow emission components were attributed to separate mechanisms.[186,187] Moreover, the emission efficiency was found to be independent of particle size[190] and particle shape.[186,187]

In analogy to these observations, Varnavski *et al.* found that for both GNS and GNR, the fast emission peak emerges consistently at 530 nm, independent from the excitation wavelength.[186,187] Interestingly, this 530 nm emission corresponds to the *d*-band onset of gold (∼2.34eV).[149,173,178] In addition, the relaxation process of photoexcited *sp*-electrons occurs extremely fast.[149,201] Thus, the observed fast emission was ascribed to *sp*-electron-*d*-hole recombination, with the enhancement of the incoming and outgoing fields via plasmon resonances,[186,187,190] as was initially proposed by Boyd *et al.* in 1986.[173] This attribution of the emission to the electron-*d*-hole recombination mechanism was used in calculations of ultrafast emission spectra and their results confirmed the experimental data mentioned above.[186] Moreover, they matched earlier calculations by Boyd and Apell.[173,178] Several other reports have also shown a strong correlation between these fast non-linear optical processes, involving the surface plasmon, and electron distribution change and its dynamics.[202,203]

5.3.3 NANORODS VS. NANOSPHERES

It has been observed that the photoluminescence intensity for nanorods was much stronger than for nanospheres.[147,148,186,187,200] This difference in emission intensity can be accounted for in several ways.

Here too, surface plasmons appear to play an important role, because they are related to the morphology of the nanoparticles. It has been proposed that the incoming and outgoing fields are enhanced via coupling to the local plasmon resonance.[172,173] For structures that have multiple surface plasmon resonances, all these resonances will take effect and increase local emission enhancement. Therefore, for GNR, both transverse and longitudinal surface plasmon resonances stimulate photon emission, whereas in spherical structures, emission enhancement is limited to a single plasmon.[148,188] The longitudinal plasmon changes with the aspect ratio of nanorods, and therefore influences the enhancement of the emission from GNR in a size-dependent manner. This effect is also known as the "lightning rod effect".[148,186]

The effect of multiple plasmons in fluorescence emission was illustrated by Varnasvki *et al.*, who reported a shoulder in the GNR fast emission profile (at 530 nm), using time-resolved fluorescence spectroscopy.[186,187] This peak coincides with the fast emission peak for GNS near the transverse surface plasmon resonance.[186,187]

In the case of GNS, Jian *et al.* consider an additional small-size effect. That is, the decreasing size of the particles alters the level structure and energy level splitting enables the electron transition. The accompanying emission photons can have many different frequencies, but only a few frequencies match the local plasmon, which is required for emission enhancement.[188]

In general, the enhancement of the local field associated with the plasmon of GNS is relatively low, in the order of 10.[9] Moreover, the local field enhancement decreases with increasing particle radius as a consequence of enhanced radiation damping.[184] In contrast, GNR can have very high field enhancement factors of up to 23 due to suppressed interband damping.[9] For GNR, therefore, higher levels of emission enhancement are obtained than for GNS.

5.3.4 NANOCLUSTERS

Gold nanoclusters range from small collections of gold atoms, as few as five,[164] to larger structures, containing hundreds of atoms.[180,198] There is a general consensus on the fluorescence capabilities of gold nanoclusters resulting from the many studies that have been conducted (Table 5.1).

Fluorescent emission from gold clusters was first observed in 1998 by Wilcoxon *et al.*,[191] who reported that intense photoluminescence in the visible only occurs in case the nanoclusters are sufficiently small (<5 nm). Moreover, the visible emission of gold nanoclusters appeared to be size dependent.[191] This size dependent emission has later been confirmed by different groups[164,165,183,192] who all show that with increasing cluster size, the emission peak shifts towards the red.

Initially, the mechanism for the luminescence in the visible was hypothesized to be associated with interband transitions (Figure 5.3),[180,191,192] analogue to the radiative recombination of Fermi level electrons with *sp*- or *d*-band holes as proposed by Mooradian in 1969.[149] However, there was no obvious correspondence between the emission spectra of the gold surface and nanoclusters, but this discrepancy was attributed to surfactant effects.[191,192]

More recent studies have shown, however, that the photoluminescence behaviour of gold nanoclusters is fundamentally different from that of bulk gold and other larger structures such as nanorods and nanospheres.[164,181,183] Absorption studies have shown that the electronic and optical properties of gold nanoclusters require new concepts.[183,204] Earlier, it has been proposed that nanoclusters smaller than 4 nm in radii would experience quantum

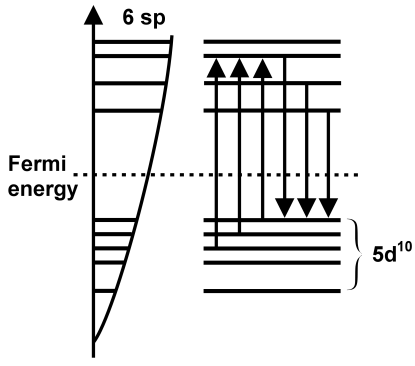

FIGURE 5.3 : Schematic model of interband excitation and emission , depicting interband transitions between the filled $5d^{10}$ band and $6(sp)^1$ conduction band, in analogy to Huang *et al.*[192]

confinement.[205] The influence of quantum-size effects scales with the particle size, that is, the smaller the nanocluster, the more dominant the quantum size effects become. In case the cluster is composed of only a few atoms, a molecular description expresses the particle's properties best.[164,181,182]

Essentially, the quantum-size effects imply the formation of quantized energy states, as they occur in molecules, in contrast to band formation in larger particles.[198] In analogy to the photophysical properties of a molecule, Link *et al.* assigned the two luminescence bands they observed from Au28 nanoclusters (Table 5.1) to the fluorescence and phosphorescence originating from singlet and triplet states, respectively (Figure 5.4).[183]

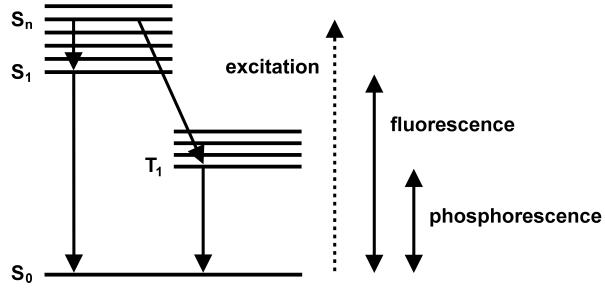

FIGURE 5.4 : Molecular model for the origin of the two luminescence bands: Excitation into higher excited states (S_n) is followed by rapid relaxation (internal conversion) to the lowest excited singlet state (S_1). Radiative recombination with the ground state (S_0), fluorescence, gives rise to the high energy luminescence band. Intersystem crossing to the lowest excited triplet state (T_1) followed by radiative relaxation to the ground state, phosphorescence, causes the luminescence band at lower energies.

Besides visible emission, broad IR emission was reported for gold nanoclusters of different sizes.[180–182] The onset of this IR emission is consistently

appearing around 1100 nm, which suggests that visible and IR luminescence are caused by different photophysical mechanisms. As discussed earlier (section 5.2 of this chapter), IR emission is attributed to intraband rather than interband transitions.[179,180,182]

Bigioni *et al.* demonstrated that the bandwidth of the IR emission of Au38 gold clusters was similar to that of clusters consisting of 145 gold atoms.[180] A change in intensity of the emission and a decrease of the band maximum to lower energies was also observed. This is consistent with the outcome of the jellium model, which predicts that energy gaps become smaller for larger nanoclusters.[164,206]

5.3.5 NANOCLUSTERS VS. NANOSPHERES

The amount of emission of gold nanospheres is small[9] and seems to require enhancement through excitation of localized surface plasmons.[172,173,186,187,190] The fast femtosecond scale photoluminescence emission is attributed to *sp*-electron-*d*-hole recombination,[172,173,186,187,190] in analogy to the emission of bulk gold.[149,171] However, the photoluminescence intensity for nanoclusters is much stronger than for nanospheres. Moreover, the emission of nanoclusters is strongly dependent on size, and can be excited in a broad wavelength range (Table 5.1). This implies a less prominent role for surface plasmons than is the case for GNS. These observations suggest different luminescence mechanisms for clusters and spheres (see section 5.3.4).[183]

Smith *et al.* proposed that gold clusters play a key role in the transition from bulk to molecular behaviour and suggested this transition takes place in a narrow size range between 55 and 13 atoms.[207] Later, Zheng *et al.* provided the connection between atomic and metallic behavior using the spherical jellium model.[164] The jellium model provides an explanation for delocalized, free conduction electron behaviour relative to the atomic cluster core,[206] and predicts that nanoparticle plasmon widths and nanocluster transition energies of true free-electron metals both scale with inverse cluster radius. Accordingly, Zheng *et al.*[164] demonstrated that the emission wavelength of the nanoclusters appears to scale with the number of atoms in gold clusters by a scaling relation of:

$$\frac{E_F}{N^{\frac{1}{3}}} \tag{5.1}$$

Here, E_F is the Fermi energy of bulk gold[206] and N the number of atoms per cluster. As nanoclusters increase in size, transition energies decrease with the increasing density of states. Consequently, electron confinement switches from being relative to the Fermi wavelength to being relative to the electron mean free path. Therefore, gold nanoclusters are considered

to provide the missing link between atomic and nanoparticle behaviour in noble metals.[164]

5.3.6 NANOCOMPOSITES

Gold nanocomposites are structures consisting of gold nanoparticles, such as GNS or GNR. With regard to the fluorescence of gold nanocomposites, findings on gold nanodendrimers and gold nanochains have been reported. Both structures can be considered assemblies of spherical gold nanoparticles.[188,193]

The fluorescence profiles of the nanocomposites reported in Table 5.1 correspond to the emission mechanisms proposed for metal rods and spheres in colloidal systems,[186,187,190,193,208] which are described in the previous paragraphs. Thus, the femtosecond emission component of gold nanodendrimers is ascribed to *sp*-electron-*d*-hole recombination,[193] as initially proposed by Mooradian *et al.*,[149] and is considered to be a property of bulk gold.[149,186,187,190] Similarly, gold nanochain fluorescence was attributed to enhancement of the emission through recombination via coupling to the local plasmon resonance,[188] as was established by Boyd *et al.*[172,173]

5.4 NON-LINEAR EFFECTS

The application of intense, short pulses of light enables the excitation of a non-linear optical response. The non-linearities can be enhanced by the presences of surface plasmons.

Table 5.2 summarizes the experimental values of non-linear induced gold luminescence which have been reported after two-photon excitation in the near-infrared (NIR). NIR excitation is very attractive for *in vivo* applications, since biological tissues are relatively transparent in this region. Successful application of two-photon imaging of gold nanoparticles was demonstrated *in vitro*,[168] as well as *in vivo*.[169] Using multiple-photon techniques, a larger spatial resolution can be achieved than with single-photon systems, because only the molecules at the focus of the femtosecond laser will be excited. For *in vivo* situations, this offers the additional advantage of less photodamage to the surrounding tissue.

Upon two-photon excitation in the NIR, broadband emissions are consistently observed around 600 nm for different gold structures (Table 5.2).[154,163,166–169,179,209,210] This is similar to the spectral emission properties excited with weak fields in linear fluorescence spectroscopy (Table 5.1) and suggests that the emission is characteristic of the gold metal.[173,178,179] In fact, two-photon-induced photoluminescence process was found to be initiated by sequential one-photon absorption for creating a pair of an electron and a hole in the *sp*- and *d*-bands,[166] in analogy to single photon luminescence.[149]

Although the photon luminescence signal is typically weaker than single photon luminescence,[167] it can be strongly enhanced by local fields,[173,179,186] illustrating the influence of surface plasmon resonances. The emission enhancing role of surface plasmons was confirmed by the size dependent emission of GNR upon multiple photon excitation.[154] Corresponding to the single photon case, this size dependent emission is explained by coupling of the emission to the longitudinal surface plasmon, which is aspect ratio dependent in the case of GNR[148,186] (as described in section 5.3.3). Because two-photon optical processes involve an additional field enhancement,[166] greater enhancement of photoluminescence compared to the single-photon case can be obtained.

Morphology		$\lambda_e m$(nm)	$\lambda_e xc$(nm)	t(fs)	By
surface	rough	525	1060	8×10^6	Boyd 1986[173]
surface	rough	600	780	200	Beversluis 2003[179]
GNR	AR 3.x	610	780	300	Park 2008[168]
GNR	AR 1.6	645	785	120	Bouhelier 2005
	AR 2.3	675			
	AR 3.3	720			
GNR	AR 3.0	518, 654	830	200	Wang 2005[209]
GNR	AR 2-50	550, 650	780	100	Imura 2005[166]
GNR	AR 3.8	400-700	770	130	Tong 2009[169]
shells	130+21 nm	494-634	780	140	Bickford 2008[210]
	254+19 nm	494-634			
shells	120+15 nm	610	780	300	Park 2008[168]
GNS	100 nm	550	780	200	Beversluis 2003[179]
	100 nm	600			
GNS	15 nm	470-680	790	100	Farrer 2005[163]
	2.5-125 nm	470-680			
GNS	10 nm	600	790	80	Nagesha 2007[167]

TABLE 5.2 : Experimental values of multiple photon induced gold luminescence in literature. The emission wavelength ($\lambda_e m$) from different gold structures is provided for given excitation wavelengths ($\lambda_e xc$) and pulse lengths (t). The surface type of gold refers to bulk surfaces, such as thin evaporated films. The dimensions of the gold structures are given refer to either the aspect ratio (AR) or the diameter for the gold nanorods (GNR) and nanospheres (GNS), respectively. For the nanoshells the diameter of the silica core plus the thickness of the gold shell are indicated.

5.5 Materials and methods

5.5.1 gold nanoparticles

Citrate-capped gold nanospheres (GNS) of 60 nm and 80 nm diameter were obtained from BBInternational (BBInternational, Cardiff, UK). GNS stock

solutions were diluted 10 times with MilliQ water (Millipore, Billerica, MA, USA). Final concentrations of the GNS solutions were 1.4×10^{10} ml^{-1} and 0.4×10^{10} ml^{-1} for the 60 nm and 80 nm spheres, respectively.

Gold nanorods (GNR) of several aspect ratios were synthesized as previously described,[14] using the seed mediated growth method.[22,150] In the GNR synthesis, gold seeds are added to a growth solution, which contains the shape directing surfactant hexadecyltrimethylammonium bromide (CTAB). CTAB is cytotoxic[37,81,144] and therefore, in general, GNR are PEGylated.[44,78,81,144] Here, we PEGylated all but one GNR sample, in the manner previously described.[81,170] In biomedical applications, PEG-GNR are directed to the cell surface using antibodies. Part of the PEG-GNR samples were conjugated with HER81 monoclonal antibody (Immunicon, Huntingdon Valley, PA, USA) using a bifunctional PEG crosslinker orthopyridyl dithio-polyethylene glycol- succinimidylpropionate (OPSS-PEG-PDP, Polypure, Oslo, Norway). The final concentrations of the GNR, PEG-GNR and Ab-PEG-GNR were approximately 10^{11} ml^{-1}.

5.5.2 ABSORBANCE SPECTROSCOPY

Absorbance (optical extinction, μ_{ext}) spectra were acquired to establish the location of the GNR plasmon bands. In addition, the amplitudes of the absorbance spectra were used for estimating number densities as previously described.[7,81,152,170]

Samples for UV-visible absorbance spectroscopy were prepared in 1.5 ml polystyrene cuvettes (Plastibrand, Sigma-Aldrich, St Louis, MO, USA). Spectra were recorded in a Shimadzu UV-2401PC spectrophotometer in the range 300-900 nm, with a 1.0 nm slit width.

Additional absorbance measurements were performed on a Tecan Safire^2 microplate reader (Tecan, Männedorf, Switzerland). Here, 200 μl aliquots of the sample solutions were pipetted in a black, micro-clear flat bottom 96 well UV-star microplate (Greiner Bio-One, Alphen a/d Rijn, The Netherlands). Absorbance spectra were acquired between 230 nm and 1000 nm, 5 nm slit width.

5.5.3 EMISSION SPECTROSCOPY

Emission spectroscopic measurements were carried out on a confocal microspectrometer similar to the setup previously described.[106] The 647 nm excitation light from a Krypton ion laser light source (Innova 90-K; Coherent Inc., Santa Clara, CA) was focused through a $40\times/0.75$ NA objective (Olympus UPFLN; Olympus, Hamburg, Germany) onto gold nanoparticle dispersions sealed under glass coverslips. The objective was used for illumination of the sample as well as for collection of scattered photons.

Before the scattered light enters the spectrograph/detector modality, it passes through a super notch filter (Kaiser Optical Systems, Inc., Ann Arbor,

MI), to suppress the laser line, and a 15 μm diameter confocal pinhole. The spectrograph was optimized for high resolution emission measurements. The incoming light was detected on a thermo-electrically cooled CCD camera (Pixis 100B, Princeton Instruments, Roper Scientific, USA).

Emission spectra were acquired in the region of 650 nm to 950 nm, corresponding to -40 - 4930 cm^{-1} with respect to the excitation wavelength. The laser beam was stepped over the sample in a raster pattern. Spectra were acquired at each position with a laser power of 4 mW under the objective and a dwell time of 0.2 s/pixel. The emission spectra of GNR dispersions were averaged over 1024 (32 $\times$ 32) measurements to obtain a smooth average response of the non-aggregated, individual nanoparticles in the dispersion.

5.6 Results and discussion

5.6.1 absorbance spectroscopy

Figure 5.5 shows the absorbance profiles of gold nanoparticle (GNP) samples of different sizes. These spectra correspond with the results by Link *et al.*,[21] who applied Gans' extension[211] of Mie's theory[212] to calculate the absorbance spectra of gold nanorods of different aspect ratios using medium dielectric constants. That is, with increasing aspect ratio of the nanorod, the longitudinal plasmon resonance peak increases in wavelength and intensity for a given concentration of nanorods.[21,213] The relation between the plasmon bands and the GNR aspect ratio is given in Table 5.3. GNP number densities were determined from the spectra as was previously described.[81,152,170]

Sample	TP(nm)	LP(nm)	AR(-)	[GNP](ml^{-1})
GNS60	536	-	-	1.36×10^{10}
GNS80	551	-	-	4.16×10^{9}
GNR646	513	646	2.0	1.76×10^{11}
GNR671	514	671	2.3	1.70×10^{11}
GNR752	521	752	2.8	1.36×10^{11}
GNR789	516	789	3.0	1.60×10^{11}

Table 5.3 : Relation between the position and intensity of the plasmon bands and particle aspect ratio (AR) and concentrations. For GNS, the Transverse Plasmon (TP) and the Longitudal Plasmon (LP) are the same.

Surfactants

The surfactants that keep the GNP in dispersion affect the absorbance profiles as well. In addition to the plasmon bands, absorbance bands of

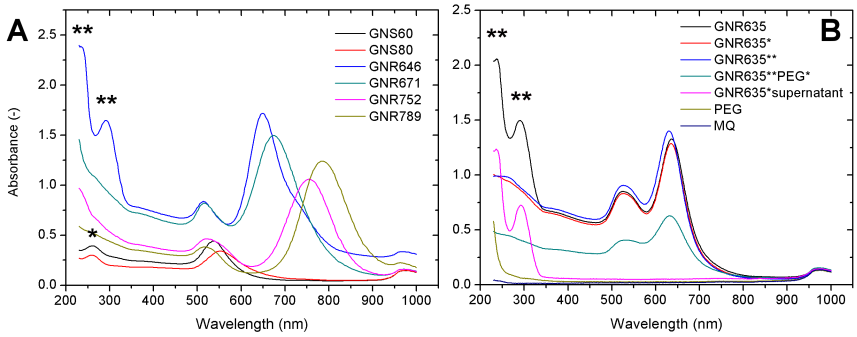

FIGURE 5.5 : A) Absorbance profiles of the different gold nanoparticles show their different plasmon bands; B) Absorbance profiles of GNR635 after the washing and reaction steps in the PEGylation process reveal the origin of the UV-absorption bands. All data acquired on the Tecan microplate reader. Surfactant contributions are marked with asterisks: CTAB (**) and citrate (*).

surfactants are present in the UV, which have been marked with an asterisk in Figure 5.5A. The absorbance profiles of GNS with a diameter of 60 nm and 80 nm respectively, exhibit a peak in the UV as well, around 265 nm. This absorbance band is related to the citrate capping of the particles.[214,215]

The GNR646 sample shows absorbance peaks in the UV at 240 nm and 295 nm (Figure 5.5A). These bands are not present in the other GNP samples. The GNR646 sample batch was not subjected to PEGylation and was still covered in CTAB. Figure 5.5B shows the absorbance profiles of GNR solution at all stages of the PEGylation process. After a first round of centrifugation (washing step), the UV peaks disappear from the GNR solution (D*) and appear in the supernatant (D*supernatant). Therefore, the observed absorbance in the UV can be attributed to CTAB surfactant. Retention of the position of plasmon peaks in the spectra (Figure 5.5B) is taken as evidence of colloidal stability during the processing steps.[14]

5.6.2 EMISSION SPECTROSCOPY

In Figure 5.6, the average emission of the GNP dispersions is depicted. Figure 5.6A shows the GNP emission after scaling to the high frequency Raman vibrations of water that are recorded between 800 and 850 nm. The fluorescence emission of similar concentrations of gold nanorods (GNR) is evident, according to the broadband emissions in the region between 650 nm and 800 nm. The absence of fluorescence emission of gold nanospheres (GNS) is in agreement with the notion that for the GNP to emit, the incoming field has to match the surface plasmon resonance (section 5.3.2),[173,186,187,190] which is not the case with 647.1 nm excitation light. Moreover, the surface plasmon absorption cross-section in GNS is much smaller than the

longitudinal absorption bands in rods (Figure 5.5A).[147]

Figure 5.6A shows that the GNR emission intensity varies with the particle aspect ratio (AR). For small-AR GNR, excitation is more efficient than for large-AR GNR, as the longitudinal plasmon absorption band exhibits more overlap with the 647.1 nm excitation wavelength (Table 5.3). This provides resonance conditions, enhancing the incoming electric field, which in turn leads to enhancement of the emission.[186,187] The degree of overlap of the excitation wavelength and the absorption profile determines the amount of enhancement.[147]

In addition, the positions of the emission maxima are related to the GNR in a size-dependent manner, as is shown in Figure 5.6B. The observed red-shift of the fluorescence emission with the increase of the GNR aspect ratio (AR) is in accordance with previous reports by Mohamed *et al.* and Eustis *et al.*[147,148] They ascribe this dependency to coupling effects with the surface plasmon resonances in GNR, which underlines the prominent role of surface plasmons in the photo-induced luminescence from GNR. The observed relations of the GNR AR with both the intensity and the position of the emission maximum are in agreement with Eustis and El-Sayed.[147] They stated that at higher AR, the emission enhancement decreases and broadens due to the diminishing coupling between the longitudinal plasmon resonance oscillations and the interband transition, leading to decreased emission.

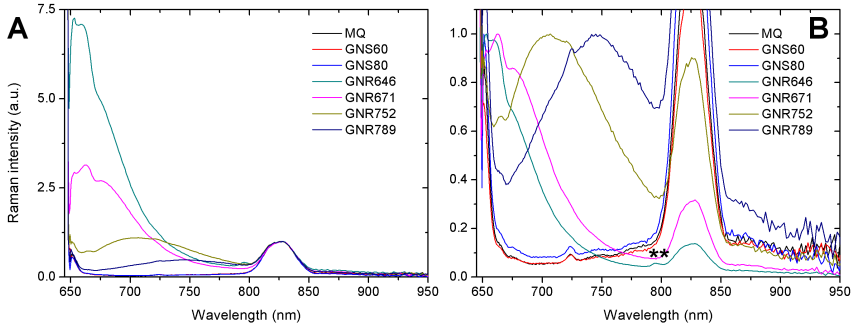

FIGURE 5.6 : Raman spectra of different GNP in solution in the wavelength region corresponding to -40 - 4930 cm^{-1} display broadband fluorescence emission. The spectra represent an average over 1024 measurements, acquired with 4 mW during 0.2 s per measurement. Data was corrected for setup response and normalized to A) the OH-stretching bands of water (800-850 nm ≈ 3000-3600 cm^{-1}) and B) the intensity of the fluorescence emission (650-795 nm ≈ 10-2900 cm^{-1}). The asterisks mark the high frequency Raman contribution of the excess CTAB surfactant in the GNR646 sample.

However, their observations of AR-dependent GNR fluorescence, show band maxima at lower wavelengths (Table 5.1) and were accordingly attributed to $sp \rightarrow d$ interband transitions.[147,148] We observe GNR emissions at

energies which are lower than those typically associated with intraband transitions (Figure 5.6). In addition, it has to be noted that different values have been reported for the energies associated with interband transitions. While originally Mooradian reported an *d-sp* interband energy of 2.2 eV (∼560 nm),[149] Link *et al.* associate this transition with an energy of 1.5 eV (∼826 nm).[182] On the other hand, luminescence emission in the IR due to intraband transitions (section 5.2) generally occurs at longer wavelengths,[182,183] because of the lower energies associated with these transitions.[179,182,183]

Fluorescence

The fluorescence nature of the emission of large-AR GNR (GNR789) was verified with a saturation experiment as was demonstrated before for small-AR GNR.[170] Figure 5.7 shows that Raman emission of both the OH-bending and the OH-stretching vibrations of the water molecules in the sample scale linearly with applied laser (dots and triangles), whereas the broadband fluorescence response of the large-AR GNR in solution shows a nonlinear behaviour (Figure 5.7, squares). Saturation of the broadband emission intensity occurs upon increasing laser power. This indicates a long-lived excited state such as fluorescence rather than a linear Raman response.

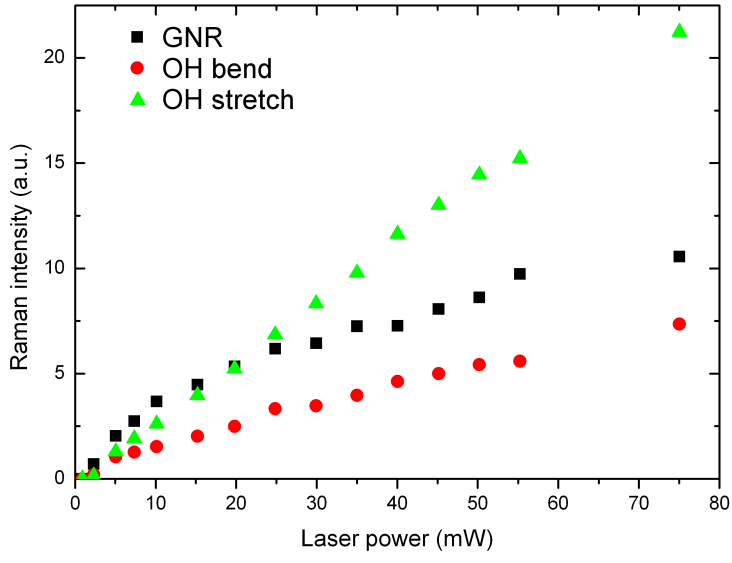

FIGURE 5.7 : The luminescence emission of the GNR780 solution shows a nonlinear behaviour with increasing laser power (black squares), while the OH-bending and stretching regions scale linearly with applied laser power (red dots and green triangles).

Fluorescence of large-AR GNR with a comparable aspect ratio was also reported by Chen *et al.*, who showed fluorescence emission profiles similar to ours (Figure 5.6B, GNR789).[143] They too, excite within the longitudinal plasmon absorption band, using an excitation wavelength of 636 nm.

Surfactants

Besides the fluorescence emission and high frequency Raman vibrations of water, Raman responses of the solvent are still present on the slopes of the fluorescence emission, as can be seen in Figure 5.6B. All GNP were dissolved in MilliQ water, which displays Raman bands around 724 nm (corresponding approximately 1620 cm^{-1}), due to the OH-bending vibrations.[216] As was shown in Figure 5.5, the GNR646 sample contained excess CTAB. Accordingly, in Figure 5.6B, the Raman contributions of CTAB are present in the high frequency region (at 795 nm, or 2880 cm^{-1}). In analogy to the absorbance profile (Figure 5.5B), the fluorescence emission profile is not affected by a change in the surfactant from CTAB to PEG.[147]

5.6.3 EMISSION ORIGIN

Our experimental results show that with increasing AR of the GNR, the longitudinal plasmon peak increases in wavelength (Figure 5.5A). The GNR fluorescence also varies with the AR, both in intensity (Figure 5.6A) and in wavelength (Figure 5.6B). These observations point at a surface plasmon enhanced emission of GNR, which is confirmed by an absence of emission in case no surface plasmon resonance occurs with the incoming field (Figure 5.6, GNS).

It can be noticed that the emission profiles (Figure 5.6) occur at energies lower than those associated with intraband transitions, but higher than those reported for interband transitions. Following references[147,217], the experimental results obtained by Mooradian[149] were tabulated and accordingly, the emission spectrum of bulk gold was plotted in Figure 5.8A (continuous line), together with the absorbance spectra of small-AR (dashed line) and large-AR GNR (dotted line) respectively. The 647 nm laser excitation line is depicted in bold red, the hatched region indicates the detection region of the spectrograph. Figure 5.8A shows that the tail of the bulk gold fluorescence emission (continuous line) covers the detection range.

In Figure 5.8B, the gold emission spectrum is multiplied with the surface plasmon absorbance curves of small-AR and large-AR GNR respectively. As the longitudinal plasmon bands overlap with the tail of the $sp \rightarrow d$ emission, enhancement of this emission can occur, as was previously suggested.[178] The degree of overlap determines the degree of enhancement, as was experimentally established in Figure 5.6A. This phenomenon has been demonstrated before for the transverse plasmon bands.[141,147,148]

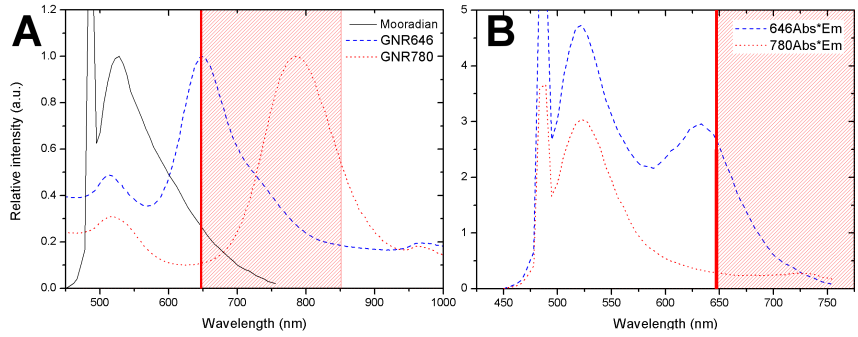

FIGURE 5.8 : A) Overlap between GNR absorbance and bulk gold emission profiles. The continuous line represents the bulk gold emission as was reported in 1969 by Mooradian,[149] the dashed line depicts the absorbance spectrum of GNR646, the dotted line the absorbance of GNR780. All spectra were normalized to one. The red line illustrates our laser excitation line; the hatched area marks the sensitive detection region of our Raman spectroscope. B) Mooradian's experimental gold $sp \rightarrow d$ emission spectrum multiplied with our experimental GNR646 and GNR780 absorbance spectra.

In addition, the overlap of the laser excitation line with the longitudinal plasmon absorption band changes with changing AR, which affects the coupling efficiency of the surface plasmon to the incoming field. Figure 5.8A illustrates that for longer AR GNR, the longitudinal plasmon gets less efficiently excited, which results in reduced enhancement of gold fluorescence emission, as was demonstrated in Figure 5.6A.

In general, the shapes and intensities of the theoretically estimated emission curves in Figure 5.8B are in good correspondence with the experimental results in Figure 5.6A. This suggests that the observed emission is the luminescence characteristic for bulk gold based on $sp \rightarrow d$ transitions. The emission mechanism itself is not affected by quantum confinement effects which could induce size- and shape-dependent effects. In analogy, we assume that the absorption profile of the $sp \rightarrow d$ transition in bulk gold is independent of the size and shape of GNP. This implies that the same electronic transition is excited in the different GNP samples.

The observed emission spectrum $S(\nu)$ depends on the $sp \rightarrow d$ absorption A_{sp-d}, the $sp \rightarrow d$ emission F_{sp-d} and the incoming field I_{laser}, according to Equation 5.2:

$$S(\nu) \sim A_{sp-d}(\nu) \times F_{sp-d}(\nu) \times I_{laser}(\nu) \tag{5.2}$$

The excitation efficiency is influenced by the local field at the GNP surface. The frequency-dependence of the field is related to the surface

plasmon absorption spectrum (Figure 5.5). In analogy to the previously reported "lightning rod effect",[147,147,148,172,173,186] the emitted luminescence is dependent on the local field factor at both the emission and the excitation wavelength:

$$S(\nu) \sim EF_{SP}A_{sp-d}(\nu) \times EF_{SP}F_{sp-d}(\nu) \times I_{laser}(\nu) \tag{5.3}$$

Here, EF_{SP} is the plasmon-based field enhancement factor. EF_{SP} is dependent on all plasmon bands present, which are, in case of GNR, both the transverse and the longitudinal plasmon bands.[148,186–188] Additional contributions to the enhancement factor include the field polarization and, accordingly, the particle orientation.[218] The extent of overlap between the plasmon bands with both the $sp \rightarrow d$ absorption, emission and the excitation wavelength determines the intensity of the observed emission spectrum $S(\nu)$.

5.7 Conclusions

Photoluminescence of gold was first reported in 1969. The luminescence behaviour occurs in both the visible and the infrared (IR). The mechanism for visible emission is based on electronic $sp \rightarrow d$ interband transitions, which lead to emission profiles with a maximum of around 560 nm. On the other hand, intraband transitions are responsible for broad emissions in the IR region between 800 nm and 1100 nm.

The photoluminescence properties of different types of gold nanoparticles was summarized. For gold nanorods (GNR), different emission profiles are reported in literature, covering both visible and IR emission. For gold nanospheres (GNS), only visible emission is reported. Very small (< 2 nm) GNS can be considered clusters of gold atoms. Here, quantum-size effects start playing a role and the clusters exhibit molecular behaviour. Their emission in both the visible and the IR can still be described by interband and intraband transition models, respectively.

Local surface plasmons play a prominent role in the emission from gold nanoparticles. In general, the emission from gold nanoparticles is attributed to the bulk emission properties of gold which are enhanced by surface plasmon coupling. This occurs when the incoming energy matches a GNP plasmon absorption band which overlaps with an emission band. In GNR, both transverse and longitudinal surface plasmon resonances stimulate photon emission. The longitudinal plasmon changes with the aspect ratio of nanorods, and therefore influences the enhancement of the emission from GNR in a size-dependent manner: the "lightning rod effect". In GNS, the emission enhancement is limited to a single plasmon.

In our experiments, we observed a broadband fluorescence emission from GNR. We ascribe this emission to the $sp \rightarrow d$ interband transitions that are characteristic for bulk gold.[149] In agreement with previous reports, the position and the intensity of the emission peak varies with the particle aspect ratio (AR) and can be attributed to the influence of surface plasmons. Whereas previous reports describe the fluorescence enhancement via high energy plasmons, corresponding to the transverse plasmon band in GNR, we observe the influence of the longitudinal plasmon absorption.

In agreement with the "lightning rod effect" described in literature, our results indicate that the degree of overlap of the plasmon absorption bands with the $sp \rightarrow d$ emission profile determines the degree of enhancement. In addition, the overlap of the excitation energy with the plasmon absorption profile affects the coupling efficiency of the surface plasmon to the incoming field. In conclusion, the variation of the surface plasmon absorption spectrum with the AR of the GNR determines what part of the $sp \rightarrow d$ emission is actually detected.

It has to be noted that both in the literature and in our experiments, averaged absorption and emission signals were acquired. However, within the cells, the GNR emission is no longer representative for the bulk solution, but rather for one or a small number of particles.[170]

CHAPTER 6

Visualization of gold nanoparticles on breast cancer cell surfaces

Gold nanoparticles (GNP) are rapidly emerging for use in biomedical applications. Characterization of the interaction and delivery of nanoparticles to cells through microscopy is important. Scanning electron microscopes (SEM) have the intrinsic resolution to visualize GNP on cells. A novel sample preparation protocol was developed to enable imaging of cells and GNP with a conventional below-lens SEM. The negative influence of "charging" on the quality of SEM images could be limited by deposition of biological cells on a conductive (gold) surface. This novel protocol enabled high resolution SEM imaging of small clusters and individual GNP on uncoated cell surfaces. GNP could be counted on cancer cells with automated routines.

Raman images were made of the same cell samples to obtain additional spectral information. However, the Raman data is dominated by effects which are difficult to interpret.

Part of this chapter has been published in Journal of Microscopy 2011 DOI: 10.1111/j.1365-2818.2011.03528.x

6.1 Introduction

Gold nanoparticles (GNP) are rapidly emerging for use in biomedical applications due to their biocompatibility and their favourable optical properties, such as an enhanced absorption cross-section.[5] The optical properties of GNP make them promising agents for diagnostics and treatment of carcinomas in general as well as early stage carcinomas. Conventional imaging suffers from low contrast of tumours with respect to the surrounding tissue. Adsorption of GNP to the tumour site greatly improves the contrast of cancer imaging, which is essential for diagnostics and treatment of early stage carcinomas. Moreover, light absorption by GNP can cause sufficient heating, to raise the local temperature and kill cells.[73]

Numerous studies[219,220] have shown that different cell types show a different response to different kinds of nanoparticles. This is presumably due to the details of the interplay of biochemical and physicochemical factors in nanoparticle-cell systems, illustrating the complexity of successful nanoparticle delivery.

A first step towards verification and characterization of GNP delivery would be to visualize nanoparticle presence and interactions with the cell membrane of biological cells. Gold nanoparticles are usually too small to distinguish clusters from individual particles by optical microscopy only. The scanning electron microscope (SEM), however, offers a high spatial resolution and good depth of field. The structure of individual particles within clusters could in principle be resolved and particle counting routines could then be employed to quantify imaging data.

SEM images of metal nanoparticles on cells[221] were acquired with a below-lens SEM. Osmium tetroxide was used to enhance the contrast. No quantitative information on numbers of nanoparticles or cluster sizes was obtained. Contrast enhancers may also obscure small details in the sample by removing structural features on the finest scale, such as microfilaments, although this may sometimes not be visible at lower magnifications.[222] Moreover, the metal coating results in increased levels of (back)scattering. This leads to loss of intensity from the backscattered electron images brightness in case metal samples, such as small GNP, are to be imaged with SEM in high resolution.[223]

So far, to our knowledge, simultaneous information on the presence of gold nanoparticles on unstained cells has not yet been captured in conventional below-lens systems. Here, we demonstrate high resolution imaging of GNP on SK-BR-3 breast cancer cells with a conventional below-lens SEM system, using a novel and simple sample preparation procedure which exploits the sample material characteristics, rather than modifying them with contrast agents such as heavy metals.

Raman spectroscopy provides molecular fingerprints and can differentiate malignant tumour tissue from normal breast tissue.[145] The presence of local surface plasmons on gold nanosurfaces can enhance the typically very weak

phenomenon of spontaneous Raman scattering: surface enhanced Raman scattering (SERS).[2,224] SERS-based gold nanoparticles enable targeted studies in living biological systems, allowing molecular analysis of e.g. cancerous environments.[155] Raman microspectroscopic techniques have become increasingly attractive for biological sample analysis and imaging, because of the ability to visualize samples down to a 500 nm resolution without the use of additional labels or sample perturbations.

Here, we demonstrate high resolution imaging of GNP on SK-BR-3 breast cancer cells with a conventional below-lens SEM system, by means of simple sample preparation procedures, using the sample material characteristics, rather than modifying them with heavy metals.

In addition, we performed Raman imaging on these samples in order to obtain spectral information. However, the Raman data is dominated by effects which we are not able to discern yet.

6.2 Materials and methods

6.2.1 substrate preparation

Glass cover slips with a diameter of 12 mm and a thickness of 170 μm were cleaned with acetic acid (analytical grade, Sigma-Aldrich, St Louis, MO, USA), rinsed with Double De-Ionized (DDI) water and cleaned with ethanol (99,9% analytical/technical grade, St Louis, MO, USA).

The cover slips were sputter-coated with pure gold (sputter coater 108auto, Cressington, Watford, UK) under 1 mBar vacuum for 50 seconds under 40 μA cathode current. The distance of the sample to the pure gold target was approximately 4 cm. Prior to cell culture, the gold coated cover slips were sterilized with 99,9% ethanol and immersed in cell proliferation medium overnight in order to allow medium proteins to adsorb on the gold surface.

Cell culture

Cells were cultured on the substrates in 24 well plates and were left to attach overnight. SK-BR-3 cells were cultured in DMEM supplemented with L-glutamine (1%), fetal calf serum (FCS, 10%) and penicillin:streptomycin (PS, 1%). The cells were seeded to obtain a confluence of approximately 60% on day 2.

6.2.2 GNP incubation

Cell fixation

Cells were fixed with 4% formaldehyde solution (from 37% formaldehyde solution, Sigma-Aldrich, St Louis, MO, USA) in Phosphate Buffer Saline (PBS, 1X) for 20 minutes at 4°C and subsequently rinsed with copious

amounts of PBS buffer. Gold nanoparticles were administered to the cells after fixation, to visualize nanoparticle presence at and interactions with the cell membrane.

Salt aggregation of gold spheres

Solutions of citrate capped gold nanospheres (80 nm and 40 nm, BBInternational, Cardiff, UK) were diluted with 1X PBS to approximately 3×10^9 particles per ml and added to the fixed cells. Rapid nanoparticle aggregation was induced by adding 35 μl of concentrated salt solution (10X PBS) up to a total volume of 3.5 ml per well and 30 minutes of incubation. In general, salts neutralize the citrate capping of the nanoparticles, which subsequently leads to particle aggregation and sedimentation, causing both individual and aggregate particles adhere to cells.[225,226] Subsequently, the cells with attached nanoparticles were rinsed twice with DDI water to remove excess salt.

Targeting with gold nanorods

Gold nanorods of 20×40 nm were synthesized as previously described[14] using the seed-mediated method,[22,150] in which gold seeds are added to a growth solution which contains the shape-directing surfactant hexadecyltrimethylammonium bromide (CTAB). The cytotoxicity of CTAB[37,144] was amended by PEGylation[44,78,144] as previously described by Rayavarapu *et al.*,[81] largely replacing CTAB.

However, the PEG coating shields GNR from biological interactions. Therefore, to direct the GNR to the cell surface, HER81 monoclonal antibody (Immunicon, PA) was conjugated to gold nanorods with a bifunctional PEG crosslinker orthopyridyl dithio-polyethylene glycol-succinimidylpropionate (OPSS-PEG-PDP, Polypure, Oslo, Norway). The monoclonal murine antibody Her81 is raised against the extracellular domain of the HER2/neu receptor, which is overexpressed in SK-BR-3 breast cancer cells.[107,227] The antibody-PEG-GNR (Ab-PEG-GNR) were suspended in PBS and incubated for 30 minutes with the fixed cells, at a concentration corresponding to approximately one thousand GNP per cell, and subsequently rinsed with PBS.

6.2.3 CRITICAL POINT DRYING

All samples were rinsed with DDI water before being subjected to dehydration by gradients of ethanol:DDI water. The cover slips were placed for 10 minutes in 50%, 70%, 80%, 90% and 100% ethanol in DDI water solutions, respectively, in order to remove the water from the samples. Ethanol was subsequently removed by critical point drying (CPD) with liquid CO_2 (Bal-tec CPD 030, Leica Microsystems, Liechtenstein).

6.2.4 SEM IMAGING

The samples were applied to aluminium SEM stubs with double-sided conductive carbon tape. An additional thin layer of carbon paint was applied at the edges of the cover slips to ensure conductivity.

SEM imaging was performed on a FEI XL30 scanning electron microscope (FEI, Eindhoven, The Netherlands) operated under high vacuum ($<1.3\times10^{-3}$ mbar). The FEI XL30 is a conventional SEM with an Everhart-Thornley (E-T) detector located below the lens. The FEI XL30 SEM is equipped with a field emission gun (FEG) source, secondary (SE) and backscattered (BSE) imaging capabilities and an energy-dispersive X-ray spectroscope (EDS).

In SE imaging mode, acceleration voltages ranging from 1 to 20 kV were used, depending on the local charging effects. BSE imaging was performed with 20 kV. Default working distance was 10 mm with spotsize 3.

6.2.5 PARTICLE COUNTING

The ImageJ toolbox was used to count gold nanoparticles in the SEM images. The scale bar in the SEM images was used for scale calibration in ImageJ. The thresholding function converted grey scale images to black and white images. High contrast SEM images were directly thresholded. Lower contrast SEM images were filtered using minimum and maximum filters to determine a background, which was then subtracted from the original SEM image to increase the image contrast before thresholding. The resulting black and white images were analyzed using the "Analyze Particles" routine from ImageJ, which returns a surface area. The number of particles in an aggregate or cluster of particles can either be determined based on calculated areas of single particles, or by analyzing a higher-magnification image. No filter for particle shape differences was used, rendering all GNP irrespective of aggregate state or orientation.

6.2.6 RAMAN IMAGING

Raman measurements were carried out on a confocal Raman microspectrometer, similar to the setup previously described by Van Manen *et al.*[89] The 647.1 nm excitation light from a Krypton ion laser light source (Innova 90-K; Coherent Inc., Santa Clara, CA) was focused through a $40\times/0.75$ NA objective (Olympus UPlan FL 40, Tokyo, Japan) onto single cancer cells.

The Raman image plane was selected to be at the same height above the gold coated substrate in all strongly adhered cells. The height was adjusted based on either the intensity of optical reflections of the substrate in the low wavenumbers or on the maximum SNR, i.e. the highest signal intensity, which we assume to be in the middle of the cell.

Hyperspectral Raman imaging was performed by stepping the laser beam over the sample in a 64×64 raster pattern and spectral acquisition at

each position with a laser power of 3.85 mW under the objective and dwell time of 0.1 seconds per pixel, with a step size of 0.5 μm. Univariate and multivariate analyses were performed on the hyperspectral Raman data as described earlier.[95,96]

6.2.7 RAMAN DATA ANALYSIS

Noise in the resulting 3D (spatial × spatial × spectral dimension) data matrix was reduced by singular value decomposition.[95,125] Hierarchical cluster analysis (HCA) was performed on Raman imaging data matrices to visualize regions in cells with high Raman spectral similarities. In the cluster analysis routine, principal component analysis scores were taken as input variables, squared Euclidean distances were used as distance measure, and Ward's algorithm was used to partition Raman spectra into clusters. All data manipulations were performed in routines written in MATLAB 7.6 (MathWorks, Natick, MA).

6.3 RESULTS AND DISCUSSION

6.3.1 SAMPLE PREPARATION PROTOCOL

Figure 6.1 shows a schematic representation of the protocol for the preparation of a sample of cells with nanoparticles for SEM analysis. Glass cover slips with a diameter of 12 mm and a thickness of 170 μm serve as the substrate for cell culture. To remove fatty residues, the cover slips are first washed with 10% acetic acid (Figure 6.1, step1). After drying in an oven and sputter coating, the gold coated cover slips are sterilized with 100% ethanol (Figure 6.1, step 2).

Conductive coating of the cover slips is necessary to reduce charging of the sample during SEM imaging,[228] as biological cells have a low conductivity. Here, the substrates were first coated with gold before cell adhesion. Gold has a high electrical conductivity. The gold we used to sputter the cover slips contained no impurities that could reduce conductivity.

The discharging ability of a gold layer is determined by the morphology and the interconnectivity of the gold layer.[229] Thus, by adjusting the sputtering parameters, we are able to accurately control the homogeneity and thickness of the gold layer and thereby the conductivity of the substrate. Gold coated substrates were achieved by sputtering for 50s, which resulted in a gold layer of sufficient homogeneity and thickness (approximately 30 nm) for our purposes. The upper surface of the cells was then exposed to the electron beam to enable detection of nanoparticles.

Before cell adhesion, gold-coated substrates were incubated overnight in cell culture medium. Proteins from the medium attached to the gold surface through non-specific adsorption (Figure 6.1, step 3). The protein layer

promotes cell attachment [230–232] and, in addition, stabilizes the connection of the gold layer to the glass. [232]

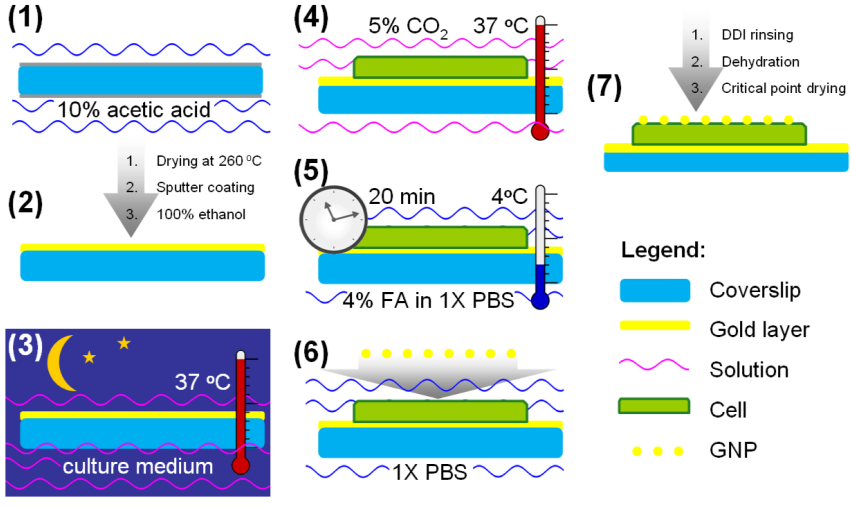

FIGURE 6.1 : Seven steps to prepare a sample of cells covered with gold nanoparticles for conventional SEM.

Cells were seeded and left to attach to the substrate by spontaneous adhesion (Figure 6.1, step 4). Relatively low cell densities were seeded on the surface of the gold sputtered cover slips. Cells were fixed at a surface coverage of approximately 60%. This allows for sufficient free gold surface to decrease charging effects.

Cell fixation is carried out at 4°C for 20 minutes, using a 4% formaldehyde (FA) solution in PBS (Figure 6.1, step 5). In general, fixation processes are performed at 4°C to stall the biological processes of the cell. However, since a rather high concentration of FA is used, fixation at room temperature is also possible.

After rinsing with PBS, gold nanoparticles (GNP) suspended in PBS solution (Figure 6.1, step 6) are added to the cells and incubated for 30 minutes. Particle size and surface chemistry influence particle diffusion rates. [233] However, particle incubation times can be decreased by inducing GNP aggregation with the addition of salt solution. [3,177] We performed salt-induced particle aggregation in case of the gold spheres. However, salts from the PBS can form crystals on the sample surface, creating artefacts in SEM imaging. Therefore, the nanoparticle-cell samples were rinsed with DDI water to remove the salty PBS residues.

The cells were further prepared for SEM imaging by dehydration and critical point drying (Figure 6.1, step 7). Dehydration was performed by

immersion for 10 minutes in a range of ethanol concentrations (50-100%) at 4°C (see materials and methods). An immersion time of 10 minutes per alcohol concentration was sufficient to permeate the single cell layer of biological material completely. The dehydration steps were carried out at low temperature to limit alcohol evaporation. The surface tension was minimized by carefully controlled removal of ethanol at the critical point.[229]

6.3.2 CELL IMAGING

Figure 6.2 illustrates the effect of different electron acceleration energies on the SEM image of SK-BR-3 cells grown on a gold coated cover slip. At low acceleration voltages (2.0 kV) the cell membrane is visible. An increase of the acceleration voltage enables the incoming electrons to penetrate deeper in biological materials.[234]

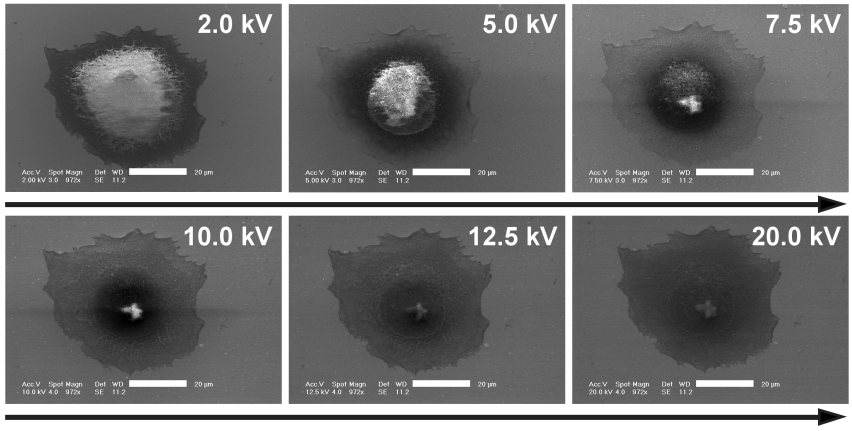

FIGURE 6.2 : Increased electron acceleration energies result in increased depth information of an SK-BR-3 cell on a 50 s gold sputtered cover slip. Acceleration voltage of the electron beam increases per row of SEM images from 2.0 kV in the upper left image to 7.5 kV to the upper right image and from 10.0 kV in the lower left image to 20.0 kV in the lower right image. Scale bars denote 20 μm.

At low acceleration voltages, surface charging of cellular structures is observed (Figure 6.2, top row). An increase of the electron acceleration increases the penetration depth and improves the drainage of electrons by the gold-coated surface. As a result, the charging artefacts in the SEM images are almost completely absent. Thin cell sections, which are common in adhering cells, can also be examined at low acceleration voltages, since these sections are sufficiently well connected to the conducting coat. Incubation of the substrate surface has been used to improve cell spreading.[230–232] For this purpose, we made use of the proteins present in the cell proliferation medium (see section 6.2.1).

An increase of the acceleration energy reveals increasingly more internal structure of SK-BR-3 cells on gold coated substrates (Figure 6.2). A precise assignment of the sub-cellular structures is presently not possible due to electron scattering and concomitant loss in resolution.[234]

6.3.3 GOLD NANOPARTICLES ON CELLS

SEM image contrast is limited by charging effects at the cell surface. The (back)scattering efficiency of the particles rapidly decreases with particle size. Application of higher electron acceleration voltages circumvents charging effects (Figure 6.2). Higher acceleration voltages generate more backscattered electrons (BSE) from gold nanoparticles.[234]

The electron scattering from biological materials is low. Details from the cell surface arise mainly from secondary electrons (SE). At increased electron acceleration voltages, the number of secondary electrons is reduced (Figure 6.2). The increased contrast between gold nanoparticles and cells at elevated voltages is therefore due to the increased ratio of BSE to SE. Figure 6.3 illustrates the high scattering efficiency of GNP and the excellent contrast with low-scattering biological materials, such as the SK-BR-3 cells.

As the (back)scattering efficiency of GNP decreases with their size, higher acceleration voltages of the electron beam enable visualization of smaller gold nanoparticles. This is shown in Figure 6.3. Spheres with a diameter of 80 nm have been visualized at 10.0 kV (Figure 6.3A), while for 40 nm nanospheres 12.5 kV is more suitable (Figure 6.3B). The even smaller gold nanorods require acceleration voltages of at least 15 kV (Figure 6.3C) to obtain sufficient levels of contrast.

Figure 6.4 illustrates high resolution SEM images of GNR targeted to fixed SK-BR-3 cells. In a conventional below-lens SEM, high resolution SEM images of small GNP such as the 20×40 nm GNR can still be maintained at higher magnifications by applying high electron beam acceleration voltages.

However, as the cell surface scatters the electrons from the beam less efficiently at high acceleration voltages, electrons penetrate into the cell more efficiently. This reveals more intercellular details (Figure 6.2), but reduces the contrast of the cell surface topography. Although this makes it impossible to image both the cell membrane and the gold nanoparticles with similarly high contrast in the same image (Figure 6.4), it opens the possibility to visualize GNP that are internalized in the cells. An acceleration voltage of 15.0 kV was used as an optimal voltage for imaging gold nanorods on SK-BR-3 cancer cells, as is illustrated in Figures 6.3C and 6.4B.

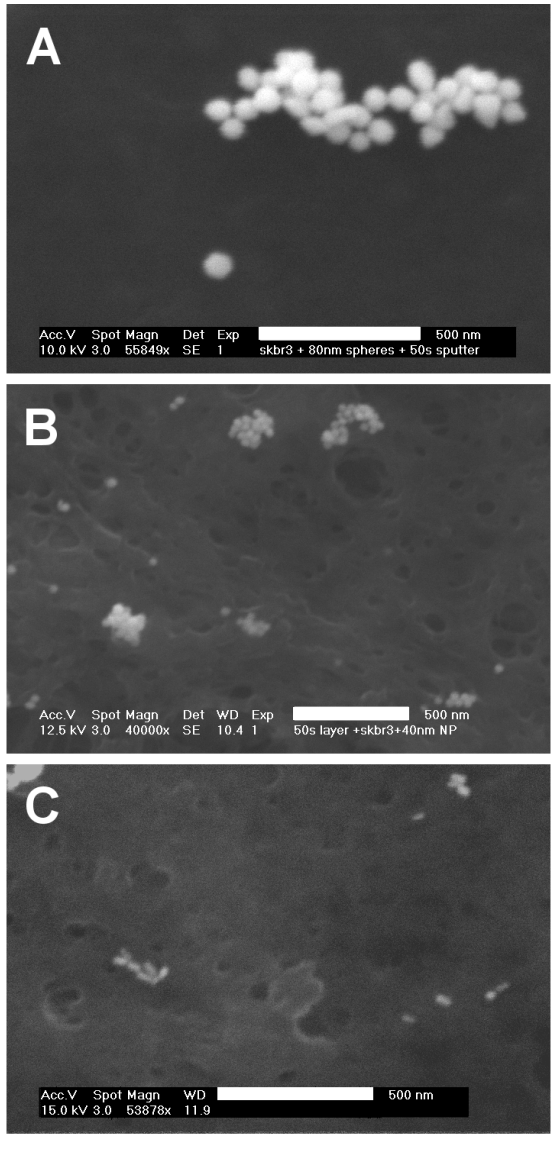

FIGURE 6.3 : The smaller the particles, the higher the electron acceleration voltage is required. SEM images of different gold nanoparticles on SK-BR-3 cells showing A) 80 nm spheres imaged with 10.0 kV B) 40 nm spheres imaged with 12.5 kV and C) 20×40 nm gold nanorods imaged with 15.0 kV. Scale bars denote 500 nm.

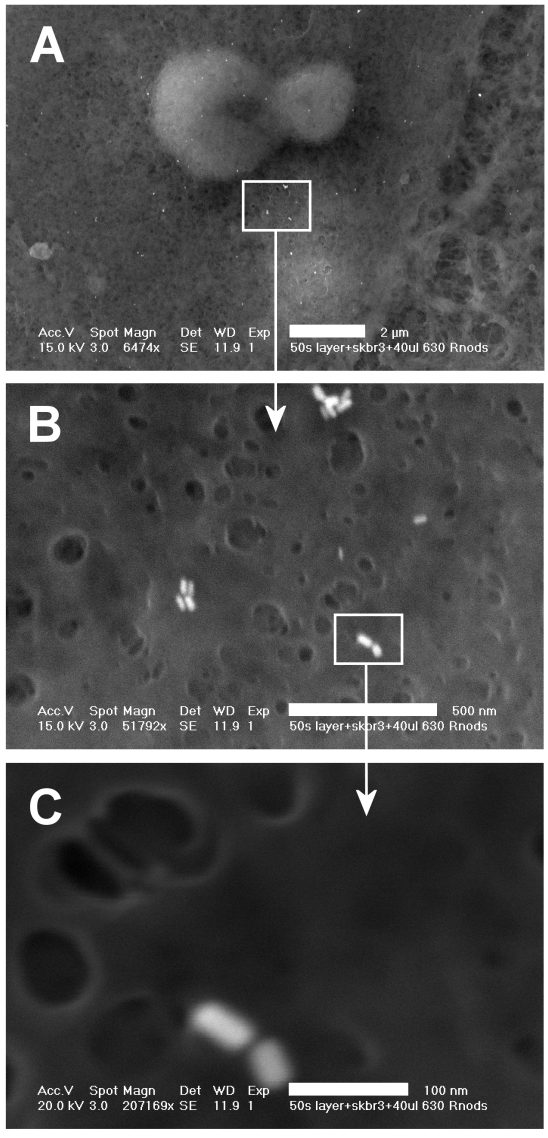

FIGURE 6.4 : SEM images of 20×40 nm gold nanorods on SK-BR-3 cells on 50 s gold sputtered glass at different magnifications. Scale bar depicts A) 2 μm, B) 600 nm and C) 100 nm. Due to the high electron acceleration voltages (15.0-20.0 kV), gold nanorods and cellular structures originate from different focal planes.

6.3.4 GOLD NANOPARTICLE QUANTIFICATION

Overview SEM images of GNP on the surface of cells are of interest for quantification purposes in, for example, targeting efficiency studies. Structures with high atomic weight, such as GNP, have a high backscattering efficiency and are therefore easily detected with the backscattered electron (BSE) detector. Moreover, biological materials such as cells produce a lot less BSE and consequently appear very dark in BSE images, providing increased contrast with the GNP. Therefore, GNP on cells can be detected with high accuracy using a BSE detector.

Figure 6.5A shows BSE detection of small single GNR (20×40 nm) on an SK-BR-3 cell. The distribution of nanoparticles can easily be observed. The contrast is sufficiently high for a particle counting routine to quantify numbers of nanoparticles on the cells (Figures 6.5C and 6.5D). Figure 6.5B shows a histogram of the GNP area versus the number of counted events of GNR on the SK-BR-3 cell depicted in Figure 6.5A. As expected, the numbers of GNR on the cells were relatively small.

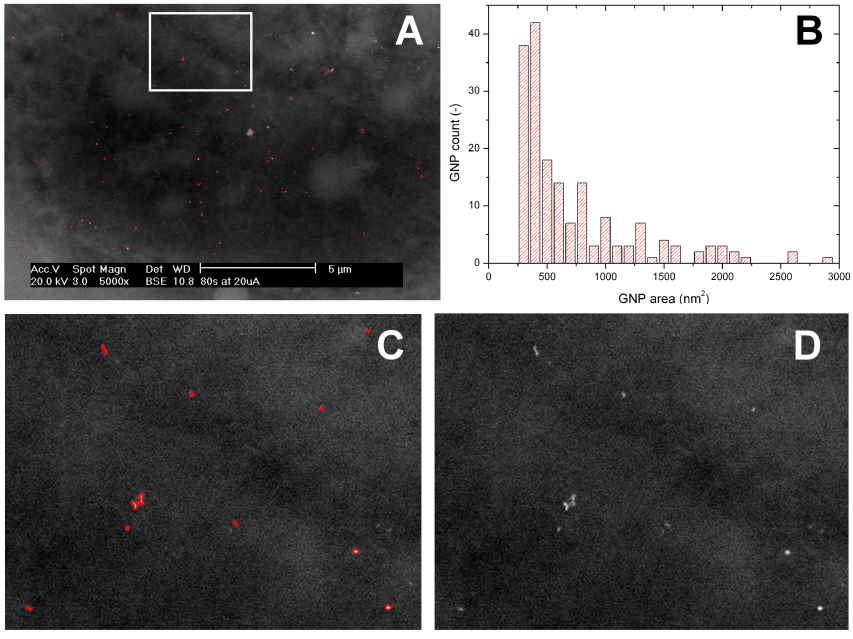

FIGURE 6.5 : Counting 20×40 nm gold nanorods on SK-BR-3 cells using an automated counting routine on SEM images acquired with the BSE detector. A) All particles marked in red are identified and included in counting. B) The histogram shows the area distribution of the counted particles. C) Higher magnification of the marked region in A. D) Higher magnification area without the red markers.

If we consider a gold nanorod as a cylinder capped with two hemispheres, GNR of 20×40 nm have a minimum surface area of approximately 315 nm^2 if the GNR would stand on-end (axial orientation) and a maximum surface area of approximately 675 nm^2 if the GNR would be imaged side-on (lateral orientation, in a two dimensional projection). The histogram in Figure 6.5B has a bin size of 100 nm^2 and shows that the smallest area detected with our counting routine is 250-350 nm^2. This area corresponds to the axial orientation of the particle. In addition, the GNR solutions also contained some spherical particles, which is a byproduct of the GNR synthesis. The events with an area larger than 750 nm^2 are caused by clusters of particles. Examples of such clusters are shown in Figures 6.3C and 6.4B.

6.3.5 RAMAN IMAGING

Subsequently, single-cell confocal Raman microspectroscopic imaging was performed on the samples prepared for SEM to obtain spectral information in order to gain additional information on the location of the GNP on the cells. Figure 6.6 shows both Raman and SEM images of an SK-BR-3 cell incubated with Ab-PEG-GNR. In Figure 6.6A, a fixed SK-BR-3 cell on a gold sputtered glass substrate is depicted by SEM. Using a low electron acceleration voltage, the cell membrane and its boundaries are visualized. Figure 6.6B depicts the BSE image of the same cell, of which an area is extricated in Figure 6.6C, showing the presence of gold nanoparticles on the cell.

The focal plane can be set at different heights to image the cell and parts of it, because the cell sample thickness is several orders of magnitude larger than the depth of the focal plane. In order to see the effect of the focal plane on the recorded Raman data, we focused just above the gold layer (Figures 6.6D and 6.6E) as well as in the middle of the cell (Figures 6.6F and 6.6G).

In Figure 6.6D, the cell is clearly distinguished from the background (black). Within the contours of the cell, some specific features are clustered. The average cluster Raman spectra (Figure 6.6E) show a few highly intense clusters (blue traces) displaying broadband features around 1380 cm^{-1} and 1590 cm^{-1}, denoted as carbon specific D- and G-bands in literature.[235] These bands fluctuate intensely (Figures 6.6E and 6.6G), which indicates both conformational changes and changes in the chemical bonds and groups within carbon networks.[235,236]

We attribute these relatively intense and broad bands of amorphous carbon[235–238] to burning events, caused by locally increased temperatures. Although low laser doses are used, the cell samples are prone to burning because they are dry and reside on a gold layer. Moreover, gold nanoparticles are present, which are very sensitive to heating because the laser wavelength of 647 nm lies well within their longitudinal plasmon absorption band.[152]

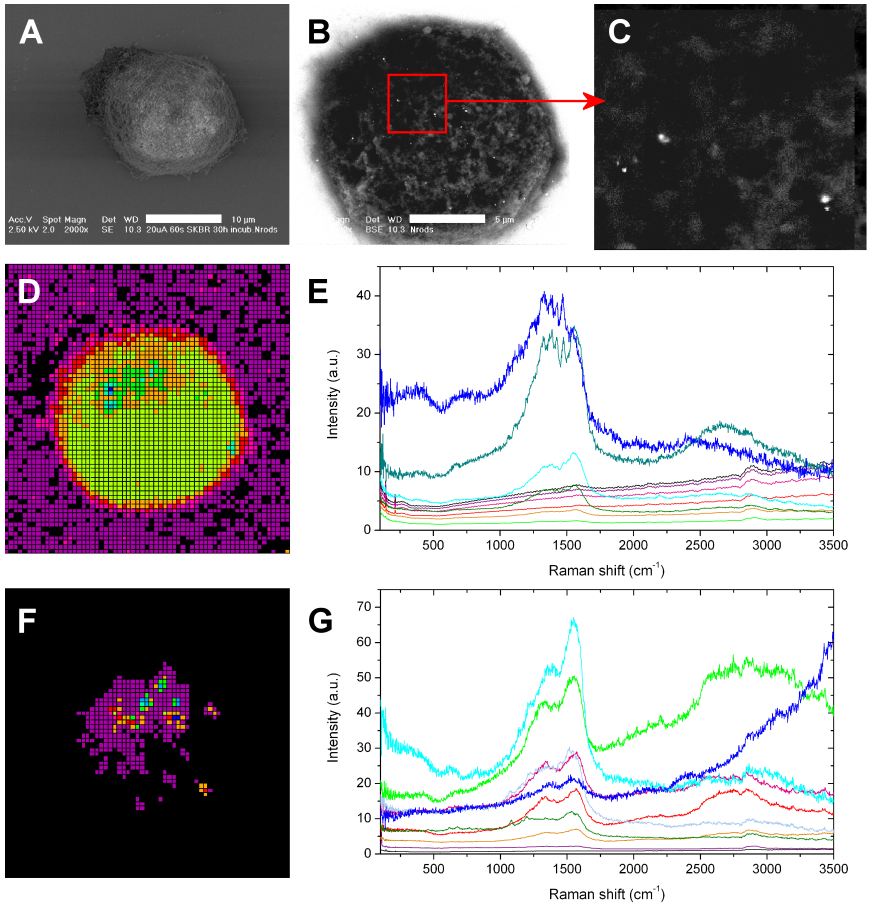

FIGURE 6.6 : SEM and Raman imaging of an SK-BR-3 cell after 24 hours of incubation with Ab-PEG-GNR A) SE image acquired with 2.5 kV electron acceleration. Scale bar denotes 10 μm; B) BSE image acquired with 10 kV electron acceleration. Scale bar denotes 5 μm; C) Detail of BSE image of GNR on the cell (zoom factor = 500x); D) 10 level hierarchical cluster image obtained from a 64×64 raster scan acquired with 3.85 mW and 0.1 s acquisition time. During imaging we focused on the gold substrate; E) Cluster average Raman spectra corresponding to cluster image in D; F) 10-level hierarchical cluster image obtained from a 64×64 raster scan acquired with 3.85 mW and 0.1 s acquisition time, while focused inside the cell; G) Cluster average Raman spectra corresponding to the cluster image in F.

Figure 6.7 shows that the gold layer is neither homogeneous, nor completely interconnected. Therefore, heat dissipation from a highly energetic source such as the Raman excitation laser is limited and causes locally very high temperatures.[4,229,239–241] Furthermore, when the surface features are smaller than the wavelength of the illuminating light, as is the case in our samples (Figure 6.7), oscillating plasmons start to play a signal enhancing role.[224]

Remarkably, the background cluster average spectra (black and purple traces in Figure 6.6E), are of higher intensity than the cluster averages assigned to the cell.

This elevated background is likely to have been caused by the position of the focal plane which was set in the gold layer. When cell material scatters the Raman signal of the gold substrate, less Raman signal of the substrate is collected, resulting in reduced intensity of the background (gold) signal at the location of the cell material.

Figures 6.6F and 6.6G show Raman cluster analysis data from the same cell, but acquired in the middle of the cell. In this plane, the cell outline is no longer visible in the cluster images at low analysis levels, due to the dominant broadband features (Figure 6.6G). As in Figure 6.6E, the fluctuating broad Raman features around 1380 cm^{-1} and 1590 cm^{-1} are ascribed to carbon specific D- and G-bands.[235]

Thus, carbonizing still takes place in this focal place, although the influence of substrate structures is expected to be less than near or at the surface. Besides burning effects, which in this case can ascribed to the presence of gold nanoparticles, several other broadband shapes can be distinguished. Previously, we observed that GNR in SK-BR-3 cells can be identified by their fluorescence emission (Chapter 4).[170] It was shown that the shape of this GNR characteristic fluorescence emission changes for nanorods at different locations in the cells. The spatial information from the cluster image (Figures 6.6D and 6.6F) and the BSE images (Figures 6.6B and 6.6C) suggests a co-localization of broadband fluorescence and carbon related Raman responses with the gold nanoparticles.

Taking a closer look, cell specific Raman bands can be observed in the cluster average spectra. Figure 6.8 shows the Raman cluster average signal of the purple cluster in Figures 6.6F and 6.6G. Raman bands that are characteristic for cellular material can be recognized both in the fingerprint region (Figure 6.8A: 500-1700 cm^{-1}) and in the higher wavenumbers (Figure 6.8B: 2700-3100 cm^{-1}).

The bands at 1130, 1313 and 1451 cm^{-1} are assigned to lipids, as are most of the displayed high wavenumber bands.[109,127,242–244] The amide regions contain mainly protein contributions,[245,246] and a weak contribution of phenylalanine at 996 cm^{-1} can be distinguished.[127,247] The bands at 780, 823 and 1196 cm^{-1} can be assigned to DNA.[127,244,248] Interestingly, a clear band occurs at 1036cm^{-1} which we have observed before in SK-BR-3 cells and of which the origin is unclear to us.[107]

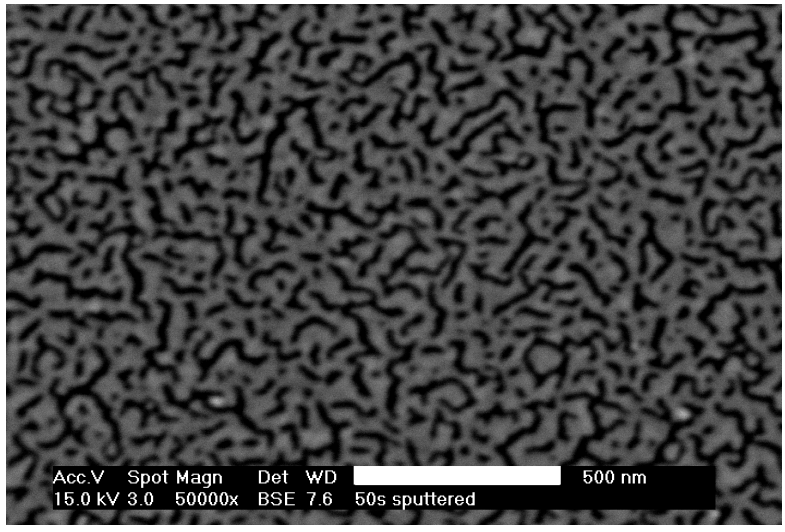

FIGURE 6.7 : SEM image of 50 seconds gold sputtered glass substrate as are used for SEM sample preparation showing the nanoscale structures in the gold layer. Sputtering introduces SERS enabling conditions such as surface roughness, disconnectivity / interconnectivity and structures smaller than the incoming laser wavelength of 647 nm. The scale bar denotes 500 nm.

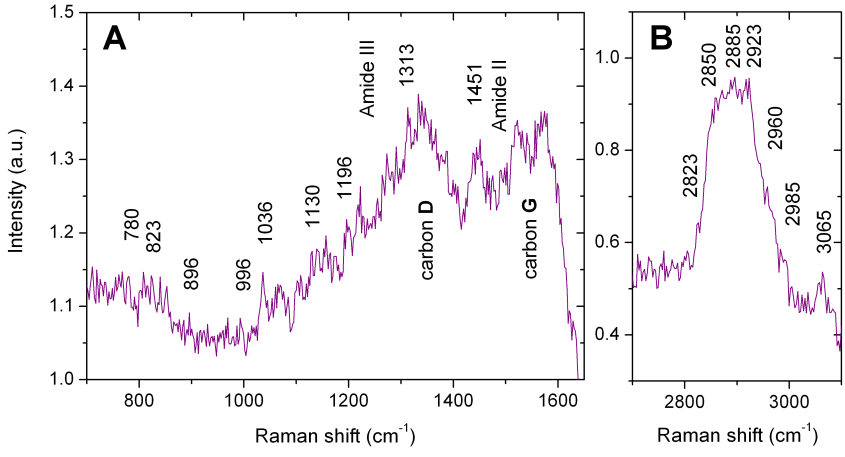

FIGURE 6.8 : Cluster average Raman spectrum of the purple cluster in Figure 6.6F A) in the fingerprint region (500-1700 cm^{-1}) and B) in the high wavenumbers (2700-3100 cm^{-1}). The same cluster average spectrum was depicted in Figure 6.6G, but was overshadowed by the dominant intensities of the other clusters. Cell specific Raman bands as well as the carbon features are marked.

However, the above data have to be interpreted with caution, as burning effects are strongly interfering with the cell signals. Figure 6.8 shows that the Raman baseline appears to be affected by the appearance of the carbon specific bands at 1380 cm^{-1} and 1590 cm^{-1}. Moreover, SERS effects can be induced by local hot spot formation due to the surface roughness of either the gold substrate or the gold nanoparticles.[146,175,177,249]

In addition, sample fixation can induce artefacts in Raman spectra (Chapter 2). Fixing the sample offers the advantage of immobilizing the cells, preventing motion artefacts. However, fixatives alter the chemical composition of the cells and may promote additional artefacts such as autofluorescence[250] as well as the carbonizing effects discussed above.[235–238] Although the amount of fixative was kept to a minimum by briefly fixing with mild, short chain fixatives, effects of the fixative on the Raman signal can not be excluded.

Although increasing the level of cluster analysis usually provides more specific information about various structures in the cell,[251] the fluctuation of the carbon and fluorescence emission bands has a dramatic effect on the cluster analysis, dominating few-pixel clusters (Figures 6.6E and 6.6G). Additionally, the signal-to-noise ratio (SNR) of the cell cluster spectra is rather low (Figure 6.8) as a result of the low laser doses applied. This low SNR in combination with the dominating broadband signatures leads to difficulties in interpreting the cell specific Raman data. Therefore, we have not been able to distinguish cell specific Raman signals at the GNR locations which are dominated by broadband and carbonizing contributions.

6.4 Conclusions

A sample preparation procedure was developed to enable high resolution imaging of gold nanoparticles on uncoated and cultured SK-BR-3 breast cancer cells in a conventional below-lens SEM system. Charging effects were suppressed by sputter coating a gold layer on a standard optical microscope glass substrate. Substrates were prepared for cell adhesion by incubation in cell medium. Subsequently, cells were seeded and cultivated to approximately 60% confluence. The cells were fixed using standard procedures. Gold nanoparticle (GNP) solutions were added and GNP attached to the cell membrane. Excess GNP were rinsed leaving only adhered nanoparticles on the cells. Samples were dehydrated for SEM imaging using alcohol gradients and critical point drying.

Natural differences in electron scattering efficiency between cellular and metallic materials were sufficient to generate an excellent contrast between cells and gold nanoparticles. Individual gold nanorods of 20×40 nm could be visualized and quantitated on SK-BR-3 breast cancer cells. We conclude that conventional SEM provides promising approaches to study gold nanoparticle interactions with cancer cells.

Raman imaging of cell samples prepared according to the developed protocol allowed the GNR to be detected in the cells by their fluorescence responses as well as by their susceptibility to heat generation. Nevertheless, because of the low laser doses applied in order to minimize sample burning, low SNR in combination with dominating broadband emissions obstructed specific assignment of subcellular locations.

Since the roughness of the gold cell substrate can introduce carbonizing and, possibly, SERS effects, different gold sputtering parameters are required to optimize the cell substrate for Raman purposes.

CHAPTER 7

Towards near-infrared dyes as Raman markers for gold nanorods

Near-infrared (NIR) dye encoded gold nanoparticles (GNP) are rapidly emerging as contrast agents in many bio-imaging and sensing applications. The coding process is usually carried out without control or a clear understanding of the metal-liquid interface properties which, on the contrary, are critical in determining the type and extension of dye-metal interaction.

In this chapter, we investigated the effect of gold surface composition on the adsorption of Indocyanine Green (ICG) on GNP, simulating the surface conditions of gold nanorods on citrate-capped gold nanospheres. These substrates allowed a careful control of the metal-liquid interface composition and, thus, detailed absorption and fluorescence concentration studies of the effects of each individual chemical in the colloidal solution (i.e. bromide anions, Cetyl trimethylammonium ions and Ag^{+}-ions) on the ICG-gold interaction. This study reveals the drastic effect that these experimental parameters can have on the ICG adsorption on GNP.

This chapter has been published in Nanoscale, 2011 DOI: 10.1039/c1nr10551e

7.1 Introduction

Indocyanine Green (ICG) is a water soluble, amphiphilic tricarbocyanine near-infrared (NIR) emitting dye, which is approved by the Food and Drug Administration (FDA) for *in vivo* applications. Currently, ICG is used extensively as a marker in clinical imaging applications [252–255] with a major role in the detection of tumor metastases. For example, ICG is applied in intra-operative surgery to detect the sentinel lymph nodes of breast cancer, gastric cancer and colon cancer. [256–258]

In this field of *in vivo* cell and tissue targeting, gold nanoparticles (GNP) are rapidly emerging as contrast agents. GNP need to be functionalized with various (bio)chemicals for different applications. For bio-imaging and sensing they are usually coded with NIR dye reporters [48,62] such as indocyanine green (ICG). However, the coding process is not a trivial issue, as the metal-liquid interface composition plays a key role in determining the type of interaction and the extent of analyte adsorption on the GNP. [259] Nevertheless, labelling gold surfaces is usually carried out by simple addition of dye molecules to a GNP suspension without control or a clear understanding of the interface properties which affect the dye tagging of the nanomaterial.

Among GNP, gold nanospheres have been the most widely employed so far because the synthesis of monodisperse colloidal populations in a wide range of diameters (1.5-100 nm) is relatively easy and controllable. [63] However, their optical properties are poorly tunable: their strong plasmon peak remains in the neighbourhood of 520 nm in the green region. This restricts their use in tissue since light penetration in this wavelength region is low. Recently, a large number of different nanostructures have become available which have unique plasmonic signatures in the far-red and near-infrared (NIR) regions, the so-called "biomedical window" of tissue, where light penetration is improved.

Structures such as nanoprisms, nanobars, nanoplates, nanocubes, nanorice and star-shaped GNP have been produced. [260–266] Of these, gold nanorods (GNR) have attracted enormous attention due to the relative ease with which they can be synthesized with an exquisite control of their plasmon peaks. For this reason, they are being actively investigated for medical applications in (bio)chemical sensing and imaging, drug delivery and cancer therapy. [18,81,267–270]

Here, we aim to systematically investigate the effect of gold surface composition on the adsorption of ICG, in order to acquire insights of the roles played by each experimental factor on the coding process of the nanostructure. Specifically, we simulated GNR surface conditions on citrate-capped gold nanospheres. These substrates allowed careful control of the metal-liquid interface composition and, consequently, detailed absorption and fluorescence concentration studies of the effects of each individual chemical in the colloidal solution (i.e. bromide anions, cetyl trimethylammonium ions and Ag^+-ions) on the ICG-gold interaction. Such investigations are more complex on GNR because of their more involved synthesis [17,23,68,69,271] and high susceptibility to aggregation and reshaping upon surface reactions. [16,50,53]

GNR of different size and aspect ratios are grown from seed gold nanospheres in the presence of CTA^+Br^- (CTAB), which acts as surface directing agent. [22,268] CTAB regulates the shape of the GNR by forming densely packed CTA^+ bilayers on specific facets on gold surfaces, directing gold deposition to other facets, which

contributes to the anisotropic growth of gold nanocrystals.[14,53,272] The bromide counterion plays an important role in nanorod formation.[23] Furthermore, Ag^+ is commonly added to the growth mixture to generate higher yields of rod-shaped gold nanoparticles with controllable aspect ratios.[14,22,272]

Since gold nanostructures quench the fluorescence of dye molecules in close proximity to the metal surface,[273] fluorescence spectroscopy directly informs about the ICG monomer population in the bulk solution. On the other hand, absorption measurements provide qualitative and quantitative information about the overall populations of both ICG monomer and dimer in the GNP suspensions. The amphiphilic character of ICG results in reversible self-organization into highly ordered aggregates upon an increase in concentration, predominantly caused by Van der Waals forces and hydrophobic interactions.[274–276] The organization of ICG in dimers, oligomers and higher order aggregates is accompanied by changes in optical properties, which allows complementary information to be gathered from different spectroscopic techniques.

Here, we demonstrate that changes in relative CTAB concentration and presence of Ag^+ may have a dramatic effect on the ICG adsorption on the gold substrate. This suggests that careful control of these parameters is crucial for the effective labeling of the nanostructure. Based on our results, we propose a model describing the dynamics of ICG adsorption to the gold surface in relation to the dye monomer-dimer equilibrium in the bulk solution.

7.2 Materials and methods

7.2.1 chemicals

All reagent grade chemicals were used as received. MilliQ water was used throughout the experiments. Indocyanine Green (ICG) was purchased from Fluka. Gold(III) chloride hydrate ($HAuCl_4 \mathring{u} n H_2O$) >99.9% was provided by Aldrich (St Louis, MO, USA). Cetyltrimethylammonium bromide (CTAB) >99% was obtained from Sigma. Silver Nitrate ($AgNO_3$) >99% was purchased from Sigma-Aldrich. All chemicals were ordered via Sigma-Aldrich (St Louis, MO, USA).

7.2.2 citrate-capped gold nanoparticles (GNP)

Citrate-capped gold nanoparticles of ∼15 nm diameter (0.29 nM) were prepared by reduction of chloroauric acid with sodium citrate.[277] 0.1 ml of $HAuCl_4$ 0.118 M solution was added to 50 ml of MilliQ water. Then 1 ml of sodium citrate 0.0388 M solution was added under stirring. The mixture was boiled for 5 minutes under reflux. Fresh ICG solutions, from 10^{-5} M to 10^{-2} M, were prepared in methanol before every set of measurements. The photostability and thermal stability of ICG molecules in methanol is considerably higher than in water.[278] Besides, the tendency for ground state dimer formation is very weak in methanol, and ICG is predominantly present as a monomer up to a concentration of about $5{\times}10^{-2}$ M.[279] In this way, ICG molecules were always added as monomers to different samples, independently from the stock solution concentration. Salt solution contains sodium citrate ($5{\times}10^{-4}$ M), hydrochloric acid ($5{\times}10^{-4}$ M) and potassium bromide (10^{-3} M) and shows the same pH of the gold colloid

(pH∼6). ICG concentration-dependent behaviour was investigated in this salt solution instead of pure MilliQ water in order to broadly reproduce the pH and ionic strength conditions of the GNP suspension after the addition of KBr. In fact, these two parameters slightly affect the distribution of ICG molecules in solution.[274]

7.2.3 BR/GNP

By adding 20 μL of a KBr 0.05 M water solution to 1 ml of GNP suspension, Br/GNP were prepared. The final bromide concentration in the suspension is 10^{-3} M, which was selected as optimum concentration to provide large number of active sites for ICG adsorption without inducing observable NP aggregation in the experimental time-scale (Figure B.1 of Appendix B).

7.2.4 BR/AG/GNP

To an aqueous solution to 1 ml of Br/GNP colloid, 5 μL of $AgNO_3$ 1.5×10^{-2} M was added. CTA/Br/Ag/GNP samples were prepared as for CTA/Br/GNP except that 5 μL of $AgNO_3$ 1.5×10^{-2} M aqueous solution was added to 1 ml of Br/GNP colloid before the addition of CTAB 0.4 M solution.

7.2.5 CTA/BR/GNP

A large excess of CTAB (0.125 ml of CTAB 0.4 M) was mixed with 1 ml of GNP. CTAB-capped GNP were centrifuged from one to three times to progressively decrease the surfactant concentration: (1) 1st centrifugation: 12K rpm, 30'; (2) 2^{nd} centrifugation: 12K rpm, 30'; and (3) 3^{rd} centrifugation: 12K rpm, 5' or 20'. We will refer to these systems as CTA/Br/GNP (1), (2) and (3), respectively. The first two centrifugations do not produce significant NP aggregation as judged from the absorption spectra, whereas the third centrifugation step causes a profound aggregation regardless of the centrifugation time (Figure B.2 of Appendix B).

7.2.6 INSTRUMENTATION

Fluorescence spectra were measured with a Fluoromax-4 (Horiba Jobin Yvon, Longjumeau, France) spectrofluorometer with the following set-up: excitation 780 nm, excitation slit 5 nm/emission slit 10 nm, applied voltage 700 V. Samples for UV-visible absorption spectroscopy were prepared in the same way as those for the corresponding emission spectra and were recorded in a Shimadzu UV-2401PC spectrophotometer (Shimadzu, Kyoto, Japan).

Fluorescence and UV-Vis absorption measurements were performed on Citrate/GNP, Br/GNP, Br/Ag/GNP and CTAB solution by adding to 1 ml suspension different aliquots of ICG stock solutions up to the desired concentration. For both fluorescence and absorption measurements, samples were measured in 1 ml polystyrene cuvettes (Plastibrand standard disposable cuvettes, Sigma-Aldrich).

7.3 Results and discussion

7.3.1 ICG adsorption on GNP

Figure 7.1A shows the ICG absorption spectrum in aqueous salt solution which roughly reproduces the ionic strength and pH of GNP colloid. Figure 7.1A illustrates the reversible self-organisation into dimers upon a concentration increase as a result of ICG's amphiphilic character.[274–276] At low dye concentration ($\leq 10^{-7}$ M) the mole fraction of dimers is negligible[275] and the absorption profile is dominated by the band at $\sim$ 780 nm. An increase of the dye concentration to the range of 10^{-7}-10^{-4} M results in dimer formation and a relative intensity increase of the feature at $\sim$ 705 nm.[22] The progressive shift of the $M \leftrightarrow D$ equilibrium towards the dimer form upon an increase in dye concentration is represented in Figure 7.1B (black squares), by plotting the absorption ratio at $\sim$780 nm (H_{780}) and $\sim$ 705 nm (H_{705}) against the ICG concentration in logarithmic scale.

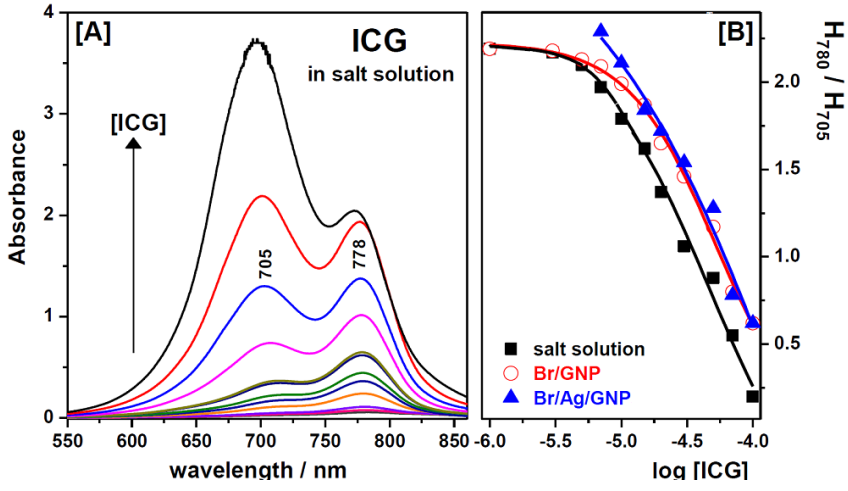

Figure 7.1 : Self-organization from ICG monomers (λ_{abs} = 778nm) into dimers (λ_{abs} = 705 nm) upon ICG concentration increase. A) Concentration-dependent absorption spectra of ICG in salt solution; from the top to the bottom, [ICG] = 7×10^{-5} M, 5×10^{-5} M, 3×10^{-5} M, 2×10^{-5} M, 1.5×10^{-5} M, 1×10^{-5} M, 7×10^{-6} M, 5×10^{-6} M, 3×10^{-6} M, 1×10^{-6} M, 7×10^{-7} M and 5×10^{-7} M. B) Experimental values of the spectral parameter H_{780}/H_{705} at different dye concentration for ICG dissolved in salt solution, Br/GNPs and Br/Ag/GNPs colloids.

Figure 7.2 shows the fluorescence emission of ICG 3×10^{-6} M in salt solution (black line). Fluorescence intensity of ICG in salt solution initially increases with the ICG concentration (Figure 7.2B, black squares) reaching a maximum fluorescence at $\sim$ 5×10^{-6} M. At higher concentrations, quenching of the fluorescence emission signal occurs due to the formation of ICG dimers and larger aggregates.[280] In the presence of citrate/GNP, fluorescence emission decreases for ICG concentration below $\sim$ 10^{-5} M, and the maximum fluorescence intensity

shifts towards higher ICG concentrations (Figure 7.2B, green stars).

The quenching effect is more pronounced for Br/GNP (Figure 7.2, red). This is consistent with the preferential adsorption of monomer ICG on the metal surface, whose fluorescence emission is subsequently quenched via an increased non-radiative relaxation of the excited state due to energy and/or electron transfer with the plasmonic nanostructures.[281] This conclusion is further supported by the data shown in Figure 7.1B, since the adsorption of ICG monomers at the Br/GNP surface shifts the $M \leftrightarrow D$ equilibrium in solution towards monomers suggesting an overall increase of monomer populations at the expense of dimers. However, it is not possible from absorbance and fluorescence spectra alone to determine potential self-assembly of monomers after adsorption on the GNP surface.

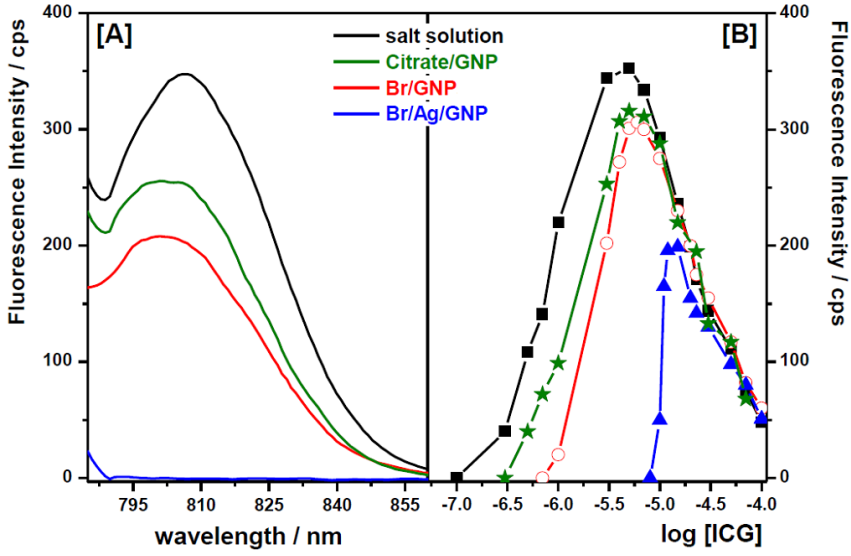

FIGURE 7.2 : Fluorescence intensity of ICG vs. A) ICG concentration and B) logarithmic value of ICG concentration, for dye molecules dissolved in salt solution, and Br/GNP and Br/ Ag/GNP colloids.

Addition of silver ions to Br/GNP solutions shifts the maximum of the fluorescence emission to even higher concentrations (ICG $< \sim 3\times10^{-5}$ M, Figure 7.2, blue triangles), which indicates that Ag^+ deposition on the gold surface provides a more effective adsorption of monomer ICG to gold nanoparticles. This is also in excellent agreement with the data from absorption spectroscopy (Figure 7.1).

Above 1×10^{-5} M, the dimer formation is no longer affected by the presence of GNP, in agreement with the results of absorption spectroscopy (Figure 7.1B). For dye concentrations larger than $\sim 3\times10^{-5}$ M, the fluorescence intensity of ICG-GNP solutions converges to similar values as for ICG in salt solution. Furthermore, it can be noted that a high ICG concentration does not induce GNP aggregation

(Figure B.3 of Appendix B), which is advantageous for the potential use of ICG as a GNP marker, as other fluorescent dyes show a tendency to produce GNP aggregation at high surface coverage.[282,283]

Like other organic molecules,[284] ICG possesses in its structure a positively charged aromatic nitrogen atom in the benzo[e]indole ring which has a high tendency to interact with the metal NP through Coulomb interaction with previously adsorbed halide anions such as Cl^-, Br^- and I^-, which are known to adsorbs strongly on gold and silver surfaces.[273] Therefore, we suggest that ICG interacts with the gold surface via binding with residual chloride anions from the GNP synthesis (in the case of citrate/GNP) or with the larger number of bromide anions added *a posteriori* to the colloid (Br/GNP). Moreover, in a recent paper, Sanchez-Cortes *et al.* demonstrated the self-adsorption of Ag^+ ions on GNP surfaces with the formation of strong Ag^+-Cl^- bonds and consequential marked alteration of the electronic properties of the halide anions at the metal surface.[285] Accordingly, we can ascribe the drastic increase of ICG adsorption on Br/Ag/GNP surfaces to the improved electron donor ability of bromide anions resulting from their interaction with self-assembled Ag^+ ions onto the gold surface.

The previous results support the notion that ICG adsorbs to GNP as a monomer, effectively shifting the well-known monomer-to-dimer equilibrium of ICG in aqueous solution to the monomer state. In Figure 7.3A and 7.3B the adsorption behaviour of ICG onto gold nanoparticles in the presence of Br^- (Figure 7.3A) and Br^- and Ag^+-ions (Figure 7.3B) has been outlined for relevant ranges of the concentration of ICG. The relations between monomers M and dimers D are described, both in the bulk solution and with respect to the corresponding situation in aqueous solutions (no GNP).

At a dye concentration below 8×10^{-6} M, (Figure 7.3A, pane (1)), the mole fraction of ICG dimers in solution is negligible ($[M_b] \gg [D_b]$). The presence of silver enhances the adsorption of ICG and further reduces the concentration of monomers in bulk (Figure 7.3B(1)). The adsorption of ICG monomers on the metal surface (M_s) and the subsequent quenching of the fluorescence emission leads to a proportional decrease of the fluorescence intensity as compared to ICG in aqueous solution (Figure 7.2) in the absence of GNP.

At an intermediate concentration of $\sim 8\times10^{-6}$ M, (Figure 7.3A(2)), the dimer population of ICG becomes more relevant as the ICG state in solution has to be described by the $M_b \leftrightarrow D_b$ equilibrium. As a result, a loss in $[M_b]$, caused by the adsorption of ICG on the GNP, is counterbalanced by a shift of the $M_b \leftrightarrow D_b$ equilibrium toward the monomer state (Figure 7.2B). This effect leads to an appreciable increase of the H_{780}/H_{705} ratio towards higher ICG concentrations with respect to aqueous solution in Figure 7.1B. This tendency is increased in the presence of silver ions (Figure 7.1B).

The presence of silver ions drastically enhances monomer ICG adsorption as indicated by the complete quenching of dye fluorescence up to a [ICG] concentration of $\sim 8\times10^{-6}$ M. The concentration of GNP is 0.29 nM and the onset of fluorescence emission in the presence of Br/Ag/GNP is therefore consistent with a full surface coverage of GNP (Figure 7.3B(2)). As a direct consequence, silver deposition also increases the minimally required dye concentration to observe dimer formation in the bulk solution (Figure 7.3B(3)).

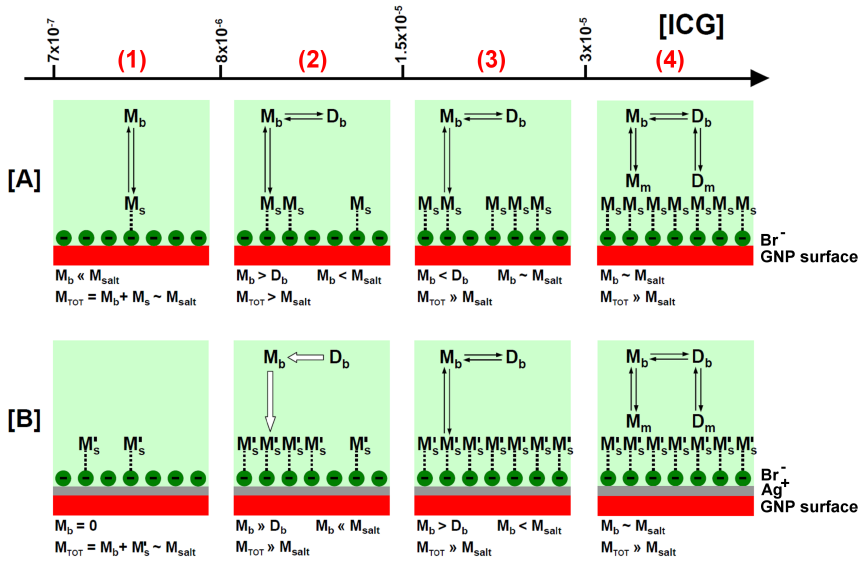

FIGURE 7.3 : ICG adsorption scheme on A) Br/GNP and B) Br/Ag/GNP surfaces at different dye concentration. Monomer is labelled M, dimer D. The subscripts indicate: b for "bulk", referring to M and D existing in the bulk aqueous solution; s for "surface", referring to M chemisorbed on the gold surface. M_m and D_m stands for "multilayer", which refers to M and D physisorbed on the first ICG layer surrounding the NP. M_{salt} stands for monomer dye molecules in pure aqueous solution (no GNP). The overall monomer population in the colloidal suspension is indicated as M_{TOT} ($=M_b + M_s$).

The GNP-induced shift in the monomer-dimer equilibrium cannot be detected when the ICG concentration is raised above $\sim 1.5\times10^{-5}$ M (Figure 7.3(3)), because at elevated concentrations the dimer population becomes dominant in the bulk. In fact, a high D_b concentration maintains an approximately constant monomer concentration in the bulk, roughly independent of the fraction of dye molecules M_s adsorbed to the GNP surface. As a result the effect of silver ions on the $M_b \leftrightarrow D_b$ equilibrium is limited (Figure 7.3B(3)).

Accordingly, the $M_b \leftrightarrow D_b$ equilibrium is hardly influenced by the presence of GNP, either in the absence or the presence of silver, once full surface coverage is achieved upon a further increase in ICG concentration, over $\sim 3\times10^{-5}$ M (Figure 7.3(4)). The dimer population becomes dominant and unspecific physical multilayer deposition may occur, i.e. both monomers and dimers from the aqueous solution may adsorb onto the dye covered surface. As a result, both H_M/H_D and fluorescence and data converge to the values observed for ICG in salt solution (Figures 7.1B and 7.2).

7.3.2 EFFECT OF CTAB

CTAB plays a key role in the production of many different morphologies of gold nanoparticles. The production of gold nanospheres does not require CTAB and the concentration of CTAB can therefore be adjusted at will. ICG is known to incorporate itself into the interface of CTAB micellar structures, which affects its optical properties.[275]

Figure 7.4 shows that the concentration of unbound CTAB in aqueous solutions modifies the aggregation states of ICG. In Figure 7.4A, the peak height ratio H_M/H_D calculated from absorption spectra of ICG dissolved in CTAB solutions at different concentrations is plotted against the ICG/CTAB concentration ratio. The corresponding absorption spectra of 3×10^{-5} M ICG in aqueous solutions with different CTAB concentrations are shown in Figure 7.4B.

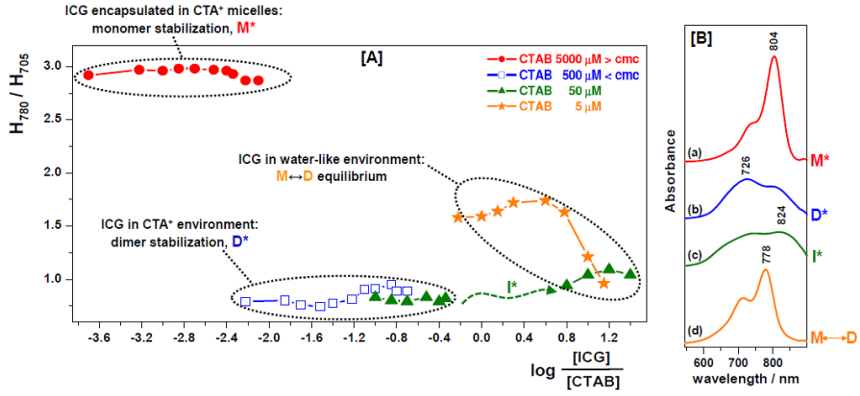

FIGURE 7.4 : A) Experimental values of the spectral parameter H_M/H_D for ICG at different concentration in CTAB solutions (5000 μM, 500 μM, 50 μM and 5 μM) against [ICG]/[CTAB] ratio (logarithmic scale). B) Absorption spectra of ICG 3×10^{-5} M in CTAB aqueous solutions at different surfactant concentration: (a) 5000 μM, (b) 500 μM, and (d) 5 μM. (c) Absorption spectrum of ICG 3.7×10^{-5} M in CTAB aqueous solution 50 μM.

Above the critical micelle concentration (cmc) of ∼1.2 mM for CTAB,[286,287] the dye molecules are highly stabilized as monomer encapsulated in CTAB micelles,[255] referred to as M* (red, trace a). Micellar encapsulation of ICG reduces the formation of dye dimers and higher-order aggregates,[255] leading to an absorption spectrum dominated by monomeric responses (Figure 7.4B(a)). In addition, ICG micellar encapsulation results in an up-shift of ∼10-25 nm for absorption maxima, for both monomers and dimers, compared to the spectrum of the dye in water (Figure 7.1A).[275]

However, when the CTAB concentration is decreased to just below the cmc value, ICG molecules form dimers (D*) even at very low dye concentrations (blue, trace b). Thus, CTAB affects ICG dimerization in aqueous environments. When the CTAB concentration is further decreased, a sudden change of the optical properties of ICG occurs (green, trace c). This change indicates a transition

from the highly dimerized state in a CTAB environment (blue, trace b) to a state reflecting the dye molecules in a water-like surrounding (yellow, trace d). This transition takes place for [CTAB] ∼ [ICG] and shows a broad absorption at ∼820 nm (Figure 7.4B(c)), which we suggest can be attributed to an intermediate form, labelled as I*. This marked red-shift of the absorption maximum may suggest the formation of larger ordered aggregates, similar to those reported for J-aggregates.[274,278]

7.3.3 EFFECT OF SILVER-IONS

Since the concentration of unbound CTAB in aqueous solutions modifies the aggregation states of ICG, the corresponding effect on affinity of the dye to the GNP surface was verified. We capped citrate-GNP with a large excess of CTAB (≫cmc) and performed several centrifugation steps. While the first two centrifugation steps do not produce significant GNP aggregation, the third round of centrifugation causes an irreversible aggregation of GNP, regardless of the centrifugation time (Figure B.3 of Appendix B). This suggests a decrease of CTAB concentration at the metal-liquid interface, disrupting the surfactant double layer around the GNP, which causes aggregation (Figure 7.5, top scheme). We name these CTAB-capped GNP suspensions as CTA/Br/GNP (1), CTA/Br/GNP (2) and CTA/Br/GNP (3), where the number in brackets refers to the centrifugation steps carried out. CTA/Br/Ag/GNP systems were created by functionalizing GNP with a thin shell of silver Ag^+ prior to the CTAB addition.

The bottom graphs in Figure 7.5 show the ICG fluorescence spectra of the CTA/Br/GNP. Figure 7.5A shows that in the CTA/Br/GNP (1) system, dye molecules appear as highly stabilized as monomer M*, emitting at ∼820-830 nm. Since the fluorescence of ICG adsorbed on GNP is quenched,[273] the fluorescence emission spectra mainly address the monomer population in the bulk solution, as was demonstrated above (Figures 7.1 and 7.2).

In the CTA/Br/GNP (2) system, the CTAB concentration has dropped below the cmc and extremely weak fluorescence is observed (Figure 7.5B) which can be assigned to few dye molecules existing as M, judging from the maximum of emission centered at ∼802 nm.

Note that the position of the emission maximum is caused by variations in fluorescence intensity, due to quenching effects of dimers D*,[280] and metal-dye interactions,[273] as was illustrated in Figure 7.2. As before (Figures 7.1 and 7.2), absorption and emission spectra of ICG suggest that silver deposition leads to an overall increase in ICG adsorption on the metal surface (Figures 7.5A and 7.5B).

A third centrifugation (CTA/Br/GNP (3)) further decreases the surfactant concentration, leading to an enhancement in fluorescence signal (Figure 7.5C), which is attributed to ICG monomers M_b. However, due to the irreversible aggregation occurring in CTA/Br/GNP (3) and CTA/Br/Ag/GNP (3) systems (Figure B.3 of Appendix B), it is not possible to address changes in ICG optical behaviour uniquely to the silver deposition on the GNP.

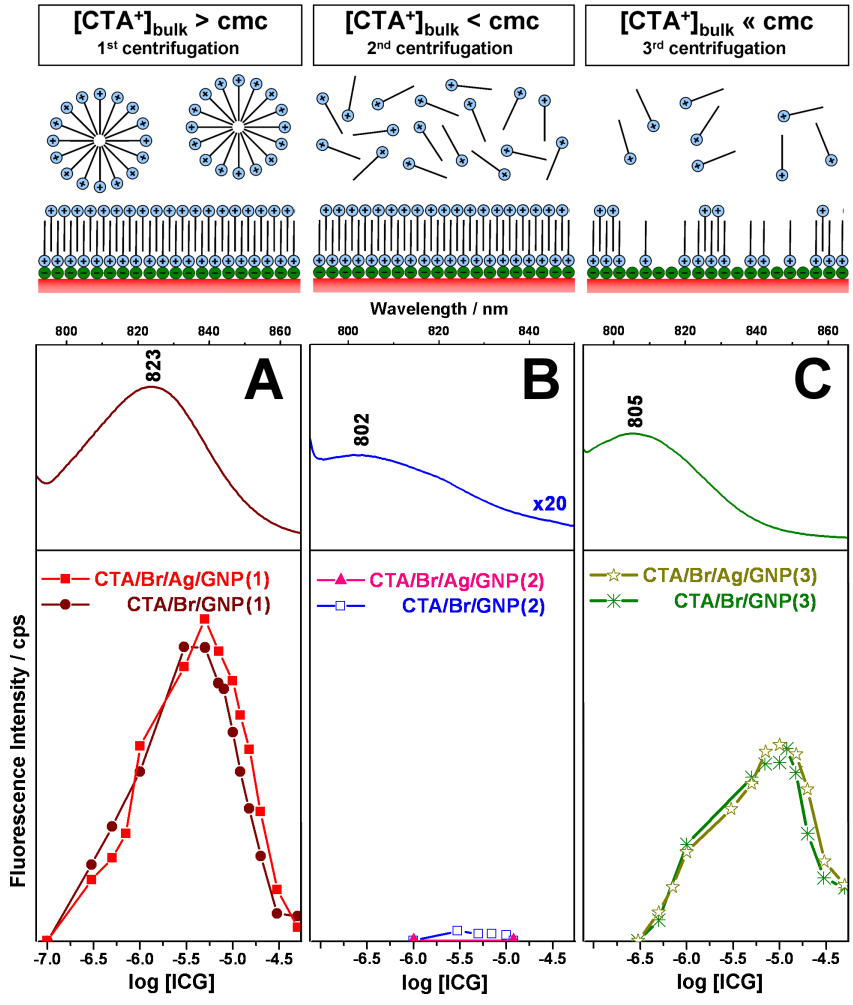

FIGURE 7.5 : Top scheme: Schematic representation of the surfactant distribution in CTAB-capped NP colloids after each step of centrifugation. Bottom graphs: Fluorescence emission spectra of ICG 7×10^{-6} M in CTA/Br/GNPs (1), (2) and (3) colloids and ICG fluorescence intensity against ICG concentration (logarithmic scale) for dye molecules dissolved in CTA/Br/GNPs and CTA/Br/Ag/GNPs colloids after each step of centrifugations: A)(1), B)(2) and C)(3).

7.4 Conclusions

Citrate-capped spherical gold nanoparticles were chosen as an experimental model for the interaction of gold nanoparticle surfaces with the medical contrast agent ICG. Since spherical gold nanoparticles do not require either Ag^+ or CTAB during synthesis, addition of these compounds in varying concentrations offers an opportunity to investigate the potential role of Ag^+ and CTAB on the adsorption of ICG. ICG adsorption to gold nanoparticles and the effect of the presence of Ag^+ and CTAB on the ICG adsorption was studied with fluorescence emission and UV-Vis absorption spectroscopy. Fluorescence emission of ICG adsorbed to gold is quenched,[273,280] and the absorption spectra provide quantitative information about the overall monomer and dimer populations in solution and colloidal suspensions.

ICG in aqueous solution exists in equilibrium between monomers, dimers and higher order aggregates. Both the fluorescence emission data and the absorption data show that the presence of gold nanospheres shifts the equilibrium to increased monomer contribution. This result suggests that the ICG-dye adsorbs as a monomer to the gold surface. The observed ICG adsorption is summarized in Figure 7.3 for the relevant range of concentrations for which the existence of a monomer-dimer equilibrium is noticeable. Although slightly different in detail, Br/GNP solution behaved similar to Br/Ag/GNP solution.

CTAB, which is an essential component in gold nanorod production and the production of other gold nanoparticle geometries, affects the adsorption of ICG to gold nanoparticles because CTAB micellar structures compete for the available ICG. In the presence of CTAB above the critical micellar concentration (cmc), ICG intercalates in the micelles, which prevents ICG adsorption onto GNP. When the surfactant concentration is decreased to just below the cmc value, the monomer-to-dimer ratio decreases, suggesting stabilization of ICG in the form of dimers.

Thus, the unbound surfactant concentration in the colloidal suspension may dramatically modify the dye aggregation state in the mixture and, in turn, its affinity to the metal surface. In addition, as CTAB constantly exchanges from the GNP surrounding bilayer to the solution, the CTAB concentration in the bulk plays a key role in the release of the surfactant from the GNP.[288] Additional Ag^+ deposition on GNP leads to an overall increase in ICG adsorption on the metal surface, as a result of a drastic strengthening of the dye-metal interaction.

These results show that the ICG adsorption on spherical gold nanoparticles metal substrate can be very different even for slight changes in the experimental parameters, such as concentrations of ICG, CTAB and presence of Ag^+. Therefore, careful control of these variables is crucial for the effective dye labeling of gold nanostructures.

CHAPTER 8

3D Spatial distribution of gold nanoparticles in breast cancer cells

Although the biomedical application of gold nanoparticles has a long history, recently in particular gold nanorods (GNR) have attracted attention. From a biocompatability point of view as well as from an optical angle, GNR are promising contrast enhancing agents in tumour detection. However, before GNR can be applied in the clinic, their safety will have to be assessed and approved. Throughout this thesis, we have used mainly Raman microspectroscopy to characterise GNR as well as their interactions with breast cancer cells.

First, the Raman response of unperturbed ductal breast carcinoma cells was determined. Then, the interaction of GNR with SK-BR-3 cancer cells has been investigated using both Raman imaging for live cell imaging and scanning electron microscopy on fixated cell samples.

Raman mapping of SK-BR-3 cells incubated with GNR revealed that the optical response of intracellular GNR differs from the response of GNR in solution. Moreoever, the spectral distribution of GNR emission from withing the cells appeared to be spatially non-uniform. The fluorescence-like emission profiles from GNR were further discussed by comparing their absorption and emission characteristics to literature values.

In addition, live Raman cell mapping showed a coincidence of the GNR signature with that of increased lipid signals, which indicated local accumulation of GNR within intracellular lipid vesicles. To increase the signal specificity of the GNR, Raman markers can be incorporated into the GNR coating. Therefore, we investigated the adsorption of the near-infrared dye indocyanine green to GNR-like surfaces.

So far, only two-dimensional information has been obtained, from selected focal planes. To gain better insignth into the spatial distribution of the GNR within breast cancer cells and their local intracellular interactions, we extended the data acquisition in the Raman microspectroscope to 3D imaging.

In this chapter, we characterise the optical resolution of this 3D system and we show the results of initial 3D Raman mapping experiments, in which we mapped fixated SK-BR-3 breast cancer cells both with and without the addition of GNR.

8.1 Introduction

Gold nanoparticles (GNP) possess surface plasmon absorption bands that invoke favourable optical properties, such as an enhanced absorption cross-section.[5] This makes them promising contrast agents. Possible applications of contrast enhancing GNP lie in the diagnostics and treatment of early stage carcinomas, as was discussed in Chapter 1. Whereas conventional tumour imaging suffers from low contrast with respect to the surrounding tissue, by administering GNP to the tumour site, high contrast non-invasive cancer imaging can be achieved (Figure 1.6).

In cell applications mostly gold nanospheres (GNS) are used. Due to their well-known and controllable synthesis procedures (section 1.2) GNS are widely available. However, for non-invasive detection and treatment gold nanoshells and gold nanorods (GNR) are of particular interest, because their plasmon bands are tunable (Figures 1.2 and 5.6). This enables application within the near-infrared optical window.

Previous reports have shown a remarkable variance in the cytotoxicity and uptake of gold nanoparticles by cells because the interaction of GNP with cells appears to be dependent on particle characteristics, such as functionalization, surfactant coating (section 1.3), size, and shape (Table 5.1). In addition, the invoked particle reaction depends on the type of cells involved as well. Since responses are dependent on many parameters, proper characterization of GNP and their interactions with and effects on cancer cells is necessary before *in vivo* therapeutic studies commence.

Earlier, GNR have been tracked in cells using techniques such as darkfield microscopy,[289,290] transmission electron microscopy (TEM)[35,81,158], scanning electron microscopy (Chapter 6) and surface enhanced Raman spectroscopy (SERS).[62,155,157,291]

Alternatively, the use of the intrinsic fluorescence of GNR in cancer cell detection can be further explored. In chapter 4, we demonstrated that the fluorescence of GNR is detectable from within SK-BR-3 cancer cells using two-dimensional (2D) Raman microspectroscopic imaging (Figure 4.4). However, the Raman cross section of lipids is relatively large compared to that other cellular components (Figure 2.7)[217,242] and lipids are prominently present in SK-BR-3 cells.[107] This may cause lipids to be detected from outside the focal spot, leading to a deceptive 2D image of the distribution of components throughout the cell and raising questions about the exact locations of the GNR within the cells. In addition, the microspectroscopic measurements were performed on living cells, which leads to complex situations because the cells and their interiors move while being measured.

Three-dimensional (3D) spectroscopic imaging techniques that are optimized for imaging speed could provide more detailed information on the position of GNR within cancer cells, improving insight in the interaction of GNR with breast cancer cells on a biochemical level. Here, we describe our trajectory towards 3D Raman microspectroscopic imaging. To establish system specifications, we determined the resolution of the Raman imaging setup in the both lateral and axial direction. Accordingly, the setup is adjusted to enable depth imaging at an appropriate resolution. Initial depth measurements were presented which resulted in z-stacked images of fixated SK-BR-3 breast cancer cells with and without GNR.

8.2 Materials and methods

8.2.1 sample preparation

Polystyrene beads

In general, to determine the axial resolution of optical systems, the optical system response of the laser spot illuminating a sub-resolution particle is used. This procedure is also known as the Point Spread Function (PSF). We use a polystyrene (PS) spherical bead with a diameter of 100 nm (Polybead microspheres 0.1 μm, Polysciences Inc, Warrington, PA) as a point source. PS has a well known Raman spectrum, possessing a prominent peak around 1003 cm^{-1}.

The PS beads were suspended in a 2 wt% polyvinyl alcohol (PVA) in water solution at 1 : 100 μl. A 10 μl droplet of this solution was spincoated at 6000 rpm for 10 seconds on a 20 mm diameter calciumfluoride (CaF_2) slide (Crystran Ltd., Dorset, UK). The sample was then covered with a cover slip.

Cell culture

SK-BR-3 mammary adenocarcinoma cells were maintained using Dulbecco's Modified Eagle Medium (DMEM) medium supplemented with 1% glutamine, 10% Fetal Bovine Serum (FBS) and 1% antibiotics (Penicillin Streptomycin). The cells were passaged every 3 days.

One day before measurements, SK-BR-3 cells were harvested from culture flasks and dispersed in SK-BR-3 culture medium containing PEG-GNR in a GNR to cell ratio of approximately 1.6×10^6 : 1. The PEG-GNR are approximately 20×40 nm and have a longitudinal plasmon absorption maximum at 640 nm. Subsequently, this dispersion was seeded on calcium fluoride (CaF_2) slides (20 mm diameter, 2 mm thickness) to obtain approximately 16.000 cells/cm^2 and incubated overnight. SK-BR-3 cells cultured in medium without PEG-GNR were used as a control.

Before Raman measurements, the culture media were removed and the cells were washed with Phosphate Buffered Saline (PBS) at least three times. The cells were fixated by submersion in a 1% paraformaldehyde (PFA) solution for at least 20 minutes at room temperature. After fixation, the samples were again rinsed thrice with PBS.

8.2.2 3D raman imaging

Raman imaging was carried out using a home-built confocal Raman microspectroscope, described in Chapter 2. For 3D imaging, the setup was expanded with a NV40/1 CLE piezo objective stepper (PiezosystemJena, Jena, Germany), which allows the objective to be moved axially. The stepper's scan range is adjustable from 0 to 400 μm (± 40 nm), corresponding to 0 to 10 V. Actuation is achieved by an external power source which is in turn controlled by LabView.

Polystyrene beads

For axial resolution establishment experiments, PS beads of 100 nm diameter were selected for imaging using brightfield imaging. The selected PS beads were

scanned in the z direction, over an axial distance of 30 μm with a 100 nm step size. Spectral integration time was 1 s, laser power under the 60×/1.2 NA water immersion objective (Olympus U-Plan S APO; Olympus, Tokyo, Japan) objective was 35 mW.

A z-stack of images was obtained scanning a 20×20 μm area. An additional zoom factor of 0.10 was applied, resulting in an imaged region of 2×2 μm. Hyperspectral Raman imaging was performed by stepping the laser beam over the sample in a 16×16 raster pattern. The total axial distance was set to 2 μm and 7 images were acquired, resulting in an axial step size of approximately 333 nm.

Cell samples

In analogy to previous work,[107] cells were selected based on their appearance in brightfield. 3D images were obtained by acquiring a z-stack of 32×32 images. The number of steps in the z direction varied. The scan area equaled 17.5×17.5 μm, resulting in a lateral resolution of 0.55 μm per pixel. Axial distance between the image planes was set to 1.5 μm. The first image was obtained within the substrate. The initial imaging position was determined using the reflection of the laser bundel on the substrate, as well as the Raman signal strength of the 322 cm^{-1} peak of CaF_2. Images were acquired with a laser power of 40 mW under the objective, with an acquisition time of 100 ms per pixel. For cell imaging, a 63×/1.0 NA water immersion objective (Zeiss W-Plan Apochromat; Carl Zeiss MicroImaging GmbH, Göttingen, Germany) was used.

8.2.3 DATA ANALYSIS

As decribed in the previous chapters, the acquired data was corrected for cosmic rays, CCD offset and setup response. Noise was reduced by singular value decomposition.[95,125]

Fitting models

The axial resolution of the 3D system is expressed in the Full Width Half Maximum (FWHM) of the laser spot intensity profile. In order to determine the FWHM, the intensity profile is fitted with a Gaussian function (Equation 8.1). The fitting parameters are determined by using the curve fitting toolbox in Matlab 7.6.0 (The Mathworks Inc, Natick, MA, USA).

$$f(x) = a \cdot \exp\left(-\left(\frac{x-b}{c}\right)^2\right) + d \cdot x + e \tag{8.1}$$

Here, a is the amplitude, b the central mean and c the standard deviation. In case the signal background is offset or slanted, the extensions in the form of a linear function $d \cdot x$ or starting value e can be used. From c, the FWHM can be deducted using Equation 8.2:

$$FWHM_{Gaus} = 2\sqrt{\log 2} \cdot c \tag{8.2}$$

The axial profile of the focal spot is described from the Lorentzian fit (Equation 8.3):

$$f(x) = \sum_i a_i \frac{\left(\frac{c_i}{2}\right)^2}{(x - b_i)^2 + \left(\frac{c_i}{2}\right)^2} \tag{8.3}$$

Where, a is the amplitude, b the central mean and c the FWHM of the Lorentzian function.

8.3 Results and discussion

8.3.1 axial resolution

Theoretical

The theoretical axial resolution of the Raman microspectroscope was approximately 1.5 μm for a 1.0 NA objective (Chapter 2). Since samples containing different refractive indices may affect the resolution, the axial resolution was determined empirically, using the Point Spread Function (PSF).

Empirical

Figure 8.1A shows the univariate intensity Raman image of a z-scan over the 950-1050 cm^{-1} band of a 100 nm PS bead on CaF_2, covered in PVA. Although the bead is spherical, the image shows an elliptical particle shape. This is expected, as the system resolution in the z direction is lower than in the x and y resolutions.

Figure 8.1B depicts the intensity profile (squares) of the 1003cm^{-1} band of PS (990 - 1020 cm^{-1}), fitted with a Lorentzian curve (line). The FWHM is calculated from the fitting parameter c in Equation 8.3. Here, the FWHM comprises approximately 27 pixels, corresponding to an axial resolution of the system of 1.85 μm ($FWHM_{PSF}$). The empirically obtained axial resolution approaches the theoretical value of 1.5 μm rather well.

8.3.2 lateral resolution

Theoretical

The lateral resolution or spot size for a diffraction limited lens can be calculated following Equation 8.4,[90,91] as discussed in Chapter 2:

$$\omega_0 = 1.2 \times \left(\frac{1.83\lambda_0}{4NA}\right) \tag{8.4}$$

Here, λ_0 is the laser wavelength in vacuum and NA the numerical aperture of the objective. In case a 1.2 NA objective is used in combination with an excitation wavelength of 647.1 nm, λ_0 is approximately 300 nm.

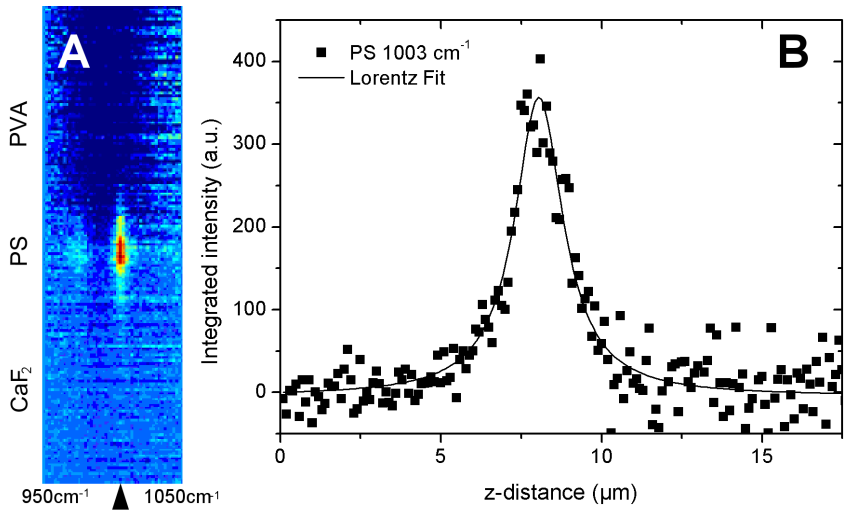

FIGURE 8.1 : A) Univariate image of the 950 - 1050 cm^{-1} region of the Raman spectra of a 100 nm PS sphere in PVA on CaF_2. The Raman image was acquired using a line scan routine covering an axial distance of 30 μm with a 100 nm step size. The image was acquired with 35 mW laser power under the objective and a spectral integration time of 1s. B) The intensity profile of the 1003 cm^{-1} peak of PS along the z-axis (black squares) fitted with a Lorentzian (line). The profile was obtained at the position indicated with the arrowhead in A) and the intensity was determined by integration from 990 - 1020 cm^{-1}.

Empirical - laser reflection

Empirical verification of the lateral resolution of the brightfield imaging path was carried out by fitting a Gaussian profile to an image of the reflection of the laser spot (Figure 8.2, inset). The Gaussian shaped focal profile can then be calculated by integration of the pixel intensities in either x or y direction, as is shown in Figure 8.2.

From the Gaussian fits in Figure 8.2, the FWHM can be calculated using the c parameter (Equation 8.1). The pixel size of the CCD equals 75 nm and is taken into account by multiplying the FWHM in Equation 8.2 with 75 nm/pixel. It follows that the resolution in the x direction is 415 nm, and the y resolution is 468 nm. This is slightly larger than the 300 nm resolution that followed from the theoretical calculation. Theoretically, the x and y resolution should have a similar value. However, asymmetry in the intensity distribution in the focal plane may be due to differences in the refractive indices of the sample layers.[292,293]

Empirical - PS bead

The lateral resolution was also determined based on a z-stack of images of a 100 nm PS bead, described above (section 8.3.1).

Figure 8.3 shows the resulting z-stack of univariate images over the 1003 cm^{-1}

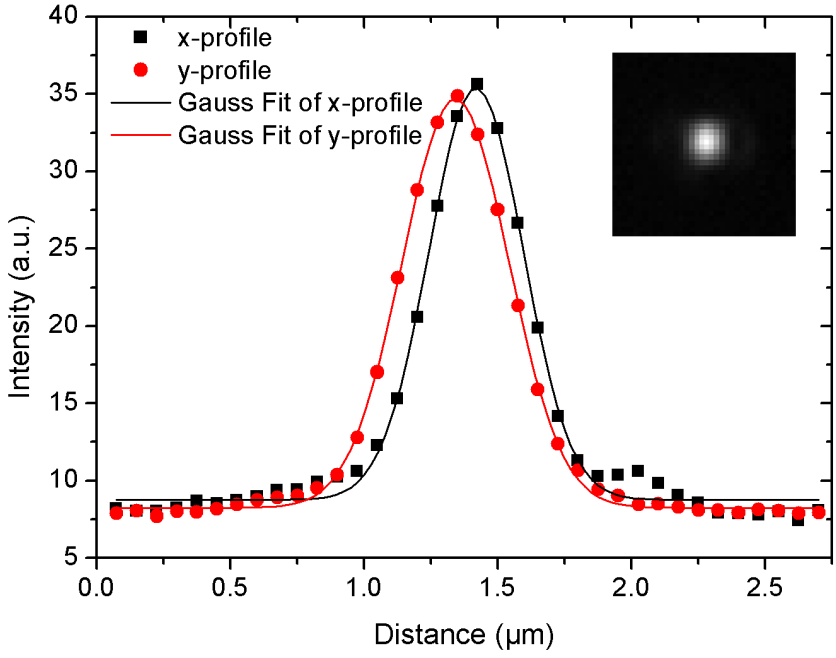

FIGURE 8.2 : A) The focal spot intensity profiles in x (black squares) and y (red dots) direction, fitted with a Gaussian function. The inset shows the camera image of the reflection of the laser spot in glass. Because the x and y signal originate from slightly different planes, the curves are shifted with respect to each other.

peak of PS. The first image (Figure 8.3, pane 1) is acquired within the interface of the CaF_2 substrate. Because the last image is taken close to the cover glass (Figure 8.3, pane 7), the background Raman signal is relatively large.

The shape of the PSF is expected to be between that of an airy disk and a Gaussian, because the laser beam is truncated at the objective. The PSF can be calculated by integrating the pixel intensities in x and y directions. The FWHM of the profiles, determined using Equation 8.2, take into account a conversion factor of 125 nm per pixel. This resulted in a measured lateral resolution of approximately 450 nm.

The data show that the focal spot is slightly oval, as indicated above. This astigmatism may be due to the setup that focuses the rays in y direction slightly above the rays in x direction, reducing the lateral resolution. Moreover, focal deviations also affect the axial resolution, as was indicated above (section 8.3.1). In addition, it has to be noted that we are working with a convolution of the signal of the 100 nm sphere with the real PSF. Therefore, the calculated PSF will be larger than the real PSF, as demonstrated here.

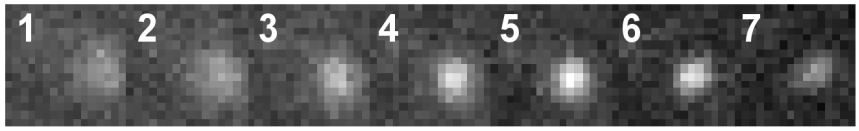

FIGURE 8.3 : 7×16×16 z-stack of Raman images of a 100 nm PS sphere in PVA on a CaF_2 substrate. The step sizes are 125×125×333 nm for respectively x, y and z directions. Image 1 was acquired within the the interface of the CaF_2 substrate. Images 2-6 depict PS intensity at different heights in the sphere. The final image 7 is obtained close to the cover glass.

8.3.3 3D CELL IMAGING

Taking into account the resolutions as determined above, optimal measurement settings for 3D Raman imaging are established. Preferably, scanning step sizes in lateral directions should not exceed 0.5 μm, to prevent undersampling.

The size of the area that is imaged is limited by the range of the scanning mirror to 17.5×17.5 μm for the 63×/1.0 NA objective used. In addition, the applied laser power can be varied to reduce the overall acquisition time, as was already indicated in Chapter 2. The product of applied laser power P and acquisition time t results in the laser dose D_{laser} that is applied to the sample (Equation 8.5):

$$D_{laser} = P \cdot t \tag{8.5}$$

The applied D_{laser} determines the signal-to-noise ratio (SNR) of the obtained Raman signal. Thus, when the applied laser power is increased, the acquisition time can be lowered according to Equation 8.5, without affecting the SNR of the acquired spectra.[107] The extent to which the overall acquisition time can be reduced depends on both the maximum output power of the laser, which is approximately 40 mW under the objective, and the maximum acquisition frequency of the setup. The latter is limited by the readout rate of the CCD camera, which is 2.5 MHz per pixel, equalling approximately 1 ms for a 1600 pixel full spectrum.

The Raman data of the fixated cells were acquired using a laser power under the objective of 40 mW and a 100 ms acquisition time per pixel to provide high SNR within a reasonable overall 3D measurement time of little over 15 minutes per cell. However, for live cell measurements, the acquisition time has to be reduced to prevent cell motion artifacts. In addition, cell viability drastically reduces when cells are removed from the incubator. It has to be noted that, once GNR are incorporated in the sample, D_{laser} should not exceed the threshold for particle reshaping.[290,294,295]

8.3.4 FIXATED CELLS

For 3D Raman imaging, SK-BR-3 cells were selected based on their appearance in brightfield microscopy. The cells were tested for adherence by gentle stirring and were observed to be adhered. Attached, round SK-BR-3 cells are just as viable as spread SK-BR-3 cells. The round morphology is caused by a relatively low cell confluence.[126] In Raman chemical analysis, round SK-BR-3 cells differ from spread ones in phospholipid content, which is possibly related to their proliferative state.[107,126,134] Whereas in previous work,[107] SK-BR-3 were imaged at the highest SNR plane, 3D imaging allows stacking of planes, thereby covering the entire contents of the cell. Thus, 3D imaging enables further investigation of the cellular constituents to a greater detail.

3D Raman imaging was carried out on the marked region in Figure 8.4A, covering both lipid rich regions and part of the nucleus of two fixated SK-BR-3 cells. Figure 8.4B shows the corresponding z-stack of 9×32×32 Raman intensity images of the CH-stretching vibrations in the high wavenumbers (2800-3050 cm^{-1}). These vibrations contain many lipid contributions, as is confirmed by the brightfield image that clearly shows the presence of lipid droplets (Figure 8.4A). In Figure 8.4B, image plane 1 was acquired at the interface of the substrate. The following images show the presence of the lipid droplets in different planes, while focusing slowly out of the cell towards plane 9.

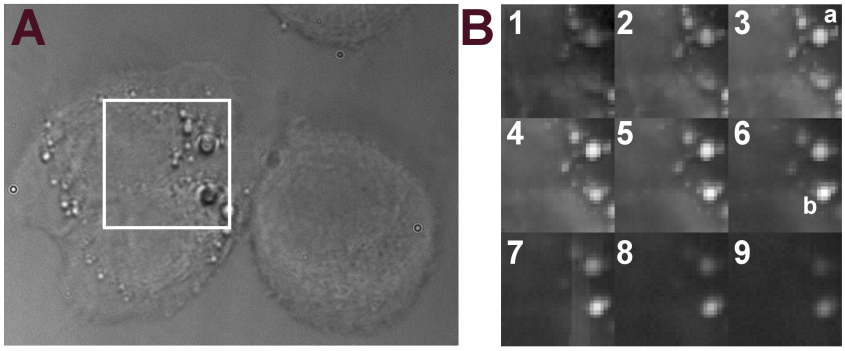

FIGURE 8.4 : A) brightfield image of a fixated SK-BR-3 cell culture. Within the marked region of what appears to be a divided cell, a 3D Raman image was acquired, depicting in B) the Raman intensity of the CH-stretching vibrations between 2800cm^{-1} and 3050 cm^{-1}. The sequence of images shows that droplet a is located lower in the cell than droplet b.

Figure 8.5 shows a Raman intensity image overlay of lipids and proteins from the marked area in Figure 8.4A. The intensity images were constructed on the 2850cm^{-1} lipid band (red) and the 1001cm^{-1} band of the phenyl group that is characteristic for proteins (blue). False colours were assigned to these respective intensities to aid visualisation of the local concentrations of the components.

The Raman signature of lipids appears to be confined to lipid vesicles, as seen in Figure 8.4B. High lipid expression in SK-BR-3 cells may be due to their

intensified cell membrane synthesis in the cell division process,[134] as previously suggested.[107]

On the other hand, proteins appear to be present in the entire cell. The highest concentration of proteins is located in what appears to be the nuclei, based on the whitelight image in Figure 8.4A. SK-BR-3 cells are expected to contain high amounts of nuclear proteins, because of high reproduction rates related to their tumorigenic nature.[122]

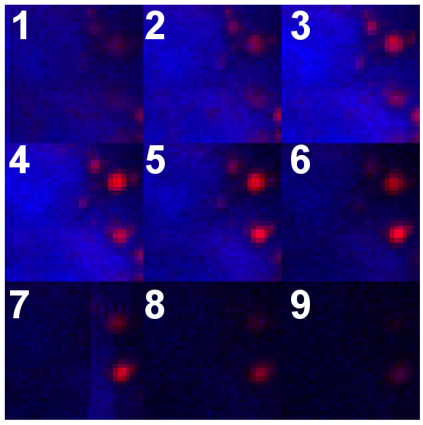

FIGURE 8.5 : Z-stack of nine combined univariate Raman images of the marked region of PFA fixated SK-BR-3 cells on a CaF_2 substrate from Figure 8.4A. Band integration was performed over ten wavenumbers around the 2850cm^{-1} lipid band, which is mapped in red, as well as over three wavenumbers around the protein characteristic band at 1001 cm^{-1}, false coloured in blue. Pixel step sizes are 1550×550×1500 nm for the x, y and z direction, respectively.

3D imaging enables more detailed localization of intracellular components by providing depth resolution. Figure 8.5 suggests that the nuclei of the cells lie close to the substrate, based on the signal (and thus colour) intensities. Signal of both lipids and proteins are strongest in image plane 4. The lipid droplets are also clearly present further from the substrate and appear more towards the cell surface (Figure 8.5, plane 6-8).

More than 70 SK-BR-3 cells were subjected to 3D Raman imaging and in general, they show a similar composition. The average SK-BR-3 nucleus is located close to the substrate, in the center of the cell. Within the nucleus several regions with an increased DNA peak amplitude can be distinguished, these were assigned as nucleoli. Lipids are often concentrated in spherical structures within the cytoplasma, surrounding the nucleus, whereas proteins are present throughout the entire cell in locally varying concentrations.

8.3.5 GNR INCUBATED CELLS

Figure 8.6 shows the distribution of lipids (red) and DNA(blue) in a 32×32×13 pixel RGB image, covering an area of 17.5×17.5×18 μm. The image is overlaid with a GNR intensity image. The top image in Figure 8.6 clearly illustrates the 3D resolving power of the Raman imaging system. The first image plane (Figure 8.6(1))was acquired at the interface of the CaF_2 substrate and shows GNR fluorescence. The presence of GNR at the substrate, thus below the cell, is very well possible, as they were applied to the CaF_2 simultaneously with the SK-BR-3 cells. Therefore, the GNR can have sedimented before the cells attached.

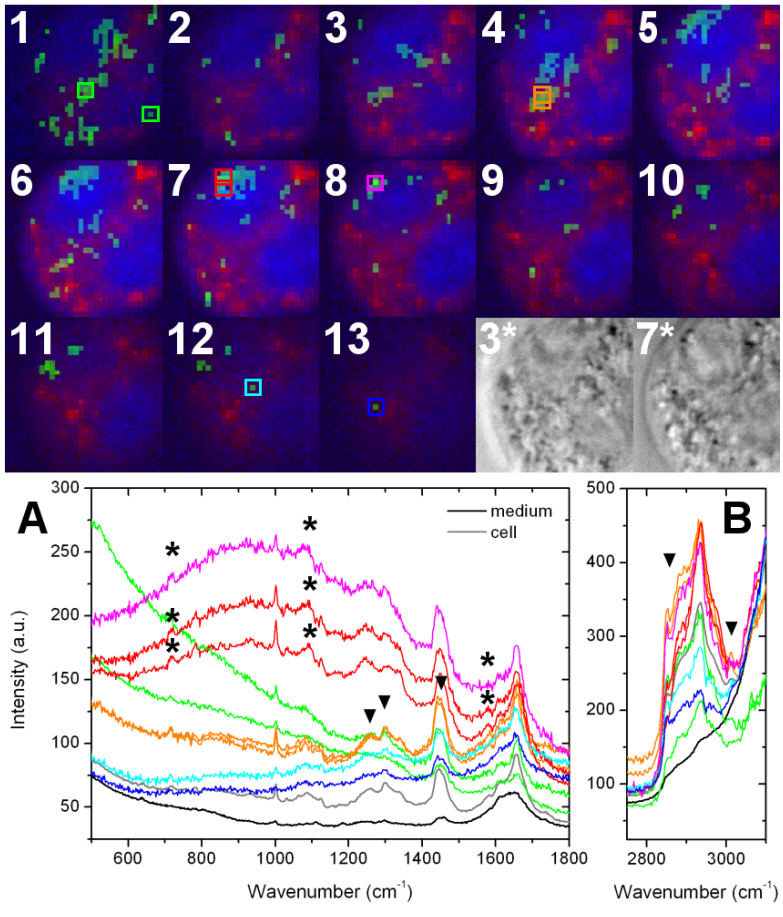

FIGURE 8.6 : Top image: z-stack of thirteen combined univariate Raman images of a PFA fixated GNR-incubated SK-BR-3 cell on a CaF_2 substrate (panes 1-13). Band integration was performed the 2850 cm^{-1} lipid band (2845 - 2855 cm^{-1}, see Figure C.1 in Appendix C), which is mapped in red, as well as over the 780 cm^{-1} DNA band (777 - 786 cm^{-1}, see Figure C.3 in Appendix C), which is false coloured in blue. The green overlay represents the GNR fluorescence that was detected between 600cm^{-1} and 2500 cm^{-1}. Image resolutions are 550×550×1500 nm for each voxel. Panes 3* and 7* show the brightfield images of the cell corresponding to Raman image panes 3 and 7. Bottom graph: Raman spectra of selected pixels from the top figure. Colours of the spectra correspond to the colours of the marking boxes in the top figure. The black and grey spectra represent the average Raman spectra of the surrounding PBS medium and the cell, respectively. Band positions marked with an asterisk indicate DNA contributions, the triangles mark lipid characteristic bands.

The Raman spectra corresponding to the selected pixels of Figure 8.6(1) are shown in Figure 8.6A and 8.6B in green. These green spectra show a broadband emission that is very similar to that of GNR646 in solution, as was shown in Figure 5.6 in Chapter 5. The GNR646 have a longitudinal plasmon absorption peak at 646 nm, whereas here PEG-GNR were used with a longitudinal plasmon absorption peak at 640 nm. The plasmon absorption profile of the PEG-GNR overlaps with the bulk gold emission in a similar extent to that of GNR646 (Figure 5.8A) and therefore a similar fluorescence emission is expected. In addition, the Raman contribution of the SK-BR-3 cell in the green spectra is limited, because half of the focus is in the substrate. Figure 8.6(1) thus confirms the presence of GNR between the CaF_2 and the cell.

The last image planes (Figure 8.6(12-13)) show fluorescence from outside the cell. These events are likely to occur at the cell membrane, since excess free GNR in the cell medium were removed during the rinsing and fixation steps. Because the emission originates from single pixel events, it is weak, as is illustrated by the corresponding spectra in Figure 8.6A and B (blue and cyan traces). The offset of blue and cyan spectra is higher than both the average PBS and the average cell spectra (black and grey traces), which indicates the presence of GNR. Corresponding to the green traces, the relative intensity of the Raman bands of the cell material on these curves are less intense than in the average cell spectrum, confirming that the pixels concerned are located outside the cell.

From the images acquired through the cell (Figure 8.6(2-12)), it becomes clear that there are two nuclei present that float well above the substrate, in contrast to the single nucleus situation that was depicted in Figures 8.4 and 8.5. The presence of two nuclei in a single cell is illustrated by the brightfield images that were acquired in the panes marked 3^* and 7^* (Figure 8.6, top image), corresponding to the Raman imaging positions 3 and 7. Judging by the intensity of the DNA signal (Figure C.3 in Appendix C), the cell may be in mitosis, which would also account for the location of the nuclei within the cell.

In the upper left corner of image planes 5-7 a similar group of green pixels occurs. The corresponding Raman spectra (red and magenta in Figure 8.6A and B) suggest the presence of clusters of GNR. The fluorescence emission band in these spectra has a consistent shape and there is little difference in the accompanying Raman features as well.

The spectral shape of the fluorescence emission differs from the emission that is expected from individual particles based on the $sp \rightarrow d$ transition mechanism discussed in Chapter 5. However, in Chapter 5 we also illustrated that GNR fluorescence varies with the dimensions of the particles (Figure 5.6).[147,148]. Therefore, GNR clusters can account for different shapes and intensities of the observed fluorescence responses, which were also shown in Chapter 4 (Figure 4.4D and 4.6C).

The results in Chapter 4 also suggested the uptake of GNR in lipid vesicles, as was indicated previously[81] and by others as well.[35,78,158,159] These results are supported by Figure 8.6(3-5), which shows a GNR cluster just left of the centre, marked with orange boxes in Figure 8.6(4). The surrounding red pixels indicate a lipid rich region. The Raman spectra corresponding to the selected pixels (orange boxed) from this region (Figure 8.6A and B)) confirm this by clearly showing lipid contributions at 1265, 1300, 1440, 2850 and 3015 cm^{-1}, which are characteristic for SK-BR-3 cells, as was established in Chapter 3 (Figure 3.5).

The Raman signatures that are present on the fluorescence background in the selected red and magenta spectra from Figure 8.6(7-8) show DNA contributions at 780, 1090 and 1575 cm^{-1} (marked with an asterisk in Figure 8.6A). This indicates the presence of GNR in the nuclei, as is also suggested by the RGB planes in the middle of the z-stack. The indicated presence of GNR in the nuclei of SK-BR-3 cells is remarkable, because unless specifically targeted,[296,297] nanoparticles have not yet been reported in the nuclei of cells. The presumed mitotic state of the cell may have contributed to this result, although also in regularly shaped SK-BR-3 cells DNA contributions could be recognized in colocalisation with GNR fluorescence emission (data not shown). This may be due to the tendency of internalized GNR to migrate toward the nucleus.[78]

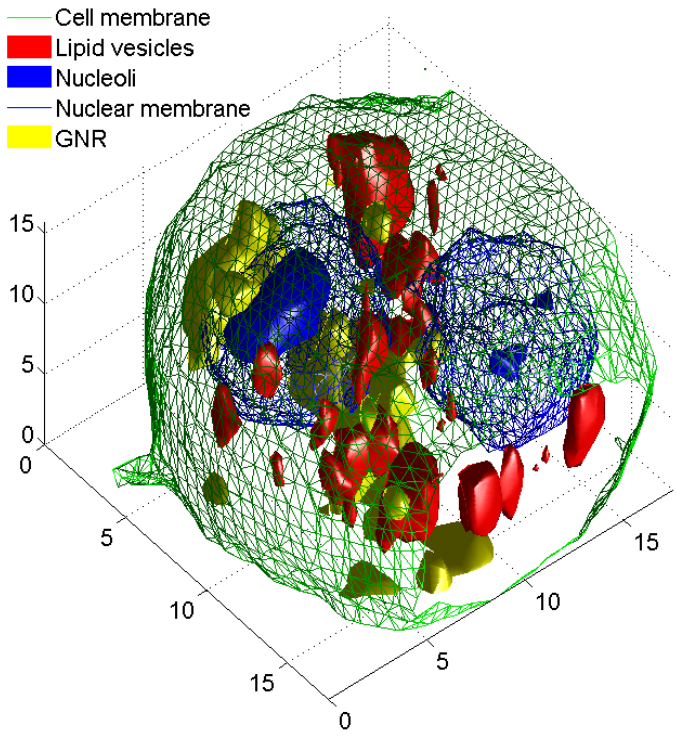

FIGURE 8.7 : 3D contour plot of the PFA fixated GNR-incubated SK-BR-3 cell on a CaF_2 substrate, also depicted in Figure 8.6. The blue raster marks the edges of the cell's nuclei, in which the solid blue marks the contents of the nucleoli. Lipid rich regions are indicated in red. The boundaries of the locations dominated by GNR fluorescence are depicted in yellow. The green mesh marks the borders of the cell, the cell membrane.

A more illustrative representation of the subcellular locations of the GNR can be obtained by constructing a 3D contour plot. Figure 8.7 shows a 3D contour plot of the GNR incubated SK-BR-3 cells from Figure 8.6, that was obtained by applying a threshold on the Raman intensity of DNA, lipids and protein. The

plot depicts the location of the nuclei with nucleoli in blue, lipid droplets in red and the cell membrane in green. The locations of the GNR are shown in yellow.

Figure 8.7 depicts several GNR rich regions in proximity to the nucleus, as well as an occasional GNR region close to a lipid vesicle. Although the spectral information from Figure 8.6A and B suggest otherwise, no unambigious correlations are present the contour plot, neither on the presence of GNR in the nuclei, nor within lipid vesicles.

Interpretation of the contour plot is not straightforward. The spatial resolution suggested by mesh structure does not represent the actual size of the voxels that were measured. In addition, the plotting routine smoothens the threshold edges. Moreover, one has to take into account that these thresholds were manually set. The threshold values were established well below the average Raman intensities, to ensure that the plotted contour does not exceed the margins of the actual structure. However, this may lead to underestimation of the actual structures.

Therefore, to be conclusive on the exact locations of the GNR with respect to both the cell nucleus and intracellular lipid vesicles, several improvements are recommended.

8.3.6 RECOMMENDATIONS

The current Raman data is acquired with an axial resolution that is four times larger than the lateral resolution. With an improved z resolution, more detail could be resolved in the 3D Raman microspectroscope. By increasing the number of lateral scanning steps from 32×32 to 64×64, a larger area can be mapped, with slightly larger detail.

However, the scanning range is limited by the serving area of the scanning mirror and the acquisition time per voxel is limited by the software that is controlling the scanning mirror. Therefore, increasing the number of scanning steps currently affects mainly the total scanning time. Reduction of the voxel acquisition time requires the setup to be adapted.

The 3D Raman data has a rather low SNR, because the applied laser doses were kept low, to prevent the samples from being damaged as well as to keep the measurement time short. As discussed above, shorter acquisition times are not possible within the current setup. Although the applied laser power may still be increased, care has to be taken not to exceed the threshold for particle reshaping which already can occur at very short laser pulses.[290,294,295]

In addition, the 3D contour plotting could be improved by optimizing the thresholding routine. Currently, thresholds are set manually and are rather arbitrary. Ideally, thresholding would be automated to obtain unbiased and comparable results.

8.4 Conclusions and outlook

Throughout this thesis, we have shown that Raman microspectroscopy provides a powerful technique in the characterization of gold nanorods (GNR, Chapter 5) and their interaction with breast cancer cells (Chapters 3 and 4). With Raman microspectroscopic imaging of live, unperturbed breast cancer cells, subtle difference in chemical compositions between different cell lines could be addressed

(Chapter 3). Additionally, the emission characteristics of GNR were determined, both in dispersion (Chapter 5) and within live SK-BR-3 breast cancer cells (Chapters 4 and 5). Raman data on GNR-cell systems showed location-dependent emission of the GNR coinciding with increased local lipid expression of the cells (Chapter 4). This suggests that the uptake of GNR by cells is followed by accumulation in intracellular lipid vesicles. To gain better insight in the spatial distribution of the GNR within cells and their local intracellular interactions, initial 3D Raman experiments were performed.

At first, the axial and lateral resolutions of the confocal Raman setup were determined by theoretical calculations as well as in an empirical way. The empirically obtained values were larger than the theoretical values. This difference was attributed to the optical responses of the components in the setup that were not included in the theoretical approximation, such as beam splitters and mirrors. Based on the resolution of the Raman setup, optimal imaging conditions were determined.

The nature of the samples set additional requirements, such as reduced imaging time and low laser powers. Especially, when live cells incorporating GNR are to be 3D-mapped with Raman microspectroscopy, the data acquisition will need to be optimized for speed. This limits the influence of the incoming light on the GNR properties and reduces ambiguity in cell signal interpretation introduced by cell movement.

Initial 3D Raman experiments were performed on fixated SK-BR-3 cells and allowed the assignment and localization of intracellular components with depth resolution. Lipids could easily be distinguished due to their characteristic, intense Raman signals and were merely concentrated in vesicles within the cells. Proteins appeared to be present in high concentrations in the nuclei of SK-BR-3 cells. Both observations are in agreement with the tumorigenic nature of the cell line.

Within fixated GNR-incubated SK-BR-3 cells, GNR fluorescence was detected at several intracellular locations. The fluorescence emission corresponds to the previous results in Chapters 4 and 5 and is in good agreement with the $sp \rightarrow d$ interband emission mechanism described in Chapter 5. Accordingly, as the emission profiles are dependent on GNR dimensions, GNR clusters within the cells show different emission profiles.

The fluorescence emission appeared in colocalization with Raman signatures of the cell nucleus as well as of lipid structures. This confirms the presumptions made in Chapter 4 with regard to particle uptake in lipid vesicles in the cell, but raises questions on the interaction of GNR with cell nuclei. Improvement of the axial resolution of the 3D Raman imaging system, that still is a factor 4 lower than the lateral resolution, may provide answers. This is especially important, because GNR exhibit fluorescence behaviour and are expected to have a large absorption cross-section (Chapter 5).

To gain deeper understanding of the intercellular mechanisms involved in the uptake of GNR and the corresponding GNR emission characteristics, live breast carcinoma cells incubated with GNR should be subjected to 3D Raman imaging. The distribution and fate of GNR in breast cancer cells can be monitored by studying the cells in different stages of Her2/neu receptor targeted GNR incubation. In addition, the interaction of GNR with different breast cancer cell lines should be investigated, because of a large variance in results in expected, due to the complexity of biological processing.

APPENDIX A

RAMAN THEORY

The polarizability is a measure of the extent to which incident radiation can displace the electrons in a molecule relative to its nuclei. According to the classical theory developed by Placzek [298] the polarizability is defined as the ratio of the induced dipole moment $\vec{P}$ of an atom to the field $\vec{E}$ that produces this dipole moment (Equation A.1):

$$\vec{P} = \alpha \vec{E} \tag{A.1}$$

With

$$\vec{E} = E_0 \cos(\omega_0 t) \tag{A.2}$$

Note that the polarizability α as defined above is second rank tensor. The polarizability depends on the precise vibration in the molecule, which is expressed by expanding each of the components $\alpha_{\rho\sigma}$ of the tensor α in a Taylor series with respect to the normal coordinates of the molecular vibrations.

Using an electrical harmonic approximation that only takes into account the first order derivative, for one normal mode of vibration Q_k with vibrational frequency ω_k, $\alpha_{\rho\sigma}$ can be rewritten as:

$$(\alpha_{\rho\sigma})_k = (\alpha_{\rho\sigma})_0 + \left(\alpha'_{\rho\sigma}\right)_k Q_k \tag{A.3}$$

With

$$\left(\alpha'_{\rho\sigma}\right)_k = \left(\frac{\delta\alpha_{\rho\sigma}}{\delta Q_k}\right)_0 \tag{A.4}$$

The electrical induced dipole moment $\vec{P}$ that includes the influence of the kth vibrational state of a molecule can be written as:

$$\vec{P} = P(\omega_1) + P(\omega_1 - \omega_k) + P(\omega_1 + \omega_k) \tag{A.5}$$

With

$$P(\omega_1) = \alpha_0 E_0 \cos(\omega_1 t) \tag{A.6}$$

And

$$P(\omega_1 \pm \omega_k) = \frac{1}{2}\alpha'_k Q_{k0} E_0 \cos(\omega_1 t \pm \omega_k t \pm \delta_k) \tag{A.7}$$

The first term in Equation A.5 relates to the Rayleigh scattering, scattered light of the original frequency. The second term represents the Stokes and anti-Stokes Raman scattering, respectively. The cosines in Equations A.5 and A.6 define the frequencies of the induced dipoles. Although the classical theory as described above gives correct predictions of the Raman scattered frequencies, the intensities of the bands can only be obtained using quantum mechanical theory, [299] using the differential cross section $d\sigma/d\Omega$ as [300]:

$$P = 4\pi N \left(\frac{d\sigma}{d\Omega}\right) P_0 \tag{A.8}$$

Where N is the number of molecules in the measuring volume,Ω the solid angle and P_0 the excitation power. Typical cross section values for non-resonant Raman scattering are 10^{-34} m^2/Sr.

APPENDIX B

GNP AGGREGATION

Additional details concerning the effects of ICG and bromide concentrations, as well as the amount of centrifugation steps on GNP aggregation are provided here.

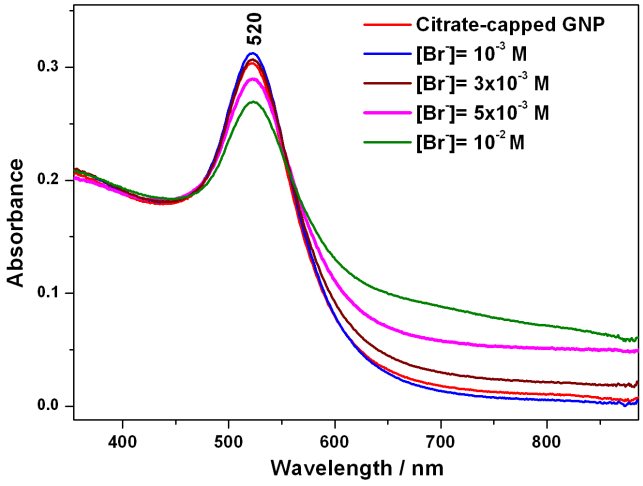

FIGURE B.1 : Absorption spectra of Citrate-capped GNP after the addition of different aliquots of KBr 0.5 M aqueous solution (the final bromide concentration in the colloidal suspension is reported in the figure). The extinction spectra of the GNP were monitored over 10 minutes after the bromide addition (experimental time scale). The results indicate that a final concentration of Br in the colloidal suspension of 10^{-3} M (2 μL aliquot of the Br stock solution), corresponds to the highest halide concentration which does not produce significant GNP aggregation.

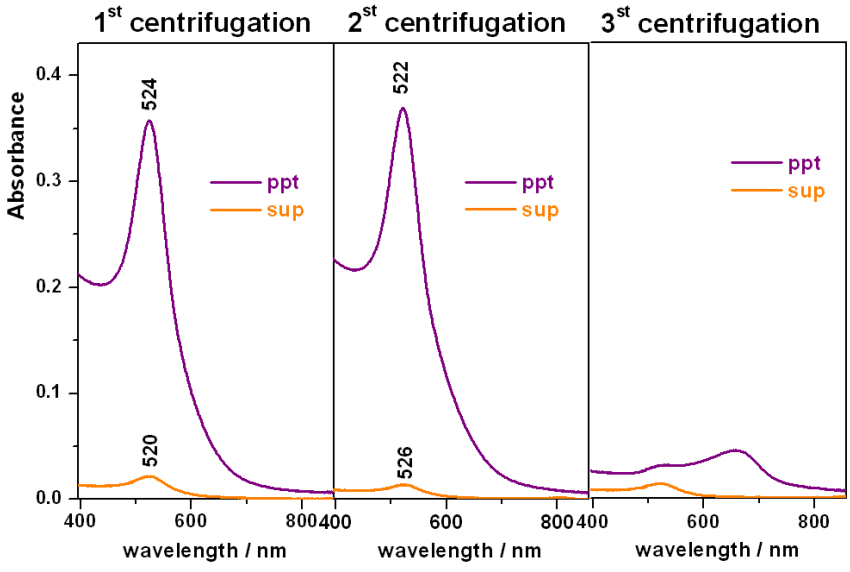

FIGURE B.2 : Extinction spectra of redispersed precipitate and supernatant of CTAB-capped GNP (CTA/Br/GNP) after 3 steps of centrifugation: (1) 12000 rpm for 30 minutes, (2) 12000 rpm for 30 minutes and (3) 12000 rpm for 20 minutes. The first two centrifugations do not produce significant GNP aggregation, whereas the third centrifugation step causes a profound aggregation, as is indicated by the stability of the plasmon band.

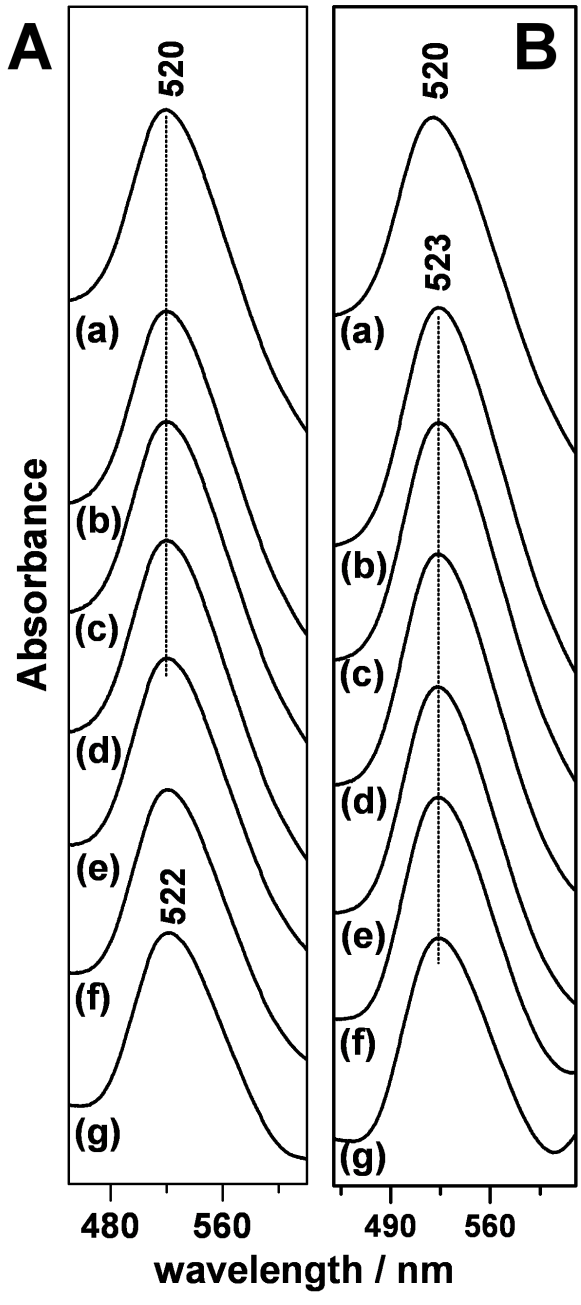

FIGURE B.3 : Detail of the low wavelength region of the ICG absorption spectra in [A] Br/GNP and [B] Br/Ag/GNP suspension at increasing dye concentration: (a) 0, (b) 7×10^{-6} M, (c) 1×10^{-5} M, (d) 1.5×10^{-5} M, (e) 2×10^{-5} M, (f) 3×10^{-5} M and (g) 5×10^{-5} M. The plasmon absorption band appearing at ∼520 nm undergoes a slight red-shift only for very high ICG concentration (5×10^{-5} M). This shift is attributed to the change in refractive index resulting from the large dye adsorption on the gold surface and indicates the absence of GNP aggregation.

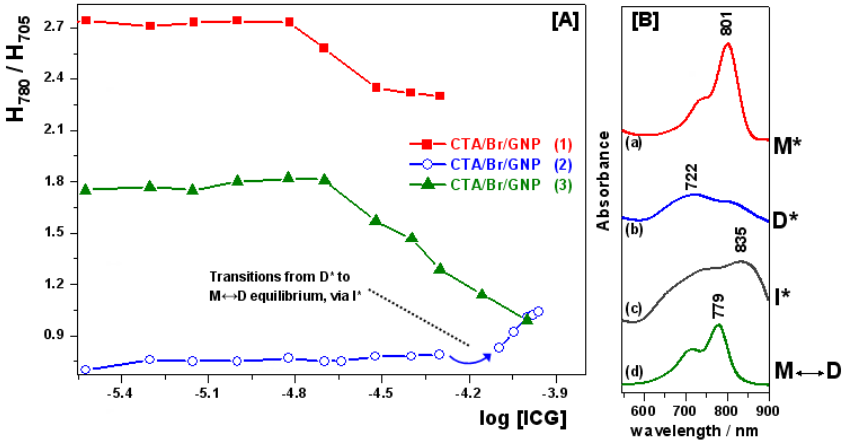

FIGURE B.4 : A) Experimental values of the spectral parameter H_{780}/H_{705} for ICG in CTA/Br/NPs and CTA/Br/Ag/NPs colloids after (1), (2) and (3) centrifugation steps at different dye concentration (logarithmic scale). B) Absorption spectra of ICG 3×10^{-5} M in (a) CTA/Br/GNPs (1), (b) CTA/Br/GNPs (2) and (d) CTA/Br/GNPs (3) colloids. (c) Absorption spectrum of ICG 7.8×10^{-5} M in CTA/Br/GNPs (2) colloid.

The results reported in Figure B.4 suggest that the surfactant concentration in solution strongly affects the ICG state. Based on these findings, we capped citrate-gold NPs with a large excess of CTAB ($\gg$ cmc) and performed several centrifugation steps in order to test the ICG adsorption at different surfactant concentrations, both in the bulk and at the metal-liquid interface (CTAB constantly exchanges from the bilayer at the metal-solvent interface to the solution). However, we cannot determine the exact surfactant concentration after each centrifugation.

Figure B.3 shows that the first two centrifugation steps do not produce significant GNP aggregation, whereas the third one causes an irreversible assembly of metal nanoparticle into large cluster, also observed by the deposition of large amount of GNP at the bottom of the vial regardless of the time of centrifugation. This suggests a decrease of CTAB concentration at the metal-liquid interface induces the disruption of the surfactant double layer around the GNP leading to their irreversible aggregation. We labelled these CTAB-capped GNP suspensions as CTA/Br/GNP (1), CTA/Br/GNP (2) and CTA/Br/GNP (3), where the number into brackets refers to the centrifugation steps carried out on the colloidal system.

Absorption data (Figure B.4) indicates that the dye exists as $M*$ in the CTA/Br/GNP (1), and as highly stabilized dimer $D*$ in CTA/Br/ GNP (2). As previously observed for ICG in CTAB 50 μM salt solution (Figure 7.4), a transition from $D* \rightarrow I* \rightarrow M/D$ occurs when increasing the dye concentration. In the CTA/Br/ GNP (3) system, ICG molecules exist in M and D forms at all dye concentrations but, again, the position of the $M \leftrightarrow D$ equilibrium is largely affected by the remaining surfactant molecules in the bulk solution. By

comparison to the data illustrated in Figure 7.4, these results suggest that we progressively decrease the unbound CTAB amount in CTA/Br/ GNP suspensions from surfactant concentration above cmc, to ∼1 order of magnitude smaller and, finally, to ∼2 order of magnitude smaller after each step of centrifugations, respectively. On the whole, the ICG behaviour in CTAB solution (Figure 7.4) and in CTA/Br/ GNP suspensions (Figure B.4) is very similar. This seems to indicate that the optical properties of ICG molecules are largely determined by the unbound surfactant molecules in the bulk solution rather than by the interaction with the metal surface, even though it is not possible to separate these two effects.

APPENDIX C

3D INTENSITY MAPS

This appendix contains intensity images of lipids, DNA, proteins and GNR in a fixed SK-BR-3 cell in PBS. Before fixation, the cell was incubated with $\sim 1 \times 10^6$ GNR. Fixation was carried out with 1% paraformaldehyde (PFA) in Phosphate Buffered Saline (PBS) for at least 20 minutes at room temperature. The sample was rinsed with PBS before data acquisition. Raman data was acquired as a $32 \times 32 \times 13$ pixel hyperspectral matrix, covering a region of $17.5 \times 17.5 \times 18$ μm, with 70 mW under the objective ($63\times/1.0$ NA water immersion) and a pixel dwell time of 100 ms.

For the overlay in the top image of Figure 8.6, the GNR intensity image was thresholded to enhance the contrast and better distinguish between GNR fluorescence emission and intense Raman signals from e.g. lipids (Chapter 2) or from autofluorescence contributions of the cells.[210]

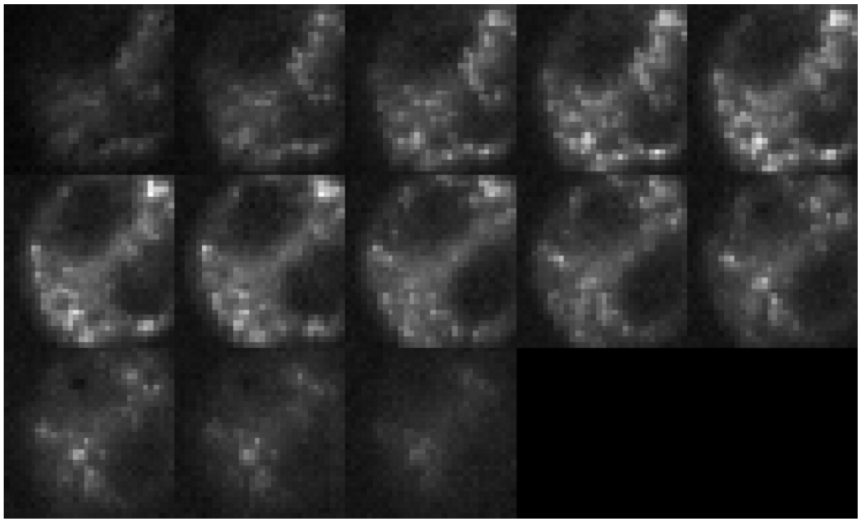

FIGURE C.1 : Intensity image of lipids in a fixed SK-BR-3 cell that was incubated with GNR. Intensity was determined by integrating over the lipid characteristic CH-vibrations at 2850 cm^{-1} in the interval 2845-2855 cm^{-1}.

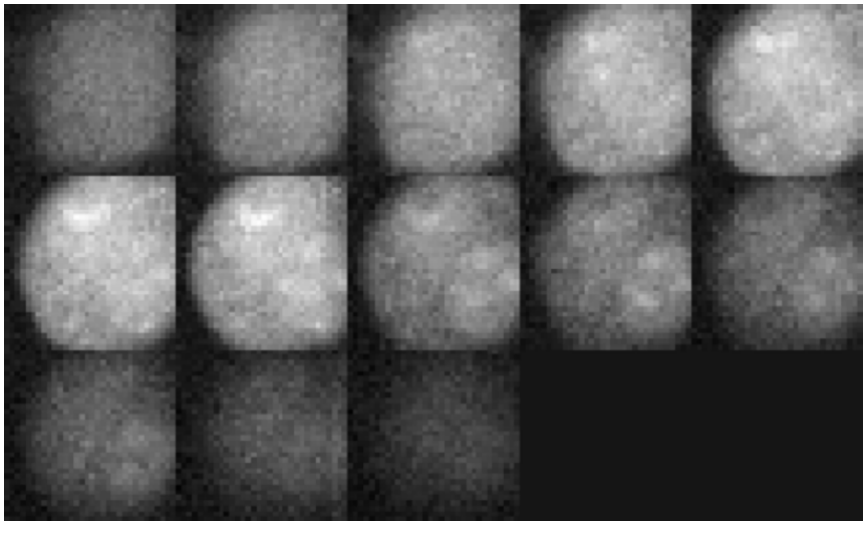

FIGURE C.2 : Intensity image of proteins in a fixed SK-BR-3 cell that was incubated with GNR. Intensity was determined by integrating over the phenylalanine peak at ∼1001 cm^{-1} in the interval 1000-1003cm^{-1}.

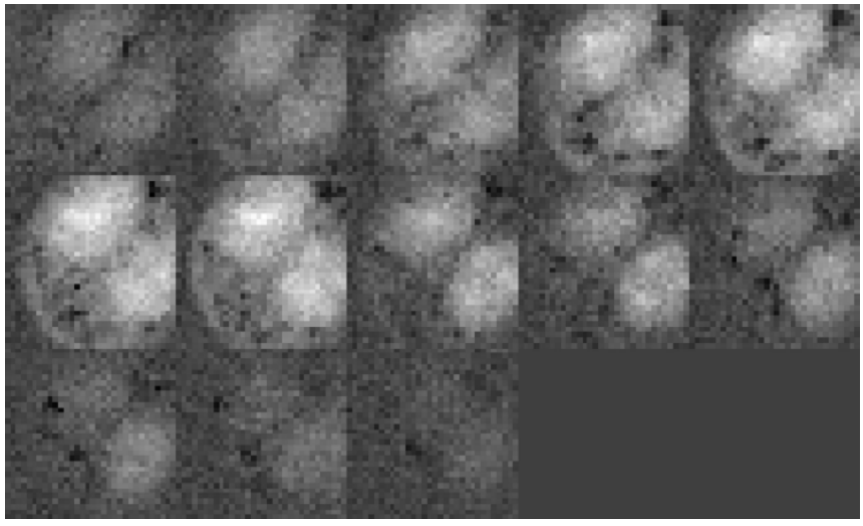

FIGURE C.3 : Intensity image of DNA in a fixed SK-BR-3 cell that was incubated with GNR. Intensity was determined by integrating over the DNA band at 780 cm^{-1} in the interval 777-786cm^{-1}.

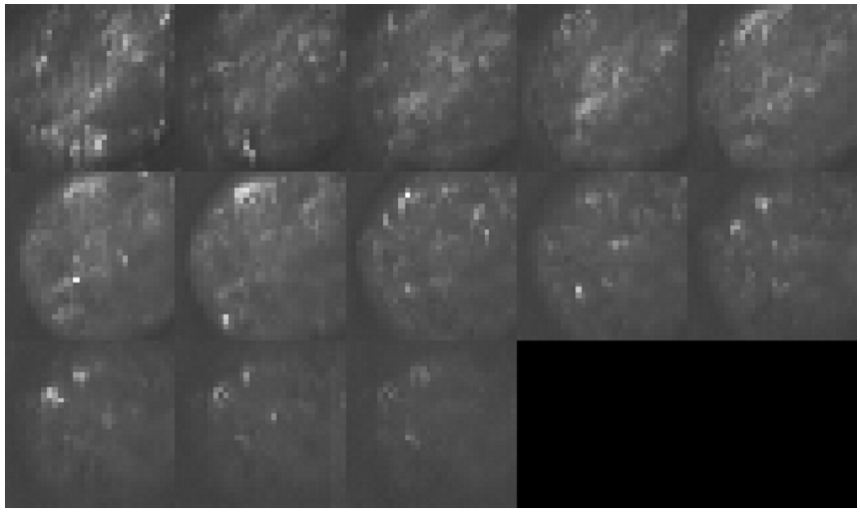

FIGURE C.4 : Intensity image of GNR fluorescence in a fixed SK-BR-3 cell that was incubated with GNR. Intensity was determined by integrating over the broadband emissions that were observed in the region from 600cm^{-1} to 2500 cm^{-1}.

Bibliography

[1] C. F. Shaw, "Gold-based therapeutic agents," *Chemical Reviews*, vol. 99, no. 9, pp. 2589–2600, 1999.

[2] K. Kneipp, H. Kneipp, and J. Kneipp, "Surface-enhanced raman scattering in local optical fields of silver and gold nanoaggregatess - from single-molecule raman spectroscopy to ultrasensitive probing in live cells," *Accounts of Chemical Research*, vol. 39, no. 7, pp. 443–450, 2006.

[3] S. M. Nie and S. R. Emory, "Probing single molecules and single nanoparticles by surface-enhanced raman scattering," *Science*, vol. 275, no. 5303, pp. 1102–1106, 1997.

[4] K. Kneipp, H. Kneipp, I. Itzkan, R. R. Dasari, and M. S. Feld, "Surface-enhanced raman scattering and biophysics," *Journal of Physics-Condensed Matter*, vol. 14, no. 18, pp. R597–R624, 2002.

[5] M. A. El-Sayed, "Some interesting properties of metals confined in time and nanometer space of different shapes," *Accounts of Chemical Research*, vol. 34, no. 4, pp. 257–264, 2001.

[6] G. C. Papavassiliou, "Optical-properties of small inorganic and organic metal particles," *Progress in Solid State Chemistry*, vol. 12, no. 3-4, pp. 185–271, 1979.

[7] C. Ungureanu, A. Amelink, R. G. Rayavarapu, H. J. C. M. Sterenborg, S. Manohar, and T. G. van Leeuwen, "Differential pathlength spectroscopy for the quantitation of optical properties of gold nanoparticles," *Acs Nano*, vol. 4, no. 7, pp. 4081–4089, 2010.

[8] B. Khlebtsov, V. Zharov, A. Melnikov, V. Tuchin, and N. Khlebtsov, "Optical amplification of photothermal therapy with gold nanoparticles and nanoclusters," *Nanotechnology*, vol. 17, no. 20, pp. 5167–5179, 2006.

[9] C. Sonnichsen, T. Franzl, T. Wilk, G. von Plessen, J. Feldmann, O. Wilson, and P. Mulvaney, "Drastic reduction of plasmon damping in gold nanorods," *Physical Review Letters*, vol. 88, no. 7, pp. –, 2002.

[10] R. D. Averitt, S. L. Westcott, and N. J. Halas, "Ultrafast optical properties of gold nanoshells," *Journal of the Optical Society of America B-Optical Physics*, vol. 16, no. 10, pp. 1814–1823, 1999.

[11] R. D. Averitt, S. L. Westcott, and N. J. Halas, "Linear optical properties of gold nanoshells," *Journal of the Optical Society of America B-Optical Physics*, vol. 16, no. 10, pp. 1824–1832, 1999.

[12] S. J. Oldenburg, R. D. Averitt, S. L. Westcott, and N. J. Halas, "Nanoengineering of optical resonances," *Chemical Physics Letters*, vol. 288, no. 2-4, pp. 243–247, 1998.

[13] J. Turkevich, G. Garton, and P. C. Stevenson, "The color of colloidal gold," *Journal of Colloid Science*, vol. 9, no. 6, pp. S26–S35, 1954.

[14] G. Rayavarapu, W. Petersen, C. Ungureanu, J. Post, T. v. Leeuwen, and S. Manohar, "Synthesis and bioconjugation of gold nanoparticles as potential molecular probes for light-based imaging techniques," *International Journal of Biomedical Imaging*, vol. 2007, p. 10, 2007.

[15] A. Agarwal, S. W. Huang, M. O'Donnell, K. C. Day, M. Day, N. Kotov, and S. Ashkenazi, "Targeted gold nanorod contrast agent for prostate cancer detection by photoacoustic imaging," *Journal of Applied Physics*, vol. 102, no. 6, pp. –, 2007.

[16] H. Ding, K. T. Yong, I. Roy, H. E. Pudavar, W. C. Law, E. J. Bergey, and P. N. Prasad, "Gold nanorods coated with multilayer polyelectrolyte as contrast agents for multimodal imaging," *Journal of Physical Chemistry C*, vol. 111, no. 34, pp. 12552–12557, 2007.

[17] N. J. Durr, T. Larson, D. K. Smith, B. A. Korgel, K. Sokolov, and A. Ben-Yakar, "Two-photon luminescence imaging of cancer cells using molecularly targeted gold nanorods," *Nano Letters*, vol. 7, no. 4, pp. 941–945, 2007.

[18] X. H. Huang, I. H. El-Sayed, W. Qian, and M. A. El-Sayed, "Cancer cell imaging and photothermal therapy in the near-infrared region by using gold nanorods," *Journal of the American Chemical Society*, vol. 128, no. 6, pp. 2115–2120, 2006.

[19] X. H. Huang, P. K. Jain, I. H. El-Sayed, and M. A. El-Sayed, "Plasmonic photothermal therapy (pptt) using gold nanoparticles," *Lasers in Medical Science*, vol. 23, no. 3, pp. 217–228, 2008.

[20] N. R. Jana, L. Gearheart, and C. J. Murphy, "Seed-mediated growth approach for shape-controlled synthesis of spheroidal and rod-like gold nanoparticles using a surfactant template," *Advanced Materials*, vol. 13, no. 18, pp. 1389–1393, 2001.

[21] S. Link and M. A. El-Sayed, "Spectral properties and relaxation dynamics of surface plasmon electronic oscillations in gold and silver nanodots and nanorods," *Journal of Physical Chemistry B*, vol. 103, no. 40, pp. 8410–8426, 1999.

[22] B. Nikoobakht and M. A. El-Sayed, "Preparation and growth mechanism of gold nanorods (nrs) using seed-mediated growth method," *Chemistry of Materials*, vol. 15, no. 10, pp. 1957–1962, 2003.

[23] K. T. Yong, Y. Sahoo, M. T. Swihart, P. M. Schneeberger, and P. N. Prasad, "Templated synthesis of gold nanorods (nrs): The effects of cosurfactants and electrolytes on the shape and optical properties," *Topics in Catalysis*, vol. 47, no. 1-2, pp. 49–60, 2008.

[24] P. R. Evans, W. R. Hendren, R. Atkinson, and R. J. Pollard, "Optical transmission measurements of silver, silver-gold alloy and silver-gold segmented nanorods in thin film alumina," *Nanotechnology*, vol. 19, no. 46, pp. –, 2008.

[25] K. Kneipp, H. Kneipp, I. Itzkan, R. R. Dasari, and M. S. Feld, "Surface-enhanced non-linear raman scattering at the single-molecule level," *Chemical Physics*, vol. 247, no. 1, pp. 155–162, 1999.

[26] K. Kneipp, H. Kneipp, R. Manoharan, E. B. Hanlon, I. Itzkan, R. R. Dasari, and M. S. Feld, "Extremely large enhancement factors in surface-enhanced raman scattering for molecules on colloidal gold clusters," *Applied Spectroscopy*, vol. 52, no. 12, pp. 1493–1497, 1998.

[27] K. Kneipp, H. Kneipp, R. Manoharan, I. Itzkan, R. R. Dasari, and M. S. Feld, "Near-infrared surface-enhanced raman scattering can detect single molecules and observe 'hot' vibrational transitions," *Journal of Raman Spectroscopy*, vol. 29, no. 8, pp. 743–747, 1998.

[28] D. I. Gittins and F. Caruso, "Spontaneous phase transfer of nanoparticulate metals from organic to aqueous media," *Angewandte Chemie-International Edition*, vol. 40, no. 16, pp. 3001–3004, 2001.

[29] J. S. Bradley, B. Tesche, W. Busser, M. Masse, and R. T. Reetz, "Surface spectroscopic study of the stabilization mechanism for shape-selectively synthesized nanostructured transition metal colloids," *Journal of the American Chemical Society*, vol. 122, no. 19, pp. 4631–4636, 2000.

[30] D. E. Cliffel, F. P. Zamborini, S. M. Gross, and R. W. Murray, "Mercaptoammonium-monolayer-protected, water-soluble gold, silver, and palladium clusters," *Langmuir*, vol. 16, no. 25, pp. 9699–9702, 2000.

[31] T. S. Ahmadi, Z. L. Wang, T. C. Green, A. Henglein, and M. A. ElSayed, "Shape-controlled synthesis of colloidal platinum nanoparticles," *Science*, vol. 272, no. 5270, pp. 1924–1926, 1996.

[32] S. Lee, S. Kim, J. Choo, S. Y. Shin, Y. H. Lee, H. Y. Choi, S. H. Ha, K. H. Kang, and C. H. Oh, "Biological imaging of hek293 cells expressing plc gamma 1 using surface-enhanced raman microscopy," *Analytical Chemistry*, vol. 79, no. 3, pp. 916–922, 2007.

[33] M. Michaelis, A. Henglein, and P. Mulvaney, "Composite pd-ag particles in aqueous-solution," *Journal of Physical Chemistry*, vol. 98, no. 24, pp. 6212–6215, 1994.

[34] J. M. Bergen, H. A. Von Recum, T. T. Goodman, A. P. Massey, and S. H. Pun, "Gold nanoparticles as a versatile platform for optimizing physicochemical parameters for targeted drug delivery," *Macromolecular Bioscience*, vol. 6, no. 7, pp. 506–516, 2006.

[35] B. D. Chithrani, A. A. Ghazani, and W. C. W. Chan, "Determining the size and shape dependence of gold nanoparticle uptake into mammalian cells," *Nano Letters*, vol. 6, no. 4, pp. 662–668, 2006.

[36] J. M. de la Fuente, C. C. Berry, M. O. Riehle, and A. S. G. Curtis, "Nanoparticle targeting at cells," *Langmuir*, vol. 22, no. 7, pp. 3286–3293, 2006.

[37] E. E. Connor, J. Mwamuka, A. Gole, C. J. Murphy, and M. D. Wyatt, "Gold nanoparticles are taken up by human cells but do not cause acute cytotoxicity," *Small*, vol. 1, no. 3, pp. 325–327, 2005.

[38] M. Eghtedari, A. Oraevsky, J. A. Copland, N. A. Kotov, A. Conjusteau, and M. Motamedi, "High sensitivity of in vivo detection of gold nanorods using a laser optoacoustic imaging system," *Nano Letters*, vol. 7, no. 7, pp. 1914–1918, 2007.

[39] C. Eliasson, A. Loren, J. Engelbrektsson, M. Josefson, J. Abrahamsson, and K. Abrahamsson, "Surface-enhanced raman scattering imaging of single living lymphocytes with multivariate evaluation," *Spectrochimica Acta Part a-Molecular and Biomolecular Spectroscopy*, vol. 61, no. 4, pp. 755–760, 2005.

[40] T. S. Hauck, A. A. Ghazani, and W. C. W. Chan, "Assessing the effect of surface chemistry on gold nanorod uptake, toxicity, and gene expression in mammalian cells," *Small*, vol. 4, no. 1, pp. 153–159, 2008.

[41] J. F. Hillyer and R. M. Albrecht, "Gastrointestinal persorption and tissue distribution of differently sized colloidal gold nanoparticles," *Journal of Pharmaceutical Sciences*, vol. 90, no. 12, pp. 1927–1936, 2001.

[42] S. Keren, C. Zavaleta, Z. Cheng, A. de la Zerda, O. Gheysens, and S. S. Gambhir, "Noninvasive molecular imaging of small living subjects using raman spectroscopy," *Proceedings of the National Academy of Sciences of the United States of America*, vol. 105, no. 15, pp. 5844–5849, 2008.

[43] Y. L. Liu, M. K. Shipton, J. Ryan, E. D. Kaufman, S. Franzen, and D. L. Feldheim, "Synthesis, stability, and cellular internalization of gold nanoparticles containing mixed peptide-poly(ethylene glycol) monolayers," *Analytical Chemistry*, vol. 79, no. 6, pp. 2221–2229, 2007.

[44] T. Niidome, M. Yamagata, Y. Okamoto, Y. Akiyama, H. Takahashi, T. Kawano, Y. Katayama, and Y. Niidome, "Peg-modified gold nanorods with a stealth character for in vivo applications," *Journal of Controlled Release*, vol. 114, no. 3, pp. 343–347, 2006.

[45] A. K. Oyelere, P. C. Chen, X. H. Huang, I. H. El-Sayed, and M. A. El-Sayed, "Peptide-conjugated gold nanorods for nuclear targeting," *Bioconjugate Chemistry*, vol. 18, no. 5, pp. 1490–1497, 2007.

[46] G. F. Paciotti, D. G. I. Kingston, and L. Tamarkin, "Colloidal gold nanoparticles: A novel nanoparticle platform for developing multifunctional tumor-targeted drug delivery vectors," *Drug Development Research*, vol. 67, no. 1, pp. 47–54, 2006.

[47] N. Pernodet, X. H. Fang, Y. Sun, A. Bakhtina, A. Ramakrishnan, J. Sokolov, A. Ulman, and M. Rafailovich, "Adverse effects of citrate/gold nanoparticles on human dermal fibroblasts," *Small*, vol. 2, no. 6, pp. 766–773, 2006.

[48] X. M. Qian, X. H. Peng, D. O. Ansari, Q. Yin-Goen, G. Z. Chen, D. M. Shin, L. Yang, A. N. Young, M. D. Wang, and S. M. Nie, "In vivo tumor targeting and spectroscopic detection with surface-enhanced raman nanoparticle tags," *Nature Biotechnology*, vol. 26, no. 1, pp. 83–90, 2008.

[49] J. M. Stern, J. Stanfield, Y. Lotan, S. Park, J. T. Hsieh, and J. A. Cadeddu, "Efficacy of laser-activated gold nanoshells in ablating prostate cancer cells in vitro," *Journal of Endourology*, vol. 21, no. 8, pp. 939–943, 2007.

[50] H. Takahashi, Y. Niidome, T. Niidome, K. Kaneko, H. Kawasaki, and S. Yamada, "Modification of gold nanorods using phospatidylcholine to reduce cytotoxicity," *Langmuir*, vol. 22, no. 1, pp. 2–5, 2006.

[51] A. G. Tkachenko, H. Xie, D. Coleman, W. Glomm, J. Ryan, M. F. Anderson, S. Franzen, and D. L. Feldheim, "Multifunctional gold nanoparticle-peptide complexes for nuclear targeting," *Journal of the American Chemical Society*, vol. 125, no. 16, pp. 4700–4701, 2003.

[52] A. G. Tkachenko, H. Xie, Y. L. Liu, D. Coleman, J. Ryan, W. R. Glomm, M. K. Shipton, S. Franzen, and D. L. Feldheim, "Cellular trajectories of peptide-modified gold particle complexes: Comparison of nuclear localization signals and peptide transduction domains," *Bioconjugate Chemistry*, vol. 15, no. 3, pp. 482–490, 2004.

[53] C. X. Yu, L. Varghese, and J. Irudayaraj, "Surface modification of cetyltrimethylammonium bromide-capped gold nanorods to make molecular probes," *Langmuir*, vol. 23, no. 17, pp. 9114–9119, 2007.

[54] C. C. Chen, Y. P. Lin, C. W. Wang, H. C. Tzeng, C. H. Wu, Y. C. Chen, C. P. Chen, L. C. Chen, and Y. C. Wu, "Dna-gold nanorod conjugates for remote control of localized gene expression by near infrared irradiation," *Journal of the American Chemical Society*, vol. 128, no. 11, pp. 3709–3715, 2006.

[55] J. Chen, F. Saeki, B. J. Wiley, H. Cang, M. J. Cobb, Z. Y. Li, L. Au, H. Zhang, M. B. Kimmey, X. D. Li, and Y. Xia, "Gold nanocages: Bioconjugation and their potential use as optical imaging contrast agents," *Nano Letters*, vol. 5, no. 3, pp. 473–477, 2005.

[56] J. Y. Chen, B. Wiley, Z. Y. Li, D. Campbell, F. Saeki, H. Cang, L. Au, J. Lee, X. D. Li, and Y. N. Xia, "Gold nanocages: Engineering their structure for biomedical applications," *Advanced Materials*, vol. 17, no. 18, pp. 2255–2261, 2005.

[57] H. Ditrich and H. Splechtna, "Processing of colloidal gold particles in the glomerular mesangium and macula densa of the duck kidney," *Tissue & Cell*, vol. 20, no. 6, pp. 891–898, 1988.

[58] C. M. Goodman, C. D. McCusker, T. Yilmaz, and V. M. Rotello, "Toxicity of gold nanoparticles functionalized with cationic and anionic side chains," *Bioconjugate Chemistry*, vol. 15, no. 4, pp. 897–900, 2004.

[59] J. F. Hainfeld, D. N. Slatkin, and H. M. Smilowitz, "The use of gold nanoparticles to enhance radiotherapy in mice," *Physics in Medicine and Biology*, vol. 49, no. 18, pp. N309–N315, 2004.

[60] R. Hong, G. Han, J. M. Fernandez, B. J. Kim, N. S. Forbes, and V. M. Rotello, "Glutathione-mediated delivery and release using monolayer protected nanoparticle carriers," *Journal of the American Chemical Society*, vol. 128, no. 4, pp. 1078–1079, 2006.

[61] X. H. Huang, I. H. El-Sayed, W. Qian, and M. A. El-Sayed, "Cancer cells assemble and align gold nanorods conjugated to antibodies to produce highly enhanced, sharp, and polarized surface raman spectra: A potential cancer diagnostic marker," *Nano Letters*, vol. 7, no. 6, pp. 1591–1597, 2007.

[62] J. Kneipp, H. Kneipp, W. L. Rice, and K. Kneipp, "Optical probes for biological applications based on surface-enhanced raman scattering from indocyanine green on gold nanoparticles," *Analytical Chemistry*, vol. 77, no. 8, pp. 2381–2385, 2005.

[63] M. C. Daniel and D. Astruc, "Gold nanoparticles: Assembly, supramolecular chemistry, quantum-size-related properties, and applications toward biology, catalysis, and nanotechnology," *Chemical Reviews*, vol. 104, no. 1, pp. 293–346, 2004.

[64] R. C. Johnson, J. T. Li, J. T. Hupp, and G. C. Schatz, "Hyper-rayleigh scattering studies of silver, copper, and platinum nanoparticle suspensions," *Chemical Physics Letters*, vol. 356, no. 5-6, pp. 534–540, 2002.

[65] Z. Liu, W. B. Cai, L. N. He, N. Nakayama, K. Chen, X. M. Sun, X. Y. Chen, and H. J. Dai, "In vivo biodistribution and highly efficient tumour targeting of carbon nanotubes in mice," *Nature Nanotechnology*, vol. 2, no. 1, pp. 47–52, 2007.

[66] M. Brust, M. Walker, D. Bethell, D. J. Schiffrin, and R. Whyman, "Synthesis of thiol-derivatized gold nanoparticles in a 2-phase liquid-liquid system," *Journal of the Chemical Society-Chemical Communications*, no. 7, pp. 801–802, 1994.

[67] N. R. Jana, L. Gearheart, and C. J. Murphy, "Wet chemical synthesis of high aspect ratio cylindrical gold nanorods," *Journal of Physical Chemistry B*, vol. 105, no. 19, pp. 4065–4067, 2001.

[68] J. X. Gao, C. M. Bender, and C. J. Murphy, "Dependence of the gold nanorod aspect ratio on the nature of the directing surfactant in aqueous solution," *Langmuir*, vol. 19, no. 21, pp. 9065–9070, 2003.

[69] R. G. Rayavarapu, C. Ungureanu, P. Krystek, T. G. van Leeuwen, and S. Manohar, "Iodide impurities in hexadecyltrimethyl ammonium bromide (ctab) products: Lot-lot variations and influence on gold nanorod synthesis," *Langmuir*, vol. 26, no. 7, pp. 5050–5055, 2010.

[70] A. S. Barnard and L. A. Curtiss, "Modeling the preferred shape, orientation and aspect ratio of gold nanorods," *Journal of Materials Chemistry*, vol. 17, no. 31, pp. 3315–3323, 2007.

[71] N. W. S. Kam, Z. A. Liu, and H. J. Dai, "Carbon nanotubes as intracellular transporters for proteins and dna: An investigation of the uptake mechanism and pathway," *Angewandte Chemie-International Edition*, vol. 45, no. 4, pp. 577–581, 2006.

[72] D. O. Lapotko, E. Lukianova, and A. A. Oraevsky, "Selective laser nano-thermolysis of human leukemia cells with microbubbles generated around clusters of gold nanoparticles," *Lasers in Surgery and Medicine*, vol. 38, no. 6, pp. 631–642, 2006.

[73] X. H. Huang, P. K. Jain, I. H. El-Sayed, and M. A. El-Sayed, "Gold nanoparticles: interesting optical properties and recent applications in cancer diagnostic and therapy," *Nanomedicine*, vol. 2, no. 5, pp. 681–693, 2007.

[74] K. H. Lee, S. J. Chen, J. Y. Jeng, Y. C. Cheng, J. T. Shiea, and H. T. Chang, "Fluorescence and interactions with thiol compounds of nile red-adsorbed gold nanoparticles," *Journal of Colloid and Interface Science*, vol. 307, no. 2, pp. 340–348, 2007.

[75] K. C. Grabar, R. G. Freeman, M. B. Hommer, and M. J. Natan, "Preparation and characterization of au colloid monolayers," *Analytical Chemistry*, vol. 67, no. 4, pp. 735–743, 1995.

[76] T. H. Chung, S. H. Wu, M. Yao, C. W. Lu, Y. S. Lin, Y. Hung, C. Y. Mou, Y. C. Chen, and D. M. Huang, "The effect of surface charge on the uptake and biological function of mesoporous silica nanoparticles 3t3-l1 cells and human mesenchymal stem cells," *Biomaterials*, vol. 28, no. 19, pp. 2959–2966, 2007.

[77] A. De La Zerda, C. Zavaleta, S. Keren, S. Vaithilingam, S. Bodapati, Z. Liu, J. Levi, B. R. Smith, T. J. Ma, O. Oralkan, Z. Cheng, X. Y. Chen, H. J. Dai, B. T. Khuri-Yakub, and S. S. Gambhir, "Carbon nanotubes as photoacoustic molecular imaging agents in living mice," *Nature Nanotechnology*, vol. 3, no. 9, pp. 557–562, 2008.

[78] T. B. Huff, M. N. Hansen, Y. Zhao, J. X. Cheng, and A. Wei, "Controlling the cellular uptake of gold nanorods," *Langmuir*, vol. 23, no. 4, pp. 1596–1599, 2007.

[79] W. D. James, L. R. Hirsch, J. L. West, P. D. O'Neal, and J. D. Payne, "Application of inaa to the build-up and clearance of gold nanoshells in clinical studies in mice," *Journal of Radioanalytical and Nuclear Chemistry*, vol. 271, no. 2, pp. 455–459, 2007.

[80] S. M. Moghimi, A. C. Hunter, and J. C. Murray, "Long-circulating and target-specific nanoparticles: Theory to practice," *Pharmacological Reviews*, vol. 53, no. 2, pp. 283–318, 2001.

[81] R. G. Rayavarapu, W. Petersen, L. Hartsuiker, P. Chin, H. Janssen, F. W. B. van Leeuwen, C. Otto, S. Manohar, and T. G. van Leeuwen, "In vitro toxicity studies of polymer-coated gold nanorods," *Nanotechnology*, vol. 21, no. 14, pp. 1–10, 2010.

[82] K. Kim, S. W. Huang, S. Ashkenazi, M. O'Donnell, A. Agarwal, N. A. Kotov, M. F. Denny, and M. J. Kaplan, "Photoacoustic imaging of early inflammatory response using gold nanorods," *Applied Physics Letters*, vol. 90, no. 22, pp. –, 2007.

[83] D. Piras, W. F. Xia, W. Steenbergen, T. G. van Leeuwen, and S. Manohar, "Photoacoustic imaging of the breast using the twente photoacoustic mammoscope: Present status and future perspectives," *Ieee Journal of Selected Topics in Quantum Electronics*, vol. 16, no. 4, pp. 730–739, 2010.

[84] C. M. Pitsillides, E. K. Joe, X. B. Wei, R. R. Anderson, and C. P. Lin, "Selective cell targeting with light-absorbing microparticles and nanoparticles," *Biophysical Journal*, vol. 84, no. 6, pp. 4023–4032, 2003.

[85] V. P. Zharov, E. N. Galitovskaya, C. Johnson, and T. Kelly, "Synergistic enhancement of selective nanophotothermolysis with gold nanoclusters: Potential for cancer therapy," *Lasers in Surgery and Medicine*, vol. 37, no. 3, pp. 219–226, 2005.

[86] V. P. Zharov, R. R. Letfullin, and E. N. Galitovskaya, "Microbubbles-overlapping mode for laser killing of cancer cells with absorbing nanoparticle clusters," *Journal of Physics D-Applied Physics*, vol. 38, no. 15, pp. 2571–2581, 2005.

[87] R. Visaria, J. C. Bischof, M. Loren, B. Williams, E. Ebbini, G. Paciotti, and R. Griffin, "Nanotherapeutics for enhancing thermal therapy of cancer," *International Journal of Hyperthermia*, vol. 23, no. 6, pp. 501–511, 2007.

[88] C. V. Raman and K. S. Krishnan, "A new type of secondary radiation," *Nature*, vol. 121, pp. 501–502, 1928.

[89] H. J. van Manen, A. Lenferink, and C. Otto, "Noninvasive imaging of protein metabolic labeling in single human cells using stable isotopes and raman microscopy," *Analytical Chemistry*, vol. 80, no. 24, pp. 9576–9582, 2008.

[90] M. J. Buzawa, "Lens system for laser scanners," *Laser Focus with Fiberoptic Technology*, vol. 16, no. 9, pp. 82–, 1980.

[91] W. Smith, *Modern Optical Engineering*. New York: SPIE Press / McGraw-Hill, 2008.

[92] H. Haus, *Waves and fields in optoelectronics*. New Jersey: Prentice-Hall, 1984.

[93] C. J. De Grauw, N. M. Sijtsema, C. Otto, and J. Greve, "Axial resolution of confocal raman microscopes: Gaussian beam theory and practice," *Journal of Microscopy-Oxford*, vol. 188, pp. 273–279, 1997.

[94] N. Uzunbajakava, A. Lenferink, Y. Kraan, B. Willekens, G. Vrensen, J. Greve, and C. Otto, "Nonresonant raman imaging of protein distribution in single human cells," *Biopolymers*, vol. 72, no. 1, pp. 1–9, 2003.

[95] N. Uzunbajakava, A. Lenferink, Y. Kraan, E. Volokhina, G. Vrensen, J. Greve, and C. Otto, "Nonresonant confocal raman imaging of dna and protein distribution in apoptotic cells," *Biophysical Journal*, vol. 84, no. 6, pp. 3968–3981, 2003.

[96] H. J. van Manen, Y. M. Kraan, D. Roos, and C. Otto, "Single-cell raman and fluorescence microscopy reveal the association of lipid bodies with phagosomes in leukocytes," *Proceedings of the National Academy of Sciences of the United States of America*, vol. 102, no. 29, pp. 10159–10164, 2005.

[97] I. Haq, B. Z. Chowdhury, and J. B. Chaires, "Singular value decomposition of 3-d dna melting curves reveals complexity in the melting process," *European Biophysics Journal with Biophysics Letters*, vol. 26, no. 6, pp. 419–426, 1997.

[98] P. Shaw, *Multivariate statistics for the environmental sciences*. London: Oxford University Press, 2003.

[99] J. H. Ward, "Hierarchical grouping to optimize an objective function," *Journal of the American Statistical Association*, vol. 58, no. 301, pp. 236–244, 1963.

[100] M. Lacroix and G. Leclercq, "Relevance of breast cancer cell lines as models for breast tumours: an update," *Breast Cancer Research and Treatment*, vol. 83, no. 3, pp. 249–289, 2004.

[101] S. Rehman, Z. Movasaghi, A. T. Tucker, S. P. Joel, J. A. Darr, A. V. Ruban, and I. U. Rehman, "Raman spectroscopic analysis of breast cancer tissues: identifying differences between normal, invasive ductal carcinoma and ductal carcinoma in situ of the breast tissue," *Journal of Raman Spectroscopy*, vol. 38, no. 10, pp. 1345–1351, 2007.

[102] X. L. Yan, R. X. Dong, L. Zhang, X. J. Zhang, and Z. W. Zhang, "Raman spectra of single cell from gastrointestinal cancer patients," *World J Gastroenterol*, vol. 11, no. 21, pp. 3290–2, 2005.

[103] Z. Movasaghi, S. Rehman, and I. U. Rehman, "Raman spectroscopy of biological tissues," *Applied Spectroscopy Reviews*, vol. 42, no. 5, pp. 493–541, 2007.

[104] L. G. Boros, M. Cascante, and W. N. P. Lee, "Metabolic profiling of cell growth and death in cancer: applications in drug discovery," *Drug Discovery Today*, vol. 7, no. 6, pp. 364–372, 2002.

[105] R. J. DeBerardinis, N. Sayed, D. Ditsworth, and C. B. Thompson, "Brick by brick: metabolism and tumor cell growth," *Current Opinion in Genetics & Development*, vol. 18, no. 1, pp. 54–61, 2008.

[106] V. V. Pully, A. Lenferink, and C. Otto, "Hybrid rayleigh, raman and two-photon excited fluorescence spectral confocal, microscopy of living cells," *Journal of Raman Spectroscopy*, vol. 41, no. 6, pp. 599–608, 2010.

[107] L. Hartsuiker, N. J. L. Zeijen, L. W. M. M. Terstappen, and C. Otto, "A comparison of breast cancer tumor cells with varying expression of the her2/neu receptor by raman microspectroscopic imaging," *Analyst*, vol. 135, no. 12, pp. 3220–3226, 2010.

[108] N. S. Gulyak, N. S. Sergeeva, E. N. Slavnova, V. I. Chissov, A. V. Babarina, V. P. Demidov, D. D. Pak, and S. K. Dzhubalieva, "Proliferative activity of tumor cells as a prognostic factor in breast cancer," *Bulletin of Experimental Biology and Medicine*, vol. 120, no. 8, pp. 858–860, 1995.

[109] C. Krafft, L. Neudert, T. Simat, and R. Salzer, "Near infrared raman spectra of human brain lipids," *Spectrochimica Acta Part a-Molecular and Biomolecular Spectroscopy*, vol. 61, no. 7, pp. 1529–1535, 2005.

[110] J. W. Chan, D. S. Taylor, and D. L. Thompson, "The effect of cell fixation on the discrimination of normal and leukemia cells with laser tweezers raman spectroscopy," *Biopolymers*, vol. 91, no. 2, pp. 132–139, 2009.

[111] J. Ferlay, H. Shin, F. Bray, D. Forman, C. Mathers, and D. Parkin, "Globocan 2008, cancer incidence and mortality worldwide: Iarc cancerbase no. 10 [internet].," July 12 2010.

[112] D. J. Slamon, G. M. Clark, S. G. Wong, W. J. Levin, A. Ullrich, and W. L. Mcguire, "Human-breast cancer - correlation of relapse and survival with amplification of the her-2 neu oncogene," *Science*, vol. 235, no. 4785, pp. 177–182, 1987.

[113] D. J. Slamon, W. Godolphin, L. A. Jones, J. A. Holt, S. G. Wong, D. E. Keith, W. J. Levin, S. G. Stuart, J. Udove, A. Ullrich, and M. F. Press, "Studies of the her-2/neu proto-oncogene in human-breast and ovarian-cancer," *Science*, vol. 244, no. 4905, pp. 707–712, 1989.

[114] J. Baselga and L. Norton, "Focus on breast cancer," *Cancer Cell*, vol. 1, no. 4, pp. 319–322, 2002.

[115] P. M. Ravdin and G. C. Chamness, "The c-erbb-2 protooncogene as a prognostic and predictive marker in breast-cancer - a paradigm for the development of other macromolecular markers - a review," *Gene*, vol. 159, no. 1, pp. 19–27, 1995.

[116] G. D. L. Phillips, G. M. Li, D. L. Dugger, L. M. Crocker, K. L. Parsons, E. Mai, W. A. Blattler, J. M. Lambert, R. V. J. Chari, R. J. Lutz, W. L. T. Wong, F. S. Jacobson, H. Koeppen, R. H. Schwall, S. R. Kenkare-Mitra, S. D. Spencer, and M. X. Sliwkowski, "Targeting her2-positive breast cancer with trastuzumab-dm1, an antibody-cytotoxic drug conjugate," *Cancer Research*, vol. 68, no. 22, pp. 9280–9290, 2008.

[117] J. A. Menendez, "Fine-tuning the lipogenic/lipolytic balance to optimize the metabolic requirements of cancer cell growth: Molecular mechanisms and therapeutic perspectives," *Biochimica Et Biophysica Acta-Molecular and Cell Biology of Lipids*, vol. 1801, no. 3, pp. 381–391, 2010.

[118] D. H. Zhang, L. K. Tai, L. L. Wong, L. L. Chiu, S. K. Sethi, and E. S. C. Koay, "Proteomic study reveals that proteins involved in metabolic and detoxification pathways are highly expressed in her-2/neu-positive breast cancer," *Molecular & Cellular Proteomics*, vol. 4, no. 11, pp. 1686–1696, 2005.

[119] M. M. Mariani, L. J. Maccoux, C. Matthaus, M. Diem, J. G. Hengstler, and V. Deckert, "Micro-raman detection of nuclear membrane lipid fluctuations in senescent epithelial breast cancer cells," *Analytical Chemistry*, vol. 82, no. 10, pp. 4259–4263, 2010.

[120] T. M. Trost, E. U. Lausch, S. A. Fees, S. Schmitt, T. Enklaar, D. Reutzel, L. R. Brixel, P. Schmidtke, M. Maringer, I. B. Schiffer, C. K. Heimerdinger, J. G. Hengstler, G. Fritz, E. O. Bockamp, D. Prawitt, B. U. Zabel, and C. Spangenberg, "Premature senescence is a primary fail-safe mechanism of erbb2-driven tumorigenesis in breast carcinoma cells," *Cancer Research*, vol. 65, no. 3, pp. 840–849, 2005.

[121] J. W. Chan, D. S. Taylor, T. Zwerdling, S. M. Lane, K. Ihara, and T. Huser, "Micro-raman spectroscopy detects individual neoplastic and normal hematopoietic cells," *Biophysical Journal*, vol. 90, no. 2, pp. 648–656, 2006.

[122] E. O. Aboagye and Z. M. Bhujwalla, "Malignant transformation alters membrane choline phospholipid metabolism of human mammary epithelial cells," *Cancer Research*, vol. 59, no. 1, pp. 80–84, 1999.

[123] J. M. Rae, C. J. Creighton, J. M. Meck, B. R. Haddad, and M. D. Johnson, "Mda-mb-435 cells are derived from m14 melanoma cells - a loss for breast cancer, but a boon for melanoma research," *Breast Cancer Research and Treatment*, vol. 104, no. 1, pp. 13–19, 2007.

[124] S. Sellappan, R. Grijalva, X. Y. Zhou, W. T. Yang, M. Bar Eli, G. B. Mills, and D. H. Yu, "Lineage infidelity of mda-mb-435 cells: Expression of melanocyte proteins in a breast cancer cell line," *Cancer Research*, vol. 64, no. 10, pp. 3479–3485, 2004.

[125] H. J. van Manen, Y. M. Kraan, D. Roos, and C. Otto, "Intracellular chemical imaging of heme-containing enzymes involved in innate immunity using resonance raman microscopy," *Journal of Physical Chemistry B*, vol. 108, no. 48, pp. 18762–18771, 2004.

[126] D. E. Ingber, D. Prusty, Z. Q. Sun, H. Betensky, and N. Wang, "Cell shape, cytoskeletal mechanics, and cell cycle control in angiogenesis," *Journal of Biomechanics*, vol. 28, no. 12, pp. 1471–1484, 1995.

[127] N. Stone, C. Kendall, J. Smith, P. Crow, and H. Barr, "Raman spectroscopy for identification of epithelial cancers," *Faraday Discussions*, vol. 126, pp. 141–157, 2004.

[128] A. J. Ruiz-Chica, M. A. Medina, F. Sanchez-Jimenez, and F. J. Ramirez, "Characterization by raman spectroscopy of conformational changes on guanine-cytosine and adenine-thymine oligonucleotides induced by aminooxy analogues of spermidine," *Journal of Raman Spectroscopy*, vol. 35, no. 2, pp. 93–100, 2004.

[129] Z. W. Huang, A. McWilliams, H. Lui, D. I. McLean, S. Lam, and H. S. Zeng, "Near-infrared raman spectroscopy for optical diagnosis of lung cancer," *International Journal of Cancer*, vol. 107, no. 6, pp. 1047–1052, 2003.

[130] L. Silveira, S. Sathaiah, R. A. Zangaro, M. T. T. Pacheco, M. C. Chavantes, and C. A. G. Pasqualucci, "Correlation between near-infrared raman spectroscopy and the histopathological analysis of atherosclerosis in human coronary arteries," *Lasers in Surgery and Medicine*, vol. 30, no. 4, pp. 290–297, 2002.

[131] U. Utzinger, D. L. Heintzelman, A. Mahadevan-Jansen, A. Malpica, M. Follen, and R. Richards-Kortum, "Near-infrared raman spectroscopy for in vivo detection of cervical precancers," *Applied Spectroscopy*, vol. 55, no. 8, pp. 955–959, 2001.

[132] N. J. Kline and P. J. Treado, "Raman chemical imaging of breast tissue," *Journal of Raman Spectroscopy*, vol. 28, no. 2-3, pp. 119–124, 1997.

[133] C. J. Frank, R. L. Mccreery, and D. C. B. Redd, "Raman-spectroscopy of normal and diseased human breast tissues," *Analytical Chemistry*, vol. 67, no. 5, pp. 777–783, 1995.

[134] J. Ruizcabello and J. S. Cohen, "Phospholipid metabolites as indicators of cancer cell-function," *Nmr in Biomedicine*, vol. 5, no. 5, pp. 226–233, 1992.

[135] H. Sadeghijorabchi, P. J. Hendra, R. H. Wilson, and P. S. Belton, "Determination of the total unsaturation in oils and margarines by fourier-transform raman-spectroscopy," *Journal of the American Oil Chemists Society*, vol. 67, no. 8, pp. 483–486, 1990.

[136] Z. W. Huang, H. Lui, X. K. Chen, A. Alajlan, D. I. McLean, and H. S. Zeng, "Raman spectroscopy of in vivo cutaneous melanin," *Journal of Biomedical Optics*, vol. 9, no. 6, pp. 1198–1205, 2004.

[137] S. D. Meng, D. Tripathy, E. P. Frenkel, S. Shete, E. Z. Naftalis, J. F. Huth, P. D. Beitsch, M. Leitch, S. Hoover, D. Euhus, B. Haley, L. Morrison, T. P. Fleming, D. Herlyn, L. W. M. M. Terstappen, T. Fehm, T. F. Tucker, N. Lane, J. Q. Wang, and J. W. Uhr, "Circulating tumor cells in patients with breast cancer dormancy," *Clinical Cancer Research*, vol. 10, no. 24, pp. 8152–8162, 2004.

[138] R. Cailleau, M. Olive, and Q. V. J. Cruciger, "Long-term human breast carcinoma cell lines of metastatic origin - preliminary characterization," *In Vitro-Journal of the Tissue Culture Association*, vol. 14, no. 11, pp. 911–915, 1978.

[139] M. Hedegaard, C. Krafft, H. J. Ditzel, L. E. Johansen, S. Hassing, and J. Popp, "Discriminating isogenic cancer cells and identifying altered unsaturated fatty acid content as associated with metastasis status, using k-means clustering and partial least squares-discriminant analysis of raman maps," *Analytical Chemistry*, vol. 82, no. 7, pp. 2797–2802, 2010.

[140] M. Hu, J. Y. Chen, Z. Y. Li, L. Au, G. V. Hartland, X. D. Li, M. Marquez, and Y. N. Xia, "Gold nanostructures: engineering their plasmonic properties for biomedical applications," *Chemical Society Reviews*, vol. 35, no. 11, pp. 1084–1094, 2006.

[141] S. Eustis and M. A. El-Sayed, "Why gold nanoparticles are more precious than pretty gold: Noble metal surface plasmon resonance and its enhancement of the radiative and nonradiative properties of nanocrystals of different shapes," *Chemical Society Reviews*, vol. 35, no. 3, pp. 209–217, 2006.

[142] Y. W. Wang, X. Y. Xie, X. D. Wang, G. Ku, K. L. Gill, D. P. O'Neal, G. Stoica, and L. V. Wang, "Photoacoustic tomography of a nanoshell contrast agent in the in vivo rat brain," *Nano Letters*, vol. 4, no. 9, pp. 1689–1692, 2004.

[143] J. J. Chen and J. Irudayaraj, "Quantitative investigation of compartmentalized dynamics of erbb2 targeting gold nanorods in live cells by single molecule spectroscopy," *Acs Nano*, vol. 3, no. 12, pp. 4071–4079, 2009.

[144] N. Lewinski, V. Colvin, and R. Drezek, "Cytotoxicity of nanoparticles," *Small*, vol. 4, no. 1, pp. 26–49, 2008.

[145] R. E. Kast, G. K. Serhatkulu, A. Cao, A. K. Pandya, H. Dai, J. S. Thakur, V. M. Naik, R. Naik, M. D. Klein, G. W. Auner, and R. Rabah, "Raman spectroscopy can differentiate malignant tumors from normal breast tissue and detect early neoplastic changes in a mouse model," *Biopolymers*, vol. 89, no. 3, pp. 235–241, 2008.

[146] M. Moskovits, "Surface-enhanced spectroscopy," *Reviews of Modern Physics*, vol. 57, no. 3, pp. 783–826, 1985.

[147] S. Eustis and M. El-Sayed, "Aspect ratio dependence of the enhanced fluorescence intensity of gold nanorods: Experimental and simulation study," *Journal of Physical Chemistry B*, vol. 109, no. 34, pp. 16350–16356, 2005.

[148] M. B. Mohamed, V. Volkov, S. Link, and M. A. El-Sayed, "The 'lightning' gold nanorods: fluorescence enhancement of over a million compared to the gold metal," *Chemical Physics Letters*, vol. 317, no. 6, pp. 517–523, 2000.

[149] A. Mooradian, "Photoluminescence of metals," *Physical Review Letters*, vol. 22, no. 5, pp. 185–187, 1969.

[150] A. V. Alekseeva, V. A. Bogatyrev, L. A. Dykman, B. N. Khlebtsov, L. A. Trachuk, A. G. Melnikov, and N. G. Khlebtsov, "Preparation and optical scattering characterization of gold nanorods and their application to a dot-immunogold assay," *Applied Optics*, vol. 44, no. 29, pp. 6285–6295, 2005.

[151] B. T. Draine and P. J. Flatau, "Discrete-dipole approximation for scattering calculations," *Journal of the Optical Society of America a-Optics Image Science and Vision*, vol. 11, no. 4, pp. 1491–1499, 1994.

[152] C. Ungureanu, R. G. Rayavarapu, S. Manohar, and T. G. van Leeuwen, "Discrete dipole approximation simulations of gold nanorod optical properties: Choice of input parameters and comparison with experiment," *Journal of Applied Physics*, vol. 105, no. 10, pp. –, 2009.

[153] M. Z. Liu and P. Guyot-Sionnest, "Mechanism of silver(i)-assisted growth of gold nanorods and bipyramids," *Journal of Physical Chemistry B*, vol. 109, no. 47, pp. 22192–22200, 2005.

[154] A. Bouhelier, R. Bachelot, G. Lerondel, S. Kostcheev, P. Royer, and G. P. Wiederrecht, "Surface plasmon characteristics of tunable photoluminescence in single gold nanorods," *Physical Review Letters*, vol. 95, no. 26, pp. –, 2005.

[155] J. Kneipp, H. Kneipp, M. McLaughlin, D. Brown, and K. Kneipp, "In vivo molecular probing of cellular compartments with gold nanoparticles and nanoaggregates," *Nano Letters*, vol. 6, no. 10, pp. 2225–2231, 2006.

[156] G. von Maltzahn, A. Centrone, J. H. Park, R. Ramanathan, M. J. Sailor, T. A. Hatton, and S. N. Bhatia, "Sers-coded gold nanorods as a multifunctional platform for densely multiplexed near-infrared imaging and photothermal heating," *Advanced Materials*, vol. 21, no. 31, pp. 3175–+, 2009.

[157] J. Kneipp, H. Kneipp, A. Rajadurai, R. W. Redmond, and K. Kneipp, "Optical probing and imaging of live cells using sers labels," *Journal of Raman Spectroscopy*, vol. 40, no. 1, pp. 1–5, 2009.

[158] C. G. Wang, J. Chen, T. Talavage, and J. Irudayaraj, "Gold nanorod/fe$_3$o$_4$ nanoparticle "nano-pearl-necklaces" for simultaneous targeting, dual-mode imaging, and photothermal ablation of cancer cells," *Angewandte Chemie-International Edition*, vol. 48, no. 15, pp. 2759–2763, 2009.

[159] J. W. Liaw, S. W. Tsai, K. L. Chen, and F. Y. Hsu, "Single-photon and two-photon cellular imagings of gold nanorods and dyes," *Journal of Nanoscience and Nanotechnology*, vol. 10, no. 1, pp. 467–473, 2010.

[160] D. Lankveld, R. G. Rayavarapu, P. Krystek, A. Oomen, H. Verharen, T. v. Leeuwen, W. d. Jong, and S. Manohar, "Blood clearance and tissue distribution of pegylated and non-pegylated gold nanorods after intravenous administration in rats," *Nanomedicine*, vol. in print, 2010.

[161] S. D. Conner and S. L. Schmid, "Regulated portals of entry into the cell," *Nature*, vol. 422, no. 6927, pp. 37–44, 2003.

[162] N. Yoshida, M. Kinjo, and M. Tamura, "Microenvironment of endosomal aqueous phase investigated by the mobility of microparticles using fluorescence correlation spectroscopy," *Biochemical and Biophysical Research Communications*, vol. 280, no. 1, pp. 312–318, 2001.

[163] R. A. Farrer, F. L. Butterfield, V. W. Chen, and J. T. Fourkas, "Highly efficient multiphoton-absorption-induced luminescence from gold nanoparticles," *Nano Letters*, vol. 5, no. 6, pp. 1139–1142, 2005.

[164] J. Zheng, C. W. Zhang, and R. M. Dickson, "Highly fluorescent, water-soluble, size-tunable gold quantum dots," *Physical Review Letters*, vol. 93, no. 7, pp. –, 2004.

[165] Y. P. Bao, C. Zhong, D. M. Vu, J. P. Temirov, R. B. Dyer, and J. S. Martinez, "Nanoparticle-free synthesis of fluorescent gold nanoclusters at physiological temperature," *Journal of Physical Chemistry C*, vol. 111, no. 33, pp. 12194–12198, 2007.

[166] K. Imura, T. Nagahara, and H. Okamoto, "Near-field two-photon-induced photoluminescence from single gold nanorods and imaging of plasmon modes," *Journal of Physical Chemistry B*, vol. 109, no. 27, pp. 13214–13220, 2005.

[167] D. Nagesha, G. S. Laevsky, P. Lampton, R. Banyal, C. Warner, C. DiMarzio, and S. Sridhar, "In vitro imaging of embryonic stem cells using multiphoton luminescence of gold nanoparticles," *International Journal of Nanomedicine*, vol. 2, no. 4, pp. 813–819, 2007.

[168] J. Park, A. Estrada, K. Sharp, K. Sang, J. A. Schwartz, D. K. Smith, C. Coleman, J. D. Payne, B. A. Korgel, A. K. Dunn, and J. W. Tunnell, "Two-photon-induced photoluminescence imaging of tumors using near-infrared excited gold nanoshells," *Optics Express*, vol. 16, no. 3, pp. 1590–1599, 2008.

[169] L. Tong, W. He, Y. S. Zhang, W. Zheng, and J. X. Cheng, "Visualizing systemic clearance and cellular level biodistribution of gold nanorods by intrinsic two-photon luminescence," *Langmuir*, vol. 25, no. 21, pp. 12454–12459, 2009.

[170] L. Hartsuiker, W. Petersen, R. G. Rayavarapu, A. Lenferink, A. Poot, L. W. M. M. Terstappen, T. G. van Leeuwen, S. Manohar, and C. Otto, "Raman and fluorescence spectral imaging of live breast cancer cells incubated with gold nanorods," *Journal of Applied Spectroscopy*, p. under review, 2011.

[171] D. J. Whittle, P. H. Avouris, and E. Burstein, "Inelastic light-scattering by silver in the near ultraviolet," *Journal of the Optical Society of America*, vol. 71, no. 12, pp. 1650–1650, 1981.

[172] G. T. Boyd, T. Rasing, J. R. R. Leite, and Y. R. Shen, "Local-field enhancement on rough surfaces of metals, semimetals, and semiconductors with the use of optical 2nd-harmonic generation," *Physical Review B*, vol. 30, no. 2, pp. 519–526, 1984.

[173] G. T. Boyd, Z. H. Yu, and Y. R. Shen, "Photoinduced luminescence from the noble-metals and its enhancement on roughened surfaces," *Physical Review B*, vol. 33, no. 12, pp. 7923–7936, 1986.

[174] F. J. Adrian, "Charge-transfer effects in surface-enhanced raman-scattering," *Journal of Chemical Physics*, vol. 77, no. 11, pp. 5302–5314, 1982.

[175] R. L. Birke, J. R. Lombardi, and J. I. Gersten, "Observation of a continuum in enhanced raman-scattering from a metal-solution interface," *Physical Review Letters*, vol. 43, no. 1, pp. 71–75, 1979.

[176] J. R. Lombardi, R. L. Birke, T. H. Lu, and J. Xu, "Charge-transfer theory of surface enhanced raman-spectroscopy - herzberg-teller contributions," *Journal of Chemical Physics*, vol. 84, no. 8, pp. 4174–4180, 1986.

[177] A. Otto, I. Mrozek, H. Grabhorn, and W. Akemann, "Surface-enhanced raman-scattering," *Journal of Physics-Condensed Matter*, vol. 4, no. 5, pp. 1143–1212, 1992.

[178] P. Apell, R. Monreal, and S. Lundqvist, "Photoluminescence of noble-metals," *Physica Scripta*, vol. 38, no. 2, pp. 174–179, 1988.

[179] M. R. Beversluis, A. Bouhelier, and L. Novotny, "Continuum generation from single gold nanostructures through near-field mediated intraband transitions," *Physical Review B*, vol. 68, no. 11, pp. –, 2003.

[180] T. P. Bigioni, R. L. Whetten, and O. Dag, "Near-infrared luminescence from small gold nanocrystals," *Journal of Physical Chemistry B*, vol. 104, no. 30, pp. 6983–6986, 2000.

[181] D. Lee, R. L. Donkers, G. L. Wang, A. S. Harper, and R. W. Murray, "Electrochemistry and optical absorbance and luminescence of molecule-like au-38 nanoparticles," *Journal of the American Chemical Society*, vol. 126, no. 19, pp. 6193–6199, 2004.

[182] S. Link, A. Beeby, S. FitzGerald, M. A. El-Sayed, T. G. Schaaff, and R. L. Whetten, "Visible to infrared luminescence from a 28-atom gold cluster," *Journal of Physical Chemistry B*, vol. 106, no. 13, pp. 3410–3415, 2002.

[183] S. Link, M. A. El-Sayed, T. G. Schaaff, and R. L. Whetten, "Transition from nanoparticle to molecular behavior: a femtosecond transient absorption study of a size-selected 28 atom gold cluster," *Chemical Physics Letters*, vol. 356, no. 3-4, pp. 240–246, 2002.

[184] A. Wokaun, J. P. Gordon, and P. F. Liao, "Radiation damping in surface-enhanced raman-scattering," *Physical Review Letters*, vol. 48, no. 14, pp. 957–960, 1982.

[185] E. J. Heilweil and R. M. Hochstrasser, "Nonlinear spectroscopy and picosecond transient grating study of colloidal gold," *Journal of Chemical Physics*, vol. 82, no. 11, pp. 4762–4770, 1985.

[186] O. P. Varnavski, M. B. Mohamed, M. A. El-Sayed, and T. Goodson, "Relative enhancement of ultrafast emission in gold nanorods," *Journal of Physical Chemistry B*, vol. 107, no. 14, pp. 3101–3104, 2003.

[187] O. P. Varnavski, T. Goodson, M. B. Mohamed, and M. A. El-Sayed, "Femtosecond excitation dynamics in gold nanospheres and nanorods," *Physical Review B*, vol. 72, no. 23, pp. –, 2005.

[188] Z. Jian, H. Liqing, W. Yongchang, and L. Yimin, "Fluorescence spectrum properties of gold nanochains," *Physica E: Low-dimensional Systems and Nanostructures*, vol. 25, no. 1, pp. 114–118, 2004.

[189] J. U. Kang, "Observation of random lasing in gold-silica nanoshell/water solution," *Applied Physics Letters*, vol. 89, no. 22, pp. –, 2006.

[190] E. Dulkeith, T. Niedereichholz, T. A. Klar, J. Feldmann, G. von Plessen, D. I. Gittins, K. S. Mayya, and F. Caruso, "Plasmon emission in photoexcited gold nanoparticles," *Physical Review B*, vol. 70, no. 20, pp. –, 2004.

[191] J. P. Wilcoxon, J. E. Martin, F. Parsapour, B. Wiedenman, and D. F. Kelley, "Photoluminescence from nanosize gold clusters," *Journal of Chemical Physics*, vol. 108, no. 21, pp. 9137–9143, 1998.

[192] T. Huang and R. W. Murray, "Visible luminescence of water-soluble monolayer- protected gold clusters," *Journal of Physical Chemistry B*, vol. 105, no. 50, pp. 12498–12502, 2001.

[193] O. Varnavski, R. G. Ispasoiu, L. Balogh, D. Tomalia, and T. Goodson, "Ultrafast time-resolved photoluminescence from novel metal-dendrimer nanocomposites," *Journal of Chemical Physics*, vol. 114, no. 5, pp. 1962–1965, 2001.

[194] C. Loo, A. Lin, L. Hirsch, M. H. Lee, J. Barton, N. Halas, J. West, and R. Drezek, "Nanoshell-enabled photonics-based imaging and therapy of cancer," *Technology in Cancer Research & Treatment*, vol. 3, no. 1, pp. 33–40, 2004.

[195] R. D. Averitt, S. L. Westcott, and N. J. Halas, "Ultrafast electron dynamics in gold nanoshells," *Physical Review B*, vol. 58, no. 16, pp. 10203–10206, 1998.

[196] C. L. Nehl, N. K. Grady, G. P. Goodrich, F. Tam, N. J. Halas, and J. H. Hafner, "Scattering spectra of single gold nanoshells," *Nano Letters*, vol. 4, no. 12, pp. 2355–2359, 2004.

[197] C. Radloff and N. J. Halas, "Plasmonic properties of concentric nanoshells," *Nano Letters*, vol. 4, no. 7, pp. 1323–1327, 2004.

[198] S. L. Logunov, T. S. Ahmadi, M. A. ElSayed, J. T. Khoury, and R. L. Whetten, "Electron dynamics of passivated gold nanocrystals probed by subpicosecond transient absorption spectroscopy," *Journal of Physical Chemistry B*, vol. 101, no. 19, pp. 3713–3719, 1997.

[199] T. G. Schaaff, M. N. Shafigullin, J. T. Khoury, I. Vezmar, R. L. Whetten, W. G. Cullen, P. N. First, C. GutierrezWing, J. Ascensio, and M. J. JoseYacaman, "Isolation of smaller nanocrystal au molecules: Robust quantum effects in optical spectra," *Journal of Physical Chemistry B*, vol. 101, no. 40, pp. 7885–7891, 1997.

[200] Z. Jian, W. Yongchang, and L. Yimin, "Fluorescence spectra characters of silver-coated gold colloidal nanoshells," *Colloids and Surfaces A: Physicochemical and Engineering Aspects*, vol. 232, no. 2-3, pp. 155–161, 2004.

[201] V. P. Zhukov, F. Aryasetiawan, E. V. Chulkov, I. G. de Gurtubay, and P. M. Echenique, "Corrected local-density approximation band structures, linear-response dielectric functions, and quasiparticle lifetimes in noble metals," *Physical Review B*, vol. 64, no. 19, pp. art. no.–195122, 2001.

[202] M. Perner, P. Bost, U. Lemmer, G. vonPlessen, J. Feldmann, U. Becker, M. Mennig, M. Schmitt, and H. Schmidt, "Optically induced damping of the surface plasmon resonance in gold colloids," *Physical Review Letters*, vol. 78, no. 11, pp. 2192–2195, 1997.

[203] S. L. Qu, Y. L. Song, H. F. Liu, Y. X. Wang, Y. C. Gao, S. T. Liu, X. R. Zhang, Y. L. Li, and D. B. Zhu, "A theoretical and experimental study on optical limiting in platinum nanoparticles," *Optics Communications*, vol. 203, no. 3-6, pp. 283–288, 2002.

[204] M. M. Alvarez, J. T. Khoury, T. G. Schaaff, M. N. Shafigullin, I. Vezmar, and R. L. Whetten, "Optical absorption spectra of nanocrystal gold molecules," *Journal of Physical Chemistry B*, vol. 101, no. 19, pp. 3706–3712, 1997.

[205] R. H. Doremus, "Optical properties of small gold particles," *Journal of Chemical Physics*, vol. 40, no. 8, pp. 2389–2396, 1964.

[206] W. A. Deheer, "The physics of simple metal-clusters - experimental aspects and simple-models," *Reviews of Modern Physics*, vol. 65, no. 3, pp. 611–676, 1993.

[207] B. A. Smith, D. M. Waters, A. E. Faulhaber, M. A. Kreger, T. W. Roberti, and J. Z. Zhang, "Preparation and ultrafast optical characterization of metal and semiconductor colloidal nano-particles," *Journal of Sol-Gel Science and Technology*, vol. 9, no. 2, pp. 125–137, 1997.

[208] T. Goodson, O. Varnavski, and Y. Wang, "Optical properties and applications of dendrimer-metal nanocomposites," *International Reviews in Physical Chemistry*, vol. 23, no. 1, pp. 109–150, 2004.

[209] H. F. Wang, T. B. Huff, D. A. Zweifel, W. He, P. S. Low, A. Wei, and J. X. Cheng, "In vitro and in vivo two-photon luminescence imaging of single gold nanorods," *Proceedings of the National Academy of Sciences of the United States of America*, vol. 102, no. 44, pp. 15752–15756, 2005.

[210] L. Bickford, J. Sun, K. Fu, N. Lewinski, V. Nammalvar, J. Chang, and R. Drezek, "Enhanced multi-spectral imaging of live breast cancer cells using immunotargeted gold nanoshells and two-photon excitation microscopy," *Nanotechnology*, vol. 19, no. 31, pp. –, 2008.

[211] R. Gans, "Über die form ultramikroskopischer goldteilchen," *Annalen der Physik*, vol. 342, no. 5, pp. 881–900, 1912.

[212] G. Mie, "Beiträge zur optik trüber medien, speziell kolloidaler metallösungen," *Annalen der Physik*, vol. 330, no. 3, pp. 377–445, 1908. 1521-3889.

[213] S. Link, C. Burda, Z. L. Wang, and M. A. El-Sayed, "Electron dynamics in gold and gold-silver alloy nanoparticles: The influence of a nonequilibrium electron distribution and the size dependence of the electron-phonon relaxation," *Journal of Chemical Physics*, vol. 111, no. 3, pp. 1255–1264, 1999.

[214] R. P. Buck, S. Singhadeja, and L. B. Rogers, "Ultraviolet absorption spectra of some inorganic ions in aqueous solutions," *Analytical Chemistry*, vol. 26, no. 7, pp. 1240–1242, 1954.

[215] Y. Z. Hamada, B. L. Carlson, and J. T. Shank, "Potentiometric and uv-vis spectroscopy studies of citrate with the hexaquo fe3+ and cr3+ metal ions," *Synthesis and Reactivity in Inorganic and Metal-Organic Chemistry*, vol. 33, no. 8, pp. 1425–1440, 2003.

[216] D. M. Carey and G. M. Korenowski, "Measurement of the raman spectrum of liquid water," *Journal of Chemical Physics*, vol. 108, no. 7, pp. 2669–2675, 1998.

[217] J. F. Brennan, T. J. Romer, R. S. Lees, A. M. Tercyak, J. Kramer, J. R., and M. S. Feld, "Determination of human coronary artery composition by raman spectroscopy," *Circulation*, vol. 96, no. 1, pp. 99–105, 1997.

[218] W. Ahmed, E. S. Kooij, A. van Silfhout, and B. Poelsema, "Quantitative analysis of gold nanorod alignment after electric field-assisted deposition," *Nano Letters*, vol. 9, no. 11, pp. 3786–3794, 2009.

[219] A. Verma and F. Stellacci, "Effect of surface properties on nanoparticle-cell interactions," *Small*, vol. 6, no. 1, pp. 12–21, 2010.

[220] R. Lévy, U. Shaheen, Y. Cesbron, and V. Sée, "Gold nanoparticles delivery in mammalian live cells: a critical review," *Nano Reviews*, vol. 1, no. 1, 2010.

[221] A. K. Gupta and A. S. G. Curtis, "Surface modified superparamagnetic nanoparticles for drug delivery: Interaction studies with human fibroblasts in culture," *Journal of Materials Science-Materials in Medicine*, vol. 15, no. 4, pp. 493–496, 2004.

[222] A. L. Koh, C. M. Shachaf, S. Elchuri, G. P. Nolan, and R. Sinclair, "Electron microscopy localization and characterization of functionalized composite organic-inorganic sers nanoparticles on leukemia cells," *Ultramicroscopy*, vol. 109, no. 1, pp. 111–121, 2008.

[223] S. Schadler, C. Burkhardt, and A. Kappler, "Evaluation of electron microscopic sample preparation methods and imaging techniques for characterization of cell-mineral aggregates," *Geomicrobiology Journal*, vol. 25, no. 5, pp. 228–239, 2008.

[224] M. Moskovits, "Surface-enhanced raman spectroscopy: a brief retrospective," *Journal of Raman Spectroscopy*, vol. 36, no. 6-7, pp. 485–496, 2005.

[225] Z. Adamczyk and P. Weronski, "Application of the dlvo theory for particle deposition problems," *Advances in Colloid and Interface Science*, vol. 83, no. 1-3, pp. 137–226, 1999.

[226] S. Bhattacharjee and M. Elimelech, "Prediction of dlvo interaction energy and particle deposition rates for rough surfaces.," *Abstracts of Papers of the American Chemical Society*, vol. 214, pp. 40–Coll, 1997.

[227] B. Clinchy, A. Gazdar, R. Rabinovsky, E. Yefenof, B. Gordon, and E. S. Vitetta, "The growth and metastasis of human, her-2/neu-overexpressing tumor cell lines in male scid mice," *Breast Cancer Research and Treatment*, vol. 61, no. 3, pp. 217–228, 2000.

[228] H. Pluk, D. J. Stokes, B. Lich, B. Wieringa, and J. Fransen, "Advantages of indium-tin oxide-coated glass slides in correlative scanning electron microscopy applications of uncoated cultured cells," *J Microsc*, vol. 233, no. 3, pp. 353–63, 2009.

[229] P. Echlin, *Handbook of Sample Preparation for Scanning Electron Microscopy and X-ray Microanalysis*. Springer, 2009.

[230] J. C. Adams and F. M. Watt, "Regulation of development and differentiation by the extracellular-matrix," *Development*, vol. 117, no. 4, pp. 1183–1198, 1993.

[231] P. B. Vanwachem, T. Beugeling, J. Feijen, A. Bantjes, J. P. Detmers, and W. G. Vanaken, "Interaction of cultured human-endothelial cells with polymeric surfaces of different wettabilities," *Biomaterials*, vol. 6, no. 6, pp. 403–408, 1985.

[232] M. S. Lord, M. Foss, and F. Besenbacher, "Influence of nanoscale surface topography on protein adsorption and cellular response," *Nano Today*, vol. 5, no. 1, pp. 66–78, 2010.

[233] M. Iijima and H. Kamiya, "Surface modification for improving the stability of nanoparticles in liquid media," *Kona Powder and Particle Journal*, no. 27, pp. 119–129, 2009.

[234] W. Zhou and Z. L. Wang, *Scanning microscopy for nanotechnology: techniques and applications*. New York: Springer, 2006.

[235] A. Kudelski and B. Pettinger, "Sers on carbon chain segments: monitoring locally surface chemistry," *Chemical Physics Letters*, vol. 321, no. 5-6, pp. 356–362, 2000.

[236] A. Otto, "What is observed in single molecule sers, and why?," *Journal of Raman Spectroscopy*, vol. 33, no. 8, pp. 593–598, 2002.

[237] P. Etchegoin, H. Liem, R. C. Maher, L. F. Cohen, R. J. C. Brown, H. Hartigan, M. J. T. Milton, and J. C. Gallop, "A novel amplification mechanism for surface enhanced raman scattering," *Chemical Physics Letters*, vol. 366, no. 1-2, pp. 115–121, 2002.

[238] P. J. Moyer, J. Schmidt, L. M. Eng, and A. J. Meixner, "Surface-enhanced raman scattering spectroscopy of single carbon domains on individual ag nanoparticles on a 25 ms time scale," *Journal of the American Chemical Society*, vol. 122, no. 22, pp. 5409–5410, 2000.

[239] A. Merlen, V. Gadenne, J. Romann, V. Chevallier, L. Patrone, and J. C. Valmalette, "Surface enhanced raman spectroscopy of organic molecules deposited on gold sputtered substrates," *Nanotechnology*, vol. 20, no. 21, pp. –, 2009.

[240] M. D. King, S. Khadka, G. A. Craig, and M. D. Mason, "Effect of local heating on the sers efficiency of optically trapped prismatic nanoparticles," *Journal of Physical Chemistry C*, vol. 112, no. 31, pp. 11751–11757, 2008.

[241] Y. Seol, A. E. Carpenter, and T. T. Perkins, "Gold nanoparticles: enhanced optical trapping and sensitivity coupled with significant heating," *Optics Letters*, vol. 31, no. 16, pp. 2429–2431, 2006.

[242] K. E. Shafer-Peltier, A. S. Haka, M. Fitzmaurice, J. Crowe, J. Myles, R. R. Dasari, and M. S. Feld, "Raman microspectroscopic model of human breast tissue: implications for breast cancer diagnosis in vivo," *Journal of Raman Spectroscopy*, vol. 33, no. 7, pp. 552–563, 2002.

[243] S. Koljenovic, T. B. Schut, A. Vincent, J. M. Kros, and G. J. Puppels, "Detection of meningioma in dura mater by raman spectroscopy," *Analytical Chemistry*, vol. 77, no. 24, pp. 7958–7965, 2005.

[244] I. Notingher, C. Green, C. Dyer, E. Perkins, N. Hopkins, C. Lindsay, and L. L. Hench, "Discrimination between ricin and sulphur mustard toxicity in vitro using raman spectroscopy," *Journal of the Royal Society Interface*, vol. 1, no. 1, pp. 79–90, 2004.

[245] M. Gniadecka, H. C. Wulf, N. N. Mortensen, O. F. Nielsen, and D. H. Christensen, "Diagnosis of basal cell carcinoma by raman spectroscopy," *Journal of Raman Spectroscopy*, vol. 28, no. 2-3, pp. 125–129, 1997.

[246] A. R. Viehoever, D. Anderson, D. Jansen, and A. Mahadevan-Jansen, "Organotypic raft cultures as an effective in vitro tool for understanding raman spectral analysis of tissue," *Photochemistry and Photobiology*, vol. 78, no. 5, pp. 517–524, 2003.

[247] R. Malini, K. Venkatakrishna, J. Kurien, K. M. Pai, L. Rao, V. B. Kartha, and C. M. Krishna, "Discrimination of normal, inflammatory, premalignant, and malignant oral tissue: A raman spectroscopy study," *Biopolymers*, vol. 81, no. 3, pp. 179–193, 2006.

[248] P. G. L. Andrus and R. D. Strickland, "Cancer grading by fourier transform infrared spectroscopy," *Biospectroscopy*, vol. 4, no. 1, pp. 37–46, 1998.

[249] B. N. J. Persson and A. Baratoff, "Theory of photon-emission in electron-tunneling to metallic particles," *Physical Review Letters*, vol. 68, no. 21, pp. 3224–3227, 1992.

[250] M. M. Mariani, P. Lampen, J. Popp, B. R. Wood, and V. Deckert, "Impact of fixation on in vitro cell culture lines monitored with raman spectroscopy," *Analyst*, vol. 134, no. 6, pp. 1154–1161, 2009.

[251] V. V. Pully, A. Lenferink, H. J. van Manen, V. Subramaniam, C. A. van Blitterswijk, and C. Otto, "Microbioreactors for raman microscopy of stromal cell differentiation," *Analytical Chemistry*, vol. 82, no. 5, pp. 1844–1850, 2010.

[252] W. R. Chen, R. L. Adams, S. Heaton, D. T. Dickey, K. E. Bartels, and R. E. Nordquist, "Chromophore-enhanced laser-tumor tissue photothermal interaction using an 808-nm diode-laser," *Cancer Letters*, vol. 88, no. 1, pp. 15–19, 1995.

[253] V. Ntziachristos, A. G. Yodh, M. Schnall, and B. Chance, "Concurrent mri and diffuse optical tomography of breast after indocyanine green enhancement," *Proceedings of the National Academy of Sciences of the United States of America*, vol. 97, no. 6, pp. 2767–2772, 2000.

[254] K. Licha, B. Riefke, V. Ntziachristos, A. Becker, B. Chance, and W. Semmler, "Hydrophilic cyanine dyes as contrast agents for near-infrared tumor imaging: Synthesis, photophysical properties and spectroscopic in vivo characterization," *Photochemistry and Photobiology*, vol. 72, no. 3, pp. 392–398, 2000.

[255] J. M. Devoisselle, S. Soulie-Begu, S. Mordon, T. Desmettre, and H. Maillols, "A preliminary study of the in vivo behaviour of an emulsion formulation of indocyanine green," *Lasers in Medical Science*, vol. 13, no. 4, pp. 279–282, 1998.

[256] C. Hirche, D. Murawa, Z. Mohr, S. Kneif, and M. Hunerbein, "Icg fluorescence-guided sentinel node biopsy for axillary nodal staging in breast cancer," *Breast Cancer Research and Treatment*, vol. 121, no. 2, pp. 373–378, 2010.

[257] Y. Tajima, K. Yamazaki, Y. Masuda, M. Kato, D. Yasuda, T. Aoki, T. Kato, M. Murakami, M. Miwa, and M. Kusano, "Sentinel node mapping guided by indocyanine green fluorescence imaging in gastric cancer," *Annals of Surgery*, vol. 249, no. 1, pp. 58–62, 2009.

[258] M. H. G. M. van der Pas, G. A. M. S. van Dongen, F. Cailler, A. Pelegrin, and W. J. H. J. Meijerink, "Sentinel node procedure of the sigmoid using indocyanine green: feasibility study in a goat model," *Surgical Endoscopy and Other Interventional Techniques*, vol. 24, no. 9, pp. 2182–2187, 2010.

[259] L. Guerrini, Z. Jurasekova, C. Domingo, M. Perez-Mendez, P. Leyton, M. Campos-Vallette, J. V. Garcia-Ramos, and S. Sanchez-Cortes, "Importance of metal-adsorbate interactions for the surface-enhanced raman scattering of molecules adsorbed on plasmonic nanoparticles," *Plasmonics*, vol. 2, no. 3, pp. 147–156, 2007.

[260] F. Hao, C. L. Nehl, J. H. Hafner, and P. Nordlander, "Plasmon resonances of a gold nanostar," *Nano Letters*, vol. 7, no. 3, pp. 729–732, 2007.

[261] N. R. Jana, "Shape effect in nanoparticle self-assembly," *Angewandte Chemie-International Edition*, vol. 43, no. 12, pp. 1536–1540, 2004. 805TW Times Cited:94 Cited References Count:33.

[262] R. C. Jin, Y. W. Cao, C. A. Mirkin, K. L. Kelly, G. C. Schatz, and J. G. Zheng, "Photoinduced conversion of silver nanospheres to nanoprisms," *Science*, vol. 294, no. 5548, pp. 1901–1903, 2001.

[263] J. S. Shumaker-Parry, H. Rochholz, and M. Kreiter, "Fabrication of crescent-shaped optical antennas," *Advanced Materials*, vol. 17, no. 17, pp. 2131–+, 2005.

[264] B. J. Wiley, Y. C. Chen, J. M. McLellan, Y. J. Xiong, Z. Y. Li, D. Ginger, and Y. N. Xia, "Synthesis and optical properties of silver nanobars and nanorice," *Nano Letters*, vol. 7, no. 4, pp. 1032–1036, 2007.

[265] C. J. Murphy and N. R. Jana, "Controlling the aspect ratio of inorganic nanorods and nanowires," *Advanced Materials*, vol. 14, no. 1, pp. 80–82, 2002.

[266] J. M. McLellan, Z. Y. Li, A. R. Siekkinen, and Y. N. Xia, "The sers activity of a supported ag nanocube strongly depends on its orientation relative to laser polarization," *Nano Letters*, vol. 7, no. 4, pp. 1013–1017, 2007.

[267] X. H. Huang, S. Neretina, and M. A. El-Sayed, "Gold nanorods: From synthesis and properties to biological and biomedical applications," *Advanced Materials*, vol. 21, no. 48, pp. 4880–4910, 2009.

[268] J. Perez-Juste, I. Pastoriza-Santos, L. M. Liz-Marzan, and P. Mulvaney, "Gold nanorods: Synthesis, characterization and applications," *Coordination Chemistry Reviews*, vol. 249, no. 17-18, pp. 1870–1901, 2005.

[269] S. Abalde-Cela, P. Aldeanueva-Potel, C. Mateo-Mateo, L. Rodriguez-Lorenzo, R. A. Alvarez-Puebla, and L. M. Liz-Marzan, "Surface-enhanced raman scattering biomedical applications of plasmonic colloidal particles," *Journal of the Royal Society Interface*, vol. 7, pp. S435–S450, 2010.

[270] R. A. Alvarez-Puebla and L. M. Liz-Marzan, "Sers-based diagnosis and biodetection," *Small*, vol. 6, no. 5, pp. 604–610, 2010.

[271] D. K. Smith and B. A. Korgel, "The importance of the ctab surfactant on the colloidal seed-mediated synthesis of gold nanorods," *Langmuir*, vol. 24, no. 3, pp. 644–649, 2008.

[272] N. R. Jana, L. Gearheart, and C. J. Murphy, "Evidence for seed-mediated nucleation in the chemical reduction of gold salts to gold nanoparticles," *Chemistry of Materials*, vol. 13, no. 7, pp. 2313–2322, 2001.

[273] E. C. Le Ru and P. G. Etchegoin, "Phenomenological local field enhancement factor distributions around electromagnetic hot spots," *Journal of Chemical Physics*, vol. 130, no. 18, pp. –, 2009.

[274] R. Weigand, F. Rotermund, and A. Penzkofer, "Aggregation dependent absorption reduction of indocyanine green," *Journal of Physical Chemistry A*, vol. 101, no. 42, pp. 7729–7734, 1997.

[275] A. K. Kirchherr, A. Briel, and K. Mader, "Stabilization of indocyanine green by encapsulation within micellar systems," *Molecular Pharmaceutics*, vol. 6, no. 2, pp. 480–491, 2009.

[276] M. L. J. Landsman, G. Kwant, G. A. Mook, and W. G. Zijlstra, "Light-absorbing properties, stability, and spectral stabilization of indocyanine green," *Journal of Applied Physiology*, vol. 40, no. 4, pp. 575–583, 1976.

[277] G. Frens, "Controlled nucleation for regulation of particle-size in monodisperse gold suspensions," *Nature-Physical Science*, vol. 241, no. 105, pp. 20–22, 1973.

[278] W. Holzer, M. Mauerer, A. Penzkofer, R. M. Szeimies, C. Abels, M. Landthaler, and W. Baumler, "Photostability and thermal stability of indocyanine green," *Journal of Photochemistry and Photobiology B-Biology*, vol. 47, no. 2-3, pp. 155–164, 1998.

[279] R. Philip, A. Penzkofer, W. Baumler, R. M. Szeimies, and C. Abels, "Absorption and fluorescence spectroscopic investigation of indocyanine green," *Journal of Photochemistry and Photobiology a-Chemistry*, vol. 96, no. 1-3, pp. 137–148, 1996.

[280] R. Rajagopalan, P. Uetrecht, J. E. Bugaj, S. A. Achilefu, and R. B. Dorshow, "Stabilization of the optical tracer agent indocyanine green using noncovalent interactions," *Photochemistry and Photobiology*, vol. 71, no. 3, pp. 347–350, 2000.

[281] E. C. Le Ru and P. G. Etchegoin, *Principles of Surface-Enhanced Raman Spectroscopy And Related Plasmonic Effects*. Elsevier, 2009.

[282] N. Narband, M. Uppal, C. W. Dunnill, G. Hyett, M. Wilson, and I. P. Parkin, "The interaction between gold nanoparticles and cationic and anionic dyes: enhanced uv-visible absorption," *Physical Chemistry Chemical Physics*, vol. 11, no. 44, pp. 10513–10518, 2009.

[283] L. O. Brown and S. K. Doorn, "Optimization of the preparation of glass-coated, dye-tagged metal nanoparticles as sers substrates," *Langmuir*, vol. 24, no. 5, pp. 2178–2185, 2008.

[284] M. R. Lopez-Ramirez, L. Guerrini, J. V. Garcia-Ramos, and S. Sanchez-Cortes, "Vibrational analysis of herbicide diquat: A normal raman and sers study on ag nanoparticles," *Vibrational Spectroscopy*, vol. 48, no. 1, pp. 58–64, 2008.

[285] L. Guerrini, J. V. Garcia-Ramos, C. Domingo, and S. Sanchez-Cortes, "Ultrathin silver-coated gold nanoparticles as suitable substrate for surface-enhanced raman scattering," *Journal of Raman Spectroscopy*, vol. 41, no. 5, pp. 508–515, 2010.

[286] M. A. Bahri, M. Hoebeke, A. Grammenos, L. Delanaye, N. Vandewalle, and A. Seret, "Investigation of sds, dtab and ctab micelle microviscosities by electron spin resonance," *Colloids and Surfaces a-Physicochemical and Engineering Aspects*, vol. 290, no. 1-3, pp. 206–212, 2006.

[287] A. M. Tedeschi, L. Franco, M. Ruzzi, L. Paduano, C. Corvaja, and G. D'Errico, "Micellar aggregation of alkyltrimethylammonium bromide surfactants studied by electron paramagnetic resonance of an anionic nitroxide," *Physical Chemistry Chemical Physics*, vol. 5, no. 19, pp. 4204–4209, 2003.

[288] J. Alper, M. Crespo, and K. Hamad-Schifferli, "Release mechanism of octadecyl rhodamine b chloride from au nanorods by ultrafast laser pulses," *Journal of Physical Chemistry C*, vol. 113, no. 15, pp. 5967–5973, 2009.

[289] C. X. Yu, H. Nakshatri, and J. Irudayaraj, "Identity profiling of cell surface markers by multiplex gold nanorod probes," *Nano Letters*, vol. 7, no. 8, pp. 2300–2306, 2007.

[290] C. Ungureanu, R. Kroes, W. Petersen, T. A. M. Groothuis, F. Ungureanu, H. Janssen, F. W. B. van Leeuwen, R. P. H. Kooyman, S. Manohar, and T. G. van Leeuwen, "Light interactions with gold nanorods and cells: Implications for photothermal nanotherapeutics," *Nano Letters*, vol. 11, no. 5, pp. 1887–1894, 2011.

[291] K. Kneipp, A. S. Haka, H. Kneipp, K. Badizadegan, N. Yoshizawa, C. Boone, K. E. Shafer-Peltier, J. T. Motz, R. R. Dasari, and M. S. Feld, "Surface-enhanced raman spectroscopy in single living cells using gold nanoparticles," *Applied Spectroscopy*, vol. 56, no. 2, pp. 150–154, 2002.

[292] N. Everall, J. Lapham, F. Adar, A. Whitley, E. Lee, and S. Mamedov, "Optimizing depth resolution in confocal raman microscopy: A comparison of metallurgical, dry corrected, and oil immersion objectives," *Applied Spectroscopy*, vol. 61, no. 3, pp. 251–259, 2007.

[293] P. Torok, P. Varga, and G. R. Booker, "Electromagnetic diffraction of light focused through a planar interface between materials of mismatched refractive-indexes - structure of the electromagnetic-field .1.," *Journal of the Optical Society of America a-Optics Image Science and Vision*, vol. 12, no. 10, pp. 2136–2144, 1995.

[294] H. Takahashi, T. Niidome, A. Nariai, Y. Niidome, and S. Yamada, "Photothermal reshaping of gold nanorods prevents further cell death," *Nanotechnology*, vol. 17, no. 17, pp. 4431–4435, 2006.

[295] Y. Horiguchi, K. Honda, Y. Kato, N. Nakashima, and Y. Niidome, "Photothermal reshaping of gold nanorods depends on the passivating layers of the nanorod surfaces," *Langmuir*, vol. 24, no. 20, pp. 12026–12031, 2008.

[296] A. M. Derfus, W. C. W. Chan, and S. N. Bhatia, "Intracellular delivery of quantum dots for live cell labeling and organelle tracking," *Advanced Materials*, vol. 16, no. 12, pp. 961–+, 2004.

[297] N. W. S. Kam, M. O'Connell, J. A. Wisdom, and H. J. Dai, "Carbon nanotubes as multifunctional biological transporters and near-infrared agents for selective cancer cell destruction," *Proceedings of the National Academy of Sciences of the United States of America*, vol. 102, no. 33, pp. 11600–11605, 2005.

[298] G. Placzek, *Rayleigh-Streuung und Raman-Effekt*, vol. VI. Akademische Verlag, Leipzig, 1934.

[299] D. Long, *The Raman Effect*. Chichester, England: John Wiley & Sons, Ltd., 2002.

[300] H. Schrötter and H. Klöckner, *Raman Spectroscopy of Gases and Liquids*, vol. 11. Berlin Heidelberg New York: Springer-Verlag, 1979.

Summary

Chapter 1 provides a brief summary of the biomedical applications of gold nanoparticles in the present and in the past. The popularity of gold nanoparticle application can be ascribed to gold nanoparticle biocompatibility in combination with enhanced absorption cross-sections, which are due to the presence of surface plasmons. Rod-shaped gold nanoparticles are particularly attractive for non-invasive detection and treatment, because their tunable plasmon bands enable application within the near-infrared optical window.

Particle syntesis and subsequent surface treatments are discussed, as these processes determine the absorption characteristics and the functionalisation of the particles. The latter determines the cytotoxicity and uptake of gold nanoparticles by cells.

Gold nanoparticles play an important role as contrast enhancing agents in the detection of early stage carcinomas, which is subject of many current studies. A first step in the characterisation of the interaction of gold nanoparticles with cancer cells is the detection of these particles on cancer cells. In the remainder of the thesis, both microscopic and spectroscopic imaging techniques are used and evaluated for this purpose.

The confocal Raman microspectroscopic setup that is used for the experiments in this thesis is described in **Chapter 2**. The setup is based on the principles of Raman scattering and confocal microscopy, which are both introduced in this chapter. Raman scattering describes an inelastic scattering process, causing a frequency shift in photons emitted from a molecule with respect to the incident photons. Because the Raman frequency shifts are characteristic for each molecular binding, this effect enables the molecular analysis of cellen without the use of additional stainings.

The data correction and analysis routines are explained on the basis of Raman measurements on both live and fixated SK-BR-3 breast carcinoma cells, which are a standard model in breast cancer research. We determined initial Raman fingerprints of these cells and showed the effect of standard paraformaldehyde cell fixation methods on the spectral response of the cells.

Before the effects of gold nanoparticles on cancer cells can be addressed, knowledge of the unperturbed cells is required. In **Chapter 3** the chemical composition of single live cells from the ductal breast carcinoma cell lines MDA-MB-231, MDA-MB-435s and SK-BR-3, was determined With Raman microspectroscopic imaging. These cell lines express the Her2/neu receptor in different extent. The Her2/neu proto-oncogene is amplified in 25 to 30 percent of human primary breast

carcinomas and is therefore a common prognostic and predictive factor in tumour subtype screening. Consequently, the Her2/neu receptor is often utilized as target for therapy.

Previously, Her2/neu was shown to have different relations to intracellular lipid composition. SK-BR-3 cells exhibit a Her2/neu receptor overexpression, whereas the MDA-MB cell lines show little to no expression. Our Raman experiments showed that lipids are prominently present in all three cell lines. From Raman difference spectra, it appeared that the MDA-MB cell lines contain increased lipid contents with a lower degree of fatty acid saturation, compared to the SK-BR-3 cells. Hierarchical cluster analysis was applied to verify these results and additionally showed high internal consistency of the chemical compositions in the cell lines. Although in literature, cell metabolic rate or senescence has been suggested to influence the polyunsaturated fatty acid contents of the cell, our results suggest that the degree of metastaticity of the cells plays a major role.

In **Chapter 4**, Raman microspectroscopy was used to characterize in house synthesized GNR in dispersion before they were administered to SK-BR-3 cell cultures. The GNR showed broadband emission profiles which dominate the optical emission spectra. Because this emission saturated with increasing laser power, it was characterized as fluorescence. The fluorescence emission does not change upon washing and surface treatment steps that are required to reduce GNR cytotoxicity.
Raman mapping of SK-BR-3 cells incubated with GNR revealed that the emission of GNR in the cells differs from that of GNR in aqueous dispersions. Moreover, the spectral distribution was spatially non-uniform and changes for GNR at different locations in the cells. Although the fluorescence dominates the Raman fingerprint region (500-1800 cm^{-1}), the higher wavenumbers are little or not affected. The Raman signature in this region shows a coincidence of increased lipid signals with intracellular locations of the GNR, suggesting that GNR are locally accumulating in lipid vesicles within the cells.

The fluorescence emission of GNR in dispersions was further investigated and compared with literature reports on this phenomenon in **Chapter 5**. First reports on the photoluminescence of gold date from 1969. It was found that the luminescence behaviour was due to intrinsic properties of the electronic structure of the gold metal. Emission in the visible generally peaks around 560 nm and was attributed to electronic $sp \rightarrow d$ interband transitions. Broad emissions in the infrared have also been reported and were ascribed to intraband transitions.

For gold nanorods (GNR), different emission profiles were reported in literature, covering both visible and IR emission. We observe GNR emission at energies in between the energies associated with interband or intraband transitions. The position and the intensity of the fluorescence emission peak varies with the GNR aspect ratio (AR), indicating an effect of the longitudinal surface plasmon absorption. The observed fluorescence is ascribed to $sp \rightarrow d$ interband transitions in agreement with previous reports and is analoguous to bulk gold emission. The measured variation in fluorescence emission profiles was understood to be the result of plasmon enhancement. THe maximum of the longitudinal plasmon absorption band of GNR is size-dependent and enhances the spectrally overlapping emission band.

In **Chapter 6**, the intrinsic resolution of scanning electron microscopy (SEM) was exploited to visualise the interaction of GNP with SK-BR3 breast cancer cells. In general, biological samples are coated with heavy metals in order to obtain high resolution images in conventional below lens SEM systems. We developed a sample preparation protocol for high resolution imaging of gold nanoparticles on SK-BR-3 breast cancer cells in a conventional SEM, eliminating heavy metal coating. By making use of the differences in electron scattering efficiency between cellular and metallic materials, excellent contrast between cells and GNP could be obtained. GNR as small as 20×40 nm could be visualized on SK-BR-3 breast cancer cells and quantitated with automated routines.
When these samples were subjected to Raman microspectroscopic imaging, GNR could be detected in the cells by their fluorescence responses as well as by their susceptibility to heat generation.

The dominating fluorescence emissions of GNR in cells obstruct specific assignment of subcellular locations. Therefore, in **Chapter 7** the use of the near-infrared dye indocyanine green (ICG) as a Raman marker for GNR was suggested. Currently, ICG is already in use for the detection of tumorous metastasis in clinical imaging applications. ICG exhibits an environment dependent organization due to its amphiphilic nature. These organizational changes are reflected in optical changes that can be measured with absorption and fluorescence spectroscopy. Both the absorption and the emission data show that the presence of GNP shifts the ICG monomer-dimer equilibrium towards higher monomer concentrations, suggesting that ICG adsorbs as a monomer to the gold surface.

The concentrations of Ag^+ or CTAB, which are crucial to GNR synthesis, affect the ICG monomer-dimer equilibrium. CTAB micellar structures compete for the available ICG, because ICG intercalates in the micelles. Thus, the presence of CTAB above the critical micellar concentration (cmc), limits the ICG adsorption onto GNP. On the other hand, Ag^+ deposition on GNP leads to an overall increase in ICG adsorption on the metal surface, apparently as a result of a strengthening of the dye-metal interaction. These findings stress the importance of careful control of experimental conditions for effective dye labelling of gold nanostructures.

Chapter 8 describes a promising strategy to gain better insight in the spatial distribution of the GNR within breast cancer cells and their local intracellular interactions. In this thesis, mainly two dimensional Raman microspectrscopic imaging was used. By extending the existing imaging system with a 3D modality, cells can be analysed into greater detail. The optimal imaging conditions are determined by resolution of the confocal system determines as well as by the nature of the samples. Initial measurements performed on fixated SK-BR-3 allowed the assignment and localization of intracellular components with depth resolution.

Within SK-BR-3 cells that were incubated with GNR before fixation, GNR fluorescence was detected at several intracellular locations. Both the observed emission profiles of the GNR and the intracellular chemical composition were in agreement with our previous findings in Chapters 3, 4 and 5. However, while in Chapter 4, GNR were solely detected in colocalisation with pronounced lipid signals, in 3D imaging GNR were depicted close to the nuclei as well. In order to obtain more conclusive data, the axial resolution of the 3D Raman imaging

system should be improved.

The imaging system requires additional adjustments for live cell imaging, which would enable deeper understanding of the intercellular mechanisms involved in the distribution and fate of GNR in breast cancer cells. To prevent the cells from moving and even dying during measurement, the image acquisition time has to be drastically reduced. However, the high laser power required to maintain a sufficient signal-to-noise ratio may affect the emission of the GNR if present.

Samenvatting

Dit proefschrift behandelt de optische eigenschappen van gouden nanostaafjes en de interactie van deze nanostaafjes met borstkankercellen van het ductaal carcinoomtype. Ramanmicrospectroscopie neemt hierbij een centrale positie in. Ramanmicrospectro-scopie is een optische techniek die afbeelding en analyse van chemische samenstellingen mogelijk maakt. Deze techniek verschaft inzicht in het lichtverstrooiingskarakter van de nanostaafjes, alsmede van de chemische reacties die de staafjes oproepen in de cellen.

Hoofdstuk 1 omvat een korte samenvatting van in het gebruik van gouden nanodeeltjes in biomedische toepassingen in heden en verleden. Die toepassing berust op de aantrekkelijke optische eigenschappen van gouden nanodeeltjes, die gebaseerd zijn op de aanwezigheid van oppervlakteplasmonen. Er wordt ingegaan op de synthese van gouden nanodeeltjes, die de absorptiebanden van oppervlakteplasmonen beïnvloedt. Aangezien de toepassing van lichaamsvreemd nanomateriaal in biologische systemen specifieke eisen met zich meebrengt, wordt ook ingegaan op het het geschikt maken van de nanodeeltjes voor biomedische toepassingen. Een belangrijke toepassing van gouden nanodeeltjes is die van contrastverbeteraar voor het in kaart brengen van kankergezwellen. Deze toepassing wordt nog volop onderzocht, hetgeen begint met de detectie van gouden nanodeeltjes op kankercellen door middel van onder andere microscopie en spectroscopie. Beide detectiemethoden worden in dit proefschrift verder belicht en onderzocht.

In **Hoofdstuk 2** wordt uitgelegd hoe de confocale micro-Ramanopstelling werkt die gebruikt is voor de experimenten. De achterliggende principes van het Ramanverstrooiingseffect en confocale microscopie worden geïntroduceerd. In het Ramanverstrooiingsproces treedt een frequentieverschuiving op door interactie tussen fotonen en moleculen. Hierdoor is het mogelijk de moleculaire samenstelling van cellen af te beelden zonder aanvullende kleuringen te gebruiken.

De correctie- en analysemethoden voor de verkregen Ramangegevens worden uitgelegd aan de hand van Ramanmetingen aan SK-BR-3 borstcarcinoomcellen. De metingen illustreren tevens het effect van de standaard celfixatiemethode op de spectrale respons van de cellen.

Aangezien het fixeren van cellen hun Ramanspectra beïnvloedt, beschrijft **Hoofdstuk 3** de Ramanrespons van levende borstcarcinoomcellen. De moleculaire samenstelling van een drietal cellijnen is hiermee vastgesteld. De bestudeerde cellijnen hebben verschillende expressieniveaus van de Her2/neu receptor. Deze receptor is een veelgebruikte indicator in het vaststellen en de behandeling van

borstkanker. Uit de Ramanverstrooiingsgegevens blijkt dat vetten prominent aanwezig zijn in alle onderzochte cellijnen. Het verzadigingsgehalte van de aanwezige vetzuren lijkt gerelateerd te zijn aan de mate van metastasering (uitzaaiingsgraad) van de cellijn in kwestie.

In **Hoofdstuk 4** wordt beschreven hoe de moleculaire samenstelling van SK-BR-3 borstcarcinoomcellen verandert in aanwezigheid van gouden nanostaafjes. Met behulp van Ramanspectroscopie zijn eerst de spectrale eigenschappen van de nanostaafjes in oplossing in kaart gebracht. Oplossingen van gouden nanostaafjes geven een breedbandige respons die verzadigt wanneer de hoeveelheid inkomend licht toeneemt, hetgeen fluorescentie impliceert.

Door hun fluorescente eigenschappen kunnen de gouden nanostaafjes ook gedetecteerd worden wanneer ze aan borstkankercellen toegevoegd zijn. Echter, de spectra van gouden nanostaafjes in de cellen verschillen van de oplossingsspectra. Bovendien verschillen de emissiespectra per locatie in de cel. Hoewel de fluorescente emissie grote delen van het Ramanspectrum van de cellen overschaduwt, kan uit het Ramansignaal in de hogere golflengtes afgeleid worden dat de nanostaafjes zich ophopen in de vettige transportbolletjes in de cellen.

Hoofdstuk 5 gaat dieper in op de fluorescente emissie van de gouden nanostaafjes. De eerste vermeldingen van de fluorescentie van goud in de wetenschappelijke literatuur dateren uit 1969. Het fluorescente gedrag van goud wordt hierin toegeschreven aan de elektronische structuur van het metaal en is derhalve een materiaalintrinsieke eigenschap. Goud vertoont fluorescente emissie in een tweetal spectrale gebieden, afhankelijk van de aangeslagen elektronische overgang. Emissie rond 560nm komt overeen met een overgang tussen de elektronische *sp*- en *d*-banden, een interbandovergang. In het infrarood komen breedbandigere emissies voor die veroorzaakt worden door overgangen binnen de *sp*-band, intrabandovergangen.

De door ons gemeten emissieprofielen van gouden nanostaafjes ligt hier precies tussenin. De positie van de fluorecentiemaxima verschuift met een verandering in afmeting van de staafjes: hoe langer de staafjes, hoe roder de emissie. Deze observatie komt overeen met de resultaten van anderen, en wordt getypeerd als het "bliksemafleider-effect". Oppervlakteplasmonen spelen hierin een belangrijke rol door de emissie te versterken. De mate van versterking hangt af van de mate van waarin de absorptieband van het oppervlakteplasmon overlapt met het $sp \rightarrow d$ interband emissieprofiel en met de golflengte van het inkomende licht. Het absorptiemaximum van oppervlakteplasmonen hangt samen met de afmetingen van de nanostaafjes, hetgeen de relatie tussen de gemeten emissie en de vorm van de nanostaafjes verklaart.

In **Hoofdstuk 6** wordt een nieuwe methode beschreven waarmee de gouden nanostaafjes zichtbaar te maken zijn op kankercellen met een standaard scanning elektronenmicroscoop (SEM), waarbij de elektronendetector onder de lens geplaatst is.

Contrast in de SEM is onder meer afhankelijk van de elektronische geleiding van het specimen. Om voor voldoende contrast te zorgen tussen de gouddeeltjes en biologische materialen, worden over het algmeen chemische kleurtechnieken toegepast, waarbij gebruik gemaakt wordt van zware metalen.

De nieuwe methode maakt dergelijke kleurtechnieken overbodig. Door de kankercellen te kweken op een dun goudlaagje wordt ophoping van elektronische lading voorkomen. Hierdoor kan optimaal gebruik gemaakt worden van het verschil in de hoeveelheid elektronenverstrooiing van de gouddeeltjes en het celmateriaal. Dit verschil in materiaaleigenschappen levert een contrast op dat hoog genoeg is om een beeld te krijgen van gouden nanostaafjes van 20×40nm die zich aan de oppervlakte van SK-BR-3 borstcarcinoomcellen bevinden.

De SEM-preparaten die volgens het nieuwe protocol zijn gemaakt kunnen ook gemeten worden met Ramanspectroscopie, waarbij de gouden nanostaafjes te herkennen zijn aan hun fluorescente emissie. Daarnaast zorgt de lokale warmteontwikkeling rondom de gouddeeltjes voor een herkenbaar Ramansignaal.

De breedbandige fluorescente emissie van de gouden nanostaafjes beperkt nauwkeurige plaatsbepaling van de staafjes in de cellen. De plaatsbepaling kan verbeterd worden door de nanostaafjes te voorzien van een markeermolecuul met een specifiek en sterk Ramansignaal. **Hoofdstuk 7** beschrijft een strategie om de gouden nanostaafjes te markeren met indocyanine groen (ICG), een kleurstof die oplicht in het nabij-infrarood. ICG is amfiflisch van aard, hetgeen impliceert dat de vorm waarin ICG-moleculen aanwezig zijn, afhankelijk is van de omgeving waarin ze verkeren. De vorm van ICG bepaalt tevens de optische eigenschappen van het molecuul. Hierdoor kan, middels absorptie- en fluorescentiespectroscopische detectie, het effect van gouden nanodeeltjes op de vorm van ICG bepaald worden. Zowel de absorptie- als de fluorescentieresultaten geven aan dat de aanwezigheid van gouden nanodeeltjes adsorptie van ICG aan het goudoppervlak tot gevolg heeft. Daarnaast bleken zilverionen en cetyl trimethylammoniumbromide (CTAB), stoffen die beide onontbeerlijk zijn in de synthese van gouden nanostaafjes, van invloed op de ordening van ICG-moleculen, zowel aan het goudoppervlak als in oplossing. Deze bevindingen onderstrepen het belang van goed gedefinieerde experimentele condities voor het koppelen van markeermoleculen aan gouden nanostaafjes.

Hoofdstuk 8 beschrijft een veelbelovende strategie om een beter beeld te krijgen van de verspreiding van gouden nanostaafjes in cellen. Voor de experimenten in dit proefschrift is voornamelijk tweedimensionale Ramanspectroscopische beeldvorming gebruikt. Door deze uit te breiden met een dieptecomponent kunnen cellen tot in groter detail geanalyseerd worden. De resolutie van de confocale Ramanopstelling bepaalt de randvoorwaarden voor de totstandkoming van een dergelijke uitbreiding. De optimale meetinstellingen worden tevens bepaald door de aard van het specimen.

Aan de hand van deze randvoorwaarden zijn verkennende driedimensionale Ramanmetingen uitgevoerd op gefixeerde SK-BR-3 borstcarcinoomcellen. Hierdoor is de distributie van diverse moleculen op verschillende hoogtes in deze cellen inzichtelijk gemaakt.

Het fluorescente signaal van de gouden nanostaafjes werd op verschillende lokaties in de SK-BR-3 cellen gemeten. De profielen van deze signalen, alsmede de Ramanprofielen van de cellen waren overeenkomstig de eerder gemeten profielen in Hoofdstukken 3, 4 en 5. In Hoofdstuk 4 werden de nanostaafjes vooral gevonden in de omgeving van vettige bolletjes in de cel. 3D beeldvorming suggereerde tevens hun aanwezigheid bij de celkern, hetgeen ongebruikelijk is. Het vereist

gedetaileerdere metingen om hier uitsluitsel over te kunnen geven. Hiervoor zal de axiale resolutie van het systeem verbeterd moeten worden.

Een volgende stap is het meten aan levende cellen om inzicht te krijgen in de celmechanismen die betrokken zijn bij de opname van nanodeeltjes. Dergelijke metingen zullen zo kort mogelijk moeten zijn om bewegingseffecten tegen te gaan en om te voorkomen dat de cellen tijdens de meting sterven. Echter, het vermogen van de inkomende lichtbundel zal hoog genoeg moeten zijn om te resulteren in een Ramansignaal van voldoende sterkte. In het geval er zich gouden nanodeeltjes in de cellen bevinden, zal de toegediende lichtdosis lager dan de deeltjesvervormingslimiet moeten zijn.

Dankwoord

Iedereen die deze pagina heeft weten te vinden, heeft iets voor mij betekend, betekent iets voor mij of gaat nog iets voor mij betekenen, waarvoor mijn hartelijke dank.

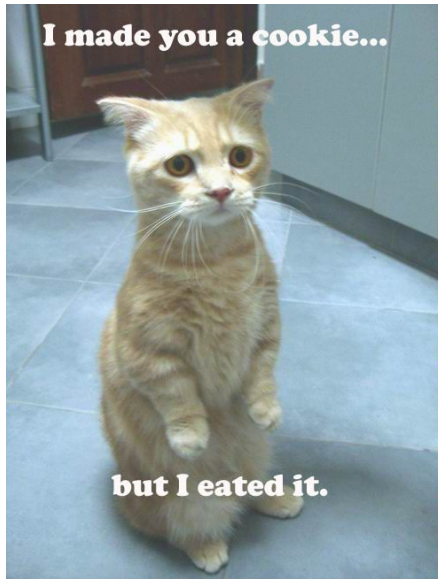

Figuur 1 : *I made you a cookie but I eated it* is a cat(ch)phrase used to reveal one's feeling of shame in taking claim to something that he or she had initially prepared for someone else. Macros containing this phrase usually depict someone or something with a sad-looking face for the cuteness overload effect. "I made you a cookie" is regarded a LOLcat classic. A LOLcat is an image combining a photograph of a cat with text, often idiosyncratic and grammatically incorrect, intended to contribute humour. Despite the poor grammar commonly associated with the LOLcat phenomenon, the phrase originates from a 2005 comic strip from the Pon and Zi web comic by the artist Azuzephre (a.k.a. Jeff Thomas).

List of publications

Journal articles

L. Guerrini, L. Hartsuiker, S. Manohar and C. Otto, "Adsorption of indocyanine green to gold nanoparticles", Nanoscale, 3, 4247-4253, July 2011

L. Hartsuiker, P. van Es, W. Petersen, T.G. van Leeuwen, L.W.M.M. Terstappen and C. Otto, "Scanning electron microscopy detection of gold nanoparticles on individual cells without staining", Journal of Microscopy, 244, Pt 2 2011, 187-193, June 2011

L. Hartsuiker, N.J.L. Zeijen, L.W.M.M. Terstappen, C. Otto, "A comparison of breast cancer tumor cells with varying expression of the Her2/neu receptor by Raman microspectroscopic imaging", Analyst, 135, 3220-3226, October 2010

R.G. Rayavarapu, W. Petersen, L. Hartsuiker, P. Chin, H. Janssen, F.W.B. van Leeuwen, C. Otto, S. Manohar and T.G. van Leeuwen, "In vitro toxicity studies of polymer-coated gold nanorods", Nanotechnology, 21, 1-10, Februari 2010

P.F. Chimento, M. Jurna, H.S.P. Bouwmans, E.T. Garbacik, L. Hartsuiker, C. Otto, J.L. Herek and H.L. Offerhaus, "High-resolution narrowband CARS spectroscopy in the spectral fingerprint region", Journal of Raman spectroscopy, 40, 9, 229-1233, September 2009

M. Jurna, M. Windbergs, C. J. Strachan, L. Hartsuiker, C. Otto, P. Kleinebudde, J. L. Herek, and H. L. Offerhaus, "Coherent Anti-Stokes Raman Scattering microscopy to monitor drug dissolution in different oral pharmaceutical tablets", Journal of Innovative Optical Health Sciences, 2, 1, 37-43, January 2009

B. J. Papenburg, S, Schüller-Ravoo, L.A.M. Bolhuis-Versteeg, L. Hartsuiker, D.W. Grijpma, J. Feijen, M. Wessling and D. Stamatialis, "Designing porosity and topography of poly(1,3-trimethylene carbonate) scaffolds", Acta Biomaterialia, 5 (2009), 3281-3294, May 2009

Journal articles in preparation

L. Hartsuiker, W. Petersen, R.G. Rayavarapu, S. Manohar, T.G. van Leeuwen, L.W.M.M. Terstappen and C. Otto, "Raman - and fluorescence spectral imaging of live breast cancer cells incubated with gold nanorods", submitted for publication to Applied Spectroscopy, June 2011

L. Hartsuiker, A.M. Pit, W. Petersen, A. Lenferink, T.G. van Leeuwen, L.W.M.M. Terstappen and C. Otto, "3D emission spectroscopy of gold nanorods reveals their distribution inside breast cancer cells", in preparation for submission to Journal of Raman Spectroscopy, October 2011

Proceeding articles

L. Hartsuiker, W. Petersen, J. Jose, P. van Es, A.T.M. Lenferink, A.A. Poot, L.W.M.M. Terstappen, T.G. van Leeuwen, S. Manohar, C. Otto, "Gold nanoparticles for tumour detection and treatment", Clinical and Biomedical Spectroscopy and Imaging II, Proceedings of SPIE/OSA Biomedical Optics, SPIE, Vol 8087, ISBN: 978-0-8194-8684-4, pp. 80871O.

L. Hartsuiker, W. Petersen, S. Manohar, T.G. van Leeuwen, C. Otto, "Raman mapping of live breast carcinoma cells", Annual Symposium of the IEEE-EMBS Benelux Chapter, November 9-10, 2009, Programme and abstract book, ISBN: 978-90-365-2933-4, pp. 32-35.

Conference contributions (oral)

L. Hartsuiker, P. van Es, W. Petersen, A.T.M. Lenferink, S. Manohar, T.G. van Leeuwen, L.W.M.M. Terstappen and C.Otto, "Visualizing gold nanorods and their broadband emission in live breast cancer cells", European Conference on the Spectroscopy of Biological Molecules 2011, August 29 - September 3, 2011, Coimbra, Portugal.

L. Hartsuiker, P. Van Es, W. Petersen, R.G. Rayavarapu, A.T.M. Lenferink, A.A. Poot, L.W.M.M. Terstappen, T.G. van Leeuwen, S. Manohar and C. Otto, "Visualizing gold nanorods and their fluorescence emission in breast cancer cells", SPIE/OSA European Conferences on Biomedical Optics, May 22-26, 2011, Munich, Germany.

L. Hartsuiker, W. Petersen, A.T.M. Lenferink, S. Manohar, T.G. van Leeuwen, L.W.M.M. Terstappen and C. Otto, "Raman and Fluorescence Emission of Gold Nanorods in Live Breast Cancer Cells", Focus on Microscopy 2011, April 17-20, 2011, Konstanz, Germany.

L. Hartsuiker, P. van Es, N.J.L. Zeijen, S. Manohar, A.A. Poot, A. Van Apeldoorn, T.G. van Leeuwen, L.W.M.M. Terstappen and C. Otto, "Visualizing Gold

Nanoparticles on and in Cancer Cells with varying expression of the Her2/neu receptor", Nederlandse Vereniging voor Technische Geneeskunde Congres, October 1, 2010, Enschede, NL.

L. Hartsuiker, P. van Es, W. Petersen, S. Manohar, T.G. van Leeuwen, A. Van Apeldoorn, A.A. Poot, L.W.M.M. Terstappen and C. Otto, "Visualizing Gold Nanoparticles on and in Cancer Cells", SPEC2010, June 26-July 1, 2010, Manchester, UK.

L. Hartsuiker, W. Petersen, S. Manohar, T.G. van Leeuwen and C. Otto, "Raman mapping of single gold nanoparticles in live cells", 4th Annual Symposium of the IEEE-EMBS Benelux Chapter, November 9, 2009, Enschede, The Netherlands.

Conference contributions (poster)

L. Hartsuiker, W. Petersen, A. Lenferink, S. Manohar, T.G. van Leeuwen, L.W.W.M. Terstappen and Cees Otto, "Gold nanorod emission in live breast cancer cells", Econos 2011 CARS Workshop, May 23-25, Enschede, The Netherlands.

L. Hartsuiker, "Broadband Raman Response of Gold Nanorods in Live Cancer Cells", Fotonica Evenement 2011, March 29-30, 2011, Nieuwegein, The Netherlands.

L. Hartsuiker, R.G. Rayavarapu, W. Petersen, L.W.M.M. Terstappen, T.G. van Leeuwen, S. Manohar and C. Otto, "Raman spectroscopy and imaging of gold nanoparticles with cells", MIRA Event Top Technology for Patients, March 31-April 1, 2010, Hengelo, The Netherlands.

L. Hartsuiker, W. Petersen. R.G. Rayavarapu, S. Manohar, T.G. van Leeuwen, L.W.M.M. Terstappen and C. Otto, "Broadband Raman Response of Gold Nanorods With And Without Cancer Cells", XXII International Conference on Raman Spectroscopy ICORS 2010, August 8-13, 2010, Boston MA, United States.

L. Hartsuiker, P. van Es, W. Petersen, S. Manohar, A.A. Poot, A. Van Apeldoorn, T.G. van Leeuwen, L.W.M.M. Terstappen and C. Otto, "Hybrid imaging of gold nanorods on and in breast cancer cells", Dutch meeting on Molecular and Cellular Biophysics, October 4-5, 2010, Veldhoven, The Netherlands.

L. Hartsuiker, R.G. Rayavarapu, W. Petersen, S. Manohar, T.G. van Leeuwen and C. Otto, "Raman mapping of single gold nanoparticles in cells", European Conference on the Spectroscopy of Biological Molecules 2009, August 28 - September 2, 2009, Palermo, Italy.

L. Hartsuiker, R.G. Rayavarapu, W. Petersen, S. Manohar, T.G. van Leeuwen and C. Otto, "Raman imaging of single gold nanoparticles in live cancer cells", Dutch meeting on Molecular and Cellular Biophysics 2009, September 28-29, 2009,

Veldhoven, The Netherlands.

L. Hartsuiker, R.G. Rayavarapu, W. Petersen, S. Manohar, C. Otto and T.G. van Leeuwen, "Raman molecular imaging of biocompatible nano-colloidal gold surfaces", Fotonica Evenement 2009, April 2, 2009, Nieuwegein, The Netherlands.

L. Hartsuiker, R.G. Rayavarapu, W. Petersen, S. Manohar, C. Otto, and T.G. van Leeuwen, "Molecular distributions at nano-colloidal gold for biocompatibility", XXI International Conference on Raman Spectroscopy ICORS 2008, August 17-22, 2008, Uxbridge, London, United Kingdom.

L. Hartsuiker, R.G. Rayavarapu, W. Petersen, A.A. Poot, I. Vermes, S. Manohar, T.G. van Leeuwen and C. Otto, "Towards biocompatible gold nanoparticles: a Raman study", Fotonica Evenement 2008, April 02, 2008, Nieuwegein, The Netherlands.

S. Manohar, L. Hartsuiker, J. Jose, W. Petersen, C. Ungureanu, R.G. Rayavarapu, A.A. Poot, I. Vermes, C. Otto and T.G. van Leeuwen, "Plasmon resonant nanoparticles for molecular tumour imaging and therapy", Workshop MESA$^+$ - University of Münster, April 1, 2008, Enschede, the Netherlands.

Stellingen

behorende bij het proefschrift

Microspectroscopic characterisation of gold nanorods for cancer cell detection

I — Alleen na excitatie kan relaxatie plaatsvinden.
(Hoofdstuk 2)

II — De pot met goud staat aan het begin van de regenboog.
(Hoofdstuk 5)

III — Zonder overlap tussen je eigenschappen en de input uit je omgeving blijf je in het duister tasten.
(Hoofdstuk 4, 5)

IV — Alvorens goud in Raman kleur kan bekennen, dient de oppervlaktechemie kristalhelder te zijn.
(Hoofdstuk 7)

V — Meer dimensies impliceren vooral meer data.
(Hoofdstuk 8)

VI — Ook met vallen en opstaan is te finishen in een goede tijd.

VII — Het plaatsen van een minteken voegt in wezen niets toe.

VIII — Online is Schrödingers kat springlevend.

IX — Het is beter naar buiten te kijken, dan op de buienradar.

X — Analoog aan electronen, kan een aangeslagen mens hogere niveaus bereiken om vervolgens te kunnen stralen.
(Dit proefschrift)